

Technische Universiteit Delft

Modelling stability of Avicennia marina mangroves under wave and wind loads

Effect of soil and root system on tree resistance

Murielle Denise van Pampus

TU Delft Deltares

Modelling stability of Avicennia marina mangroves under wave and wind loads

Effect of soil and root system on tree resistance

by

Murielle Denise van Pampus

in partial fulfilment of the degree of Master of Science
in Hydraulic Engineering and Geo Engineering,
to be defended publicly on 18-01-2023

Faculty of Civil Engineering and Geosciences
Track of Hydraulic Engineering
Specialization of
Coastal Engineering and Flood risk
and
Track of Geo Engineering

at the Delft University of Technology.

Student number: 4387449
Project duration: May, 2022 – January, 2023
Thesis committee:

Dr. ir. B. Hofland	TU Delft, Chair
Dr. ir. S. Muraro	TU Delft, supervisor
Dr. Ir. A. Gijón Mancheño	TU Delft, daily supervisor
Dr. ir. M. van der Krogt	Deltares, daily supervisor

TU Delft Deltares

Acknowledgment

Dear reader,

Before you lies my final thesis for my master in Civil Engineering, for both the track Geo Engineering and Hydraulic engineering. This thesis also marks the end of my time in Delft, which I have enjoyed very much. After 3,5 years of doing a double track, I hoped that I would not regret this decision, and I can fairly say: I do not regret doing the double track. During both tracks, I have enjoyed the combinations of water and soil, mainly on the field of Building with Nature solutions. Luckily, I was able to combine both in this thesis. Often, friends around me told me there would be a moment when I would not like doing my thesis anymore. Luckily that moment has not come. Mainly, I believe, because I find the subject that interesting and firmly believe in the capabilities of Building with Nature solution, especially if you combine them with geotechnical knowledge.
Before wishing you pleasure reading, I would like to thank some people who supported me a great deal.

First of all, I would like to thank Alejandra Gijón Mancheño and Mark van der Krogt who were my daily supervisors. The meetings brainstorming over the results and schematization were really helpfull, mainly when I had the feeling of being stuck. Secondly, I think the report really improved really improved because you helped me structure my thoughts and gave feedback on my writing. Thank you for the effort you both put in. I also want to thank Stefano Muraro for his help during this thesis. Our meetings were always very usefull, mainly when there was no data available on the needed soil property. Furthermore, I would like to thank my chair Bas Hofland for the guidance and enthausiasm during my thesis and the feedback on the report. Next, I would like to thank Su Kalloe for doing the Vane Shear tests in Suriname and Corinne van Starrenburg for letting me attend the pulling experiments performed on willows.

Last but not least, I would like to thank my family, roommates and friends for their support and grammar corrections, even when it was not your cup of tea.

Murielle Denise van Pampus
Rotterdam, 2023

Abstract

Mangroves can provide coastal protection by attenuating waves, currents, and trapping sediment (Menéndez et al., 2020; Bao, 2011). The effect of mangroves on the hydrodynamics depends on their size, location, density, distribution and morphology of the vegetation (Mendez and Losada, 2004). Mangrove loss during storm events will therefore impact the coastal protection. The soil-root interaction and influences of soil properties in the resistance of a mangrove tree against failure is neglected in most studies of flood protection by mangroves, due to a lack in understading.

This thesis improves the understanding of the soil-root interaction by deriving the schematization for multiple failure mechanisms in comparison with field observations. Firstly, the wind and wave forces are modelled to determine the different loads in the forest. Secondly, a novel schematization was developed of different failure mechanisms considering the soil properties and root system. All results are developed for a case study of a fringe forest in Demak, existing of *Avicennia marina* rooted in a silty, saturated soil. To be able to determine the difference between the seaward and landward edge of the forest, the width of the forest is increased to 500 meter. Also, due to a lack of information on the mechanical strength of *Avicennia m.*, the mechanical properties of *Rhizophora m.* are used, which will overestimate the resistance due to the higher wood density of *Rhizophora m.* (Manguriu et al., 2013).

The results show that the drag forces were largely influenced by the tree architecture (such as vegetation width and height), forest density and inundation of the tree. Larger wind and wave forces, and therefore a larger moment occured if the width of the vegetation increased. If the height of the tree increases, a smaller part of the canopy is submerged. This leads to a decreased area that is exposed to waves and therefore a declined wave force. A higher tree does enlarge the area subjected to wind forces, resulting in an increased total moment. Overall, the 2.8-meter tree analysed in this thesis experienced the largest horizontal forces and moment at the seaward edge of the forest due to the relatively large water depth at this location. Furthermore, the maximum horizontal force and moment shift to the landward edge for larger trees due to the increase of wind contribution. To investigate the stability under these loads, the different failure mechanisms need to be inspected.

The failure mechanisms of root breakage and slippage are not important because of the high safety factors and no observations in the field. The failure mechanism trunk breakage also showed a high safety factor, contradictiory to field observations pulling willow trees. The model results and field observations showed that a combination of upwind soil uplift and bending of roots was found most likely to occur. For this failure mechanism, the roots are schematized as beams with a spring-support on the leeward side of the trunk. The roots are exposed to the weight of the overlying soil and the overturning moment. The model showed that an increase in the participation angle α or root diameter, or increase in root length results in larger stresses in the windward roots. The amount of uplift enlarges when the root diameter or root length increases or the participation angle decreases. The modulus of subgrade reaction and modulus of elasticity influence the distribution of the overturning moment over the leeward and windward roots. The largest difference between the moment inside the leeward and windward roots is found with a high modulus of elasticity or high modulus of subgrade reaction. This difference is in agreement with the contrasting reaction between soil types as stated in literature (Dupuy et al., 2007).

The results show the dependence of the different failure mechanisms on soil and root properties, but also on the forest architecture. This research shows that the incorporation of mangrove stability in wave attenuation models cannot be neglected. Using an effective stress approach, instead of a total stress approach as in this thesis, would provide extra information, such as soil behaviour in time during loading. It is therefore recommended to measure pore pressures under static or cyclic loading, resulting in the progression of the effective stress over time. The inclusion of more accurate soil descriptions would enable reducing uncertainty in nature-based solutions and enables to describe the soil-root reaction to loading over time.

Contents

Acknowledgment i

Abstract ii

1 Introduction 1
- 1.1 Problem introduction . . . 1
  - 1.1.1 History of Building with Nature solutions . . . 1
  - 1.1.2 Relevance of Building with Nature solutions . . . 2
  - 1.1.3 Mangroves . . . 2
- 1.2 Objective and research questions . . . 2
- 1.3 Research approach and thesis outline . . . 3

2 Theoretical background 4
- 2.1 Decline of mangrove area . . . 4
- 2.2 Mangrove forest - outline . . . 4
  - 2.2.1 Types of mangrove forest . . . 5
  - 2.2.2 Zonation within forest . . . 6
  - 2.2.3 Sediment properties . . . 6
  - 2.2.4 Differences between mangrove species . . . 7
  - 2.2.5 Differences within mangrove species . . . 8
- 2.3 Root system mangrove species . . . 8
  - 2.3.1 Species: *Avicennia marina* . . . 8
- 2.4 Anchoring of different trees . . . 10
  - 2.4.1 Structural characteristics . . . 10
  - 2.4.2 Asymmetry . . . 11
  - 2.4.3 Anchoring in different soils . . . 11
- 2.5 Determination biomass underground and aboveground root system . . . 12
- 2.6 Rooted soil shear strength . . . 13
- 2.7 Root breakage . . . 14

3 Methodology 15
- 3.1 Project Scope . . . 15
  - 3.1.1 Different failure modes . . . 15
- 3.2 Modelling forces acting on the tree . . . 18
  - 3.2.1 Wave forces . . . 19
  - 3.2.2 Wind forces . . . 19
  - 3.2.3 Overturning moment . . . 20
- 3.3 Schematization of failure mechanisms . . . 20
  - 3.3.1 Failure mechanism: Soil bearing capacity . . . 21
  - 3.3.2 Failure mechanism: Uplift of soil at the windward side . . . 21
  - 3.3.3 Failure mechanism: Root breakage . . . 27
  - 3.3.4 Failure mechanism: Root slippage . . . 27
  - 3.3.5 Failure mechanism: Trunk breakage . . . 28

4 Parameters used for test case Demak, Indonesia 30
- 4.1 Wind and wave parameters . . . 30
  - 4.1.1 Bathymetry . . . 30
  - 4.1.2 Wave height and wave period . . . 31
  - 4.1.3 Wind velocity . . . 31
  - 4.1.4 Coefficients in wind and wave formulas . . . 32

4.2 Input tree properties . . . 32
4.2.1 Determination of above- and below-ground biomass . . . 32
4.2.2 Tree density, basal area and average tree diameter . . . 33
4.2.3 Canopy height and frontal area . . . 34
4.2.4 Varying versus constant tree height . . . 34
4.2.5 Root system depth . . . 35
4.2.6 Root contribution to the resistance . . . 35
4.2.7 Tensile, compression, bending tensile strength and Modulus of Elasticity . . . 35
4.3 Soil parameters . . . 36
4.3.1 Undrained shear strength . . . 36
4.3.2 Modulus of subgrade reaction . . . 37

5 Results/Analysis **38**
5.1 Load . . . 38
5.1.1 Magnitude of force and moment . . . 39
5.1.2 Influential factor - Tree height . . . 41
5.2 Resistance . . . 44
5.2.1 Failure mechanisms: Breakage of the roots, slippage of the roots and breakage of the trunk . . . 44
5.2.2 Failure mechanism: Bearing capacity . . . 44
5.2.3 Failure mechanism: Uplift . . . 46

6 Discussion **54**
6.1 Comparison with other calculations of tree stability . . . 54
6.2 Model limitations . . . 55
6.2.1 Loads . . . 55
6.2.2 Resistance . . . 56
6.3 Comparison of different schematizations with field observations . . . 58
6.3.1 Failure mechanism: Uplift of soil . . . 58
6.3.2 Failure mechanisms: Breakage of roots, slippage of roots and breakage of the trunk . . . 59
6.3.3 Pore pressures . . . 59
6.4 Integration over time and the total forest . . . 59
6.4.1 Time dependence . . . 59
6.4.2 Total forest . . . 59
6.5 Neglected failure modes . . . 60

7 Conclusions **61**
7.1 Sub-questions . . . 61
7.2 Main research question . . . 64

8 Recommendations **66**
8.1 Test improvements . . . 66
8.1.1 Soil and tree properties . . . 66
8.1.2 Measure windward and leeward angles . . . 67
8.2 Model improvements . . . 67
8.2.1 Root modelling . . . 67
8.2.2 Progressive failure . . . 67
8.2.3 Total forest . . . 68
8.3 Effective stress approach . . . 68
8.3.1 Time dependent modelling . . . 69

Bibliography **73**

A Extra theoretical background **83**
A.1 Rootsystem . . . 83
A.2 Mangrove growth . . . 83
A.3 Species: *Avicennia marina* . . . 84

A.4 Waves and water levels through a mangrove forest . . . 85
A.4.1 Waves . . . 85
A.4.2 Water level . . . 86
A.5 Additional eco-services of aquatic vegetation . . . 87

B Short recall of useful concepts of soil mechanics 88
B.1 Atterberg Limits: . . . 88
B.2 Shear stress and normal stress . . . 89
B.3 The Mohr-Coulomb model . . . 90
B.4 Effect of drainage conditions on shear strength . . . 91
B.5 Stress paths of saturated fine-grained soils . . . 91
B.6 Undrained strength . . . 92
B.7 Coefficient of Consolidation . . . 93

C schematization Appendix 94
C.1 Failure mechanisms which are excluded from the research . . . 94
C.2 Bearing capacity . . . 96
C.2.1 Undrained conditions . . . 96
C.2.2 Drained conditions . . . 97
C.3 Methods to determine the bonding strength . . . 99
C.3.1 Interface shear strength . . . 99
C.4 Primary schematizations Uplift . . . 100
C.4.1 Short roots - situation 1 . . . 100
C.4.2 No movement at the end of the leeward root - situation 2 . . . 100
C.4.3 No movement at the end of both roots - situation 3 . . . 101

D Modelling wave and wind forces 103
D.1 Calculation wave forces through the forest . . . 103
D.1.1 Formulas . . . 103
D.1.2 Wave breaking . . . 105
D.1.3 Breaking due to vegetation . . . 105
D.2 Calculating wind forces through the forest . . . 105

E Detailed explanation determination parameter case study Demak 107
E.1 Input parameters . . . 107
E.2 Wave height, wave period and waterlevel . . . 107
E.2.1 Offshore wave height and wave period . . . 107
E.2.2 Surge at 5.5 km offshore . . . 107
E.2.3 Waterlevel at different location in the forest . . . 108
E.3 Canopy width - vegeation with . . . 109
E.3.1 Average DHB in Demak . . . 109
E.4 Soil properties . . . 109
E.5 D_{50} . . . 109
E.5.1 Particle size distribution . . . 110
E.5.2 Bulk density . . . 111
E.5.3 Consolidation tests . . . 111
E.5.4 Vane shear tests . . . 112
E.5.5 Salt factor determination . . . 112
E.6 Result vane shear test in Suriname . . . 113

F Validation of modelling 115
F.1 Validation Vuijk . . . 115
F.2 Validation drag and inertia force . . . 116
F.3 Wind Validation . . . 117

G Extra graphs of loads **119**
G.1 Wave forces . . . 119
G.1.1 Results for daily conditions . . . 119
G.1.2 Extra results for a return period of 20 years . . . 123
G.1.3 Total wave force for different return periods . . . 126
G.2 Wind forces . . . 128
G.2.1 Wind force over the vertical for daily conditions and a return period of 20 years . . . 128
G.3 Gust factor . . . 131
G.3.1 Total force . . . 132
G.3.2 Extra results for the increase of tree height . . . 133

H Detailed results resistance modelling **137**
H.1 Breakage . . . 137
H.2 Slippage . . . 138
H.3 Shallow foundation . . . 139
H.4 Uplift . . . 139
H.4.1 Equal root length and diameter . . . 139
H.4.2 Multiple root lengths and diameters . . . 140

I Pictures mangrove trees and other species **144**
I.1 Pictures of the mangrove forest in Wijk aan Zee, Paramaribo, Suriname . . . 144
I.2 Fallen trees of other species . . . 147

J Python code **150**
J.1 Wind and wave modelling . . . 150
J.2 Failure mechanisms . . . 162
J.2.1 Root breakage . . . 162
J.2.2 Root slippage . . . 163
J.2.3 Soil movement - shallow foundation . . . 166
J.2.4 Soil movement - Uplift . . . 167

1

Introduction

1.1. Problem introduction

1.1.1. History of Building with Nature solutions

From the first human settlements, protection from water has been an important subject to avoid drowning and diseases. To protect from floods and water related diseases, the ancient Greeks avoided living near rivers (Angelakis et al., 2019; Zuidhoff and Dijkstra, 2011). The remains of Minoan and Roman flood protection works, like anti-flood dams, river diversion infrastructures and drainage works from 3200 - 1400 AD can also be found in Knossos, Aptera and Kissamos all located in Crete (Angelakis et al., 2019). In the Netherlands, the first farms in Zeeland on elevations in the salt marsh date from in the Iron Age (1800 - 500 B.C.) (Zuidhoff and Dijkstra, 2011). Moreover, some of the current protection methods were developed in ancient times. For example, planting vegetation to retain extra water, terracing hillsides to slow flow downhill, and the construction of man-made channels to divert floodwater (IWA Publishing). During the past centuries, the ways to prevent flooding were under constant development.

In the 20th century, the relationship between the water and the Dutch moved back and forth. Large land reclamations were followed by major inundation floods. The Afsluitdijk was constructed after a major flood in 1916, while the Deltawerken were constructed after a major storm surge in 1953. Those two floods, combined with the increasing influence of the central government and technical advances, led to a different approach in flood protection. The Netherlands now had an elaborated system of 53 dike ring areas. Those rings used to be divided in four groups, each having its own level of protection. These protection standards were much higher than before (Huizinga, 2012). In the 20th century, the dominant way of protection would be the 'traditional' way, using hard structures, like groins, revetments, breakwaters or dams. Currently, the probability of flooding is considered for each dike ring. The probability and consequences of a breach are determined per section. Using those two, the risk of a breach is determined: Probability times consequence equals risk (Expertisenetwerk waterveiligheid, 2017).

After a lot of research and thought about how to implement those high safety levels, the way of thinking about water protection changed. Hard structures were not the only solution for flood problems anymore. For example the program 'Room for the River' started in 2006. During the 21st century the interest in incorporating ecology and ecosystem services into coastal protection has gained volume (Borsje et al., 2010). This incorporation is triggered by two main reasons. Firstly, climate change causes multiple threats, like the accelerating sea level rise and the increasing frequency of extreme events. The need for innovative, sustainable and cost-effective coastal protection solutions to deal with these threats is strong and still increasing. Secondly, there is a need for measures that minimize anthropogenic impacts of coastal protection structures on ecosystems and that might even offer possibilities to enhance ecosystem functioning (Day et al., 2008).

1.1.2. Relevance of Building with Nature solutions

The cost of maintaining coastal safety increases when larger infrastructures are needed (Fonseca and Cahalan, 1992). The incorporation of ecology and ecosystem services can play a role in reducing these costs. Aquatic vegetation has the ability to influence the coastal hydrodynamic energy, depending on the size, location, density, distribution and morphology of the vegetation (Mendez and Losada, 2004). By producing turbulence and dissipating wave energy, aquatic vegetation can decrease the impact of the waves on the shore (Vuik, 2019). This reduces the design wave conditions, and therefore the required height of barrier structures, resulting in lower construction and maintenance costs (Mendez and Losada, 2004; Borsje et al., 2010).

Two sets of unknowns are important to determine whether a coastal ecosystem can guarantee enough safety to be incorporated into a defence scheme. The first unknown relates to the ecosystem performance during a single storm event, while the second one relates to its evolution over time (Bouma et al., 2014). For the first set of unknowns, the resistance of an ecosystem under relevant storm conditions within a site-specific time-frame should be assessed, the short-term persistence of the ecosystem. Important factors in this determination are the wave attenuation by intertidal coastal ecosystems, the importance of bio-geomorphological effects, so the combination of wave attenuation and seasonal biomass losses and the effect of the ecosystem on flood propagation over time and space.
For the second set of unknowns, the long-term persistence of the ecosystem over the site-specific time-frame should be assessed. Important factors during this assessment are the survival of the ecosystem under the effects of sea-level rise and the long-term persistence under increased storminess (Bouma et al., 2014).
Overall, without knowing the stability of a coastal ecosystem (short- and long-term), the reliability of the ecosystem cannot be guaranteed and therefore the coastal ecosystem cannot be incorporated in a coastal defence system.

1.1.3. Mangroves

Mangrove forests are an example of a coastal ecosystem that provides coastal protection as a stand alone solution or in combination with other coastal structures (Menéndez et al., 2020; Bao, 2011; Quartel et al., 2007). It is recognised that mangroves play an important role in stabilizing shorelines, minimizing impact of waves, winds and surges and trapping sediments (Bao, 2011). The dissipation of waves can be modelled quite accurately using the work done by the drag forces acting on the tree (van Hespen et al., 2021; Quartel et al., 2007; van Wesenbeeck et al., 2022). To be able to keep dissipating waves, the trees need to withstand the wave-driven loads. An important factor in this survival is the stability of trees below the ground, which is mainly determined by their roots. The soil-root interaction is not well understood, which results in a lack of knowledge about the resistance against waves and wind forces. This knowledge gap makes it very difficult to predict the extent of the damages suffered by a mangrove forest during a storm, as the resistance forces created by the root-soil interaction are unknown.

1.2. Objective and research questions

The aim of this research is to model the resistance forces of the root system of an *Avicennia marina* mangrove. The resistance forces cause stability against the loading due to wind or waves. Defining the resistance forces will enable predicting the potential failure of trees. For this research, the following research question has been formulated:

How can the stability of an *Avicennia marina* be best described in a mechanical model taking into account the soil properties and root system compared with field observations?

The research question is approached by answering the following sub-questions:

- *What are the different failure mechanisms of mangrove trees in a healthy forest under extreme storm conditions?*

- *Which loads, soil properties and forest geometry parameters influence the resistance against failure of the mangroves?*
- *How can the different failure mechanisms under wind and wave loading be schematized?*
- *How do different factors (wind, wave and soil properties) affect the stability of a mangrove tree taking into account the soil properties and root system?*

1.3. Research approach and thesis outline

In this introduction, the importance of Building with Nature solution as well as the lack of knowledge regarding the stability of mangroves was explained. This lead to the research question stated in Section 1.2 is derived.

In the second chapter, the necessary theoretical background for the development of the schematizations is explained. This chapter starts with the explanation about mangrove forest and the difference within a forest. Secondly, more detailed information about mangrove trees and their root system will be provided. Also, some information about the anchoring of different tree will be explained. The information of different tree species can be used if to make an assumption about mangrove trees.

The theoretical background combined, with some field observations, is used to determine the methodology. In this methodology the different failure mechanisms are derived. Also, the method used to model the wind and wave loads on a tree is explained. To move on to a more detailed explanation about the formulas and methods used for the schematization of every failure mechanisms. The methodology can be read in Chapter 3.

The case study of the mangrove forest in Demak, Chapter 4, is used as input of the model as explained in Chapter 3. In this chapter, the different parameter of the forest are explained. As some parameter were not available for the forest in Demak, the determination of these parameter based on literature is explained.

In Chapter 5.2, the results of the model are shown, with as input the forest in Demak. This chapter shows the detailed explanation of the different loads through the forest, as well as the influencial factors. Secondly, the results of the schematizations of the different failure mechanisms is shown including the influenctial factors of all schematizations.

In Chapter 6 the pro's and cons of the schematizations are discussed. Most importantly, in this chapter a comparison with field observations has been made.

All these chapter together lead to the conclusion in Chapter 7 combined with the recommandations in Chapter 8.

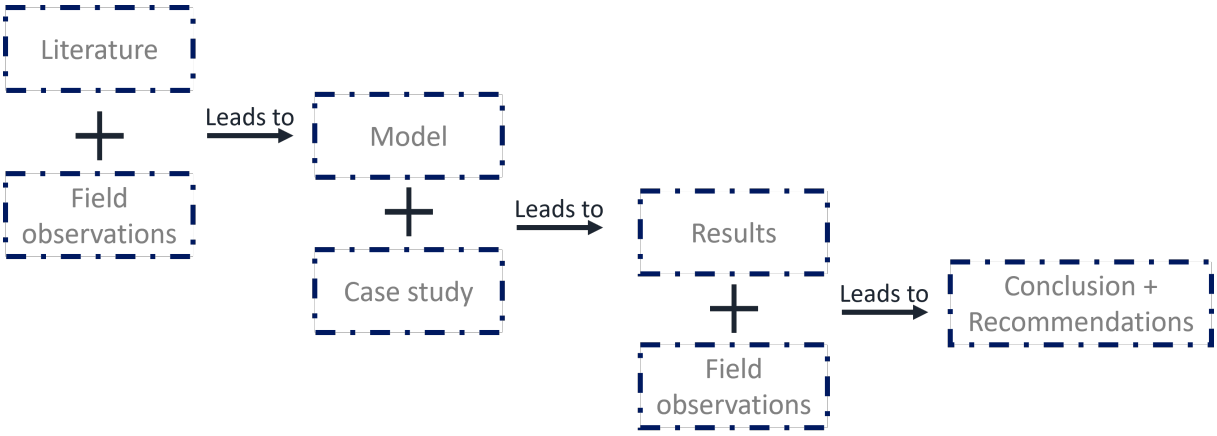


Figure 1.1: Overview of the research approach and thesis outline

2

Theoretical background

In this chapter the needed theoretical background will be explained. This chapter starts with the explanation about mangrove forest and the difference within a forest. Secondly, more detailed information about mangrove trees and their root system will be provided. Also, some information about the anchoring of different tree will be explained.

2.1. Decline of mangrove area

Although mangroves are promoted globally, in the recent decades mangrove forest have been decreasing. In the 1970s, mangroves covered $200{,}000\,\text{km}^2$ (Barbier et al., 2011). This area has decreased tremendously to $135{,}882\,\text{km}^2$ in 2016 (Spalding and Leal, 2021). This decline can be partially attributed to conversion to agriculture and aquaculture. However, it can also be partially attributed to the death of mangrove trees due to multiple possible causes, like erosion, sea level rise and storm damage. The determination of the cause is of high importance as this could have an effect on whether the mangrove forest can really be incorporated into a defense scheme. Research shows that the bandwidth and density of the mangrove forest is of high importance for the amount of wave attenuation measured, which both is influenced by the death of trees (Bao, 2011; Kelty et al., 2022). If a coastal ecosystem is incorporated into the defense scheme, its reliability has to be large and therefore, the system should be well understood. If the cause of death of the mangroves is due to sea level rise, it would largely influence the long-term persistence of the ecosystem. While if the cause of death is extreme wave of wind action, the coastal defense value of the ecosystem within a site-specific time-frame is influenced. The death of individual trees affects the effectiveness of wave dissipation of the entire mangrove forest.

Maza et al. (2021) and Bao (2011) both show the importance of the bandwidth and the density of the forest on the dissipation. If the trees do not survive a storm or are significantly damaged, those factors are decreased. This causes a decrease in the dissipation of waves, and therefore an increase in the wave loads on the structure behind the mangrove forest. To incorporate a coastal ecosystem into a coastal defense system, the reliability of the system needs to be known. This reliability is dependent on the ability of mangroves to survive certain external conditions. This ability to survive certain conditions depends on the resistance forces of a mangrove tree.

2.2. Mangrove forest - outline

In this chapter, the geometry of the mangrove forest will be described. As the geometry differs at different locations of the mangrove forest, it is important to determine these properties and the influence of these properties, as this also determines the forces on a tree and circumstances a tree lives in.

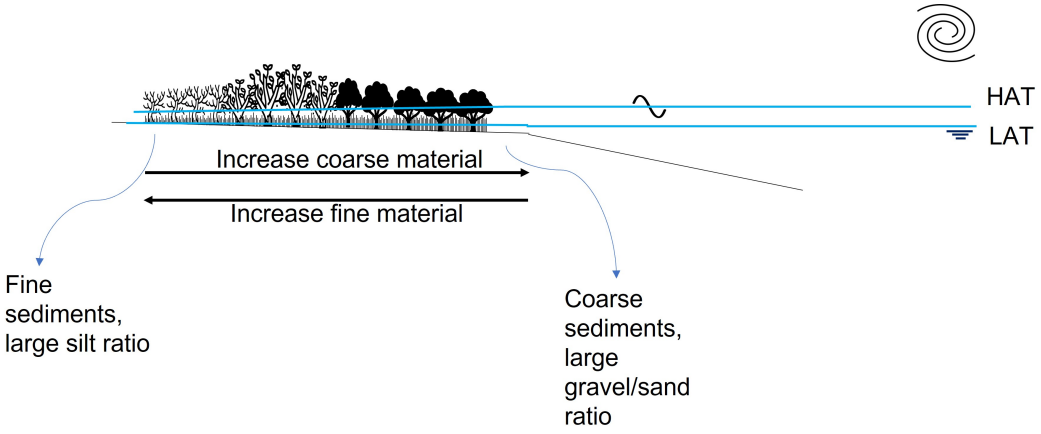


Figure 2.1: Summary of difference within the forest

Figure 2.1 shows an overview of a mangrove forest. This figure indicates the difference between the seaward, landward and interior site. The differences between these locations will be explained in the following sections.

2.2.1. Types of mangrove forest

Based on topographical factors, mangrove forests may be divided into three types: riverine forest, fringe forest and basin forest (Mazda and Wolanski, 2009; Ewel et al., 1998).

Riverine forest

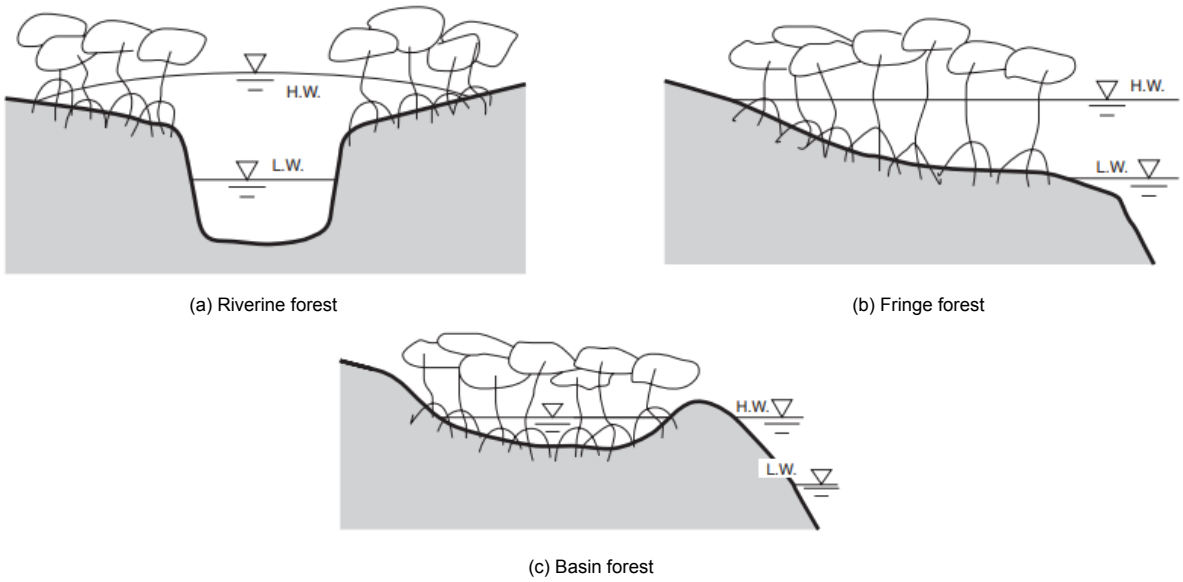
Floodplains along river drainage channels or tidal creeks, which are submerged during high tides and exposed during low tides, are considered riverine forests (Mazda and Wolanski, 2009). Tidal creeks are usually perpendicular to the shore or the estuary banks, and they are quite sinuous, interweaving with other streams inside the forest (Kobashi and Mazda, 2005). Because of the dispersion of wave energy along the lengthy tidal creeks, wind-driven waves and swell seldom travel into the marshes. Swamp water within a few meters of a tidal creek is dragged by the creek's tidal flow, and hence flows parallel to it (Kobashi and Mazda, 2005). Because of the large vegetation-induced friction and the water surface gradient between the swamp and the tidal stream, the flow is largely perpendicular to the creek further inside the swamp (Kobashi and Mazda, 2005; Mazda et al., 2005).

Fringe forest

The fringe forest consists of marshes along shorelines that face the open sea and are subjected to both tidal and sea wave action (Mazda et al., 1997; Maza et al., 2021; Kelty et al., 2022; Mazda and Wolanski, 2009).

Basin forest

The basin forest consists of partially impounded depressions that are rarely inundated by high tides during the dry season, but are flooded during the wet season by spring high tide (John and Lawson, 1990).



(a) Riverine forest

(b) Fringe forest

(c) Basin forest

Figure 2.2: Three different types of mangrove forest (Mazda and Wolanski, 2009)

2.2.2. Zonation within forest

Throughout the forest mangrove species are generally distributed in different zones.
Mangrove species may be found in a variety of ecological zones along the coast. Tidal variations, land elevation, and soil and water salinity all play a role in this zonation. There are three separate zones: proximal zone, middle zone, and distal zone (Alappatt, 2008). The proximate zone is the seaward zone where flooding occurs most frequently. This zone is located along the water's edge and is susceptible to a regular tidal action, resulting in a constant process of soil accumulation and flooding (Alappatt, 2008). For stability and anchoring, the mangrove species in this zone have developed pneumatophores, stilt roots, and prop roots (Srikanth et al., 2015; Tomlinson, 2016; Alappatt, 2008). The dominant species in this zone include *Avicennia marina* and *Sonneratia alba* in rocky or coral reef substrate. *Rhizophora apiculata*, *Rhizophora mucronata* and *Rhizophora stylosa* are found in muddy substrate. Other species found are *Avicennia spp.* and *Sonneratia caseolaris* (Alappatt, 2008).
The middle zone, located on the interior side of the mangroves, is characterized by higher soluble salts in the seawater and trees reaching their maximum height (Alappatt, 2008). Knee roots are common in plants that thrive in this zone. In this region, the dominant species are *Bruguiera gymnorhiza*, *Lumnitzera littiorea*, *Ceriops tagal*, and *Aegiceras corniculatum*. This area is also home to *Bruguiera cylindrica* and *Lumnitzera racemosa* (Alappatt, 2008).
The distal zone is the area closer to the landward side, where salinity is lower and fresh water is more abundant. In comparison to front mangroves, the duration of tidal submersion in this zone is short (Alappatt, 2008). Examples of species occuring in this area are *Heritiera littoralis*, *Cynometra iripa*, *Phoenix paludosa*, *Excoecaria agallocha* and *Xylocarpus granatum* (Alappatt, 2008).

Mangrove zonation is not straightforward and varies from location to location. Tidal activity influences the dispersal of seeds and propagules, hence the range and force of tidal action are important in the development and maintenance of zones (Alappatt, 2008). In addition, the salinity of an estuary is affected by the tides. This affects the species, as every species has a different tolerance for salt (Tomlinson, 2016; Alongi, 2002).

2.2.3. Sediment properties

Because of their location in the landscape, mangrove forests can, overall, trap and retain sediments deposited in the uplands (Parkinson et al., 1994; Lynch et al., 1989). The trapping of sediment is particularly significant in riverine forests, because river water often carries a larger amount of sediment than ocean tides (Ewel et al., 1998). Riverine sediments can in origin be deposited in fringe forest, or have been recirculated within nearshore areas. Basin swamps also trap sediments, catching the tiniest

particles brought by floods and tides past riverine and fringe forests. They may also trap sediments deposited by highland runoff along the swamp's landward edge (Ewel et al., 1998). Removal or the decrease of density of the forest, particularly along the banks of fringe and riverine mangrove forests, exposes sensitive soils to erosion and offshore sediment deposition, which can have large negative effects.

The presence of a river within the forest has a negative effect on the dissipation of waves and the reduction of the water level (Montgomery, 2021). An advantage of channelized forests is the efficient delivery of sediment through the channels, which promotes the accreation within mangroves (Montgomery, 2021). This delivery causes channelized forest to better be able to keep up pace with sea level rise than unchannelized forests (Breda et al., 2021).
Zolkhiflee et al. (2021) shows that the grain size is dependent on the distance from the sea. Which can be explained from the fact that the velocity of the water depends on the deposit of the sediment. Zolkhiflee et al. (2021) looked at three different locations Teluk Tempoyak (TT), Kuala Sungai Pinang (KSP) and Pulau Betond (PB). All three locations were divided into a lower, middle and higher zone. Location Teluk Tempoyak, shows the largest difference between the lower, middle and higher intertidal zones. The lower intertidal zone, closest to the sea has the largest amount of coarse sand particles and gravel, and a smaller amount of small particles. While the middle intertidal zone has a more sandy loam sediment character, and the higher intertidal zone has a clayey loam character. Table 2.1 shows the percentage of silt, clay and sand of the soil samples. From this table it can be concluded that the percentage of sand is higher near the seaside and the percentage decreases to the interior of the forest. From the grainsize distribution at the different locations, it can be concluded that the percentage of smaller grainsizes increases from the seaward edge to the landward edge.

		%Silt	% Clay	% Sand
TT	Lower	5.2	3.7	71.3
	Middle	10.3	5.0	66.7
	Higher	22.4	10.0	38.4
KSP	Lower	21.7	6.8	49.4
	Middle	19.6	11.7	41.6
	Higher	22.4	10.2	37.2
PB	Lower	13.4	3.8	73.4
	Middle	10.6	4.4	71.0
	Higher	17.2	6.0	58.0

Table 2.1: Particle size distribution average from data from Zolkhiflee et al. (2021)

2.2.4. Differences between mangrove species

The differences between the species is important as this influences the rate of reduction of wave height with distance (McIvor et al., 2012). van Hespen et al. (2021) observed a generic pattern across species, where thicker branches are less flexible and can withstand larger forces. The research also showed that larger leaves withstand larger forces before detaching from the tree. The trend where species that occur more seawards have significantly stronger branches but weaker leaf attachment compared to more landward species was identified. Finally, drag force experienced by mangrove branches followed a generic pattern, where branches with a larger projected surface area experienced larger drag forces than smaller ones. Leaf removal drastically reduced drag force and might protect branches from breakage during a storm, making easy leaf detachment a good adaptation for pioneer species living near the forest edge.

Between different species the wood density can vary significantly, for example *Heritiera fomes* has a wood density of 0.89 g/cm^3, while *Excoecaria agallocha* and *Avicennia marina* have a wood density of 0.43 g/cm^3 and 0.732 g/cm^3 respectively (Agroforestry). During the research of Halder et al. (2021) a significant variation in cyclonic damage between *H. Fomes* and E. agallocha in both compartments was found when diameter at breast height (dbh) of both species was of similar size. In American Samoa, Webb et al. (2014) discovered that species differed greatly in their resilience to cyclones, and

that various species features increased the likelihood of species survival during such storms. This research showed the species features wood density, growth rate, tree architecture (diameter, height and crown:bole ratio) related to the failure modes trunk snapping and uprooting. Wood density was consistently and negatively connected to the likelihood of trunk breakage and uprooting, as well as being substantially and negatively related to total severe damage. Growth rate was found to be inversely related to the likelihood of snapping but positively related to the likelihood of uprooting. For higher trees with smaller diameters, the likelihood of snapping increased, as did the percentage of the tree's height snapped. Su et al. (2020) indicated that multi-stemming had a strong positive influence on tree survival irrespective of diameter classes. But, contradictionary to other researches, stated that conspecific density and abiotic factors have very little effect on the survival of trees.

2.2.5. Differences within mangrove species

At the mangrove forest of Bangladesh, Sundarbans, Halder et al. (2021) research the difference in vulnerability of different mangrove plants to cyclones. Two different compartments in the area were both subdivided into 6 transects which were subdivided into 5 plots. Where number 1 represents the plot closest to the riverbank and plot number 5 represents the forest interior plot. The first notice was the difference in diameter at breast height (dbh) of the different mangroves at the riverbank plots to forest interior plots. For both analysed mangrove species, it can be concluded that along the 5 plots in a compartment, the diameter at breast height of the tree increases from the riverbank (so near to the water) to forest interior.

Halder et al. (2021) also noted, that it is expected that trees at the forest edge (i.e. close to river bank) have lower height to dbh ratios than trees in the forest interior which can be responsible for differences in damage intensity of trees in plots in forest edge than in forest interior. As stated by Alappatt (2008), trees in the middle zone are often the highest trees. Multiple researches have validated that within a species, larger trees are more susceptible to stem breakage or blow down than smaller trees (Smith III, 1994; Baldwin et al., 2001; Roth, 1992).

2.3. Root system mangrove species

The stability of the mangrove trees is determined by its roots. Those roots grow differently for different species. The different roots develope because of the enduring of different conditions, such as lack of oxygen or persistent wind forces. Therefore, all roots have different functions (Tomlinson, 2016). Importance factors for resistance to tree anchorage failure are root system structural characteristics, like the root diameter, the root number, root density per soil volume and the cross-sectional area (Coder, 2014). Due to the responsive character of roots, the roots are asymmetric around the trunk and have differences between the leeward and windward site, increasing their stability. Those characteristics and growth incentives of the roots are influenced by the soil properties (Fourcaud et al., 2008; Dupuy et al., 2007).

2.3.1. Species: *Avicennia marina*

Around the world, roughly 70 different species of mangroves can be found, all slightly different with different root systems. A mangrove species found all over the world is the *Avicennia marina*. The *Avicennia marina* is a Avicennia species which is often called the gray mangrove or a white mangrove (Baishya et al., 2020). The Avicennia species belong to the Acanthaceae family (Baishya et al., 2020; Almahasheer et al., 2016). *Avicennia marina* are often between the 10-14 meters (Baishya et al., 2020). The adaptive behaviour of the tree causes the ability to grow in a wide range of latitude as longitude (Almahasheer et al., 2016; Baishya et al., 2020).

The roots of the Avicennia species are characterised by a root mat which consists of cable roots, anchor roots, feeding roots and pneumatophores (Böhm, 2018; Baishya et al., 2020; Hao et al., 2021; Purnobasuki and Suzuki, 2005). Figure 2.3 and A.3 show the roots of the *Avicennia marina*. Figure 2.5a and 2.5b show pictures taken in Paramaribo, Suriname of a living and death *Avicennia marina*

tree.

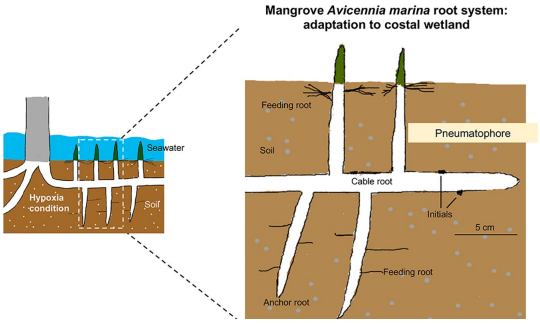


Figure 2.3: schematization of the *Avicennia marina* roots (Hao et al., 2021)

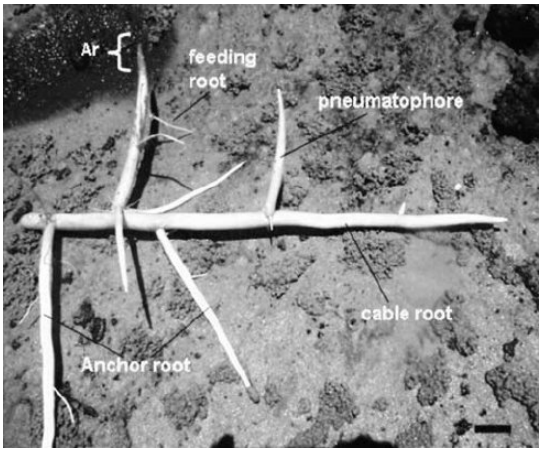


Figure 2.4: Picture of the *Avicennia marina* roots (Purnobasuki and Suzuki, 2005)



(a) Old *Avicennia marina* tree at Weg naar Zee, Paramaribo, Suriname (Kalloe, 2022o)

(b) Picture of death *Avicennia marina* tree at Weg aan Zee, Paramaribo, Suriname (Kalloe, 2022j)

Figure 2.5: Picture of an *Avicennia marina* tree and a root of an *Avicennia marina*

Figure 2.3 shows the root system of an *Avicennia marina* tree. Directly below the trunk, in the soil, the root crown is located. This part of the root system is the part where the roots originate from. In other words: following the root in the reversed growth direction, the point where the roots start to swell abruptly and a wooden ball is created (Njana et al., 2015). The cable roots originate from the root crown after which they extend horizontally through the substrate. The cable roots are important for the aerating, as the pneumatophores roots arise from the cable roots. Secondly, the cable roots are important for anchoring, causing stability due to their long horizontal distance. The pneumatophores roots make the mangrove able to 'breath' (Tomlinson, 2016; Njana et al., 2015; Böhm, 2018; Baishya et al., 2020; Hao et al., 2021; Purnobasuki and Suzuki, 2005). Appendix A explains the difference between mangrove species and the different parts of the root system more extensively.

2.4. Anchoring of different trees

In the following section, an overall analysis of trees growing on land is made, all having a root system with more vertical growth as shown by the example in Figure 2.6. The following species are analysed in the studies used:

- Pine family, like firs, larches, pines and spruces (*Picea abies*, *Picea sitchensis*, *Abies alba*, *Abies balsamea*, *Pinus pinaster* and *Larix decidua*)
- Fagaceae family, like beeches, chestnuts and oaks (*Fagus sylvatica*, (*Castanea sativa*) and *Quercus alba*)
- Olive family (*Acer pseudaplatanus* and *Fraxinus excelsior*)
- Birch family (*Corylus avellana* and *Alnus viridis*)
- Willow family (*Populus trichocarpa*, *Populus deltoides*, *Salix caprea* and *Salix purpurea*)

The friction between soil and root surfaces, as well as the shear strength, weight and size of a tree and its root system, all influence tree anchoring. The size of a tree has been discovered to be directly related to its anchorage (Coder, 2014). The research of the resistance of different tree species to rockfall in the Alps shows that for some species by increasing the diameter at breast height (DBH), the needed energy for failure increases by a factor of 30 (Stokes et al., 2005).

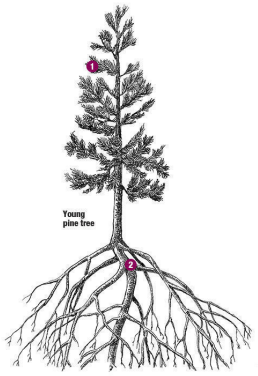


Figure 2.6: Root system of young pine tree (Tjosvold, 2017)

2.4.1. Structural characteristics

Resistance to tree anchorage failure is also linked to root system structural characteristics. Figure 2.7 depicts three types of generic roots and two regions of interest beneath a tree. The rooting zones are as follows: 1) a root plate with large diameter, structural, fast tapering roots; 2) wide-ranging, woody transport roots structurally utilized under tension to resist higher wind speeds; and 3) shallow, horizontal absorbing root fans. Figure 2.7 shows the margin of the root plate and the drip line. On average, 65% of the roots are found within the drip line (Coder, 2014).

The root diameter, the root number, root density per soil volume and the cross-sectional area are all important factors for the determination of the anchoring. Within a species, tensile strength varies with root diameter. Smaller roots have greater root strength per cross-sectional area, while larger roots have greater root stiffness. The apparent disparity in root strength between small and big root diameters is due to much higher cellulose contents (i.e., a higher proportion of cellulose in cell walls) in the smallest roots. The concentration of cellulose in root cell walls is directly responsible for root tensile strength. The percentage of cellulose in cell walls decreases as root diameter increases. Cellulose has a high tension resistance but a low bending resistance. Small roots, which have a higher amount of cellulose, are far more resistant to tensile stresses than large roots per cross-sectional area. Greater root diameter and corresponding cross-sectional area result in gradually lower tensile strength per cross-sectional area. Larger roots, as a unit, may withstand higher total tensile forces simply due to their size (Coder, 2014; Tosi, 2007; Genet et al., 2005).

The stiffness and strength of tree root systems have been genetically improved. Small diameter roots have a high tensile strength and are flexible. Roots with large diameters are strong and resist shear and bending. Small roots provide a high-friction zone between the soil and the root. Large roots function as unyielding anchors. Trees can stand because of this combination of root diameters (Bischetti et al., 2005). Therefore, the strongest anchorage includes many small, long, shallow windward roots (greater tensile resistance) and include a few large, gently tapering, deeper leeward roots (better resisting compression and bending) (Danjon et al., 2005).

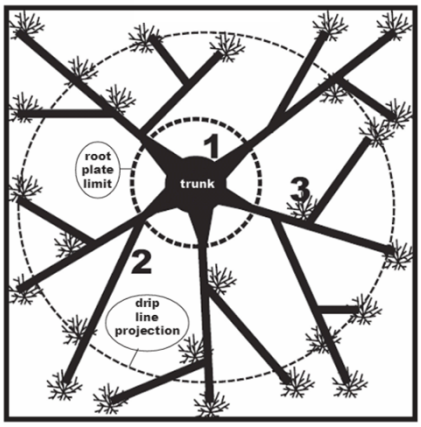


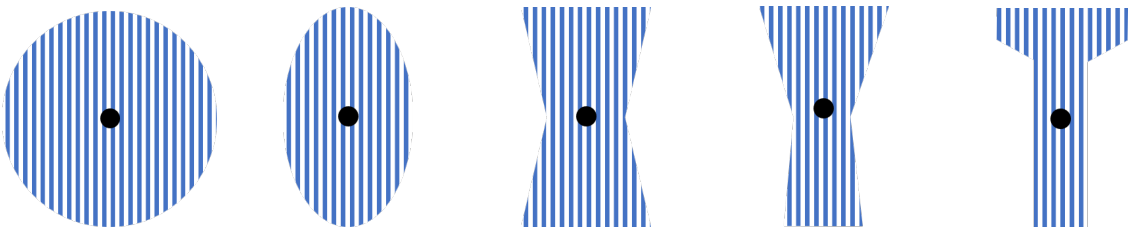
Figure 2.7: Topview of three different zones of the roots, all zones are not scaled (Coder, 2014)

In conclusion, the strength of the soil is increased by roots. The strength of the root / soil system is increased when the root diameter, root density and root tensile strength in the soil are higher and therefore the better the tree anchorage.

2.4.2. Asymmetry

Roots are often asymmetrical, which is caused by their responsive behaviour, especially to wind loads, causing trees which are continuously subjected to wind loading, to be better adapted and be more reactive. The roots react to the continuous forces by increasing the total cross-sectional area of roots and inducing greater biomass development in roots proportional to the forces. For wind loading, the tree grows more and larger roots parallel to the loading close to the trunk (Fourcaud et al., 2008; Stokes, 1999).

Due to loading, parts of the soil-root system is under compression (leeward side) and a part is under tension (windward side). The combination of the differences in tension and compression stress and strain and the responsive behaviour of trees lead to asymmetrical growth adjustments by trees (Stokes, 1999). The difference is mainly caused the largest tension forces located at a different distance from the trunk than the maximum compression forces. The difference in cross-sectional forms is dependent on the difference in tension and compression, soil conditions and possible slopes Nicoll and Ray (1996); Nicoll et al. (2006); Di Iorio et al. (2005), possible cross-sectional forms are shown in Figure 2.8.



(a) Circular (b) Elliptical (c) I-beam (d) T-beam (e) T-beam plank

Figure 2.8: Idealized cross-sections of the tree roots as reaction to unevenly distributed mechanical stress, with the root center indicated using a dot (Nicoll and Ray, 1996)

2.4.3. Anchoring in different soils

Root area ratio is an important factor in the determination of root anchorage. The root area ratio is the amount of cross-sectional area of roots in a flat vertical surface area of soil. Also the depth at which a certain density of roots holds, is important. The higher the density of roots (high root area ratio) and the larger depth this density holds, the more resistance to anchorage failure. The soil properties influence this depth and density. Roots are concentrated at a considerably shallower depth in shallow, fine-textured, or poorly drained soils (Bischetti et al., 2005).

Another important factor for anchorage is the stiffness of the root plate. The root plate or root mat is the horizontal structure of roots around the trunk. Two counteracting forces of the root plates have a large influence on the resistance to up-rooting (Coder, 2014):

- The resistance against up-turning due to the increasing dimensions of windward side of the root plate
- Up-turning is initiated by an increasing upturning force applied to entire root plate

Secondly, the symmetry of the root plate is critical to anchorage, as described in section 2.4.2. Leeward roots have sinkers that grow downward and are bigger in diameter at the surface. While windward roots

are often longer and more distally branched than leeward roots.

Soil type impacts the stability of the root plate and therefore the anchorage. In sandy-like soils, anchorage was dominantly dependent on the depth of the rooting and existing of windward roots (Dupuy et al., 2007). Also, the anchorage resistance is build up by many roots, therefore removing individual root elements will influence the resistance (Fourcaud et al., 2008).
In clayey soils, the existing of windward and leeward roots and largest root diameter were dominantly responsible for the tree anchorage (Dupuy et al., 2007; Fourcaud et al., 2008). As the anchoring is determined by the longest roots, the biomass is not suitable to determine the plate resistance to failure (Fourcaud et al., 2008).
The difference between the important factor for different soils can be described by the different uprooting mechanisms. In clay soil, the root/soil system moved around an axis directly beneath the stem. Windward side upward displacements were nearly comparable to leeward side downward displacements. The slip surface was fairly round and symmetric. The diameter of the slip surface was smaller in hard clay than soft clay, and root plastic strains occurred on large diameter lateral roots near the bole center. In sandy soil, the soil/root system revolved around a leeward-shifted axis. Permanent strains spread further on the windward side than on the leeward side. In comparison to clay soils, the slip surface was much bigger in sandy soils (Dupuy et al., 2007).

The potential bending or hinge point is dependent on the anchorage. In turn, anchorage is dependent on the constraint of roots and the shape and size of the root plate. Overall, in sandy soil the bending or hinge point on a root plate is on a larger distance from the tree compared to a clayey soil (Fourcaud et al., 2008; Dupuy et al., 2007). Looking at shallow root plates, when the root plate resistance to failure is doubled the hinge distance from the trunk base is doubled (Coder, 2014).

2.5. Determination biomass underground and aboveground root system

As stated in the Section 2.4, the root system geometry influences the resistance of a tree. The geometry of a root system is not easily determined, but a usefull parameter is the belowground biomass. Using the belowground biomass and the density of the root system a first approximation of the the total volume of the roots can be made. The same can be done for the aboveground biomass.

The forest biomass can be estimated using three main methods: the harvest method, the mean-tree method and the allometric method. The first method cannot be easily used as a mature mangrove forest easily reaches several tonnes and all trees should be destructively harvested. The second method can only be used if the forest is very homogeneous, which could be the case in a plantation. The third method estimates the whole of partial weight of a tree from measurable dimensions using allometric relationships. As in many organisms, the the growth of one feature is proportional to the growth of another feature of the organism (Komiyama et al., 2008).

For the practical use of allometric equations, it is very important to know when two sites show similarities, and especially when they do not. If two sites show dissimilarities, the same equations can not be used and the site should be investigated on their allometry to develop new equations. Alternatively, if the important factors for the variances are known, it can be determined whether adjusting the allometric equations of an already known site is possible (Ong et al., 2004; Komiyama et al., 2008). In other words, when the relationship between the biomass and the diameter at breast height (DBH) changes, the stability and reduction of wave/wind forces of the trees are affected.
Multiple researches show allometric equations for the above and below ground biomass of *Avicennia marina* in multiple locations. Table 2.2 and 2.3 give an overview of the found equations for different locations.

no.	Equation	a	b	r^2	range [cm]	Country	reference
1.	$ln(AGB) = a + b * ln(DBH) + ln(p)$	-1.786	2.471	0.99	$D_{max} = 50$		(Chave et al., 2005)
2.	$AGB = 10^{(b_0+b_1*log_{10}(DBH))}$	-0.511	2.113	0.97		Australia	(Comley and McGuinness, 2005)
3.	$AGB = ap(DBH)^b$	0.251	2.46	0.98	$D_{max} = 49$	Thailand/Indonesia	(Komiyama et al., 2005)
4.	$AGB = a(DBH)^b$	0.1848	2.3524	0.9839	6.4 - 35.2	Java, Indonesia	(Dharmawan and Siregar, 2008)

Table 2.2: Above ground biomass (AGB) with a and b regression coefficients, p specific density of wood and DBH diameter at breast height

no.	Equation	a	b	r^2	range [cm]	Country	reference
1.	$BGB = 10^{(b_0+b_1*log_{10}(DBH))}$	0.106	1.171	0.8		Australia	$(ComleyandMcGuinness,\ 2005)$
2.	$BGB = ap^{0}.899 * (DBH)^b$	0.199	2.22	0.95	$D_{max} = 45$	Thailand/Indonesia	(Komiyama et al., 2005)
3.	$BGB = a * (DBH)^b$	1.28	1.17	0.8	$D_{max} = 35cm$	Australia	$(Komiyamaet\ al.,\ 2008)$
4.	$BGB = a(DBH)^b$	0.1682	1.7939	0.8581		Java, Indonesia	$(DharmawanandSiregar,\ 2008)$

Table 2.3: Beneath ground biomass (BGB) with a and b regression coefficients, p specific density of wood and DBH diameter at breast height

no.	AGB [kg]	no.	BGB [kg]
1.	29.94	1	17.27
2.	33.92	2	20.98
3.	43.74	3	17.28
4.	34.63	4	9.10

Table 2.4: Result of the allometric relationship from Table 2.2 and 2.3 for a DBH of 9.25 cm

In Table 2.3, the equation stated in Komiyama et al. (2008) is a rewritten version of Comley and McGuinness (2005). This equation was rewritten as the equation has a more common form this way.

2.6. Rooted soil shear strength

Engineers and scientists often assess the strength of the soil and the root systems of the vegetation independently (Alam et al., 2021). This separation is used because the vegetation affects the soil by two main mechanisms (Li et al., 2022). Firstly, the plant roots cause a mechanical reinforcement of the soil and secondly, the transpiration of the plant affects the soil matric suction. The soil matric suction is affected by the absorption of water by the roots which reduces the pore water pressure (Li et al., 2022). Matric suction or matric potential is the negative water pressure. This is equal to the sum of all forces exerted on the soil water by the soil matrix, which is equal to the force retaining water in the soil and also equivalent to the work required to remove the water from the soil. The less water the soil contains, the stronger matrix forces hold onto it, the more negative the potential becomes. The amount of water in the soil at a given matric potential depends on the total porosity and pore size distribution. Due to the mangroves being in a coastal area, the soil is submerged for a large amount of time and therefore fully saturated. The fully saturated soil decreases the effect on the soil matric suction due to the absorption of water.

Overall, the capacity of roots to strengthen soils during shear is their most significant contribution. The root-soil interface's strong frictional qualities increase the stability of the root-soil system. In-situ root pull-out tests, tensile tests, and shear tests of reconstructed soil blocks reinforced with roots utilizing direct shear equipment are the main topics of several research on testing of root contribution to soil strength (Alam et al., 2018; Shahriar et al., 2016; Giadrossich et al., 2017).

Unfortunately, the soil and root integrated strength is not adequately described using these methods of testing. The in-situ soil-root bonding strength (SRBS) is described using Equation 2.1 (Alam et al., 2018). It is quite doubtful that tensile testing on a single root or shear testing on collected disturbed soil samples with and without roots in a laboratory setting will accurately depict the in-situ soil-root binding strength situation (Alam et al., 2021; Wu et al., 1979).

$$S_r = S + (\sin\theta + \cos\theta \tan\phi') \frac{\sum T a_s}{A_s} \tag{2.1}$$

In this equation S_r is the rooted soil shear strength, S is equal to the shear strength of soils without roots in N/mm^2, T is the tensile strength in N/mm^2, a is the cross-sectional area in mm^2 of a single

root specimen, while A is the accumulated area in mm^2 of all roots in the collected soil mass. ϕ' is the internal friction angle of non-rooted soil samples, while θ is the shear angle (Wu et al., 1979).

2.7. Root breakage

The breakage of the roots or branches is determined by the load and the strength of the material. Almost all strength properties of wood are correlated with the wood density of the tree, especially compression, tension, bending strength and shear (Manguriu et al., 2013; Niklas and Spatz, 2010; Roszyk et al., 2013). A larger wood density causes a larger tensile strength and modulus of elasticity. For pine wood, the wood density, and therefore tensile strength, increases with increasing cambial age or the rings (Roszyk et al., 2013). Although after the peak density, the density decreases again to a steady value.
The knowledge of the specific strength or specific modulus of elasticity would eliminate the changing wood density in the analysis of differences in mechanical properties. Multiple analyses can be done for the mechanical properties, e.g. of wood from the same tree, from various trees of the same species, or different trees altogether. These metrics allow for conclusions to be drawn on the impact of variables besides density on the mechanical properties of wood, particularly regarding the size, shape, and quality of cell walls. Overall, the wood density cannot be treated as the only influential factor of the strength parameters but is a very important parameter (Roszyk et al., 2013; Niklas and Spatz, 2010). Gindl et al. (2001) showed the possible high variability of wood density within one species, European larch wood. This variability would also indicate a large variability of mechanical properties within one species.

Santini et al. (2012) showed that the wood density of *Avicennia marina* trees in New Zealand and Western Australia are, respectively, 0.55 g/cm^3 and 0.75 g/cm^3. For different sites within the location in New Zealand, the wood density was lower for landward scrub mangroves compared with the taller trees in a seaward fringing forest and the trees in a taller landward forest. Due to the correlation between the wood density and the mechanical properties of a tree, this difference in wood density shows the possible variability of mechanical properties within this mangrove species.

Santini et al. (2012) indicated that wood density was positively connected with the amount of phloem per growth layer of wood, but negatively correlated with total vessel lumen area and fiber wall thickness. The phloem is the complex tissue of plants, responsible for transporting water and other nutrients to the plants and a lumen is a membrane-defined space that is found inside several organelles, cellular components, or structure. The lumen is the compartment where molecular oxygen is produced from water during photosynthetic light-dependent reactions (Spetea, 2012). Earlier studies found that high wood density is associated with low total vessel lumen areas and small vessel size (Preston et al., 2006; Jacobsen et al., 2007). *Avicennia marina* are able to maintain high water conductivity and mechanical strength by investing into strong fiber walls and lowering the amount of phloem per growth layer in wood. A variety of anatomical techniques may be used by trees to obtain high wood density (Santini et al., 2012).

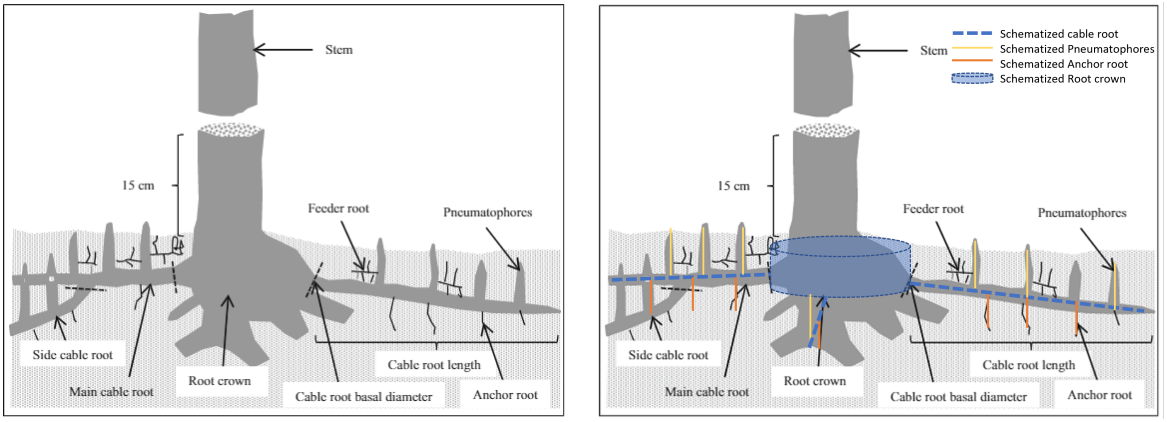
3

Methodology

In this chapter, firstly, the different failure modes of a mangrove tree are described. Secondly, the method to determine the loads due to wind and wave forces at different locations of the mangrove forest is explained. Lastly, the schematizations and analyses of the different failure mechanisms will be presented. Eventually, the modelled forces and schematizations will be applied to the general case as described in Chapter 4.

3.1. Project Scope

As explained in Chapter 2, multiple species of mangrove trees exist, all having different root system and properties. Due to their adaptive behaviour, *Avicennia marina* have the ability to grow in a wide range of latitude and longitude. Therefore, for this research the root system of the specie *Avicennia marina* will be analysed. In Figure 3.1 the root system of an *Avicennia marina* is shown, in Figure 3.1b the overal schematization of the root system is shown.



(a) Root system without schematization (Njana et al., 2015)

(b) Root system with schematization

Figure 3.1: schematization of total root system of an *Avicennia marina* tree, after (Njana et al., 2015)

3.1.1. Different failure modes

The applications and possible uses of Building with Nature solutions, like mangroves, are clear, such as the dissipation of waves, stabilizing shorelines and trapping sediment (Menéndez et al., 2020; Bao, 2011; Quartel et al., 2007). But as explained in Section 1.1.2, Building with Nature solutions can only be incorporated into a coastal defence system if they have a certain reliability. This reliability is dependent on the knowledge of the resistance forces, which are created by the root system. To be able to determine the resistance against each failure mode, first, the different failure modes need to be introduced.



(a) Healthy mangrove tree

(b) Failure due to exceeding the bearing capacity of the soil

(c) Uplift of the soil on the windward side

(d) Breakage of the roots in compression and/or tension, meaning the tree topples over

(e) Slippage of the roots, causing the tree to tipple over

(f) Breakage of the trunk

Figure 3.2: Failure mechanisms of the mangrove trees which will be analysed in this report

Eight different failure modes are introduced below. Figure 3.2 shows the failure mechanisms analysed in this thesis.

(-) Breakage of leaves and branches

(-) Mortality of the trees as the sea level is rising too fast for mangroves to compensate for it

(-) Erosion of the sediment, which makes the tree topple over

(-) Movement of soil around the trunk, which could be caused by:

  (b) Failure due to exceeding the bearing capacity of the soil

  (c) Uplift of soil on the windward side and bending of the roots

(d) Breakage of the roots in compression and/or tension

(e) Slippage of the roots

(f) Breakage of the trunk

For the situation of breakage of leaves and branches and sea level rise, the interaction between the root system and soil is not relevant. While erosion is not the failure mechanisms itself which is happening, but decreases the resistance against other failure mechanisms. As the focus for this thesis will be on the interaction between the root system and soil, the failure mechanisms breakage of leaves and branches, sea level rise and erosion will not be analysed in this research. Although the breakage of the trunk has no influence on the interaction between the roots and the soil, the failure mechanism

is analysed due to the large consequences of the trunk breakage on the dissipation of waves. Below a brief explanation of the analysed failure mechanisms is found, the explanation of the failure mechanisms not analysed can be found in Appendix C.

Looking at online pictures of fallen mangroves, it is difficult to determine if soil comes up with the roots. Mangroves live in a wet surrounding, causing the possibility of the sediment flushing away. Herefore from these pictures, it is difficult to determine whether the roots slip out, break, or the soil-root system comes up as a whole. Pictures of other falling trees and the pulling experiments of willow trees show that soil movement of the soil-root system around the trunk occurs in some cases. Two possible failure mechanisms can cause this movement, the exceeding of the bearing capacity of the soil or the uplift of the windward roots while the leeward roots stay in place. Figure 3.3 shows two pictures of fallen mangrove trees, while Figure 3.4 shows three pictures of fallen trees of other species. In Appendix I more pictures of fallen trees, mangroves and other species, are shown.



(a) Fallen mangrove tree at Weg aan Zee, Paramaribo, Suriname (Kalloe, 2022j)



(b) Fallen mangrove tree (Alamy Stock Photo)

Figure 3.3: Pictures of fallen mangrove trees



(a) Fallen mangrove tree, picture taken by pulling experiments of willows



(b) Tilted fallen tree (Alpine Tree Service, 2017)



(c) Trunk breakage (Alex, 2019)

Figure 3.4: Pictures of fallen trees of different species

(b) Failure due to exceeded bearing capacity

For this failure mechanism, the shear strength of the soil is fully mobilised, causing a sliding plane below the root mat. During this failure mode, the total root mat fails. So, the roots stay intact, while the soil surrounding the roots slides. This would mean that both sides of the root mat slide, and the roots at the leeward side don't break. An important soil property for this failure mechanism is the undrained shear strength, which can be used to calculate the maximum resistance.

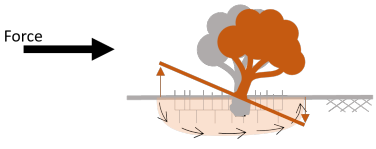


Figure 3.5: Bearing capacity of a mangrove tree

(c) Soil uplift at the windward side



Figure 3.6: Windward uplift of a mangrove tree

For this failure mode, only the windward side of the root mat shows soil movement. The moment caused by the wind and wave forces causes the windward site to bend upward, while the leeward side bends downward. As the soil cannot uptake tension, the soil starts to uplift, which causes bending in the roots. When the bending resistance of a root is exceeded, the root breaks and the moment is redistributed over the remaining roots. This failure mechanism is similar to what was observed when pulling willows in a field experiment in Gorinchem, which can be seen in Figure 3.4a.
On the leeward side, the resistance against bending downward is caused by the soil beneath the root. If forces tilt the tree, the roots start to bend, as the underlaying soil prevents the roots from moving downward into the soil. If the stresses inside the roots exceed the strength of the root, the roots break.

(d) Root breakage due to compression and/or tension
Roots can also break in direct compression and tension instead of bending. The horizontal force inside the root can exceed the resistance causing breakage. Breakage of the roots can be a starting point for multiple failures. The moment a root breaks, the forces are redistributed over the remaining roots. For the failed root, the length decreases, causing less resistance against the sliding failure mechanism. Also, the force in other roots increases, which can result in successive breaking or other failure mechanisms.

(e) Slippage of the roots
A root slips out of the soil when the resistance force (caused by the bonding strength) is less than the force acting on the root. During failure, the roots don't break, but slip out of the soil. The maximum pull out force is dependent on the circumference, length and bonding strength between soil and root.

(f) Breakage of the trunk
The forces acting on the trunk cause bending of the tree, which can ultimately lead to breakage of the stem. The bending stress inside the trunk leads to a part of the stem being subjected to tension and a part of the stem being subjected to compression. When at a certain point the tension or compression forces in the trunk exceeds the resistance, the trunk breaks. The resistance against bending is partly related to the wood density, which differs per species (Gindl et al., 2001) and also depends on the diameter of the trunk (Coder, 2014).

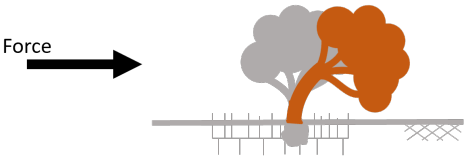


Figure 3.7: Trunk breakage

3.2. Modelling forces acting on the tree

The wave and wind action on a mangrove tree is often modelled by assuming the trunk a cylindrical pillar, which is subjected to drag forces. As the mangroves are very stiff, this assumption is considered valid for the trunk and for the largest branches. This assumption would not be valid for the leaves and branches, as those have some degree of flexibility (van Hespen et al., 2021). Considerable research has been done on dissipation of the waves to determine the amount of reduction (van Wesenbeeck et al., 2022; Quartel et al., 2007; Bao, 2011; Kelty et al., 2022). The amount of wave reduction caused by a certain forest under certain storm conditions is essential to be able to predict the decreased wave load on the structure behind the forest.

3.2.1. Wave forces

The wave forces acting on the tree are modelled using the method of Morison et al. (1950) and are calculated using equation 3.1. The waves are modelled using a drag term, dependent on the flow velocity squared and an inertia term, dependent on the flow acceleration.

$$F_w = \frac{1}{2}\rho_w C_{D,w} A N_v u^2 + \rho C_M V N_v \frac{du}{dt} \tag{3.1}$$

In this equation ρ_w is the water density, $C_{D,w}$ is the empirical drag coefficient for waves, A is the frontal area of the tree perpendicular to the wave direction, N_v is the number of trees per unit area, V the volume of the tree and u is the wave-driven water velocity relative to the tree motion.

The wave transformation through the forest is modelled according to Mendez and Losada (2004). The total energy dissipation through the forest, equation 3.2, is split into dissipation due to waves breaking and dissipation due to vegetation. The energy dissipation due to vegetation is given by 3.3, while the dissipation due to wave breaking is given by 3.4.

$$\frac{dEc_g}{dx} = -\langle \epsilon_v \rangle - \langle \epsilon_b \rangle \tag{3.2}$$

$$\langle \epsilon_v \rangle = \frac{1}{2\sqrt{\pi}} \rho_w C_{D,w} b_v N_v \left(\frac{k_p g}{2\sigma}\right)^3 \frac{\sinh^3\left(k_p h_v\right) + 3\sinh\left(k_p h_v\right)}{3k_p \cosh\left(k_p h\right)} H_{rms}^3 \tag{3.3}$$

In this equation b_v is equal to the average plant width, k_p is the wave number associated with the peak wave period, σ is the frequency associated with the peak wave period, h is the water depth and H_{rms} is the root mean square wave height.

$$\langle \epsilon_b \rangle = \frac{3\sqrt{\pi}}{16} \rho g \frac{B_b^3 f_p}{\gamma_b^4 h^5} H_{rms}^7 \tag{3.4}$$

Where B_b and γ_b are the adjusting parameters according to Mase and Kirby (1992) and f_p the average frequency corresponding to the peak wave period.

A description of the values of each parameter used in the model can be found in Chapter 4. The more detailed explanation about the use and determination of the formulas used can be found in Appendix D.

3.2.2. Wind forces

The forces acting on the tree due to the wind are modelled using a quadratic drag law, Equation 3.5.

$$F_a = \frac{1}{2}\rho_a C_{D,c} A G u_a^2 \tag{3.5}$$

Where ρ_a is the air density, $C_{D,c}$ is the drag coefficient for wind currents, A is the frontal tree area, G is the gust factor and u_a is the wind speed relative to tree motion.

It is assumed that the wind velocity follows a logarithmic decay over the vertical coordinate z. While the velocity between the trees is assumed to follow an exponential decay towards the ground, as shown in Figure 3.8. The wind speed relative to the tree motion between the trees is determined using Equation 3.7 according to Kaimal and Finnigan (1994), while the wind velocity above the vegetation is determined using Equation 3.6 according to Gardiner et al. (2016).

$$u_a(z) = \frac{u_a^*}{k} ln\left(\frac{z}{z_0}\right) \tag{3.6}$$

With z_0 being the roughness height, u_a^* the friction velocity and k the von Karman constant.

$$u_a(z) = e^{-v_e(1-z/h_v)} \tag{3.7}$$

Where v_e is the empirical reduction factor and h_v the tree height.

The input windspeed is assumed to be measured 10 meter above the ground without vegetation. The wind speed at 10 meters above the ground is not assumed equal between non-vegetated and vegetated sites, due to the different velocity profiles, as shown in Figure 3.8. At a height of 200 meters above the ground, it is assumed that the wind velocity is equal for sites with or without vegetation. This corresponding velocity is calculated using Equation 3.6, with $z_0 = 0.02$, corresponding to the rougness height of unvegetated sites (Gardiner et al., 2016). Below an elevetion of 200 meters, the wind velocity of vegetated and non-vegetated sites is assumed different. Thereafter, again Equation 3.6 is used to calculated the wind velocity on top of the forest. This time a rough boundary layer, due to the trees, is assumed with a roughness height of $z_0 = h_v/30$, with h_v equal to the tree height. To determine the wind velocity between the trees Equation 3.7 is used with a decay factor of $v_e = 1$.

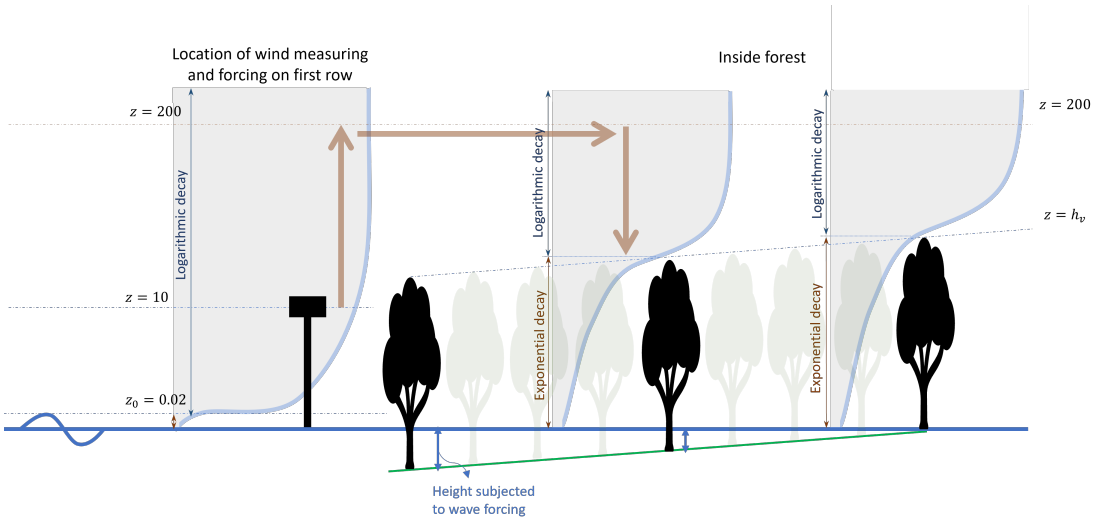


Figure 3.8: schematization of the wind and wave forces through the forest, after (Manchenõ, 2022)

The gust factor is determined according to Gardiner et al. (1997), as shown in equation 3.8

$$G = \frac{\left(2.7193\left(\frac{D}{h_v}\right) - 0.061\right) + \left(-1.273\left(\frac{D}{h_v}\right) + 0.9701\right)\left(1.1127\left(\frac{D}{h_v}\right) + 0.0311\right)^{x/h_v}}{\left(0.68\left(\frac{D}{h_v}\right) - 0.0385\right) + \left(-0.68\left(\frac{D}{h_v}\right) + 0.4785\right)\left(1.7239\left(\frac{D}{h_v}\right) + 0.0316\right)^{x/h_v}} \tag{3.8}$$

With D being the average distance between trees and x the distance from the edge of the forest.

A description of the values of each parameter used in the model can be found in Chapter 4. The more detailed explanation about the use and determination of the formulas used can be found in Appendix D.

3.2.3. Overturning moment

Utilizing the arm of the force, the moment produced by the horizontal wind and wave forces is calculated. As the force differs for every location along the x-axis, the moment will as well.

$$M_x = \int_0^{h_v} dF * z \tag{3.9}$$

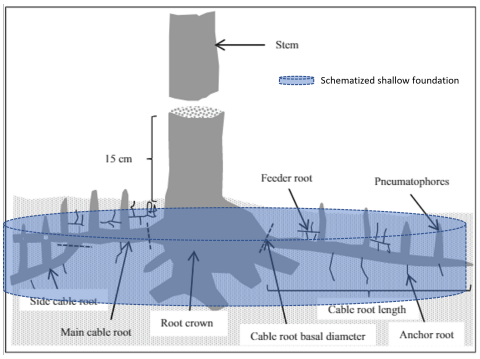
3.3. Schematization of failure mechanisms

Figure 3.1b shows the schematization of the root system. The root crown is schematised as a circular shallow foundation. This is done because the root crown is a massive volume, which is not located very deep into the soil. These geometrical properties make a shallow foundation valid as a first ap-

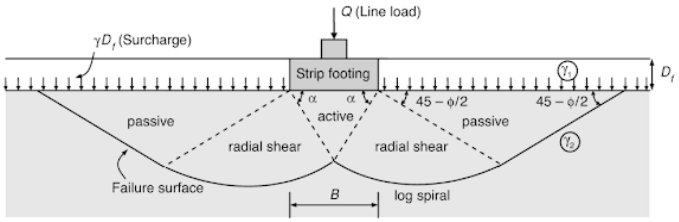
proximation. Secondly, the cable roots are schematised like anchors. The schematization is slightly adapted for every failure mechanism, which will be explained in the following section.

3.3.1. Failure mechanism: Soil bearing capacity

As the whole root mat slides, as first approximation, the whole mass can be assumed equivalent to a shallow foundation. This schematization is given in Figure 3.9a. As the pore pressures inside the soil are unknown, the calculation of the bearing capacity will be determined regarding undrained conditions.



(a) schematization shallow foundation, after Njana et al. (2015)



(b) Terzaghi's bearing Capacity Equation - Failure mode (Terzaghi, 1943)

Figure 3.9: schematization of the failure mechanism: Bearing capacity

The bearing capacity of a shallow foundation during undrained loading can be determined using equation 3.10 (Lancellotta, 2008).

$$q_{lim} = s_u N_c s_c^0 d_c^0 i_c^0 b_c^0 g_c^0 + q \tag{3.10}$$

In this equation N_c is the bearing capacity coefficient, s_c^0 is the shape coefficient, d_c^0 is the depth coefficient, i_c^0 is the horizontal load component, b_c^0 the coefficient due to inclination of the founding base, g_c^0 is the sloping ground surface coefficient and q the uniform stress. Lastly, s_u equals the undrained shear strength. An detailed explanation of the different parameters can be found in Appendix C.2.

3.3.2. Failure mechanism: Uplift of soil at the windward side

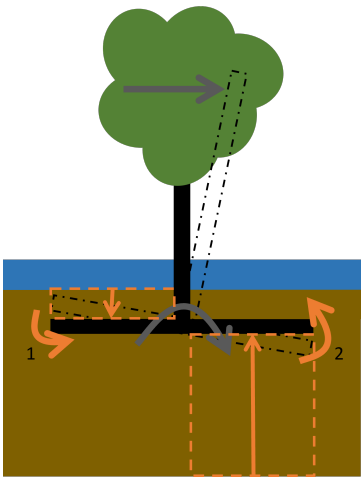


Figure 3.10: Different forces and moments on a single tree

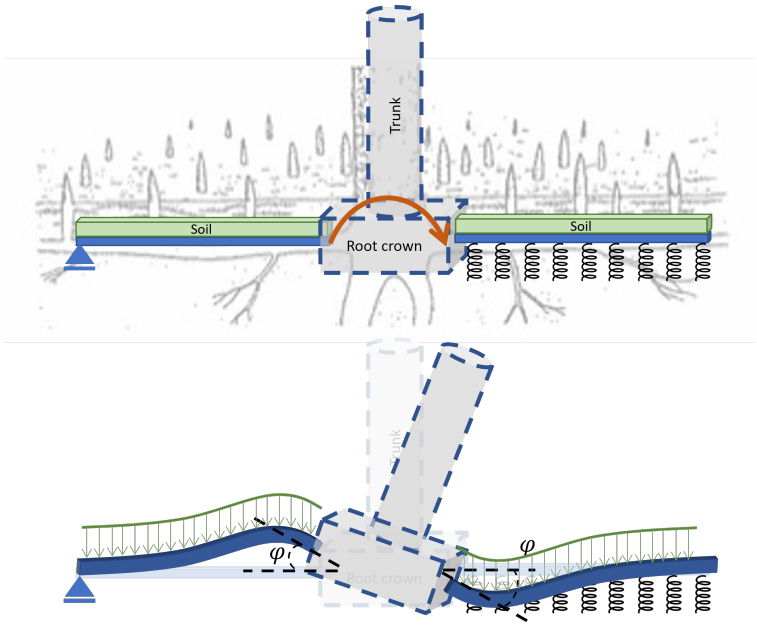


Figure 3.11: Overal schematization

In Figure 3.10 the idea behind this schematization is shown. The wind and wave forces cause a moment which is transferred to the bottom of the trunk, the root crown. Due to the moment caused by the forces, the leeward roots want to move down and the windward roots want to move up. On the windward side the overlying soil provides the resistance against this upward movement. On the leeward side the downward movement is restricted by the soil below the root. During this schematization, the anchor roots, as shown in Figure 2.3, are neglected.

To schematize this failure mechanism, every root, having its own length and diameter, is schematised as a beam. The moment equilibrium is used to determine the moments inside those beams. During the development of the model, multiple combinations of schematization are used. First, both sides of the trunk were supported by hinged, rolled or fixed supports. A more advanced model was made by schematising the soil below the leeward beam as a spring-supported beam. In Figure 3.11, the schematization with a spring-supported leeward side is given. A different situation is used on the windward side, and no spring support is used, as soil cannot take any tension. The location below the trunk can be modelled using a hinged support, as rotation is possible, but no horizontal movement is allowed.

As the roots originate from the root crown, rotation at both sides, φ in Figure 3.11, is assumed equal. This is in agreement with the assumption of the root crown to move as a whole and to be a rigid block. This equal rotation can be used to determine the moment inside every root applying the moment of equilibrium. This moment will be used to obtain the bending and compression forces inside the root and whether uplift of the soil occurs. As the moment is applied into one direction, not all roots attribute to the resistance. In Figure 3.12, the roots within the separation line attribute to resisting the applied moment, the amount of roots contribution to the resistance is determined by the participation angle α.

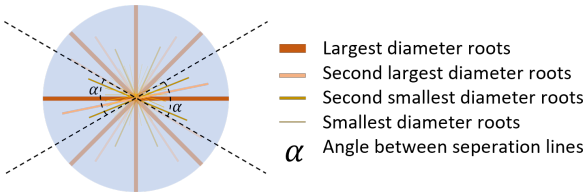


Figure 3.12: Bird view of the root system, indicating that only the roots within the separation line attribute to the resistance

The end of the roots can be modelled by a fixed or rolled support. The fixed support can be used to schematise longer roots, which have no movement or rotation at the end. Shorter roots can be modelled by a rolled support. The rolling component can be compared with the root slightly moving inside the soil. Using the rolled support, also rotation at the end of the root is possible.

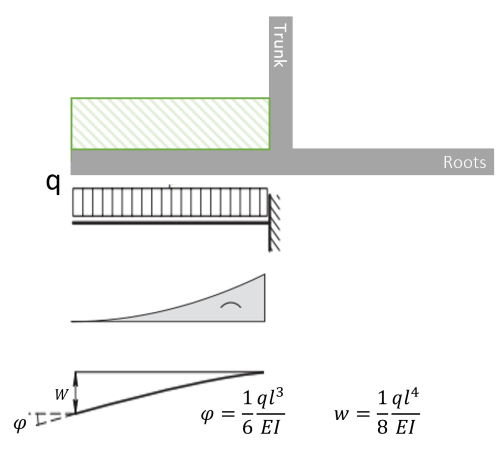


Figure 3.13: schematization of the resistance against uplift on the windward side

The weight on top of the roots on the leeward and windward site is assumed to be equal, and therefore are counteracting each other in the total moment equilibrium. Looking into the windward side of the trunk, the resistance against uplift is given by the weight on top of the roots, as soil can not take any tension. This layer of soil can be schematised as a distributed load on a fixed beam, as shown in Figure 3.13. If the moment exerted by the wind and waves causes a larger rotation of the roots than the resistance against rotation caused by the overlying soil, the soil starts to move up.

Different schemes

Five different schemes are used to schematise the roots, this schematization is used to determine the moment inside each specific root, taking into account its length, diameter, the number of roots and the way of

support at the end of the root. Using the equal rotation assumption, the moment inside each specific root is determined. For all five situations, the maximum moment inside the root is exerted below the trunk, which is comparable to a real-time situation.

In the first three models, the leeward side of the roots is not continuously spring-supported. The three schemes are combinations of long and short roots. In the first situation, the leeward and windward roots are modelled using the schematization of short root. The schematization of long and short roots is given in Figure 3.14. The difference between both, as explained above, is the support at the end of the root.

Below, a summary of the primary three schematizations will be given as well as the detailed explanation of the more advanced schematizations.

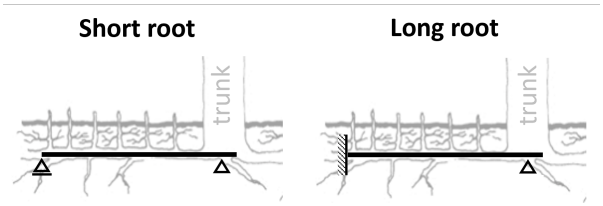


Figure 3.14: schematization used for long and short roots

In the first situation, both sides are modelled with beams supported by a rolled support on the end and with a hinge support below the trunk, modelling short roots. In the second scheme, the leeward side has long roots, while the windward side has short roots. In the third situation, both sides are schematised using long roots. During the modelling, it was concluded that the schematization of the leeward side without using the spring-support was unrealistic and did not represent the differences between soil types adequately. The schematization of all the five models are given in 3.15. A detailed explanation about the used formulas of the primary three schematizations is given in Appendix C in Section C.4.

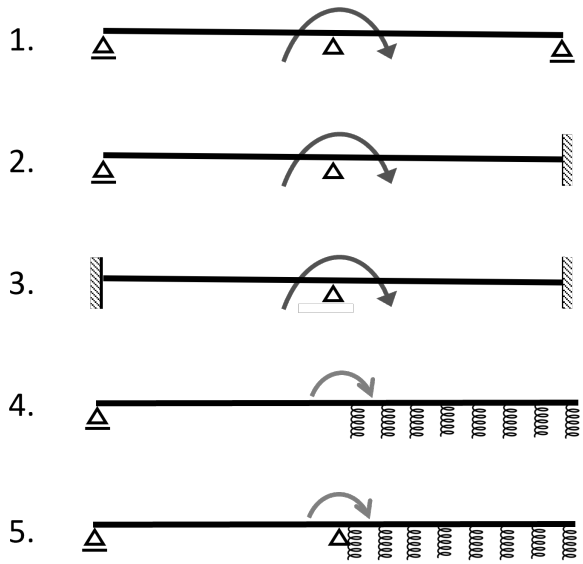


Figure 3.15: schematizations of the root system without using spring support

In this research, the maximum stress inside the root and maximum uplift is determined, which occurs near the trunk. Therefore the given angle φ and indentation w in the schemes below are for the maximum value occuring. This value is most important, as this indicated the point where failure occurs fastest.

Vertical movement of the trunk allowed - Situation 4

For the fourth situation, the leeward side of the tree is schematized as a continuously supported beam by springs. This introduces the damping constant k, which describes a linear reaction between the

vertical displacements (w) and the distributed vertical response (p) of the springs, as p = kw. If the beam rests on soil, the relationship between the reaction p and the indentation w of the soil is in fact non-linear. With increasing indentation, the soil becomes stiffer and the reaction p increases more than proportionally. A linearisation of this relationship is then an approximation, which will generally give reliable results for small displacements. For a beam with width b and a modulus of subgrade reaction c, the back pressure of the soil (force/oppressive force) is:

$$\sigma = \frac{p}{b} = \frac{k}{b}w \qquad \text{with} \quad \frac{k}{b} = c, \qquad \text{gives} \quad \sigma = cw \tag{3.11}$$

$$[q] = [p] = \text{N/m}, \quad [k] = \text{N/m}^2, \quad [c] = \text{N/m}^3 \tag{3.12}$$

If a load is applied to a beam lying on the ground, the soil next to the beam will also sink with it. The reaction of the soil, therefore, originates from an area wider than the width of the beam, and the reaction will not be proportional to the beam width, see Figure 3.16. This means that the constant c is essentially not constant, but there is a scale effect. This preservation is less than it appears at first sight. Furthermore, the diameter of the roots is relatively small compared to the construction beams. Therefore, the scale effect will not be taken into account.

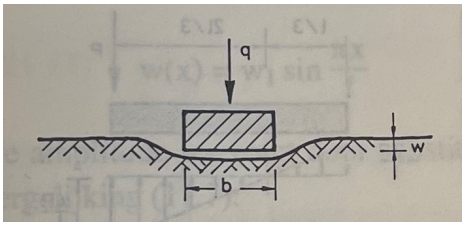


Figure 3.16: Different parameters describing the ground pressure (Bouma, 1993)

The fourth situation assumes a boundary condition under the trunk, equal to the moment caused by the wind and wave forces. The second boundary condition to solve the differential equation is that there is no transverse force at this location. In this situation, therefore, a displacement under the trunk may well reflect, causing the trunk to move upwards. The maximum uplift from the leeward side occurs at the location x=0, below the trunk. This is also where the maximum angular displacement takes place, as illustrated in Figure 3.17.

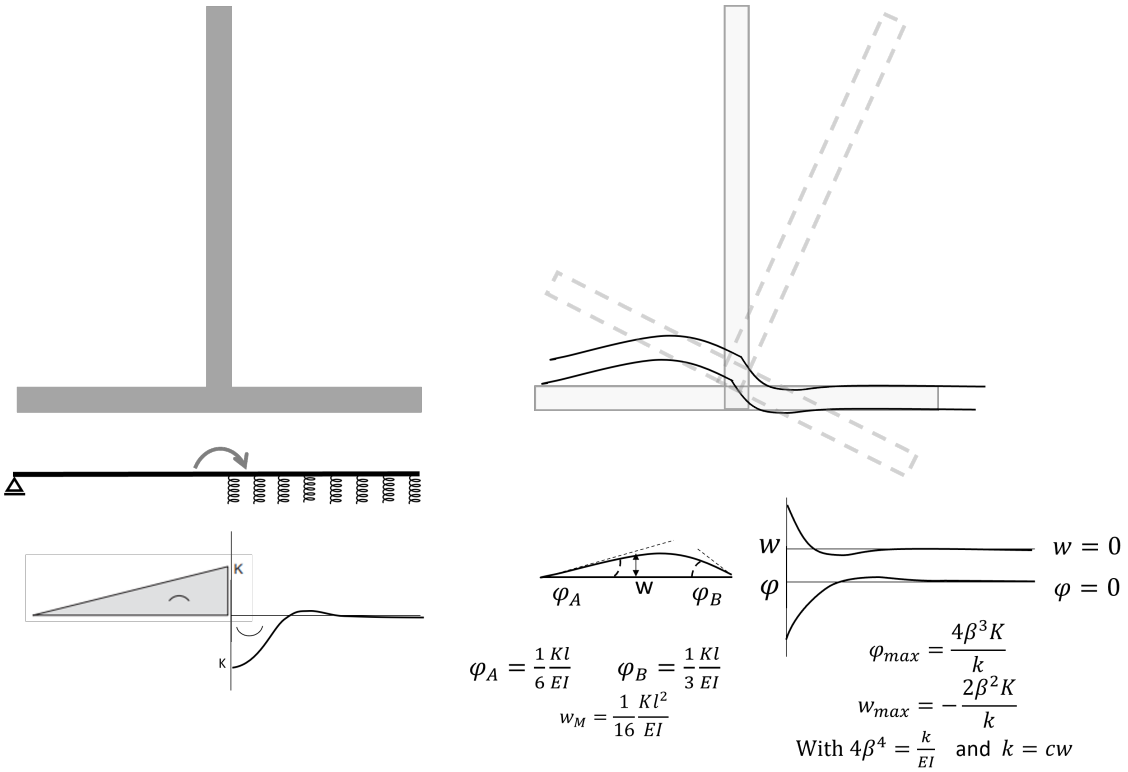


Figure 3.17: schematization of a spring supported beam with a boundary condition - situation 4

In the first three situations, the elasticity of the root is cancelled out, as it was equally important on both sides. On the leeward side, this schematization is less dependent upon the elasticity of the root. Therefore, the amount of elasticity of the root does not cancel out. On the windward side the moment is dependent on E^1, while on the leeward side it is dependent on $E^{3/4}$.

Vertical movement of the trunk restricted - Situation 5

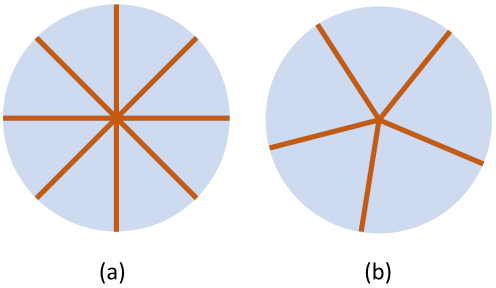


Figure 3.18: Distribution of roots with (a) roots in line with each other and (b) roots unevenly distributed

In the fifth case, below the trunk a transition condition is used instead of a boundary condition like in situation 4. Using a transition condition the roots should be inline with each other, as shown in Figure 3.18a. If the roots are unevely distributed, the transition conditions cannot be used. Although it is very unlikely that all the roots are perfectly inline with each other, there two reasons to model this situation. Firstly, the root crown is a very dense area with roots. Due to the large amount of roots in the root crown area, the difference in alignment between roots on the leeward and windward side will decrease. So, the roots will become closer to being in line with each other. Therefore, the approximation of roots being in line becomes more acceptable. Secondly, using a transition condition, the vertical displacement of the trunk is obstructed, while in situation 4 the trunk can show vertical displacement. Due to this difference between, both situation will be modelled. The second transition condition needed to solve the differential equation is the moment applied below the trunk.

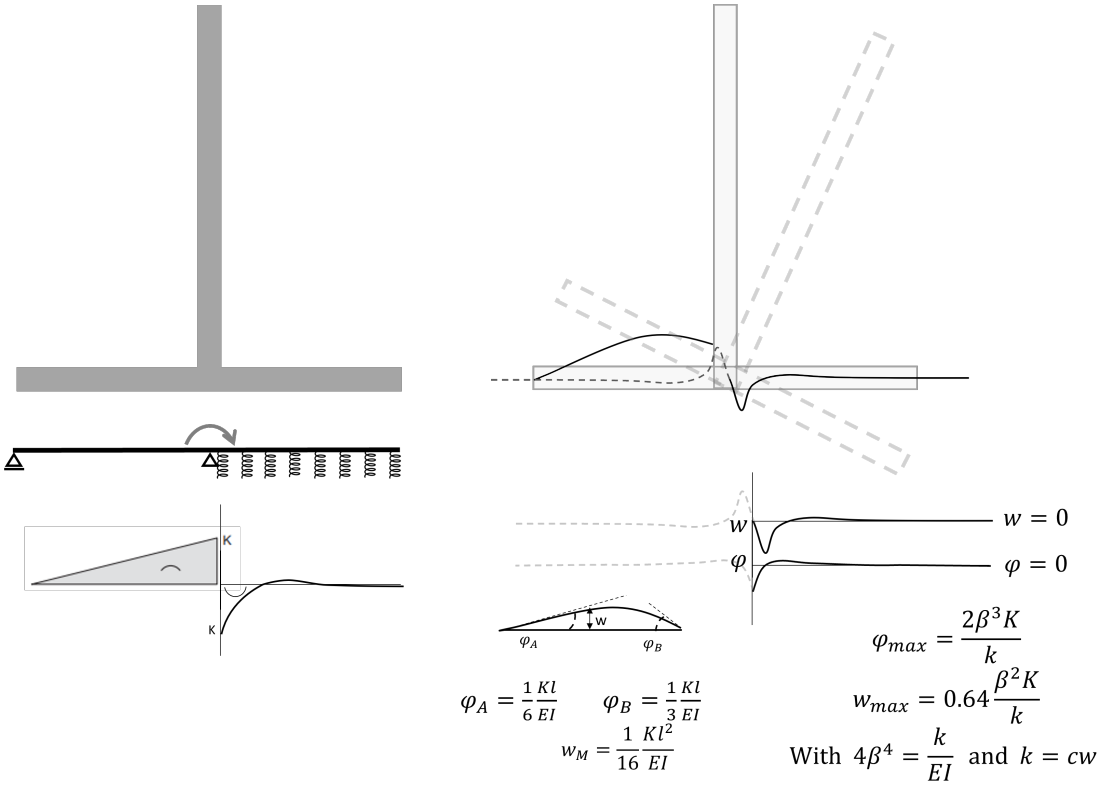


Figure 3.19: schematization of a spring supported beam with transition conditions - situation 5

In consequence of the transition condition the displacements and rotations on both sides of the trunk

will be the same, as shown in Figure 3.19. This can be explained by the root crown, from which the roots originate. From the end of the root crown, the reaction of the roots can be different. Equally, as in the fourth situation, the elasticity of the root is essential.
The schematization and needed rotations are given in Figure 3.19.

Determination maximum stress

Using the knowledge of the moment taken by the specific root, the bending tension and compression inside a root can be determined, as shown in Figure 3.20. Using the results of Manguriu et al. (2013), the bending tension and compression of a *Rhizophora mucronate* can be used to determine whether failure happens or not. The calculation of the quadratic area moment is given in Equation 3.13, while the stress at a specific location in the root is given by Equation 3.14.



Figure 3.20: Determination of maximum bending inside a root

$$I = \frac{1}{4} * \pi * r^4 \tag{3.13}$$

$$\sigma = \frac{M * y}{I} \tag{3.14}$$

With *M* being the moment at the location of determination, *r* being the radius of the root, *y* the distance from the neutral line until the location inside the root and I the quadratic area moment. For the knowledge of the maximum stress, as needed in the analysis, the maximum moment in the root is taken and y is always equal to the radius, as the maximum stress occurs at the outside of the root.

Determination uplift

The amount of uplift, in degrees, is determined by the angle created by the moment inside the root. The angle created by the moment is equal in situations 4 and 5, caused by the fact that the windward side is modelled with a rolled support in both situations. The moment inside the roots will be different, but the angle created by an equal moment does not differ and is equal to φ in Equation C.18. This angle is also given Figure 3.17 and 3.19.

$$\varphi_{1245} = \frac{\frac{1}{3} * M * L}{E * I} \tag{3.15}$$

With *M* being the maximum moment inside the root, *L* being the length of the root, *E* being the elasticity of the root and *I* being the quadratic area moment of the root.
Combining those angles created by the overturning moment with the resistance against movement will give the angle of the uplift at the location of maximal movement inside a root, see Equation 3.16. As the moment and movement along the root differ, this approach could be used to determine the angle of uplift at every location along the length of the root. In this thesis, only the maximum moment and rotation will be analysed as those points go to failure the fastest. Therefore, this formula only indicates whether uplift occurs, not the exact amount of uplift along the whole root. As on the location of maximum angle distortion, it determines wheter the distortion is upward or not.

$$\text{Uplift [degrees]} = \varphi_{1245} - \frac{\frac{1}{6} * q * L^3}{E * I} \tag{3.16}$$

With φ_{1245} equal to the angle caused by the overturning moment, *q* the distributed load caused by the overlaying soil layer.

3.3.3. Failure mechanism: Root breakage

The schematization of root breakage is done by assuming the roots act like anchors, as shown in Figure 3.21. The forces inside the root are determined using horizontal equilibrium. Combined with the assumption that the end of the root does not move, the compression and tension in the roots can be determined. The maximum resistance against tension and compression of a *Rhizophora mucronata* is used (Manguriu et al., 2013). This mangrove has a slightly higher wood density, which causes the resistance to be slightly overestimated.
The maximum force occuring in a root compared with the strength of the root determines the safety factor (SF), as shown in Equation 3.17.

$$\text{Safety Factor (SF)} = \frac{\text{Compression/tension strength}}{\text{Maximum force inside root}} \tag{3.17}$$

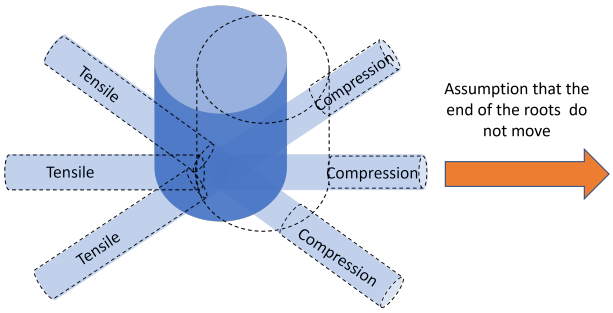


Figure 3.21: schematization of compression and tension forces in the roots

3.3.4. Failure mechanism: Root slippage

To determine the slippage, again, the forces inside the roots are determined using the horizontal equilibrium. Those forces are compared to the total resistance of a root, as shown in Figure 3.22 and 3.23. The total resistance is determined using the bonding strength and the contact area.

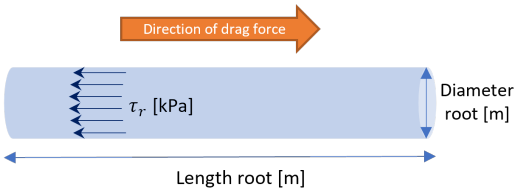


Figure 3.22: schematization of shear stresses on a single root

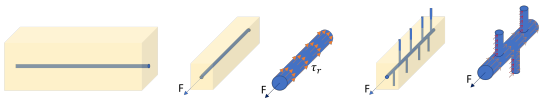


Figure 3.23: schematization of shear stress on a root including pneumatophores

The safety factor of this failure mechanisms is determined as described in Equation 3.18.

$$\text{Safety Factor (SF)} = \frac{\tau * 2\pi * r * L}{\text{Force inside the root}} \tag{3.18}$$

With τ the bonding strength, r the radius of the root and L the length of the root.

As the bonding strength between the mangrove roots and soil is unknown, it can be determined using different methods:

- Positive and negative adhesion
- Pull out force from effective stress
- Bonding strength between steel and mud
- Bonding strength of dike nailing
- Bonding strength of different tree species

The bonding strength of different tree species is used to determine the bonding strength. Other methods to determine the bonding strength were impossible due to a lack of soil information. The other methods are explained in Appendix C.

Bonding strength of different tree species
The bonding strength is influenced by the confining pressure at that certain location in the soil. Therefore, when using the bonding strength between different tree species' roots and the soil, it is important to have a confining pressure close to the confining pressure of the soil in the test case. Secondly, the type of soil should be comparable.
As no information about the pullout strength of mangrove roots is present, another tree specie needs to be used. The research of Schwarz et al. (2011) determines the pullout force of a *Picea abies*, a Norway spruce, inside a silty soil. The research determines the force needed to pull out a root in horizontal direction, as seen in Figure 3.24. Although spruce have a different root system from *Avicennia marina*, the horizontal pullout force can be compared with the movement of the horizontal root of an *Avicennia marina* root.

The force-displacement behaviour is influenced by friction between the soil matrix and the roots, which varies with soil type and water content (Schwarz et al., 2011). The soil type and confining pressure in the tests of Schwarz et al. (2011) are comparable with the soil in this research. Also, the tests are conducted in wet soil, comparable to the situation in Demak. Therefore, the results of the pullout force in the wet soil with a confining pressure of 4.5 kPa can be assumed to be a good approximation.

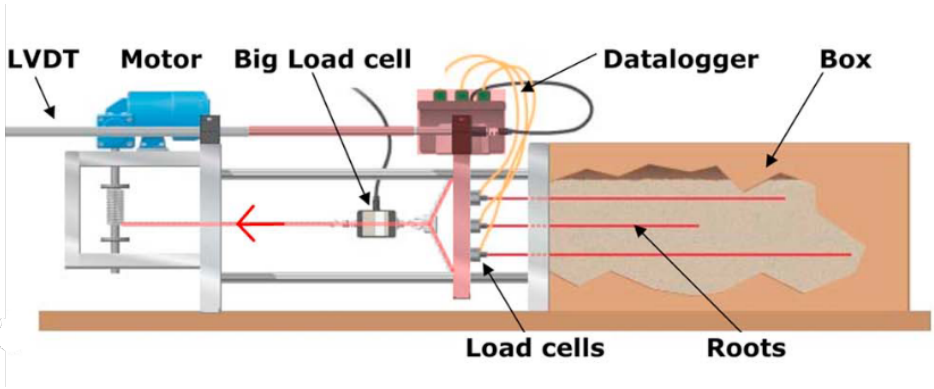


Figure 3.24: Schematic of the pullout machine used in the research of Schwarz et al. (2011)

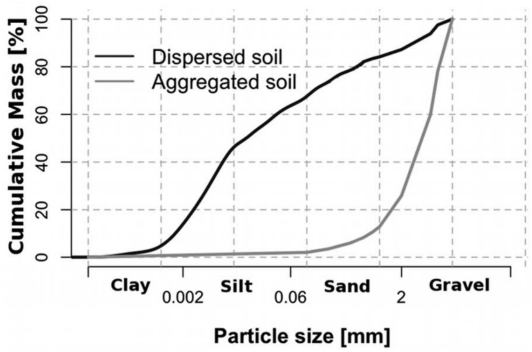


Figure 3.25: Grainsize distribution of the soil in the research of Schwarz et al. (2011)

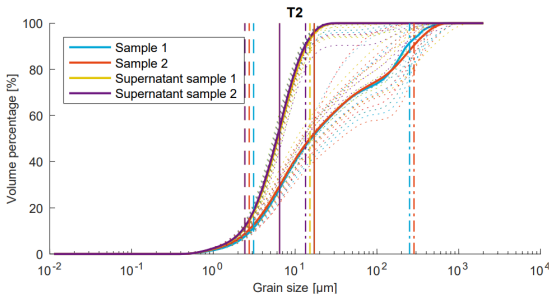


Figure 3.26: Grainsize distribution of the soil in the test case (BioManCo, 2019)

3.3.5. Failure mechanism: Trunk breakage

The breakage of the trunk can be analysed by schematising the trunk as a beam with only a single support. The wind and wave forces create a distributed load over the beam, causing a maximum moment at the bottom of the trunk.

The total moment is maximum on the bottom of the trunk and equal to the moment caused by all the forces. This maximum moment can be used to determine the stress inside the trunk. The stress inside the trunk is dependent on the diameter of the trunk, which can be assumed equal to the DBH. Equation 3.13 and 3.14 can be used to determine the maximum stress inside the trunk. The maximum moment due to the forces will be located slightly above the soil, as the arm is largest at that point, causing the maximum amount of stress to be slightly above the soil.
The safety factor against trunk breakage is defined as described in Equation 3.19.

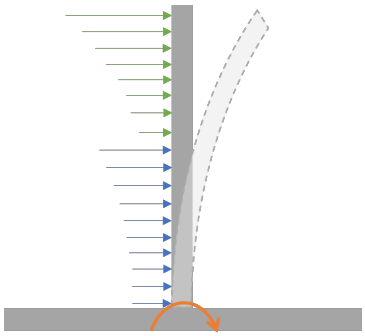


Figure 3.27: schematization of the trunk breakage

$$\text{Safety Factor (SF)} = \frac{\sigma_R}{\sigma_{max}} \tag{3.19}$$

With σ_R the compression/tension bending strength and σ_{max} the maximal occuring stress caused by the moment inside the trunk.

4

Parameters used for test case Demak, Indonesia

4.1. Wind and wave parameters

The data of Alferink (2022) is used for the bathymetry and the input variables of the Demak site. A short summary is given below and the extented explanation about how the data was retrieved and which differences are between the data is shown in Appendix E.

4.1.1. Bathymetry

The bathymetry of fringe forest in Demak is shown in Figure 4.1. The coastline of Demak shows a slope of 1:500 from a water depth of -12 untill -1 m MSL. After this depth the slope turn almost flat. For the standard situation, the slope of the model is set to 1:500 untill a water depth of 0 meters. The differences in water depth due to this situation can be seen in Figure 4.1. The bathymetry of the standard situation is shown in Figure 4.2. van Domburg (2018) shows that the width of the vegetation in Demak is approximately 50 meters. As part of the research is to determine at what location the forces are largest, the differences between these locations should become clear. This is only possible with a larger width of the forest. Therefore, the forest width is extend to 500 meter. This way the differences in forces at the edges and the interior will be more noticeable. The model should be made such a way that this parameter is adaptable.

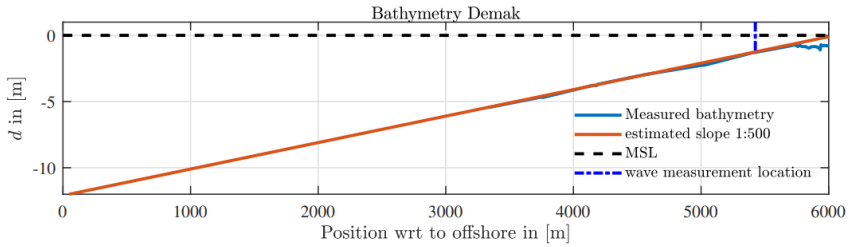


Figure 4.1: Measurements of bathymetry of Demak, Indonesia with a CTD device during the BioManCo project along two transects, (van Domburg, 2018; Alferink, 2022)

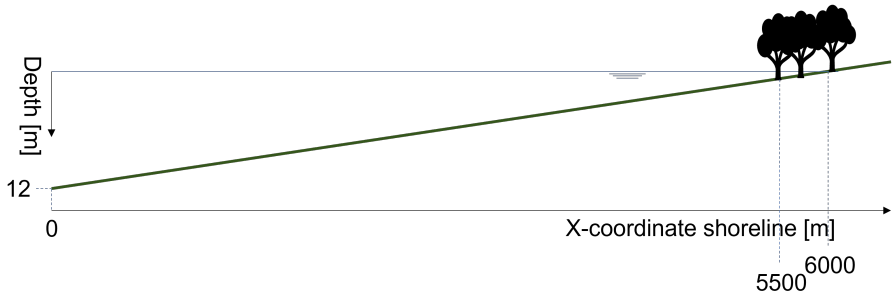


Figure 4.2: Simplyfied bathymetry of the Demak coast

4.1.2. Wave height and wave period

Return period [years]	Daily	1	5	10	15	20
Offshore wave height, H_{m0} [m]	0.25	2.08	2.39	2.47	2.52	2.53
Wave Period, T_p [s]	3	6.9	7.5	7.7	7.7	7.7
Surge [m]	0.0	0.63	0.68	0.72	0.74	0.76

Table 4.1: Summary input parameters measured at a location 5.5km offshore with a water depth of 12 meters (Alferink, 2022)

4.1.3. Wind velocity

During the upper wave events the windspeed is not known. Sugianto et al. (2017) researched, over the same time period as Alferink (2022), the relation between significant wave height and the windspeed. This relation can be used to determine the windspeed during the wave events, see eqaution 4.2. As the research is related to the significant wave height, while the root mean square wave height is needed, this would need to be transferred.

$$H_{rms} = 0.707 * H_s \tag{4.1}$$

$$H_s = 0.00162U^2 + 0.0275U \tag{4.2}$$

Return period [years]	Daily	1	5	10	15	20
Windspeed, U [m/s]	3.72	18.23	19.97	20.40	20.61	20.71

Table 4.2: Summary of wind velocity

The situation with a return period of 20 years will give the largest forces on the trees, and therefore those parameters will be chosen as main situation.

4.1.4. Coefficients in wind and wave formulas

Parameter	Symbol	Value	Unit
Drag coefficient waves	C_D	1.0	[-]
Inertia coefficient waves	C_m	2.0	[-]
Adjusting parameter B (Mase and Kirby, 1992)	B	1.0	[-]
Adjusting parameter γ (Mase and Kirby, 1992)	γ_b	0.6	[-]
Water density	ρ_w	1025	[kg/m^3]
Drag coefficient wind	$C_d c$	1.0	[-]
von Karman constant	K_c	0.4	[-]
Decay factor (Gardiner et al., 2016)	v_e	1.0	[-]
Roughness height - non-vegetated side	z_0	0.02	[m]
Roughness height - above forest	z_0	$h_v/30$	[m]
Air density	ρ_{air}	1.2041	[kg/m^3]

Table 4.3: Wind and wave coefficient inside formulas

Drag- and inertia coefficients
The drag coefficient of waves and wind and the inertia coefficient of waves are dependent on the tree geometry (diameter of the branch/trunk) and the velocity of the medium (wind/wave). The determination of the drag coefficent of waves is often done using Reynolds number or Keulegan–Carpenter number. The Reynolds number is a dimensionless quantity from fluid dynamics, used to determine whether flow is laminar of turbulent, as well as to represent similarity between two different flows. Low values represent laminar flow, while high values present turbulent flow, the switching point is different for every geometry. The Keulegan-Carpenter number in fluid dynamics is a dimensionless quantity that indicates how important drag forces are compared to inertia forces for bluff objects in an oscillatory fluid flow. Likewise, for objects that are at rest and oscillate in a fluid. Inertia dominates for small KC-numbers, whereas drag forces are significant for large numbers.
As the determination of the exact drag forces is a study in itself, an average value of different studies has been taken. Shan et al. (2019) and van Wesenbeeck et al. (2022) range drag coefficients for waves from 0.80 till 3.0, with the higher drag coefficient for lower Keulegan-Carpenter numbers. Due to the larger wave period and small diameter of the tree, the KC-value is relatively high. Therefore, a lower value of the drag coefficient is taken, equal to 1.0. The same determination has been done for the wind drag coefficient.
The inertia coefficient is also determined using the KC-value. Venugopal et al. (2009) indicates a range of inertia coefficients from 1.5 till 2.5, while most values are around 1.8 for higher KC-values. Smith (2013) indicates a common inertia coefficient of 2.0 for smooth cylinders. Throughout the model, and over one slice of the z-axis, the tree is assumed to be of equal width. Therefore, the inertia coefficient is assumed to be equal to 2.0.
Those coefficients are inline with the recommanded values according API (2014). The recommended values for the drag coefficient ranged from 0.6 to 1.2 while the inertia coefficient ranged from 1.3 to 2.0.

4.2. Input tree properties

4.2.1. Determination of above- and below-ground biomass

As described in section 2.5, multiple allometric relationships between the diameter at breast height (DBH) are available for *Avicennia marina*. All those equations for *Avicennia marina* are determined at different places. The equations of the forest with the largest similarities with Demak will be used, like a fringe forest, forest density and soil properties.
The sediment properties of the fourth allometric equation of Dharmawan and Siregar (2008) are most comparable with the location in Demak. The above ground biomass will therefore be determined by the allometric equations of Dharmawan and Siregar (2008):

$$AGB = 0.1848(DHB)^{2.3524} \tag{4.3}$$

This equations was also used in Indrayani et al. (2021) to determine the aboveground biomass in Demta, Indonesia.

For the belowground biomass, the equation of Komiyama et al. (2005) will be used. This equation has a significantly higher r-value and is also suitable for the Demak site. The value of p_w is the specific density of wood and is equal to 0.732 gcm^{-3} for *Avicennia marina*.

$$BGB = 0.199 * p_w^{0.899} * (DBH)^{2.22} \tag{4.4}$$

Table 4.4 lists the results of the above and underground biomass calculation.
Ardhani et al. (2021b) is a dataset including 815 measured trees of *Avicennia marina* and Avicennia Alba in the Demak area of Berahankulon in 2019, which is the tropical peat swamp forests in Demak. The dataset consists of 616 *Avicennia marina* trees and indicates their DBH, location, wood density, Total AGB, BG root mass, basal area per ha, sub-plot area and sub-plot design. The BG root mass indicated in this dataset is approximately the same as indicated in table 4.4, which indicates the use of the same allometric equation. The AGB does differ a bit, and the difference increases when the DBH increases. The difference is caused by the fact the dataset also uses the equations of Komiyama et al. (2005) for the aboveground biomass.

DBH [cm]	AGB through allometric equation [kg]	Average AGB through dataset [kg]	Ratio between AGB	BGB [kg]
5	8.1463	9.63	1.18	5.3550
6.9	17.3784	20.73	1.29	10.9470
7.7	22.4948	27.15	1.21	13.9655
11.5	57.7946	74.69	1.29	34.0250
16.8	140.9677	N/A	N/A	78.9287
19	188.2964	256.85	1.36	103.7245

Table 4.4: Calculation of above and underground biomass of *Avicennia marina* based on DBH and dataset of (Ardhani et al., 2021b)

Specific gravity
To transfer the belowground biomass (BGB) into a belowground volume (BGV), the root density needs to be known. Rodtassana et al. (2012) gives a specific density for the amount of pneumatophores for *Avicennia alba*, but not the total root system. As no information about the total density is known, the wood density is used to transform the BGB into the BGV.

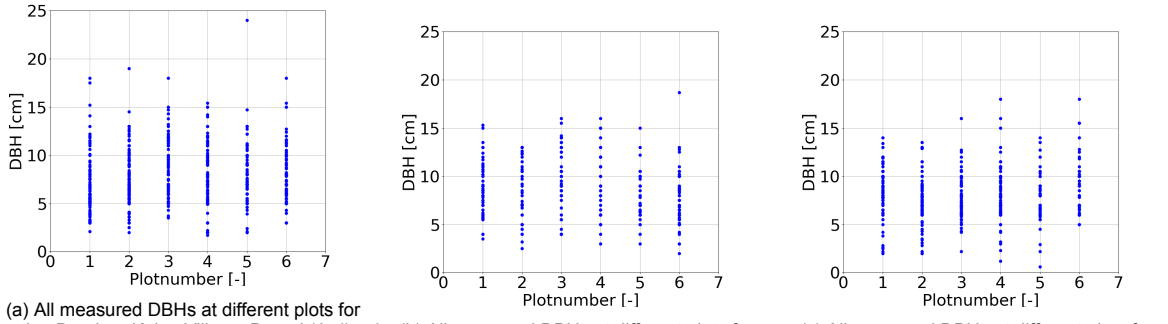
4.2.2. Tree density, basal area and average tree diameter

As explained in chapter 2, the gust factor is dependent on D/h_v, which is the distance between the trees divided by the height of the tree. This factor determines the progress of forces through the forest. The calculation of this gust factor is limited by this factor:

$$0.075 < D/h_v < 0.45$$
$$0.075 * h < D < 0.45 * h$$
$$0.075h < \sqrt{1/N_v} < 0.45h$$
$$0.006h^2 < 1/N_v < 0.203h^2$$
$$N_v < \frac{1}{0.006h_v^2}$$
$$N_v > \frac{1}{0.203h_v^2}$$

If the average density is N_v, the distance between two trees (D) is equal to $\sqrt{\frac{1}{N_v}}$.

As stated in 2.2.5, the tree diameter changes through the forest. The average DBH per plot can be determined from the data from Ardhani et al. (2021b) and Ardhani et al. (2021a). The average DBH per plot shows an parabolic function over, but as shown in Figure 4.3, the spread of different DBH's is quite similar and wide over every plot. Therefore, the DBH is taken equal over the total width of the forest. The average DBH over all measurements is 7.91 cm.



(a) All measured DBHs at different plots for location Berahan Kulon Village, Demak(Ardhani et al., 2021b)

(b) All measured DBHs at different plots for location Timbulsloko 1 (Ardhani et al., 2021a)

(c) All measured DBHs at different plots for location Timbulsloko 2 (Ardhani et al., 2021a)

Figure 4.3: Different average DBH for different distance from the sea. Plot 1 indicates the plot 15 meters from the marine ecotone. The plot number increases with inland direction

4.2.3. Canopy height and frontal area

Jerez Nova (2022) did research on the canopy density of young *Avicennia marina* in a greenhouse. During the research the density over the z-coordinate of a five year old trees was determined. The data of the five year old trees is shown in table F.2.

Table 4.5 shows the diameter at each section using the information in table F.2. Showing the different diameters, the second open tree shows the most similarity with the DBH of Ardhani et al. (2021b,a) and the basal area indicated by Ardhani et al. (2020). Therefore, in the standard situation, the second open tree will be used, with a height of 2.8 meters.

Open tree			Dense tree		
Tree height section [m]	1. 5 years old	2. 5 years old	Tree height section [m]	1. 5 years old	2. 5 years old
2.4 - 2.8	0.0025	0.0025	1.8 - 2.1	0.0067	0.0033
2.0 - 2.4	0.0425	0.0450	1.5 - 1.8	0.0467	0.0433
1.6 - 2.0	0.1025	0.1200	1.2 - 1.5	0.2967	0.2933
1.2 - 1.6	0.4500	0.3325	0.9 - 1.2	0.3267	0.3267
0.8 - 1.2	0.3500	0.3225	0.6 - 0.9	0.2467	0.2367
0.4 - 0.8	0.0850	0.0925	0.3 - 0.6	0.1400	0.1400
0.0 - 0.4	0.0550	0.0525	0.0 - 0.3	0.0967	0.0967

Table 4.5: Width of a 5 years old tree as a function of the distance from the ground calculated from table F.2

As explained in section 4.2.2, Nv and D are limited. The height of the standard tree used is equal to 2.8 meters.

For extreme conditions, so a return period of 20 years, the surge will be equal to 0.76 meters. This will give a water height of 1.73 meters at the edge of the forest. Therefore, the length of the tree subjected to wind equals 1.07 meters. For this tree height, the value of N_v will be equal to

$$N_v < \frac{1}{0.006 * 1.07^2} = 155.38 \text{trees/m}^2$$

$$N_v > \frac{1}{0.203 * 1.07^2} = 4.31 \text{trees/m}^2$$

As according to Ardhani et al. (2020) the tree density is equal to 1772 number of trees per hectare. As the formulas are limited, the tree density will have to increase. Therefore, the value of the tree density is equal to 4.4 trees/m^2.

4.2.4. Varying versus constant tree height

To determine the wind force, two different situation can be chosen. The two situations are shown in Figure 4.4. In the upper situation, the tree height stays equal over the forest, which causing the top of

the forest to be higher at the landward site. In the lower situation, the tree height decreases over the forest. This way the forest top stays at the same location. As the DBH stays approximately equal over the forest shown in Figure 4.3 (Ardhani et al., 2021b,a), it is likely that the trees have the same height. Therefore, the upper situation is chosen for further calculations in the standard situation.

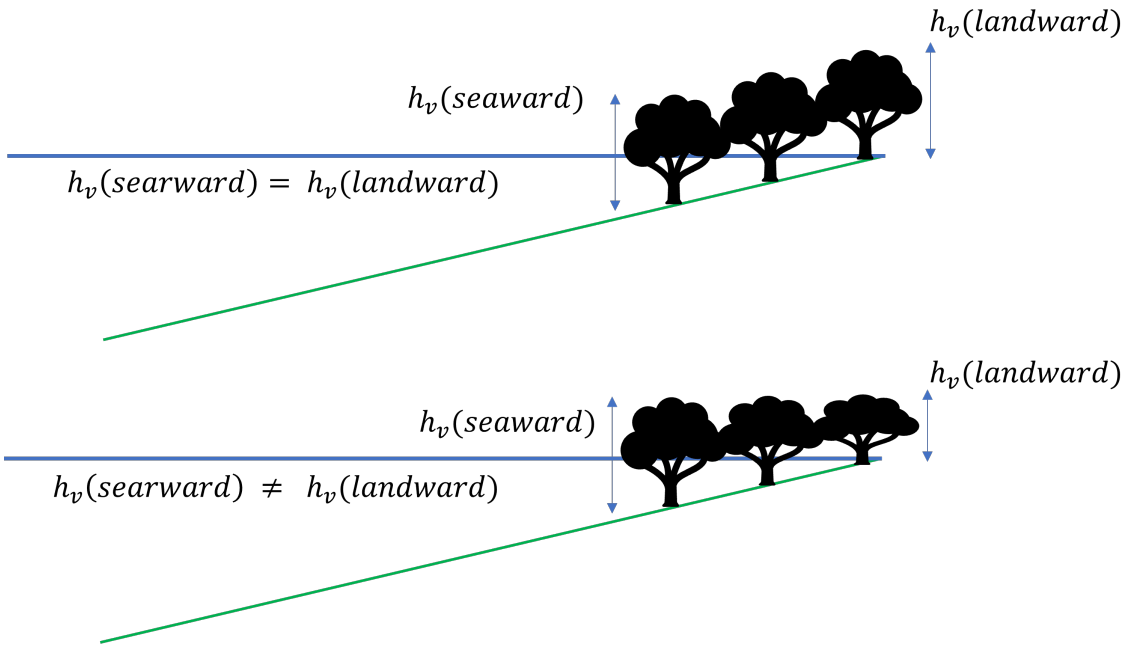


Figure 4.4: Situations changing and non-changing tree height

4.2.5. Root system depth

For the first calculations a root depth of 0.5 meter is assumed. This assumption is based upon the length of the pneumatophores measured by Böhm (2018) and literature (Vovides; Tomlinson, 2016; Srikanth et al., 2015; Raven et al., 2020).

4.2.6. Root contribution to the resistance

As explained in Figure 3.12, the roots only partly contribute to the resistance against the moment. Looking at pictures of failed trees, the angle α is assumed to be equal to 60 degrees.

4.2.7. Tensile, compression, bending tensile strength and Modulus of Elasticity

The physical and mechanical (strength) characteristics of *Rhizophora mucronata* analysed in the research of Manguriu et al. (2013) are used, as no information of about these characteristics of *Avicennia marina* are known. Due to the higher wood density of *Rhizophora mucronata*, the strength characteristics will be slightly overestimated. Also, no bending compression strength is known, therefore the compressive strength will be used.
Hilmi (2018) analysed the Modulus of Elasticity (MoE) of different mangrove trees, given a MoE for *Avicennia marina* of $6.0 * 10^6$ kPa. The MoE of *(Rhizophora mucronata* was given $1.3 * 10^7$ kPa, while Manguriu et al. (2013) indicates a MoE of $1.7 * 10^7$ kPa for *Rhizophora mucronata*. This gives an indication of the variability of the MoE.

Parameter	Value	Unit
Compressive strength	79.96	N/mm^2
Tensile strength	158.91	N/mm^2
Bending tensile strength	100.62	N/mm^2
Modulus of Elasticity	$6.0 * 10^7$	kPa

Table 4.6: Strength characteristic parameters (Manguriu et al., 2013; Hilmi, 2018)

4.3. Soil parameters

The soil present in Demak is analysed in the laboratory by BioManCo (2019). The particle size was measured using a Malvern particle sizer. The averaged particle size distribution of the six samples is given in Figure 4.5. For a pumping speed of 850 rpm some sediment was left behind in the tube, so this speed was to low. Therefore, the same test was also done for a speed of 2000 rpm. The larger peak between 1 and 10 μm can be explained from the fact the higher speed breaks the larger pieces in to smaller pieces. This demonstrates that, despite being necessary to maintain the entire sediment sample in suspension, the increased pumping speed breaks up flocs, making it unsuitable for analyzing the flocculated sample. A high pumping speed is suggested for deflocculated measurements because flocs breaking is not an issue in those circumstances. The particle size distributions of all six samples can be found in Appendix E. Overall, this soil can be determined as a silty soil.

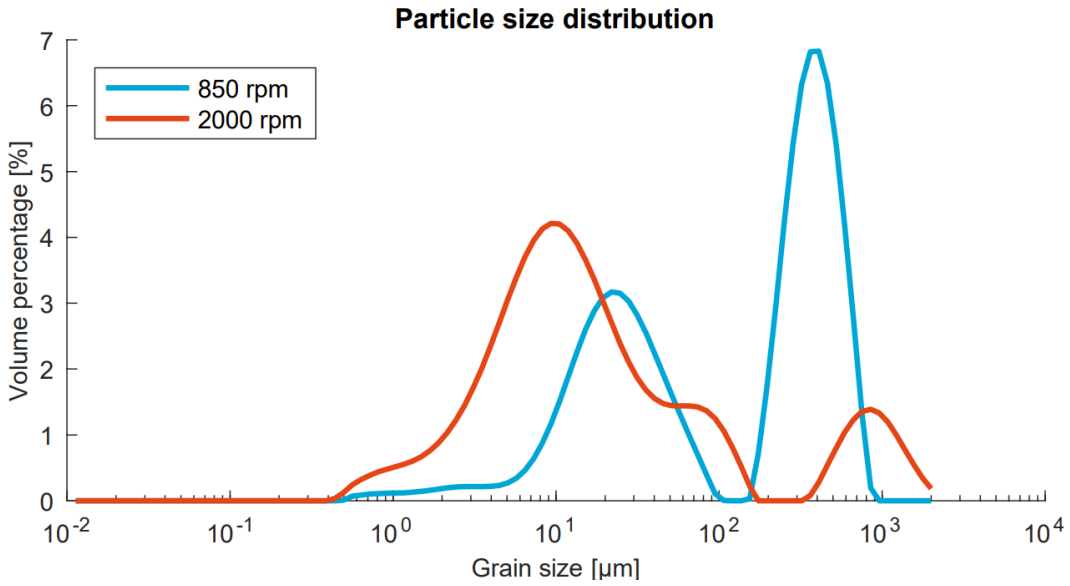


Figure 4.5: Averaged particle size distribution of six samples (BioManCo, 2019)

As the resistance for the failure mechanism uplift is determined by weight of the soil on top, the bulk density is important. The average bulk density is equal to $\rho_b = 1391.3$ g/l with a standard deviation of 3.2% and a water content of approximately 57.94% (BioManCo, 2019).

Parameter	value	Unit
Bulk density	1391.3	g/l
Water content	57.94	%
Porosity	0.78	[-]

Table 4.7: Soil properties (BioManCo, 2019)

4.3.1. Undrained shear strength

For this type of soil and application, the characterisation of the shear strength is mainly done in terms of undrained shear strength by means of a vane shear test. BioManCo (2019) has done multiple laboratory tests, resulting in an undrained shear strength of 70 Pa. Which is an extremely low undrained shear strength. To determine whether the same undrained shear strength was measured in the field, some vane shear test were done in Weg naar Zee, Paramaribo, Suriname. The soil and circumstances in this mangrove forest are comparable with the circumstances in Demak. Therefore, the order of magnitude of the insitu undrained shear strength can be determined. The results and detailed explanation can be found in Appendix E. Over this data, no significant increase in undrained shear strength over depth was noticed. Also, no significant difference near and away from roots was noticeable. Therefore, the undrained shear strength was taken equal to 17.5 kPa.

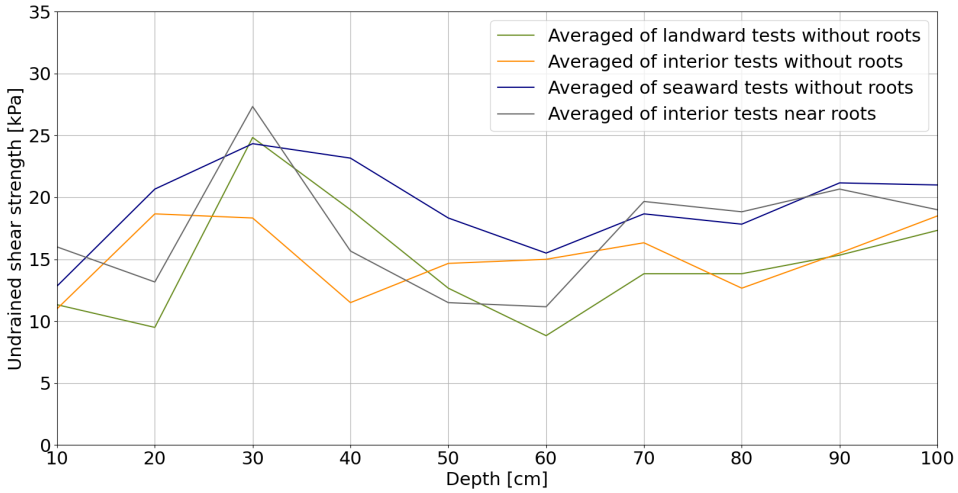


Figure 4.6: Averaged results for the vane shear test of all four locations at Weg aan Zee, Paramaribo, Suriname

4.3.2. Modulus of subgrade reaction

The modulus of subgrade reaction is important for the failure mechanism against uplift, when the leeward side is schematised as a beam supported by springs. The modulus of subgrade reaction is dependent on the compaction and grainsize distribution. Looking at the grain size distribution, as is shown in Figure 4.5 (BioManCo, 2019), the soil is a silty soil. Also, the soil is very moisterized. Barounis et al. (2009); Ikpotokin; Ubani et al. (2020); Barounis et al. (2013), all give a range of 5000 kN/m^3 untill 25000 kN/m^3. As the soil is highly saturated which influences this modulus, the assumed value is slightly beneath the average and takes as $10,000$ kN/m^3.

5

Results/Analysis

This chapter is divided into two parts. First the magnitude and influential factors of the loads on the tree will be discussed. Secondly, the different failure mechanisms and their influential factors will be discussed.

5.1. Load

The wave transformation model was validated using the paper of Vuik et al. (2016), who collected field wave measurements at a salt marsh fringe. The drag- and inertia force of the waves was validated using hand calculations. The wind force was validated using the paper of Rudnicki et al. (2004), who measured the wind force on pine trees in a wind tunnel. The detailed validation can be found in Appendix F. The parameters as indicated in Chapter 4 are implemented in the model to get the forces acting on the trees at three locations:

- At the seaward edge
- At the landward edge
- At the interior

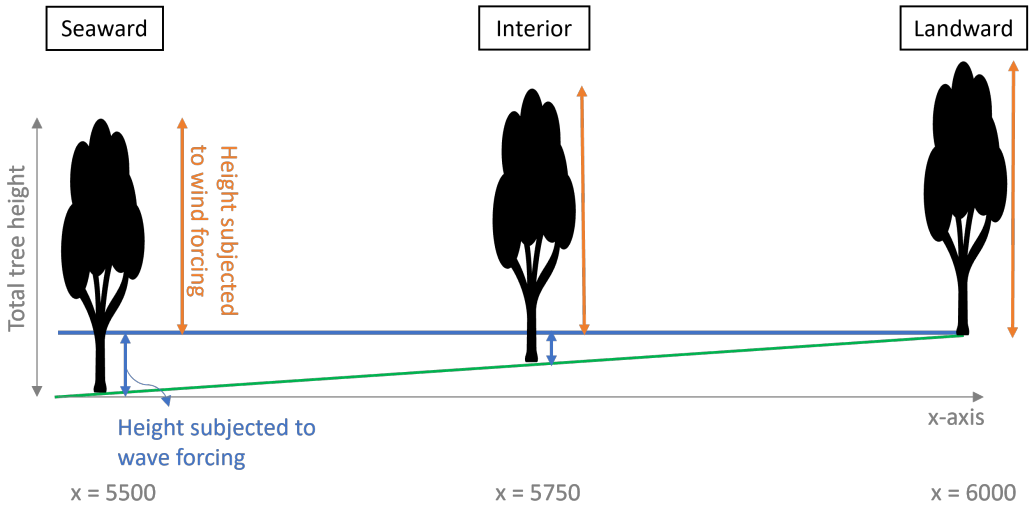


Figure 5.1: Three locations of the tree to determine forces

Through the forest the area subjected to wave forces decreases, while the area subjected to wind forces increases. For all three locations, the detailed results for the wave and wind forces can be found

in Appendix G. In this chapter the overview and most important findings are shown. Only the results of a return period of 20 years will be shown, as this is the highest return period available, giving the most extreme storm conditions.

5.1.1. Magnitude of force and moment

Figure 5.2 shows the width of the vegetation, the tree at a certain x-coordinate and the Δz. Graph 5.3 shows at a specific x-coordinate what will be the force per meter over the vertical, at a height z. This value is obtained by the force subjected to the marked area in Figure 5.2 divided by Δz. The width of the vegetation is equal to the area of the vegetation divided by Δz.

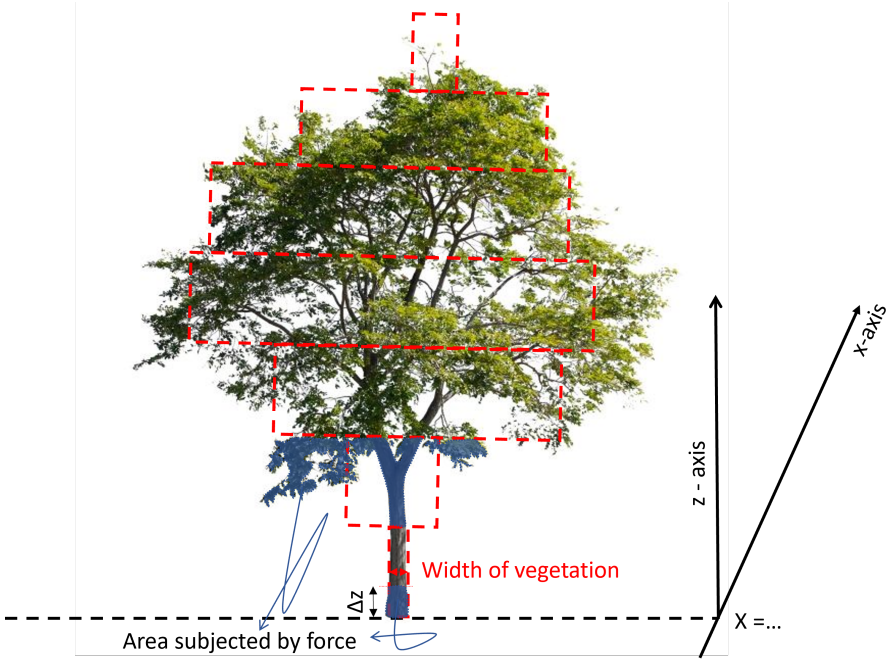


Figure 5.2: Explanation of units of the forces over the z-coordinate

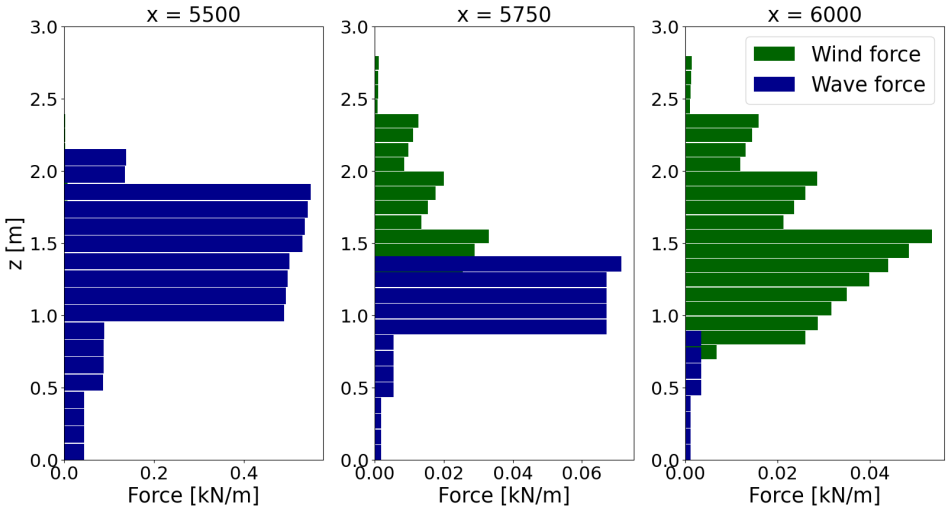


Figure 5.3: The wind and wave force over the z-coordinate for a return period of 20 years

Figure 5.3 shows the increasing windforce from the seaward edge of the forest to the landward edge, while the wave force is decreasing. This increase and decrease is also indicated in 5.4. This graph shows that at the beginning of the forest the total force on the trees is dominated by the wave force, while at the end of the forest this force is controlled by the wind force. This can be explained by the fact that at the edge of the forest only a very small part of the tree is subjected to wind, due to the large water depth.

Figure 5.5 shows the moment caused by the wind and wave forces over the x-coordinate. Comparing with Figure 5.4, it should be noticed that the point where the forces of the wind becomes larger than the forces of the waves occurs later compared to the moments caused by both. Which results from the fact that the wind and wave force act at a different acting point, creating a different moment.

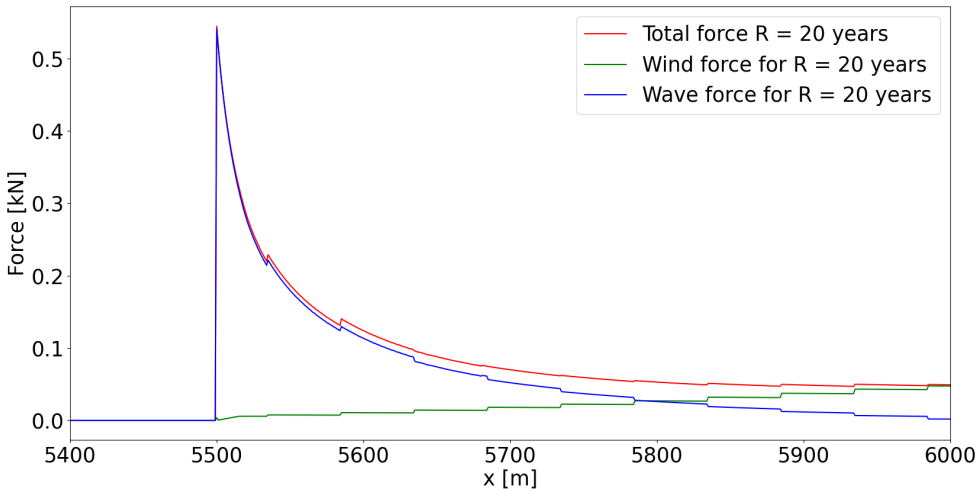


Figure 5.4: The total forces on a tree over the x-coordinate and the contribution of the wave and wind force for a return period of 20 years

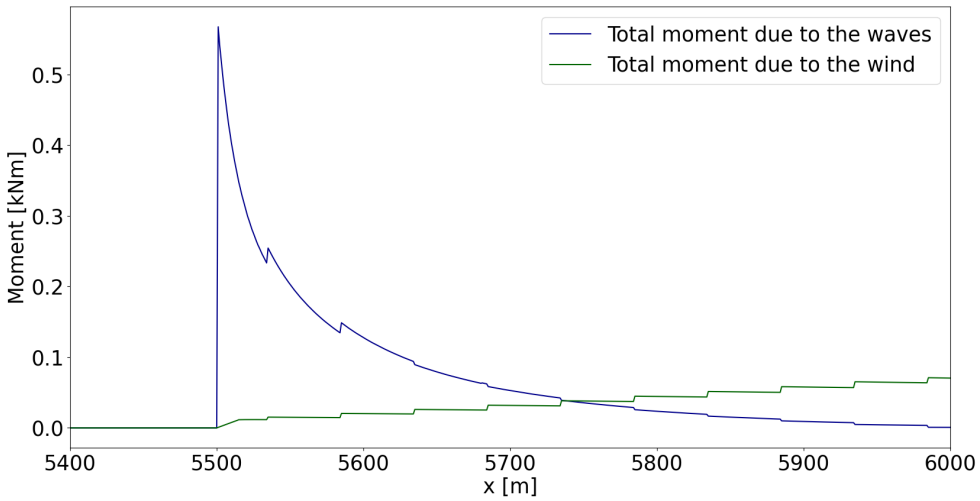


Figure 5.5: The moment caused by the wind and waves over x for a return period of 20 years

Overall, the forces and moments caused by the wind and waves can be summarized as shown in Figure 5.6. The decrease in wave force through the forest is caused by a smaller wave energy due to

the vegetation and wave breaking. Secondly, the area of the vegetation submerged in water reduces. The increase of wind force is largely caused by the rising area subjected by wind, and only little by the increase in wind velocity through the forest. The increase in wind velocity is only small, as the gust factor grows very little after x = 5550.

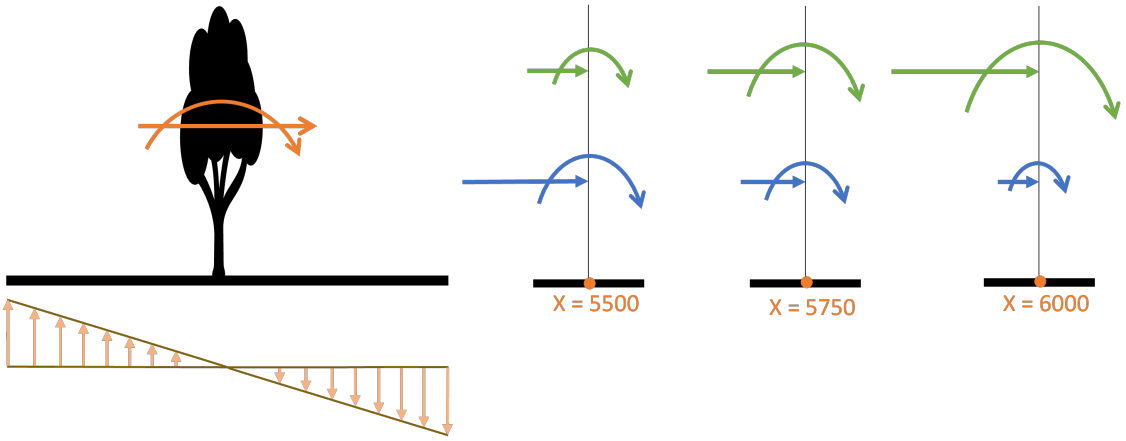


Figure 5.6: Summary of different forces and moments at different locations of the forest

5.1.2. Influential factor - Tree height

For this research, a tree height of 2.8 meters has been selected, which is equal to a tree of approximately 5 years old. Trees in mangrove forests can become much larger than this. Increasing the tree height enlarges the wind forces on the tree, but also changes the wave forces on a tree. For higher trees, often, the frontal area of the submerged part decreases due to the canopy rising above the waterline and the stem being submerged. For the tree of 2.8 meters, the water reaches above the densest area of the tree. Therefore, if the tree height increases, first, the submerged area will not decline largely and will stay approximately the same. This can be explained using Figure 5.7.

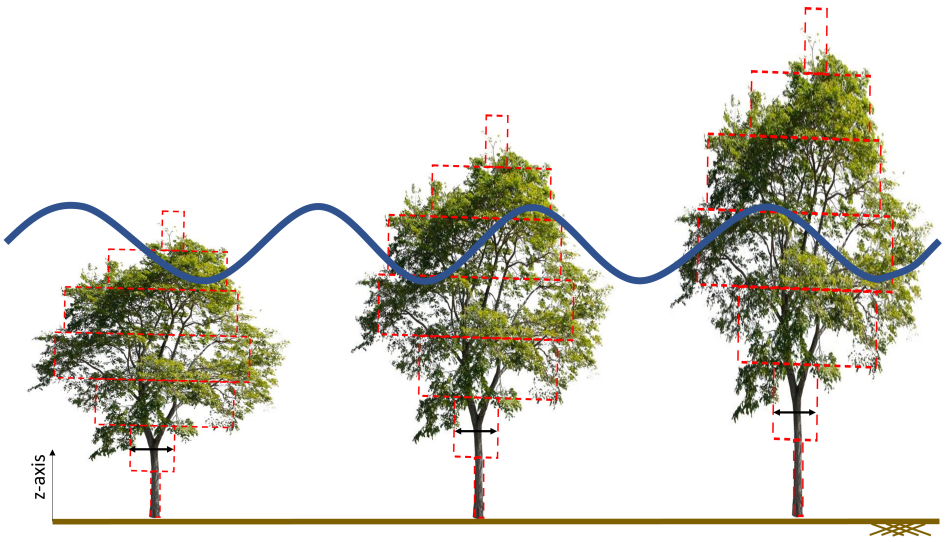


Figure 5.7: Increasing tree height

If the tree height increases, the z-axis is still divided into seven blocks. Therefore, the height of each block increases while the width stays the same. For that reason, the blocks with a smaller width above the largest width of the 2.8-meter tree arise above the waterline. Depending on the size of all the blocks submerged, the total area exposed to wave forces changes. If the tree height increases even more, the block with the largest width also rises above the water line, and the area decreases more significantly.

In reality, the width of the vegetation does change, but as no information is available on the increase in width, the blocks are taken equal to the width of a 5-year-old tree of 2.8 meters. This assumption underestimates the forces due to the fact a larger tree has a larger vegetation width.

If the submerged area increases, the wave force increase and visa versa. In Figure 5.8, it can be seen that between a tree height of 2.8 meters and 4.8 meters the wave force decreases slightly. While between 4.8 meters and 6.3 meter the wave force drops heavily. Between the 2.8-meter tree and the 4.8-meter tree, first, the more open layers arise above the waterline, while for the 6.3-meter tree, almost the whole canopy rises above the waterline.
The used Δz and approximation of the vegetation width causes the steps in the different lines. In reality, the transition of vegetation width is more smooth.

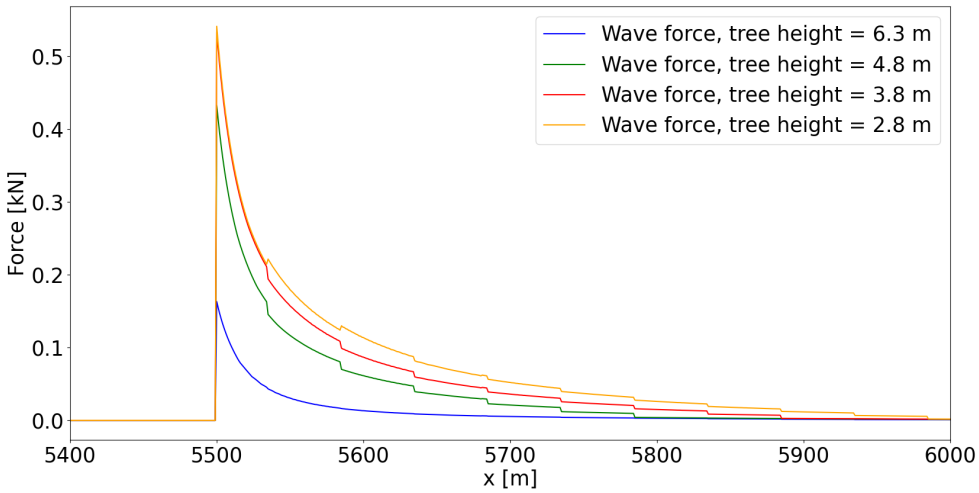


Figure 5.8: Effect of increasing tree height on wave force

The total force increases when the tree height increases, as shown in Figure 5.9. The total force increases the most at the interior and landward side of the forest. At the seaward edge of the forest, the total force decreases slightly due to the decline submerged area of the tree, causing a shrink in the wave force. As the wave force controls the total force at the seaward edge, the total force also declines slightly at this location.

In Figure 5.9, the forces created by the wind and waves for different tree heights is shown. The force at the first row of trees at the seaward side of the edge does not show a large difference between a 2.8-meter tree and 4.8 meter tree. The total force at the seaward edge is dominated by the wave force for this tree height, as shown in Figure 5.8, the decay in wave force is small between those tree heights. Therefore, the difference in total force is also small. As the wind force becomes more dominant in the total force toward the landward side, the difference between the total force for both tree heights becomes larger. For a tree height of 6.3 meter, the wave force did show a large decline compared with a 2.8-meter tree, which also shows in the total force. Secondly, the contribution of the wind in the total force is more significant at the seaward edge due to the larger part of the tree subjected to wind.

The increase in total force indicates an even larger enlargement in the wind force, as the wave force decreases with growing tree height. Figure 5.10 shows that the moments increase even more due to the larger arm of the force, and the moments caused by the wind are more dominating the total moment. In Figure 5.10, the total moment is given. In Appendix G, more detailed graphs of the force and moment due to wind and wave are given.

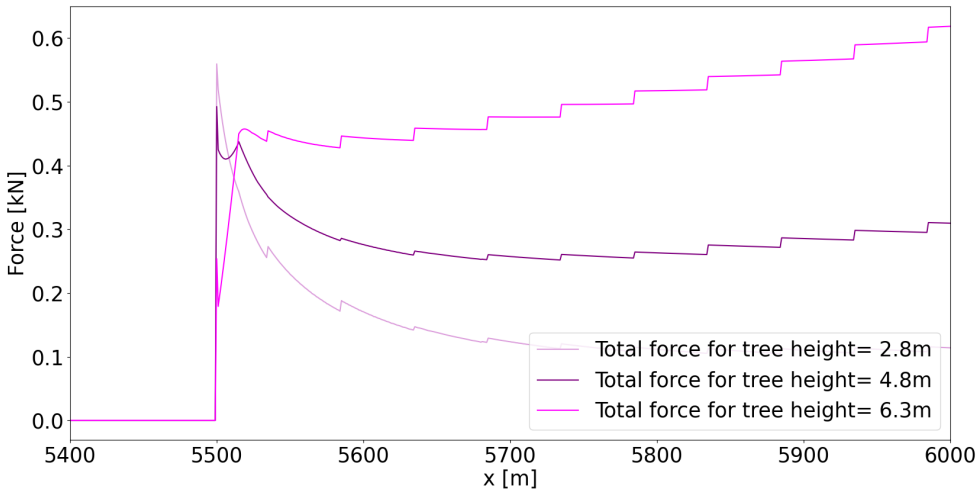


Figure 5.9: Forces caused by wind and waves over the x-coordinate for different tree heights

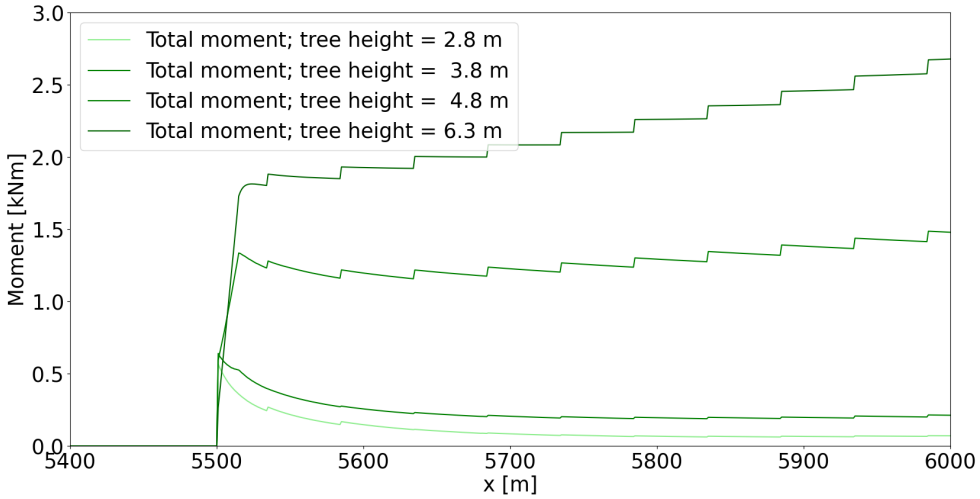


Figure 5.10: Total moment caused by wind and waves over the x-coordinate for different tree heights for a return period of 20 years

Maximum moment and force

Using a tree height of 2.8 meters and the parameters as indicated in chapter 4, the force and moment are at its maximum at the edge of the forest. For a tree of 2.8 meters and a return period of 20 years, the maximum force and moment are equal to, respectively, 0.54 kN and 0.58 kNm. If the tree height increases, the wind force becomes more significant. Therefore, the maximum moment will shift to the landward side of the forest. This moment is slightly underestimated as the vegetation width from the tree of 2.8 meters is used.

For a tree of 2.8 and 3.8 meters, the maximum moment and force occur at the same location. For larger trees, both do not occur at the same location. The maximum horizontal force occurs at the seaward edge of the forest, while the maximum moment occurs at the landward side of the forest. For a tree height of 6.3 meter, the maximum moment and force occur at the same location again, namely the back of the forest.

5.2. Resistance

In this section, the results of the modelling of the multiple failure mechanisms are shown. Detailed results of every failure mechanism can be found in Appendix C.2. If not indicated differently, the number of roots is determined using a DBH of 9.25 cm, as described in Chapter 4. In this section, the maximum force and moment action on a 2.8-meter *Avicennia marina* are used, see Table 5.1.

	Moment	**Horizontal force**
Maximum value	0.58 kNm	0.54 kN
Location	Seaward edge (x=5500)	

Table 5.1: Moment and force used in resistance calculations

5.2.1. Failure mechanisms: Breakage of the roots, slippage of the roots and breakage of the trunk

For all three failure mechanisms 'Breakage of the roots', 'Slippage of the roots' and 'Breakage of the trunk', the factor of safety is very high. For the first two failure mechanisms, all roots are assumed to have the same diameter and length. The total volume of roots is determined using the belowground biomass and the root density. As a consequence, when the diameter stays the same, but the length of the root halves, the number of roots doubles. This influences the distribution of the force.

Diameter root	**Length root**	**SF Breakage**	**SF Slippage**
6.3 mm	0.75 m	3600	130
6.3 mm	1.5 m	1800	130
6.3 cm	1.5 m	1850	13
6.3 cm	0.75 m	3500	12

Table 5.2: Safety factors for failure mechanisms breakage and slippage of the roots

The safety factor for root breakage is approximately the same for an equal root diameter, but different length, which may appear contradictory. This equal safety factor is caused by a different number of roots. Due to the difference in length (factor 2), but same total root volume, the number of roots also differ by a factor of 2. The horizontal force due to waves and wind is distributed over all the roots, causing the maximum force appearing in the shorter roots to be smaller than in the longer roots. Therefore, although the diameter is the same, the safety factor differs due to different root lengths and the same total root volume.

The same explanation can be used for the equal safety factor for slippage, while the length is different. Due to variance in root length, the number of roots differ, causing the maximum force appearing in the root to be contrasting. The maximum force occuring in the root is rougly 2 times larger for the 2 times longer root. Therefore, the safety factor of both is approximately equal.

For both failure mechanisms, the root system does not fail.

For the failure mechanism of trunk breakage, the calculation is given in Table 5.3. The maximum compressive bending strength is equal to 79.96 N/mm^2 and the maximum tensile bending strength is equal to 100.62 N/mm^2.

Moment [kNm]	**DBH [cm]**	**I [mm^4]**	**σ [N/mm^2]**	**SF [-]**
0.58	9.25	$3.6 * 10^6$	7.5	11

Table 5.3: Calculation of safety factor the the breakage of the trunk

5.2.2. Failure mechanism: Bearing capacity

The failure mode for bearing capacity is adopted with reference to undrained conditions for two reasons. Firstly, the soil pore pressures and, therefore, effective stresses are unknown for the situation in

Demak. Secondly, the mechanical characteristics of the soil are described in terms of undrained shear strength. The detailed explanation about when a soil is described in terms of undrained shear strength and what influences this can be found in Appendix B. The equation for the undrained bearing capacity is given in Equation 3.10 in section 3.3.1.

Figure 5.11 shows the eccentricity of a shallow foundation. Eccentricity affects the effective area, and therefore resistance, of the shallow foundation. The eccentricity of the mangrove and its schematized root system is influenced by the moment due to the wind and wave forces and the normal force created by the above ground biomass. The moment acting on the tree is equal to 0.58 kNm, as shown in Table 5.1. The normal force can be determined using the above groundbiomass (AGB), as described in Chapter 4. A *Avicennia marina* with a DBH of 9.25 cm has an AGB of 34.6 kg, giving a normal force of 0.34 kN. The eccentricity of the shallow foundation is $e = M/N = 0.58/0.34 = 1.71$m. As a consequence, if the foundation has a smaller width than 3.42 m, the effective width is equal to zero and the bearing capacity is non-existing.

The bearing capacity of a shallow foundation using the parameter as indicated in Table 5.4 is equal to 177 kPa. Changing the parameters, like the horizontal force, undrained shear strength, bulk density and rootplate diameter the bearing capacity changes within a range 120 - 180 kPa. The normal force 0.34 kPa gives a stress of 51 kPa. Therefore, the shallow foundation does not go to failure.

Maximum moment	0.58	kNm
Maximum horizontal force	0.54	kN
Normal force	0.34	kN
Undrained shear strength	17.5	kPa
Diameter rootplate	3.5	m
Depth root plate	0.5	m
Bulk density	1391.3	g/l
Bearing capacity coefficient (Vesic, 1975)	5.14	[-]

Table 5.4: Parameter of the schematization of the bearing capacity using a shallow foundation

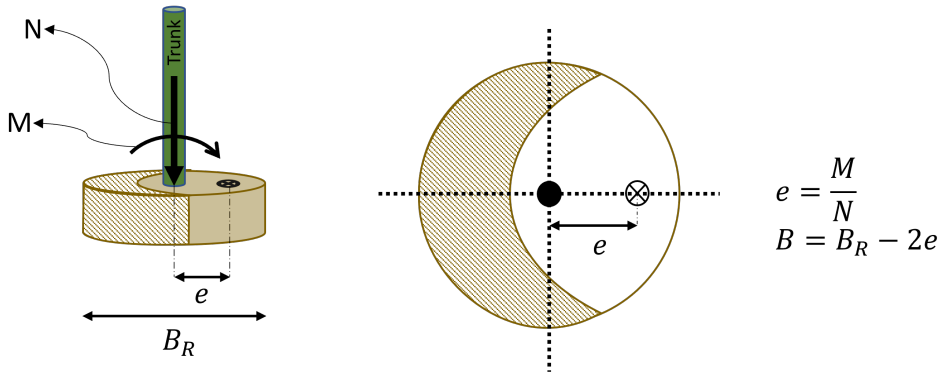


Figure 5.11: Explanation eccentricity shallow foundation

The results shows that the eccentricity caused by the horizontal force and relatively low normal force, caused by the AGB, is large. Figure 5.12 shows the maximum horizontal force for a certain diameter of the shallow foundation. If the total horizontal force becomes larger, the effective area of the foundation is zero. This causes the fact that the shallow foundation is not able to sustain the forces, as no effective foundation is present. In reality, a tree can sustain very high horizontal loads due to the contribution of the roots. As the roots contribution are not taken into account explicitly in the schematization of shallow foundation, this scheme is not an appropriate scheme for this specific problem.

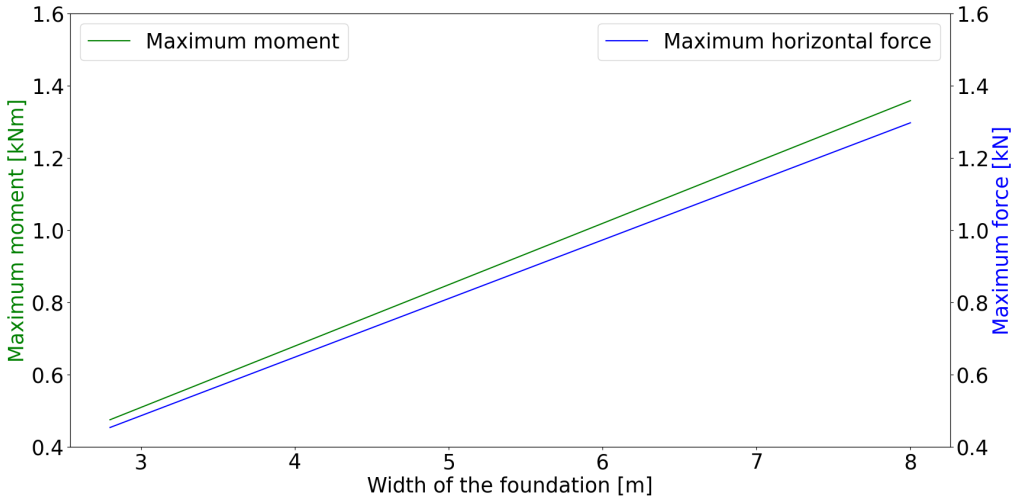


Figure 5.12: Maximum force and moment to stay within eccentricity limits of the formulas

5.2.3. Failure mechanism: Uplift

Equal root diameter and length

The last failure mechanism is soil uplift. For the first analyses the root diameter and length of every root are taken equal. The relationship between the root diameter and uplift and stress is given in Figure 5.13. The maximum stress inside a root is calculated using Equation 3.14 and whether uplift occurs is determined using Equation 3.16. From this graph it can be seen that a larger diameter causes more uplift, while a smaller diameter has a higher probability of breakage.

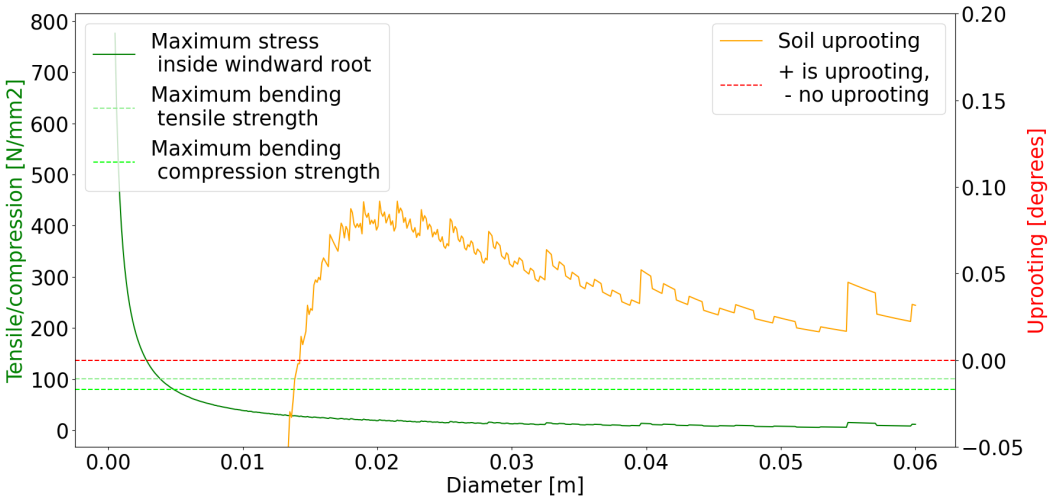
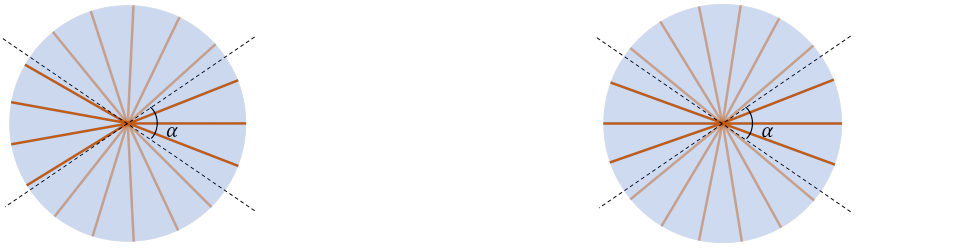


Figure 5.13: Relation between the root diameter and stress inside the root and uplift

In the line displaying the amount of uplift, oscillations are visible, which can be explained by the number of roots contributing to the resistance. Due to the uniformly distributed roots and the assumed participation angle α (equal to 60°, see Chapter 4), some roots do participate in the resistance and some do not, as shown in Figure 5.14. In Figure 5.14a, the distribution with a root diameter of 0.047m is shown, having in total 17 roots. In Figure 5.14b, a root diameter of 0.046m causes a total of 18 roots. It would be expected that due to the smaller amount of roots in the larger diameter root system, the moment inside each root would be larger compared to the smaller diameter root, but this is not the case.

In both figures, the roots participating in the resistance are indicated between the dotted black lines. It can be seen that although Figure 5.14a has less roots in total, due to the distribution, more roots engage in the resistance, namely 4, compared to Figure 5.14b. Therefore, the moment taken by each root is smaller for the larger diameter root. As a consequence, the uplift is less for the larger diameter root compared to the uplift of the smaller diameter root. Secondly, the number of roots is determined using an integer number which results in rounding errors. Both phenomonems together create the jiggling character of the line.



(a) Number of roots equal to 17, with a diameter of 0.047m

(b) Number of roots equal to 18, with a diameter of 0.046m

Figure 5.14: Difference in resistance due to the distribution of roots

Different root diameter and length

In nature, the roots system exists of different root diameters and root lengths. Therefore, for the second part of the analyses, the root diameter and length of each root can be adapted, as well as the number of roots per diameter or length. This all influences the distribution of the moment due to the wind and waves over the roots. As the total volume of roots is calculated using the DBH of 9.25 cm, which is assumed constant to the forest, the total volume of roots stays even. Below the comparision between the continiously spring-supported leeward roots with or without vertical movement is made, situation 4 and 5 respectively. The same analysis is made for the three situations without continuously spring supported leeward roots and can be found in Appendix C.2.

Table 5.5 shows a random composition. The maximum root diameter is determined based on pictures, see Figure I.5 and I.6, of *Avicennia marina* in Wijk aan Zee, Paramaribo, Suriname. The length of the roots is chosen arbitrary, but keeping in mind that in clayey soils the root system often has one longer root compared to the medium diameter roots (Fourcaud et al., 2008). Lastly, the ratio of total volume is chosen smallest for the largest diameter root and is increased for the smaller diameter. This assumption is again based on the pictures in Figure I.5 and I.6.

Root diameter [cm]	Length [m]	Ratio of total volume [-]
4	0.75	1/20
3	0.75	1/20
1.5	0.5	1/10
1.0	0.5	3/20
0.75	1.0	1/4
0.5	1.0	1/4
0.25	1.0	1/5

Table 5.5: Root composition

Figure 5.15 shows the stress inside each root and the amount of uplift for each single root. As described in Chapter 3, uplift is defined as the rotation angle caused by the forces minus the resistance against rotation by the soil layer ontop of the roots. If the angle is positive, the soil uproots. As can be seen from the graphs, no windward roots reach the maximum strength, although multiple roots do uplift.

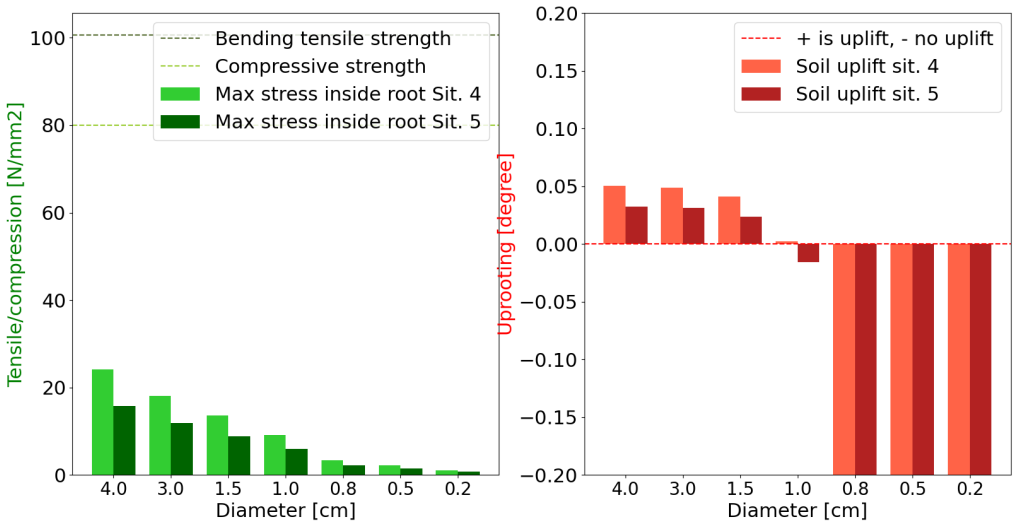


Figure 5.15: The stress inside the roots and uplift of the windward roots for situation 4 and 5

As can be seen from Figure 5.15, situation 5 has lower stresses inside the windward roots compared tot situation 4. While Figure 5.16 shows that in situation 5 the stresses on the leeward side stay higher compared to situations 4, which is a consequence of the restricted vertical movement. The distribution of moments inside each root for situation 5 can be found in Appendix C.2.

The second observation made from Figure 5.16 is that the difference in stress between the smaller and larger diameter roots is relatively small compared with the windward side. This is a consequence of the spring support on the leeward side. Because the spring constant is proportional to the diameter of the root, larger diameter roots have greater resistance. This causes the moment distribtution between roots to be proportional to the quadratic area moment and the damping constant, equal to the modulus of subgrade reaction times the diameter of the root.

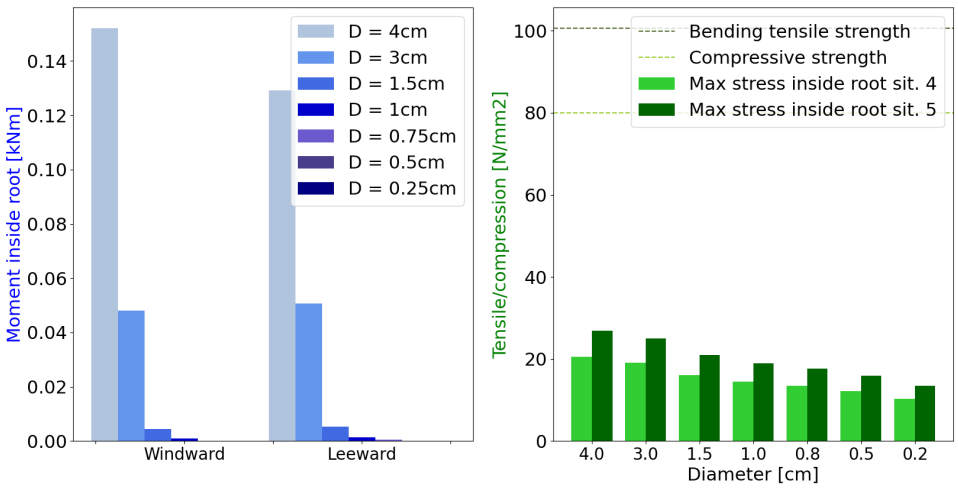


Figure 5.16: Moments inside the roots for situation 4 and the stresses inside the leeward roots for situation 4 and 5

The root composition can be chosen in any combination. Differing this composition, changes the stresses inside the roots and uplift. In the section below, the influence of each parameter is deter-

mined.

Influencial factors
To determine the influence of multiple factors, the parameters in Table 5.6 are used, while adapting one single parameter. The jumps in the graphs are, as explained above, created by the rounding of numbers and distribution of roots.

Parameter	Value	Unit
Root length	1.5	m
Root diameter	2	cm
DBH	9.25	cm
Participation angle α	60	°
Modulus of Elasticity	$6.0 * 10^6$	kPa
Modulus of subgrade reaction	10^4	kN/m^3

Table 5.6: Parameters for sensitivity analysis

Root composition
As the total root volume is assumed constant, the root length and diameter determine the number of roots. If the length of the roots becomes larger, while the diameter stays the same, the number of roots decreases. Therefore, a larger moment per root has to be taken by the same diameter root causing a larger stress inside the root.

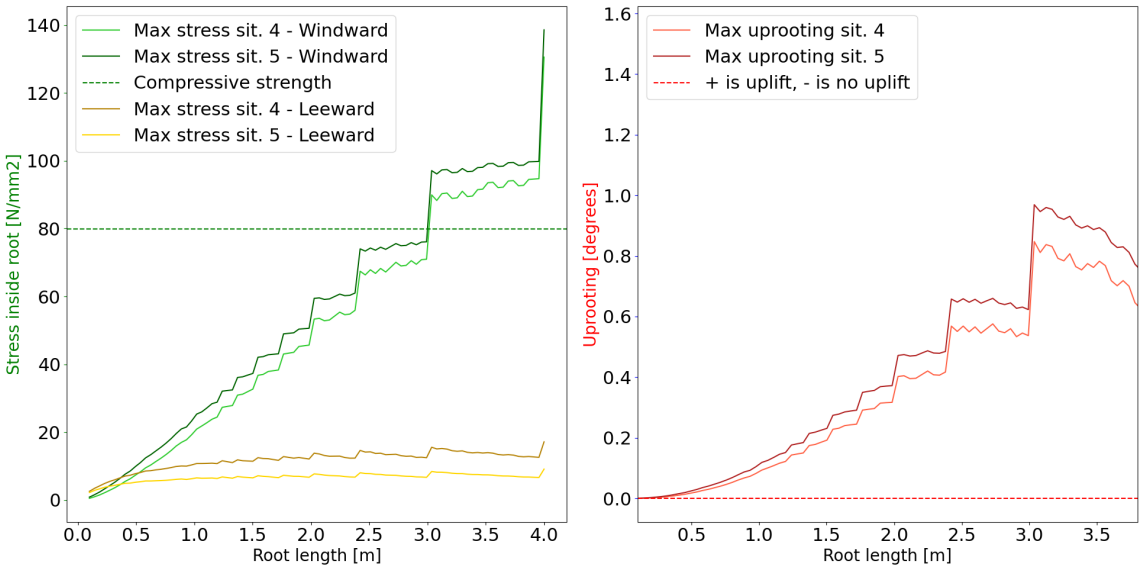


Figure 5.17: Relationship between the length of a root and uprooting and stress inside the root

In Figure 5.17, the length of the root is increases while keeping a root diameter of 2 cm. As a consequence, the number of roots decreases, and the moment inside each root increases, as a smaller amount of roots should withstand the same moment. Looking at the left figure in Figure 5.17, the stress inside the leeward roots does not increase significantly by increasing the root length, and therefore moment, which is a consequence of the spring-support. The stresses inside the windward roots do increase, as no spring-support is present. The distribution of the moment caused by the wind and waves over the roots is done by assuming the angle below the trunk at the windward side and leeward side to be equal. By the spring supported beams, the rotation at the trunk is not dependent on the length of the root, but only on the modulus of elasticity, quadratic area moment and spring constant. The spring constant is dependent on the modulus of subgrade reaction and the diameter of the root. At the windward side the rotation is dependent on the length of the root, modulus of elasticity and quadratic area moment.

Therefore, the stresses on the leeward side only increase slightly, due to the decrease of number of root. On the windward side the stresses do increase, due to the dependence on the number of roots and the root length. The increase in moment in the windward roots causes maximum stresses inside the roots.

This phenomenon also influences the uplift. The moment inside the windward roots increase with larger root length. As the amount of uplift is dependent on the moment inside the root and the length of the root, the amount of uplift also increases with increasing root length. The decline in uplift after a root length of 3.5 meter is caused by the distribution of roots.

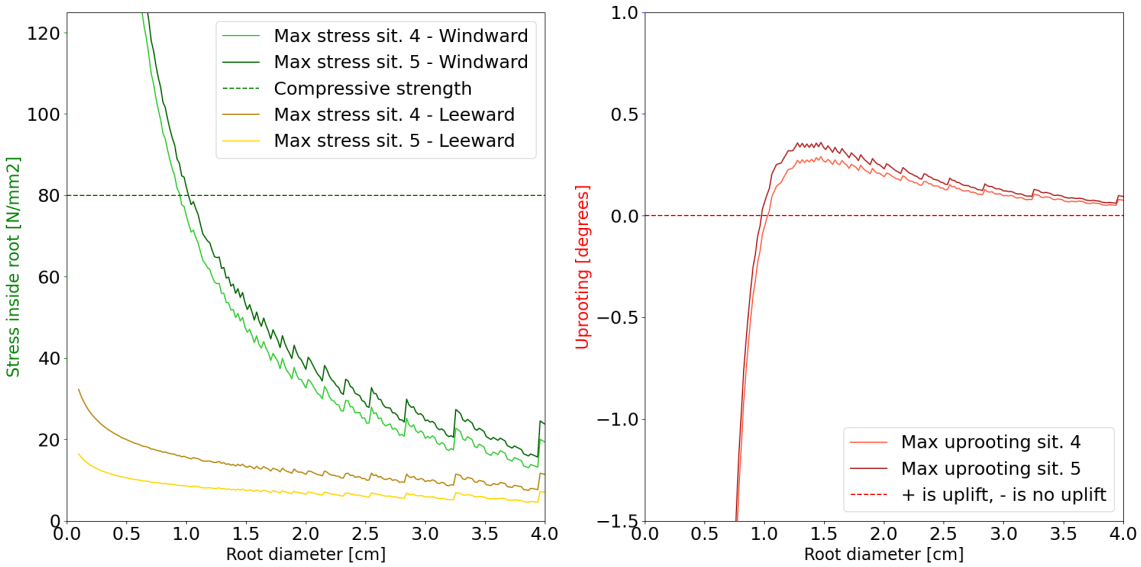


Figure 5.18: Relationship between the diameter of a root and uprooting and stress inside the root

Also, when the root diameter increases, the number of roots decreases with a constant root system volume. The moment inside each root increases, but the stress inside the root is more dependent on the diameter in the quadratic area moment. Therefore, the stress inside the root decreases for a larger diameter. As the spring constant of the spring supported beams is dependent on the diameter, the stresses in the roots on the leeward side will differ more compared to the changing root length. However, the difference in stress is still relatively small compared to the changes in stress on the windward side.
For a root with a diameter less than 1 cm, no uplift is visible. This can be explained from the fact that for this diameter the number of roots is very large, and therefore the moment inside each root is relatively small, thus, the overlying layer of soil is large enough to counteract this moment. If the root diameter increases, the moment inside the root increases and the overlying layer of soil can not counteract the moment inside the root anymore. At some point, the increase in moment inside the root is overruled by the dependence on the quadratic area moment, so diameter, decreasing the amount of uplift.

Participation angle α
Angle α determines the roots which contribute to the resisting moment, as shown in Figure 3.12 and 5.14. If α decreases, the number of roots contributing to resisting the moment due to wind and waves decreases. As a consequence, the moment inside each root increases, increasing the stresses inside these roots and the amount of uplift.

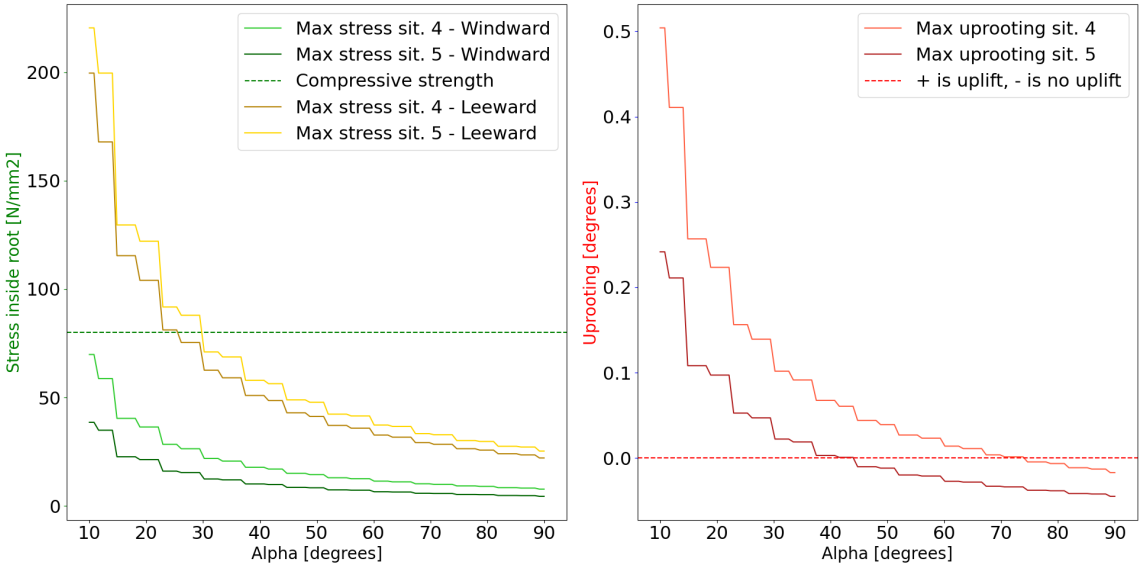


Figure 5.19: Relationship between the contributing angle α and the stress inside a root and uprooting of a root

Elasticity

In situation 4 and 5, the leeward and windward side are differently dependent on the modulus of elasticity. Therefore, the modulus of elasticity does influence the distribution of moment and the stresses inside the roots. If the Modulus of Elasticity increases, the moment on the windward side increases, causing larger stresses on the roots. From Figure 5.20 it can be noticed that when vertical movement of the trunk is allowed (situation 4), the influence of the modulus of elasticity is larger compared to no allowance of vertical movement (situation 5).

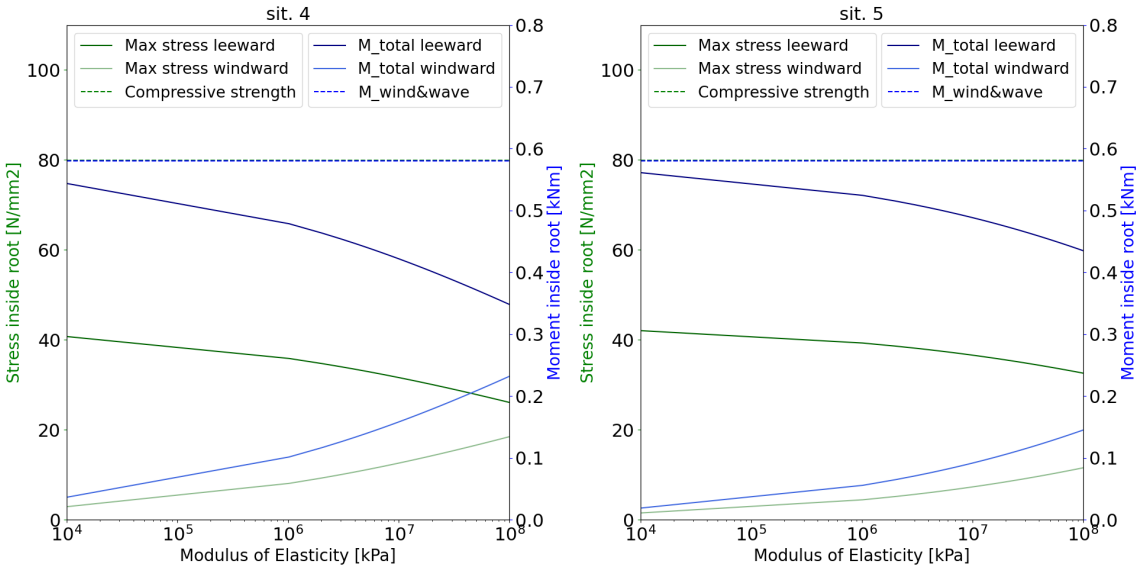


Figure 5.20: Relationship between the modulus of elasticity and the stress inside a root and the uprooting of a root

Modulus of subgrade reaction, c

For an increasing modulus of subgrade reaction the spring constant increases, increasing the contribution of the leeward side to the resisting moment. This increases the stresses inside the root of the leeward moment. As the Modulus of subgrade reaction increases, comparable with more sandy soils, the difference between the stresses inside the leeward and windward roots increases. While for a lower modulus of subgrade reaction the stresses in the leeward and windward roots are more equal. Just like the modulus of elasticity, situation 4 is more sensitive to changes in the modulus of subgrade reaction

compared to situation 5. This difference is a consequence of the boundary condition in situation 4 and the transition condition in situation 5 in the needed differential equations.

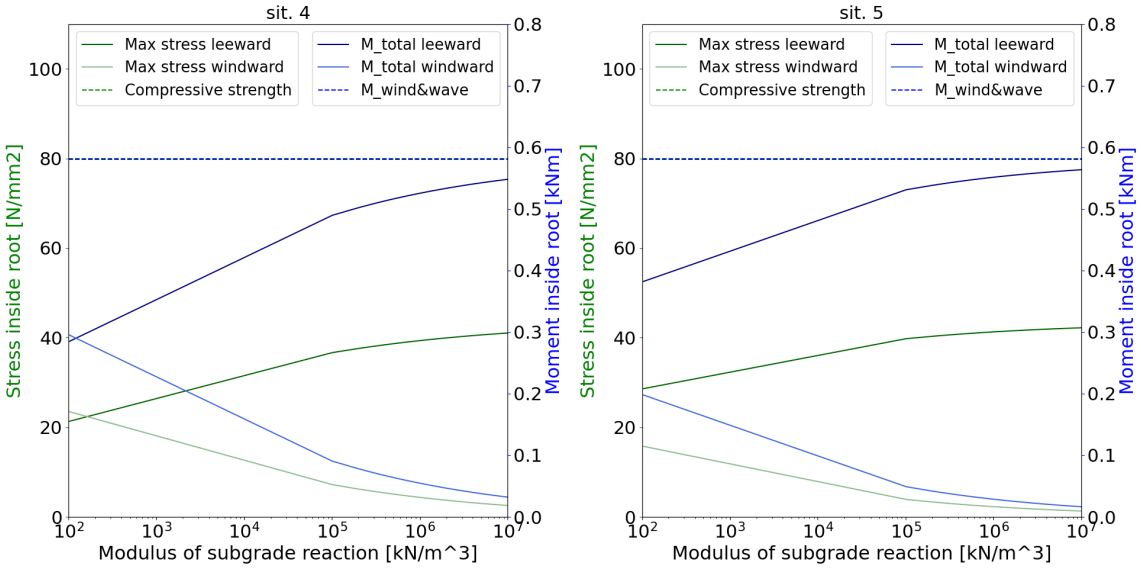


Figure 5.21: Relationship between the modulus of subgrade reaction and the stress inside a root and the uprooting of a root

Resistance against uplift

The resistance against uplift is caused by the layer of soil above, which can be schematized like a distributed load. This distributed load produces a resisting moment of $\frac{1}{2}ql^2$ below the trunk, and causes a angle of $\frac{1}{6}\frac{ql^3}{EI}$. The distributed load is dependent on the thickness of the soil layer and the density of the soil. As can be seen from Figure 5.22 and 5.23, when the rooting depth or density decreases, the resisting moment decreases. Also, the angle of rotation caused by the forces grows faster than the resistance against this rotation. So uplift occurs quicker. In Figure 5.22 and 5.23 the right figure gives the changing resistance angle when the depth or density of the soil change and the angle of uplift occuring due to loading.

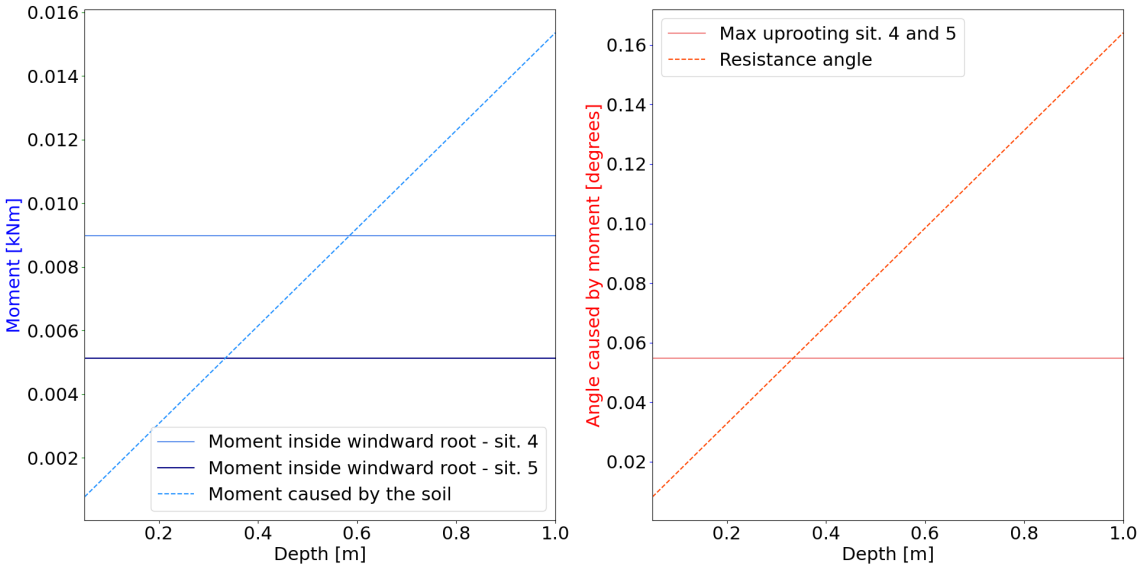


Figure 5.22: Relationship between the resisting moment and resistance against uplift and the rooting depth

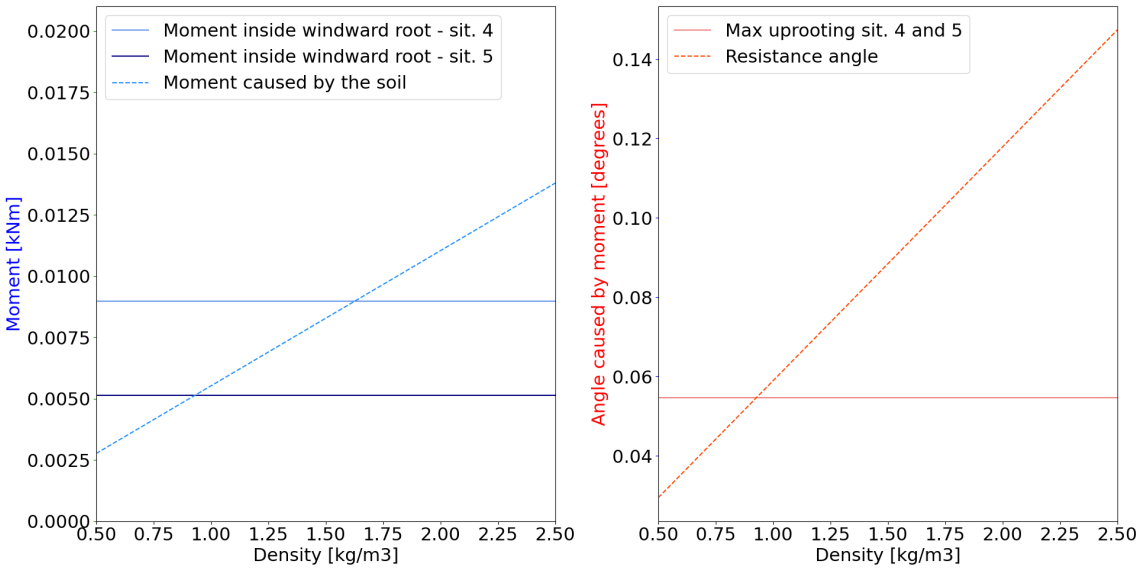


Figure 5.23: Relationship between the resisting moment and resistance against uplift and the soil density

6

Discussion

This chapter start with a comparison of the model with existing methods to determine the tree stability. Secondly, the limitations of the modelling assumptions are discussed to follow with a comparison between field observations and the model are made. Lastly, the interaction of the model between time and the total forest will be discussed.

6.1. Comparison with other calculations of tree stability

The difference between the method in this thesis and other research is the way the root system is approached. Often, the soil-root system is accessed in total (like a whole root plate or an increase in soil properties), while this thesis looks at one specific root and its interaction with the soil.

A common way to analyse the enlarged soil strength is the use of the increase of cohesion due to roots (Yamase et al., 2021; Masi et al., 2023). This method is mainly useful by the calculation of slope stability (Yamase et al., 2021). For mangrove forest, the slope stability is irrelevant due to the relatively flat slope of the shoreline. Secondly, as this thesis uses a total stress approach instead of an effective stress approach, the increase in cohesion of the soil is not useful. Looking at one specific root and the interaction between that root and the surrounding soil gives the opportunity to analyse the differences between root systems. Secondly, in this way it is possible to schematise all failure mechanisms differently, as other soil/root parameters dominate different failure mechanisms.

Kim et al. (2020) used the modulus of elasticity combined with the effective cohesion and internal friction angle to determine the stability of a tree in an unsaturated soil. The soil/root system schematised like a solid plate has been given an equivalent modulus of elasticity. This research shows that the resistance against overturning is insensative to differences in unit weight of the soil and tree, which is different from the results in this thesis. Secondly, assuming the root-soil system as a solid plate, the difference in root architecture are neglected. The results of this thesis shows that the root architecture did influence the stability of a mangrove tree.

De Petris et al. (2020) determines tree stability by comparing the tree with a building and determining the static and dynamic safety by using the rules of engineering. This method uses the parameters closer to engineers than to forestry technicians, like loads acting on the crown and trunk, trunk materials, trunk size. This method does not represents other failure mechanisms than trunk breakage very well, like uprooting and torsion fractures. The model made in this thesis, does determine the stability based on the root system, like the compression and tension strength. Although, the schematization of the failure mechanism of trunk breakage in this thesis gives a high safety factor, while field observations of pulling willow trees do show trunk breakage.

Overall, the approach used in this thesis looks at a single root and its specific contribution to resisting the moment caused by wind and wave forces. Other research often looks at the root system as a whole and/or all failure mechanisms combined instead of schematising them all differently. One of the main

reasons to schematise all failure mechanisms differently is the changing forces through the magrove forest. Every failure mechanism has a different dominating parameter, which can be initialized by the moment or the horizontal force. Therefore the main failure mechanisms can differ through the forest. If the root system and failure mechanisms were determined as a whole, the differences in failure mechanisms and dominating parameters could not have been made.

Another advantage of looking at the failure of a single root is the possibility of modelling progressive failure. Looking at the maximum occuring stress in a single root, it can be determined when a certain root breaks and the moment taken by that root is redistributed over the rest of the roos. Analysing the root system as a whole plate makes this more complicated. A disadvantage of this approach, is the need to know the root architecture, which is irrelevant when the root system is schematised as a solid plate.

6.2. Model limitations

A model is always an estimation of reality and hence limited on specific capabilitities. These limitations will be explained per topic within the following section.

6.2.1. Loads

- **Gust factor:**
  The expression of the gust factor is empirical, and restricted to D/h_v ratios between 0.075 and 0.45. Where D is the separation between the vegetation and h_v is the tree height subjected to wind, equal to 1.07 meter at the edge of the forest. Therefore, the model could only be applied to tree densities, N_v, between $\frac{1}{0.005625h_v^2} = 155$ trees/m^2 and $\frac{1}{0.2025h_v^2} = 4.31$ trees/m^2. While according to Ardhani et al. (2020) the tree density is equal to 0.1772 trees/m^2 in Demak. Besides that, inside the forest an exponential decay is applied inside the trees. This decay may not occur in very sparse vegetation fields, where the wind profile resembles a logaritmic decay. This difference in decay causes the tree to be subjected to different wind velocities, thus forces.

- **Drag and inertia coefficients:**
  The drag and inertia coefficients in the wave formulas and the drag coefficient in the wind forces are given constant values, corresponding with cylinders with high values of the Reynolds (Re) and Keulegan-Carpenter number (KC). In reality both coefficients would change as Re and KC vary with the local wave conditions. For instance, C_d values were found to change between 0.5 and 2.2 in experiments with willows by van Wesenbeeck et al. (2022); Maza et al. (2019). The drag and inertia components of the wave forces are both linearly dependent upon the coefficient, as well the wind force upon the drag coefficient. Therefore, a change in the coefficient can largely influence the wave and wind forces.

- **Vegetation width:**
  The width of the vegetation is assumed to be equal throughout the forest. In nature the width, even with equal DBH, is different for every tree. Better knowledge of the variability of the tree surface area as a function of age and species would provide better insights on how this natural diversity will influence stability predictions.

- **Tree height:**
  Since detailed data of the tree area was available for a 2.8 year-old *Avicennia marina* tree (Jerez Nova, 2022), this tree was used to determine the forces. The DBH of the tree of 2.8 meters came close to the average DBH measured by Ardhani et al. (2021b) and Ardhani et al. (2021a). As no data was available on increasing the width of the vegetation by increasing tree height, the width of the 2.8 meter tree was used. By increasing tree height, the width of the vegetation also increases. This underestimates the forces on taller trees.
  Secondly, the tree heigth is assumed equal through the forest due to the fact the DBH in the data of Ardhani et al. (2021b) and Ardhani et al. (2021a) does not change throughout the forest. Literature states, that often the DBH changes through the forest. A possible explanation would be that the width of the forest is to small to show real changes in DBH. If the DBH and therefore

the width and length of the forest changes, the forces on a tree are different at different location of the forest.

- **Wind velocity:**
  The wind velocity is determined using an empirical relation between the wave height and the wind velocity (Sugianto et al., 2017). This emperical relation is determined over the same time period as the data of the wave height, but the used wind velocities are still an approximation. Deviations from those velocities could be expected, which could have a large effect on tree stability predictions.

- **Bathymetry:**
  The bathymetry is assumed to be linear, which is not the case in Demak. As shown by the data of Alferink (2022), the bathymetry near the coast is almost flat. Different water depths would in turn change the wave-driven forces, as the wave height is depth limited. The amount of wave dissipation due to wave breaking would decrease, and therefore the forces induced by the trees increase. Secondly, the width of the forest is enlarged to be able to determine the differences in forces at the seaward edge and the landward edge of the forest. The width of the forest is important for the total amount of wave dissipation by the trees. The forces for the smaller forest will be different from the forces of a wider forest at the same x-location, due to the fact the smaller forest has experienced less wave dissipation due to vegetaion.

- **Return period:**
  The available analysis of Alferink (2022) had a maximum return period of 20 years. For coastal defence systems, often a higher return period is used. Therefore, the same analyses should be done with higher return periods. The hypothesis would be that the maximum forces and moment on the tree become higher, and therefore, the safety factor decreases.

6.2.2. Resistance

- **Sediment properties:**
  For this thesis the sediment properties were assumed to be homogeneous in space. This assumption came from the fact that the undrained shear strength as measured in the field did not change significantly over the x-coordinate and neither did the bulk unit weight change. Literature does state that the sediment properties differ over the x-coordinate of the forest (Zolkhiflee et al., 2021), which implies that the soil resistence will also change with x. This difference can only be determined when the soil properties are exactly known.

- **Undrained shear strength:**
  In the laboratory , the undrained shear strength of the soil in Demak was determined to be 70 Pa, while field tests in Weg aan Zee, Suriname show an average of 17.5 kPa. The difference could be explained by two important differences. Firstly, the samples were taken in very distant locations as the samples from the lab were taken in Demak, Indonesia. Secondly, the lab samples were taken from the uppermost layer of the soil, while the vane test was done at depth of 10 centimeter of more. Although the soil properties are comparable between the site in Suriname and Indonesia, the sites do differ. Literature show that the undrained shear strength of muddy soil can differ a lot (Baruah and Borah, 2015; Schlue et al., 2011). Therefore, it is advisable to do some insitu vane shear test in Indonesia to determine whether the insitu undrained shear strength in Indonesia is indeed much larger than the lab vane shear test.

- **Modulus of subgrade reaction:**
  The value of the modulus of subgrade reaction is based on literature (Barounis et al., 2009; Ikpotokin; Ubani et al., 2020; Barounis et al., 2013). As shown in Figure 5.21, the stresses inside the roots are dependent upon this modulus. Therefore, it would be important to determine the modulus of subgrade reaction for the specific soil, for instance by doing a plate pressure test or a CBR-test.

- **Belowground biomass / volume:**
  The belowground biomass is determined using an allometric equation. The allometric equation is based upon a different location, namely Thailand. Although the circumstances are comparable,

the allometric equation is not based on data of Demak.
The size and growth of the root system is dependent upon multiple factors, such as salinity, replanted or natural growth, avalabiltiy of nutrients and pH (Almahasheer et al., 2016; Muhammad-Nor et al., 2019; Clough, 1984; Herrera Silveira et al., 2022). As the size of the root system does influence the resistance, all these influencial factors should be taken into account by creating a allometric equation. The changes of having some influencial factors being different between site is unavoidable. Using an allometric equation of a different site will result in the risk of a wrong approximated belowgroud biomass.
The belowground biomass is translated to a belowground volume using the wood density due to lack of information on the root density. The root density is not equal to the wood density, and therefore the volume of the root system will be different.

- **Pullout strength:**
The used interface shear strength in the failure mechanism of slippage is not determined using a mangrove root, but using a Norway spruce. As stated, the interface shear strength is dependent upon the material and the soil. The value used is a first approximation of the interface shear strength, as the soil in the test is comparable with the soil present in Demak. But the differences in the soil (such as moisture content and grain size distribution) and the different tree specie will influence the interface shear strength (Fan et al., 2021b; Canakci et al., 2013).

- **Angle α:**
The angle α between the lines of separation determine which roots contribute to the resistance against the overturning moment. As shown in Figure 5.19, the influence of α is large. In the analysis done, α is assumed equal to 60 degrees. This assumption is based on pictures from fallen trees in field observations. The trees in these field observations are not mangrove trees and the soil conditions were different from the silty soil in Demak. The influence of the assumption is large, therefore more research should be done on the roots who participate in the resistance and which roots do not participate.

- **Mechanical root properties:**
The mechanical root properties used in this thesis were of a different mangrove species, as no information of *Avicennia marina* was available. The specie used, *Rhizophora mucronate*, has a larger wood density. As a larger wood density implies larger mechanical strength, it is most likely that the resistance is overestimated.
Secondly, the tension bending strength of a *Rhizophora mucronate* is only 2/3 of the tensile strength. As no compression bending strength of the tree is known, the compression strength is used as a value for the compression bending strength. The difference between the tensile strength and the tensile bending strength indicates a decrease in strength under bending conditions. This could indicate that the compressive bending strength is overestimated. Thirdly, looking at the same specie, but different location, the tensile strength can vary (Madrid et al., 2014). Madrid et al. (2014) showed the dependence of tensile strength on growth conditions like salinity. Coder (2014) indicated that within specie, the tensile strength varies with root diameter. Smaller roots have greater root strength per cross-sectional area, while larger roots have greater root stiffness. In this thesis, the mechanical properties per cross-sectional area of a root are taken equal for each diameter.

- **Asymmetry:**
The responsive behaviour of roots causes asymmetry of the root plate. For wind loading, the tree grows more and larger roots parallel to the loading close to the trunk (Stokes, 1999; Coder, 2014; Fourcaud et al., 2008). In the model, for every specific root a different length and diameter can be determined. Although the distribution of the specific diameter is still symmetrical over the circle. Therefore, the root system in the model does not show any asymmetry. Asymmetry causes the load direction to be influential of the resistance. Mainly in the case of uplift, as not all roots participate in the resistance against uplift.

6.3. Comparison of different schematizations with field observations

In this section the different schematization will be compared with field observations. For all schematization the results will be analysed and whether the results make sense, or some assumption may need to be made differently.

6.3.1. Failure mechanism: Uplift of soil

In field observations while pulling willow trees, often soil movement on the windward side of the trunk is visible and breakage of the trunk. In Figure 6.1 a close-up of the soil before the pulling experiment is shown, while Figure 6.2 and 6.3 clearly shows the soil at the windward side has come up. If the soil movement on the windward side is occurring, often also the sound of snapping roots can be heard. The slippage of the roots out of the soil, is not often viewed. Looking into the movement of the soil, as explained before, the schematization using a shallow foundation is not valid, and the root system will be better represented by using beams.



Figure 6.1: Soil of willow tree before pulling experiment



Figure 6.2: Soil of willow tree after pulling experiment



Figure 6.3: Close up of soil of willow tree after pulling experiment

As stated in the literature and explained in Section 2.4.3, different factors determine the anchoring in different soils (Coder, 2014; Dupuy et al., 2007; Fourcaud et al., 2008). This can also be seen in different uprooting mechanisms. For clayey soils, literature states, that the windward displacements are nearly comparable to leeward downward displacements. Also the slip surface was fairly round and symmetric (Dupuy et al., 2007).
Looking at both situations, the fifth situation is based on a transition condition, which indicates that at least near the trunk the displacements are equal. Away from the trunk, the displacements do not need to be equal. For clayey soil, the modulus of subgrade reaction is low. Looking at the influence of the modulus of subgrade reaction it can be noticed that the fourth situation is more dependent on the modulus of subgrade reaction. In the fourth situation the moment inside the leeward and windward roots is almost equal, while in the fifth situation the difference is larger.
Although, the fifth situation is based on an assumption of equal displacements, the fourth situation better represents the differences between soil types.
Considering the stresses inside the roots, literature states that the largest plastic strains were visible on the largest diameter lateral roots near the bole center in clayey soils (Dupuy et al., 2007). In the modelled schematizations, the largest stresses occur in the largest diameter roots, and indeed near the trunk.

Field observations on willow trees as shown in Figure 6.3, suggest that the soil properties were quite different from a clayey soil. Which could explain why the leeward and windward displacements were very different. Literature states that in sandy soils the slip surface was much bigger and the soil/root system revolved around a leeward-shifted axis (Dupuy et al., 2007). Looking at the spring-supported situations (situations 4 and 5) this corresponds with the model. The modulus of subgrade reaction is larger for sandy soils, therefore, the stress inside the leeward roots becomes significantly larger than the stresses inside the windward roots (Figure 5.21).

In nature, the potential bending or hinge point is dependent upon the anchorage. Overall, in sandy soil the bending or hinge point on a root plate is on a larger distance from the tree compared with a

clayey soil (Fourcaud et al., 2008; Coder, 2014). The model does not distinguish between soil type in the distance from the trunk to the maximum bending point. This maximum bending point is on a certain distance from the trunk dependent on the beam schematization and the length of the root.
The primary schematization without using spring-supports do not adequately model the differences between soil types. Situation 4 and 5 are both modelled using a short root on the windward side. Comparing the long and short roots in the primary situations shows that the differences in uplift and stresses is small, but this model was not convenient. Therefore, the conclusion whether the uplift and stresses between long and short roots do not differ much, is doubtable. This should be analysed using the spring-supported leeward side. Within one root composition, the model does not make a distinction between long an short roots, but this could be implemented by importing a limit. Depending on that limit the model determines what schematization (no rotation at the end of the root or possible rotation) should be used for the root.

6.3.2. Failure mechanisms: Breakage of roots, slippage of roots and breakage of the trunk

All three failure mechansims show a large factor of safety. The breakage of the root is often only observed in combination with uplift of soil. As the roots are not visible during field observations, it is hard to say whether the roots break in bending or in parallel compression/tension. As the bending strength of a root is smaller than the compression/tension strength, the most obvious conclusion would be that the roots break in bending.

The breakage of the trunk is viewed in field observations. Due to loading the trunk bends, causing bending stresses and snapping. As the trunk is assumed to be a uniform beam in the schematization, the point of largest moment would be the point of failure. In nature, the tree is not uniform over the vertical, causing stresses to be different over the vertical. As observed in the field, the breakage of the trunk is often at the lower part of the trunk (as the moment is larger at the bottom), but no necessarily at the bottom of the tree. The analyses of the tree, without assuming uniformity over the vertical, would probabily show a larger safety factor for the breakage of the trunk.
The slippage of the roots was not observed in the field during pull-out experiments using willows, which could be explained by the fact that the soil conditions were very different during these pulling experiments. Looking at failed trees in Demak, it is difficult to distinguish which part of the roots slipped out and which sediments were washed away by waves, causing the roots no be surrounded by sediments anymore after falling. Some field observations in Suriname showed that it is possible to pull the roots out using cyclic loading.

6.3.3. Pore pressures

Field evidence shows that upon cyclic loading, slippage of roots can occur. This would suggest the necessity to account for cyclic loads on the failure mechanics both in terms of pore water pressure development and disturbance of the surrounding soil which reduced the confining stress acting on the trunk and roots. The knowledge of pore pressure in the field would also help to assess the failure of the system in terms of effective stress which rules the behaviour of soil.

6.4. Integration over time and the total forest

This section explains multiple factors which are not taken into account in the model. Recommendations on these neglected factors can be found in Chapter 8

6.4.1. Time dependence

This model analyses the stability of a tree dependent on a horizontal force and moment due to that force at a certain location. The model does not incoorporate the influence of time. For example, what is the difference between a force acting on the tree for a short or long period of time and what happens when a second storm event happens within the recovery time of the forest.

6.4.2. Total forest

Failing trees do influence the efficiency of the total forest, as the density is essential for the amount of wave dissipation (Mendez and Losada, 2004). This implies that when a tree fails, the forces on

the surrounding trees increase, as the wave force increases. The model determines the stability of a single tree, based on multiple parameters determined for the forest. The model does not incoorporate the influence of surroundig trees failing.

6.5. Neglected failure modes

The failure mechanisms of the breakage of leaves and branches, erosion and sea level rise are neglected. The breakage of leaves and branches increases the likelihood of survival during a stormevent due to the decrease of area of the tree (Webb et al., 2014), nevertheless the dissipation of waves is also decreased. The breakage of leaves and branches occurs a lot, but has a smaller contribution to the mortality of trees. This failure mechanism erosion decreases the confining pressure above the roots, causing the soil to more easily uplift (soil uplift at the windward side), or indicates a less strong interaction between soil and roots (root slippage). Therefore, the situation caused by erosion gives room for different failure mechanisms to start easier. But, erosion, is not the main mechanisms which happens.

Lastly, the failure mechanism sea level rise has a large contribution to the mortality of trees. Böhm (2018) research the growth of the *Avicennia marina* in Demak subjected to relative sea level rise. Additional root mats can increase the stability of a tree. The research states that additional root mats can be developed when an *Avicennia marina* is subjected to subsidence. The possibility of growing additional root mats is a result of subsidence in combination with sedimentation and erosion event, so the amount of available sediment. The analysis of this failure mechanisms is of high importance with sea level rise occuring all over the world, but does not influence the stability of a mangrove tree.

7

Conclusions

In this chapter the research questions are answered. All research question are answered with respect to the test case in Demak and all estimated properties and schematizations. The forest in Demak is a fringe forest, due to differences in flow velocities and sediment transport, the results may be different for different kind of forests.

7.1. Sub-questions

The research question is approached by answering the following sub-questions:

- **What are the different failure mechanisms of mangrove trees in a healthy forest under extreme storm conditions?**
  From a coastal protection perspective, mangrove failure is defined as the loss of its wave attenuation capacity due to physical damage. In this thesis five failure modes for individual trees can be distinguished based on a literature study, pictures and pulling experiments of willow trees.
  - **Breakage of leaves and branches:** When the branches and leaves break, the forces on the tree decrease, which results in an increase of the safety factor with respect to its stability. If the plant area below the waterline decreases, the wave dissipation also reduces.
  - **Uplift of the soil:** The overturning moment caused by the wind and wave forces is transferred to the root mat, causing a moment and rotation inside the roots. When the resistance against rotation caused by the layer of overlying soil is smaller than the rotation caused by the moment due to wind and wave forces inside a root, the soil will uproot. The movement of the roots i.e., the uplift of soil, causes bending stresses inside the roots.
  - **Breakage of the roots:** The horizontal wave and wind forces acting on the tree are also transferred to the root system. When the force inside the roots gets larger than the tension or compression strength, the roots break.
  - **Slippage of the roots:** When the pulling force inside the roots is larger than the resistance against slipping, the roots slip out of the soil. The shear strength between the roots and soil is dependent upon the soil, the material of the root and the effective confining stress. In addition, the total pullout force is dependent upon the area of contact between the root and soil.
  - **Breakage of the trunk:** When wind and wave forces push and bend the trunk, stresses appear inside the trunk. When the stress is higher than the tensile or compressive bending strength, the trunk breaks.

  Based on pictures of fallen mangrove trees, pulling experiments and the different safety factors in this thesis, breakage of the trunk, uplift of the soil combined with root slippage and root breakage are the most likely failure mechanisms. As shown in Böhm (2018), erosion also has an impact on mangrove mortality.

Erosion reduces resistance to other failure mechanisms by reducing overlying layer of soil on the roots. As a result, the failure mechanisms analysed in this research occur more easily. As sea level rise is a problem all over the world, this neglected failure mechanism is also important. Although, if enough sediment available, mangroves are able to keep up with a certain amount of sea level rise (Böhm, 2018; Saintilan et al., 2020; Ervita et al., 2017). The breakage of leaves and branches increases the likelihood of survival during a stormevent due to the decrease of area of the tree (Webb et al., 2014), nevertheless the dissipation of waves is also decreased. The breakage of leaves and branches occurs a lot, but has a smaller contribution to the mortality of trees.

- **Which loads, soil properties and forest geometry parameters influence the resistance against failure of the mangroves?** Multiple factors determine the resistance against different failure mechanisms. The factors playing an important role are split up in three categories: the factors dependent on the properties of the tree, on the soil and on the loads.
  - **Properties of the tree**
    - *Mechanical properties*
      The mechanical properties of a tree, like the modulus of elasticity, tension and compression strength and tensile/compressive bending strength, vary for every species. These mechanical properties are related to the wood density, which depends on the species. The relationship between the modulus of elasticity and the stresses inside the roots is given in Figure 5.20.
      As explained in Section 2.7, the wood density increases with age. Therefore, the mechanical properties could change as trees grow older.

    - *Tree and root system architecture*
      Breakage is dependent on the quadratic area moment and, therefore, the diameter, as well as the maximum stresses inside a root or trunk.
      Assuming a constant root volume, the root diameter and length influence the resistance against breakage and slippage, as shown in Table 5.2. Also for uplift the root diameter and length are important as shown in Figure 5.17 and 5.18. Larger root diameters, while keeping an equal root length, did show more uplift and smaller stresses inside the roots. While increasing the root length, keeping a constant root diameter, did initiate larger stresses inside the roots. The amount of uplift appears first to increase after it decreases again, as can be seen in Figure 5.17. Combining those results, varying lengths and root diameters determined the distribution of the overturning moment over the different roots. As a result, each root endures a different amount of uplift and stress inside the root, as shown in Figure 5.15.

    - *Location of the tree within the forest:*
      The sediment size decreases from the seaward edge to the landward edge of the forest, which in turn results in different soil properties (such as porosity, interface shear strength and bulk unit weight). Therefore, the location of the tree within the forest influences its resistance.
  - **Soil properties**
    - *Soil type*
      Soil type (like clayey, silty or sandy soils) impacts the depth at which the tree roots. For more clayey soil, the rooting depth is less than for more sandy soils. The positive linear relationship between the rooting depth and resistance against uplift is shown in Figure 5.22.

    - *Interface shear strength*
      The interface shear strength is determined by the material, the soil type and the effective confining stress. The safety factor, indicated in Table 5.2, decreases when the interface shear strength decreases. The pullout resistance of one root will reduce with declining

interface shear strength, decreasing the safety factor of the failure mechanism of slippage.

- ◦ *Modulus of subgrade reaction*
  The modulus of subgrade reaction depends upon the soil type, which is therefore dependent upon the location. The modulus of subgrade reaction regulates, together with the diameter of the root, the spring constant for the support on the leeward side. This partly influences the contribution of the leeward side on the moment distribution between the leeeward and windward roots. As shown in Figure 5.21, the moment taken by the spring-supported leeward roots increases with a larger modulus of subgrade reaction. So, the modulus of subgrade reaction influences the amount of uplift and stress inside the roots.

- ◦ *Bulk unit weight of the soil*
  The bulk unit weight of the soil determines the resistance against uplift on the windward side of the tree. The moment caused by the overlying soil layer on the roots and the resistance against rotation due to this overlying soil layer is linearly dependent upon the bulk soil unit weight, as shown in Figure 5.23.

- ◦ *Moisture content*
  The moisture content influences the interface shear strength and the modulus of subgrade reaction (Zainorabidin and Agustina, 2018).

- **Load**
  - ◦ *Load direction:*
    The distribution of roots determine which roots participate in resisting the horizontal force or moment. Therefore, the load direction also determines the resistance of the roots. The asymmetry of roots is not included in this model, but also determines the importance of the load directions.

  - ◦ *Load magnitude:*
    The load magnitude determines the forces and moments inside of the different roots.

- **How can the different failure mechanisms against wind and wave loading be schematized?**
  - **Slippage:** The slippage is schematized by using the bonding strength of a different species root and a comparable soil, with comparable confining pressure. The horizontal force due to wind and waves is divided over the root, resulting in a force inside the roots. Using the bonding strength and the contact area of a single root, the force required to pull out a root can be determined.

  - **Root breakage:** The breakage of the roots is also schematized using the horizontal equilibrium. Using this equilibrium the roots will partly be under compression and partly under tension. Breakage occurs when the force inside a root exceeds a maximum tension or compression force.

  - **Uplift:** The roots can be schematized as a supported beam. The leeward side can best be schematized by a spring-supported beam, as soil below the beam causes resistance against movement. If the modulus of elasticity becomes larger, the leeward contribution in the resistance against the overturning moment decreases. This results in a larger moment, and therefore stresses, in the windward roots. If the modulus of subgrade reaction increases the moment taken by the windward roots decreases, causes lower stresses and less uplift.
    The usage of a shallow foundation for the schematization of soil movement is invalid as the contribution of the root in taking up the horizontal force is not incorporated in this schematization.

  - **Trunk breakage:** Trunk breakage can be schematized using the maximum moment and calculating the bending stresses inside the trunk. If the bending stresses exceed the strength, the trunk breaks. The factor of safety determined using this schematization are large, which disagrees with field observations while pulling willows and online pictures. The simplification of an equal diameter of the trunk influences the calculation of the stresses inside the trunk the most. Therefore, this schematization is simplified too much.

- **How do different factors (wind, wave and soil properties) affect the stability of a mangrove tree taking into account the soil properties and root system?**

  Loads
  The force on the tree depends on the wind and the waves. The tree height and water depth ratio determines the relative importance of wind and wave forces. The taller the tree, the more significant the contribution of the wind in the horizontal force. For the moment, the size of the tree matters even more due to the length of the arm. For a taller tree, the maximum moment moved towards the landward edge of the forest, shown in Figure 5.10. The maximum horizontal force shifted less quickly to the landward edge of the forest due to the more significant wave forces on the seaward side of the forest, shown in Figure 5.9. Overall, the tree height predominantly determines the difference between the location of the maximum moment and horizontal forces. The moment and horizontal force both initiate different failure mechanisms. This leads to the conclusion that different tree heights could possibly activate different failure mechanisms at other forest locations.

  Soil properties
  The failure mechanisms identified in this work require the description of the following aspects of the soil: bulk unit weight, interface shear strength and modulus of subgrade reaction. As the shallow foundation was not an adequate schematization of soil movement, the undrained shear strength has become irrelevant.
  Secondly, the rooting depth of the tree is dependent on the soil type. Roots concentrate at a considerably shallower depth in fine-textured or poorly drained soils.
  Another critical factor influencing stability is erosion. Erosion decreases the thickness of the overlying soil layer of the roots, which determines the resistance against rotation of the roots in the failure mechanism uplift. Also, this layer of soil determines the confining pressure, which influences the resistance against sliding. Therefore, the changes in the water flow velocity are also significant. If the flow velocity increases, the amount of sediment picked up increases, changing the resistance against specific failure mechanisms.

  Root system
  Lastly, the architecture of the root system is essential. When keeping the root volume equal but changing the length or diameter of the roots, the resistance against the failure mechanisms did change. Increasing the length, increased the resistance against sliding, but decreased the resistance against breakage. Increasing the length also increased the resistance against uplift and the bending forces inside the roots.

7.2. Main research question

How can the stability of an *Avicennia marina* be best described in a mechanical model taking into account the soil properties and root system compared with field observations?

Field observations often show soil movement, as can be seen in Figure 6.2, 6.3, I.15 and I.16. During the pull-out experiments of willow trees, during the uplift of soil, the snapping of roots can be heard. If the breakage of roots is combined with uplift, the breakage occurs in bending. Figure I.15 and 6.3 also show that some roots have slipped out of the soil. Overall, the most important schematization is the schematization of roots with supported beams for the failure mechanism uplift.
Field observations also show trunk breakage, while the model gives contradictory results for this failure mechanism.

Below, a more detailed explanation about the similarities and differences between field observations and the results of the model is given. The failure mechanisms root slippage and root breakage are rarely observed in isolation, which is in agreement with the results of the model. Therefore, those will not be discussed in detail.

Trunk breakage:
Although trunk breakage is not the main failure mechanism occurring, it is observed multiple times in the forest in Demak and during pulling experiments of willow trees. The high safety factors in the model, are contradictionary to the occuring mechanism in practice. This could be explained by the assumption of uniformity over the vertical axis, while in nature the trunk thickness differs over the vertical axis.

Uplift of soil:
The soil movement on the windward side of the trunk would indicate that the schematization of the bearing capacity using a shallow foundation is not valid. Because using the bearing capacity of a shallow foundation, the contribution of the root in resisting horizontal forces is not taken into account. Also, looking at the failure of a shallow foundation, the whole foundation slides. Comparing this to the root mat of an *Avicennia marina*, the whole root mat should slide, which is not observed in nature. Therefore, the movement of soil does not fit the failure mechanism that is observed in practice.

The movement of windward soil can be modelled by schematizing the roots as beams. In situations 4 and 5, the soil on the leeward side is modelled using a spring support. The larger stresses inside the leeward root compared with the windward roots are in agreement with the breakage of windward roots in field observations.
Although, some slippage of roots is visible in Figure I.15 and 6.3, this mechanism is not taken into account in the schematization of uplift. In this model, the occurring moment of uplift is defined and the stress inside the roots during this moment. Therefore, the changes in resistance against slippage of the roots are not taken into account, causing a disagreement with field observations.

The difference between situations 4 and 5 is the assumption of vertical movement of the trunk. Looking at the differential equation used for situation 4, shown in Figure 3.17, the trunk moves upwards. During field observations, the movement of the trunk was observed. Therefore, the assumption of no vertical movement, as in situation 5, seems invalid. Secondly, for situation 5 the root on the windward and leeward sides need to be in line with each other, as shown in Figure 3.18, in nature the changes of this occurring is very low.
Thirdly, situation 4 did better represent the differences in the moment distribution between soil type. As for clayey soils, so a low modulus of subgrade reaction, the displacements on the leeward and windward side are almost equal (Dupuy et al., 2007).
Overall, situation 4 did show the best agreement with field observations due to the vertical movement of the trunk and the better representation of the differences in soil type.

Concluding, it can be said that the schematization of the movement of soil on the windward side of the trunk can be most adequately modelled using a spring-supported beam on the leeward side without restricted vertical movement (situation 4) below the trunk. Breakage of the trunk can be modelled using the maximum stress due to the wind and wave forces and the maximum bending strength of the tree, but does show disagreement with field observations.

8

Recommendations

Many studies have investigated flood reduction by mangrove forests, like van Zelst et al. (2021), Menéndez et al. (2020), Menendez et al. (2018) and Montgomery (2021). The advantages of incorporating mangrove forests in coastal defence systems are big, and the dissipation of waves shown by these researches are also promising. However, those researches neglect vegetation failure and assume that the vegetation is uniform over the vertical. Both are important factors to take into account.
To be able to incorporate tree failure into the determination of the dissipation of waves, more research is needed in the following areas. First, the tree and soil parameters which need a more in depth analysis are listed. Secondly, the potential improvements of the proposed model in this thesis are discussed. Finally, using an effective stress approach to decribe the failure mechanisms is discussed.

8.1. Test improvements

8.1.1. Soil and tree properties

During this research a lot of parameters are assumed based on literature and different tree species or soil conditions. By knowing the parameter for the specific soil in Demak and the mechanical properties of *Avicennia marina*, the models reliability will increase. The following parameter would be important to determine:

- Tree properties
  - Mechanical properties of *Avicennia marina*, such as tension and compression strength, tension bending strength, compression bending strength and modulus of elasticity.
  - Tree density to determine the belowground volume of the root system
  - Tree architecture changes trough the forest
- Soil properties
  - Modulus of subgrade reaction

Static pulling tests on mangrove roots would determine the pull-out force of a single root. As field observations shows some slippage of root during uplift, this would indicate that the resistance against slippage declines during uplift. A possible reason could be a decrease in effective stress. Doing the static pulling tests, while measuring the pore pressures would indicate the influence of pore pressures on the interface shear strength. A possibility would be to use an undrained soil, increase the vertical pressure and therefore the pore pressures, while pulling out the roots. If this test is done using mulitple verticale pressure and therefore different effective stresses, this relationship can be derived.
While doing such tests, it should be noted that the size of the box should be large enough to not influence the soil properties and roots.

8.1.2. Measure windward and leeward angles

Literature states that often, in clayey soils, the windward and leeward displacements of soil are equal (Dupuy et al., 2007). Nevertheless, field observations show different soil displacements on both sides. Measuring the displacements and the angle of the trunk with the soil should determine what the displacements really are. By also measuring the angle between the trunk and the soil, it can be determine whether the assumption of equal angle at the leeward and windward side is correct. If the angle between both side is not equal, the distribution between the moment on the leeward and windward side would be different. Measuring the angles and displacements in different soil types gives information about whether the soil displacements indeed differ. The results could help to determine whether the dissimilarity between literature and field observations occurs from differences in soil type or root systems.

8.2. Model improvements

The model of the failure mechanism uplift could be improved by modelling the differences in roots more precisely and to be able to model progressive failure.

8.2.1. Root modelling

Length

Field observations show that when uplift occurs some roots break. The part which remains inside the soil does not necessarily show uplift, which would imply that the effect of the overturning moment have become neglectible and no rotation or vertical movement occurs. Simultaneously, the shorter roots of the root system show uplift over the total length. The difference between those two roots can be incorporated into the model by taking into account conditions for the length of the root. In this way, different roots will have a different beam schematization, based on whether rotation occurs at the end of the root.

Asymmetry

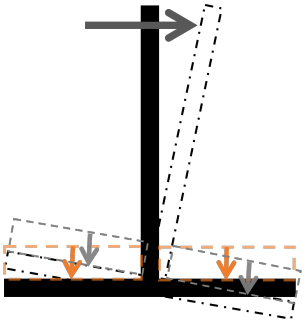
Literature states that the root system of trees shows asymmetry due to continous loading (Dupuy et al., 2007; Fourcaud et al., 2008; Coder, 2014). The model does not incorporate the asymmetry of a root system. Incorporating asymmetry into the model would show the different resistance for different loading directions.

8.2.2. Progressive failure

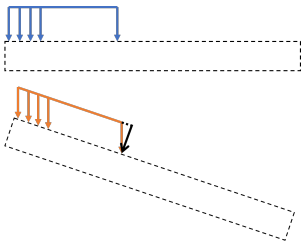
When a single root fails, due to breakage or slippage, the moment is redistributed over the other roots and the remaining part of the failed root. This could lead to progressive failure, as the forces on a single root increase. In field observations while pulling willow trees, also some slippage has been noticed. Due to bending, the forces inside a root increase causing a decreases in the safety factor against slippage. Being able to model this using an iterative process would give insight into the effects of failure of single roots.

Resistance against uplift

The resistance against uplift decreases when uplift occurs, this is caused by the fact the soil is moving up under an angle. Therefore, the arm equal to the central point of the total soil weight decreases, as shown in Figure 8.1a. When the soil is moving up, looking at the resultant of the total distributed force the arm between the grey arrow and the trunk is shorter than the arm with the orange arrow. Looking in detail to the distributed load, the soil weight causes a load in vertical direction. When the root moves up, this direction is not perpendicular with the root anymore. Therefore, in the calculation, the load perpendicular to the root (the black arrow in Figure 8.1b) is decreasing. In this model, the first rotation is taken as limiting state, so this effect is not needed. If progressive failure is modelled this effect should be taken into account.



(a) Decreasing arm of total weight of the overlying layer of soil



(b) Changing perpendicular distributed load

8.2.3. Total forest

Failing trees do influence the efficiency of the total forest, as the density is essential for the amount of wave dissipation (Mendez and Losada, 2004). This implies that when a tree fails, the forces on the surrounding trees increase, as the wave forces increases. For that reason, the forces on a tree should be re-calculated when a surrounding tree fails. Currently, with equal DBH, the resistance of every tree is equal. Thus when one tree fails, all tree fails. To include differences, in for example root architecture, between trees, probabilistics should be build in the model. Using probabilistics could also help by determining the percentage of a forest that will fail.

8.3. Effective stress approach

An effective stress approach would indicate the knowledge of pore pressure at any time and location. As the pore pressures are unknown, this thesis uses a total stress approach. As effective stress rules the behaviour of soil, this would essentially help to better asses the failure of the system.

Another essential factor would be to know the effect of increasing pore pressure or decreasing effective stress on the different failure mechanisms. By determining the effective stress path under loading, thus measuring pore pressures, the behaviour of the soil can be analysed. For example, field observations showed that roots were easier pulled out under cyclic loading.
A possibility to test the behaviour of soil and roots under loading could be to use 3D-printed roots. These 3D-printed roots could be placed in a box of soil, under a controlled environment. The confining pressure can be changed by doing these tests in a laboratory instead of in situ. Moreover, multiple soil types can be tested using the same 3D-printed root. For example, the root, or even a simplified 3D-printed tree, could be placed in a box of soil. The pore pressures inside the box can be measured while pulling or moving the roots. While using a very simplified tree, as pictured in Figure 8.2, the tree can be pulled by a constant or cyclic force. Measuring the pore pressures near the 3D-printed roots and further away from the roots gives a first indication of the development of pore pressures and the effective stress path.
Using 3D-printed roots has multiple advantages. Firstly, the differences in, for example, diameter and shape of natural root can be ruled out. As a consequence, the same test for multiple soil types gives the differences in the response between soil types without the variable of differences between roots. An essential factor of the 3D printing of roots will be the modulus of elasticity of the roots.
Secondly, the advantage of using 3D-printed roots would be that, first, some very simplified roots can be used, to later use more complex root systems. Thirdly, the maximum forces can be measured without the death of trees. An disadvantage of the 3D-printed roots is the difference between the material of the printed root and the natural root. For example, the bonding strength depends upon the material and the soil. As the material of the roots will be different, factors, like the bonding strength, will be influenced by the different material.
An advantage of using laboratory testing compared to in situ testing would be that the soil conditions can be controlled. Also, the soil in the box can be more easily changed to compare different soil types.
An disadvantage would be that the box should be large enough not to influence the soil near the roots. As a geo-

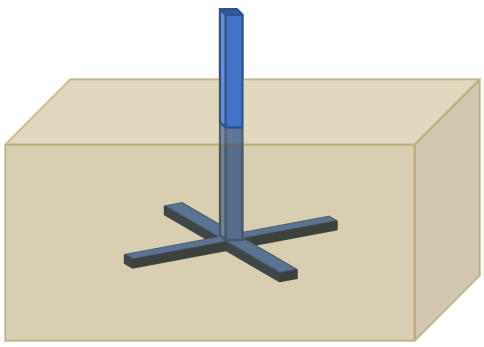


Figure 8.2: Test of the simplified tree inside a box

centrifuge has different scaling effects for the area, stress and force, this would complicate the test and influence the results. Therefore, it would be needed to do the test on true size.

8.3.1. Time dependent modelling

As explained in Chapter 6, the current model does not take into account time. Using an effective stress approach, time can be taken into account. This could give insight in what would be the difference in soil reaction when the load is applied for a long or short time. Using an effective stress approach, it would be possible to model the recovery time of the soil conditions. If the pore pressures increase inside the soil, what time would be needed to dissipate these pore pressures. The soil response is dependent on the coefficient of consolidation, as a soil is never fully drained or undrained.

Knowing the recovery time, one can look into the situation where a second storm occurs when the forest is still recovering from the first storm. What would be the influence on the resistance against multiple failure mechanisms?

The forest ability to dissipate waves is partly dependent on the density of the forest. Therefore, the time dependent behaviour and reaction of the forest to multiple storms happening within a certain timeframe is important to determine the longtime reliability.

Nomenclature

α	Participation angle [°]
ϵ_b	Time-averaged rate of energy dissipation induced by wave breaking [N/m/s]
ϵ_v	Time-averaged rate of energy dissipation induced by vegetation [$N/m/s$]
γ	Specific weight [N/m^3]
γ_b	Adjusting parameter [-]
κ	Karman constant [-]
ω	Wave angular frequency [rad/s]
ϕ	Internal friction angle of non-rooted soil [°]
ρ_a	Air density [kg/m^2]
ρ_w	Water density [kg/m^2]
σ_R	Compression/tension strength [N/mm^2]
σ_{max}	Maximal stress due to overturning moment [N/mm^2]
τ	Bonding strength [kPa]
θ	Shear angle [°]
φ	Rotation angle [°]
φ_{1245}	Rotation angle due to the overturning moment of the windward roots using the schematization of a short root
A	Frontal tree area [m^2]
a	Intercept coefficient related to the bandwidth
A_s	Accumulated area of all roots in the collected soil mass [mm^2]
a_s	Cross-sectional area of a single root [mm^2]
AGB	Above ground biomass[kg]
B	Width of the shallow foundation [m]
b	Slope coefficient related to the bandwidth [-]
b_c^0	Coefficient due to inclination of the founding base [-]
b_v	Plant area per unit height of each vegetation stand normal to u [m]
B_w	Bandwidth of the forest [m]
b_{beam}	Width of the beam [m]
B_b	Adjusting parameter [-]
BGB	Below ground biomass[kg]
c	Individual celerity [m/s]

c Modulus of subgrade reaction [N/m^3]

c_g Group celerity [m/s]

$c_{D,c}$ Drag coefficient for wind currents [-]

$C_{D,w}$ Depth-averaged drag coefficient for waves [-]

CC Canopy closure [%]

D Average distance between trees [m]

d_c^0 Depth coefficient [-]

DBH Diameter at breastheight [cm]

E Energy density [N/m]

E Modulus of elasticity [Pa]

F_a Total wind force [kN]

f_b Average frequency corresponding to T_p [1/s]

F_w Total wave force [kN]

F_x Horizontal force [kN]

G Empirical gust factor [-]

g Acceleration of gravity [m/s^2]

g_c^0 Sloping ground surface coefficient [-]

H Wave height [m]

h water depth [m]

H_h Horizontal load [kN]

h_v Vegetation heigth [m]

$H_{avg_{tree}}$ average tree height [m]

H_{m0} Offshore wave height [m]

H_{rms} Root-mean square wave height [m]

i_c^0 Horizontal load coefficient [-]

I_{wh} Initial sea wave height [cm]

k Damping constant [-]

k_p Wave number [$1/m$]

L Length of the shallow foundation [m]

L Length root [m]

M_x Moment caused by horizontal forces [kNm]

N_v Number of vegetation stands per unit horizontal area [$1/m^2$]

p Distributed vertical response [kN/m]

p_w Specific density of wood [g/cm^3]

q_{lim}	Limiting bearing capacity [kPa]
R	Return period [years]
r	Radius [m]
S	Soil shear strength [N/mm^2]
s_c^0	Shape coefficient [-]
S_r	Rooted soil shear strength [N/mm^2]
SF	Safety Factor [-]
T	Tensile strength [N/mm^2]
T_p	Peak period [s]
T_s	Wave period [s]
u	Horizontal velocity [m/s]
u_a*	Friction velocity [m/s]
u_a	Wind speed relative to tree motion
u_r	Relative horizontal velocity [m/s]
v_e	Empirical reduction factor [-]
w	Vertical displacement [m]
W_h	Wave height at the landward site of the forest [cm]
x	Onshore coordinate [m]
z	z-coordinate [m]
z_0	Roughness height [m]

Bibliography

Agroforestry, World Wood density database. URL http://db.worldagroforestry.org//wd.

Alam, Shaurav , Banjara, Ashlesh , Wang, Jay , Patterson, William B , Baral, Sujan , et al. (2018). Novel approach in sampling and tensile strength evaluation of roots to enhance soil for preventing erosion. *Open Journal of Soil Science*, 8(12):330.

Alam, Shaurav , Manzur, Tanvir , Borquist, Eric , Williams, Joseph , Rogers, Cody , Hall, David , Patterson, William B , Higuera, Joseph , Eklund, Erik , Wang, Jay , et al. (2021). In-situ assessment of soil-root bonding strength to aid in preventing soil erosion. *Soil and Tillage Research*, 213:105140.

Alamy Stock PhotoMature tree uprooted and lying on beach due to heavy cyclonic winds and soil erosion by rising sea level due to global warming. URL https://www.alamy.com/climate-change-photo-mature-tree-uprooted-and-lying-on-beach-due-to-heavy-cyclonic-w
html?imageid=6538F7A0-AC5B-4EA5-A89C-10788D8982C3&p=703676&pn=1&searchId=80c8d68cb48d029fcab85a88231656ea&searchtype=0.

Alappatt, Joju P . Structure and species diversity of mangrove ecosystem. In *Biodiversity and Climate Change Adaptation in Tropical Islands*, pages 127–144. Elsevier (2008).

Alex (2019). Let fallen trees lie. URL https://heritageconservancy.org/let-fallen-trees-lie/.

Alferink, Marijn (2022). Wave transformation through permeable structures in demak, indonesia: A design study with the numerical model swash.

Almahasheer, H. , Duarte, C.M. , and Irigoien, X. (2016). Phenology and growth dynamics of avicennia marina in the central red sea. doi: 10.1038/srep37785.

Alongi, D.M. (2002). Present state and future of the world's mangrove forests. 29:331–349. doi: 10.1017/S0376892902000231.

Alpine Tree Service (2017). How to prevent leaning tree problems. URL https://alpinetreenj.com/leaning-trees/.

Angelakis, A. , Antoniou, G.P. , Voudouris, K. , Kazakis, N. , and Dalezios, N.R. (2019). History of floods in greece: Causes and measures for protection.

API (2014). *API Recommended Practice 2A-WSD*. ISBN G2AWSD22.

Ardhani, Trialaksita Sari Priska , Murdiyarso, Daniel , and Kusmana, Cecep (2020). Effects of permeable barriers on total ecosystem carbon stocks of mangrove forests and abandoned ponds in demak district, central java, indonesia. *Biodiversitas Journal of Biological Diversity*, 21(11).

Ardhani, T.S.P , Murdiyarso, D. , and Kusmana, C. (2021a). Swamp dataset-vegetation-demak-2019-timbulsloko. URL https://doi.org/10.17528/CIFOR/DATA.00283.

Ardhani, T.S.P , Murdiyarso, D. , and Kusmana, C. (2021b). Swamp dataset-vegetation-demak-2019-berahunkulon. URL https://doi.org/10.17528/CIFOR/DATA.00283.

Baishya, S. , Banik, S.K. , Choudhury, M.D. , Talukdar, D.D. , and Talukdar, A.D. (2020). *Biotechnological Utilization of Mangrove Resources*. Academic Press.

Baldwin, A.H. , Platt, W.J. , and Ford, M. (2001). Regeneration in fringe mangrove forests damaged by hurricane andrew. 157:149–162. doi: 10.1023/A:1013941304875.

Bao, T.Q (2011). Effect of mangrove forest structures on wave attenuation in coastal vietnam. 3: 807–818. doi: doi:10.5697/oc.53-3.807.

Barbier, E.B. , Hacker, S.D. , Kennedy, C. , Koch, E.W. , Stier, A.C. , and Silliman, B.R. (2011). The value of estuarine and coastal ecosystem services. (81):169–193. doi: https://doi.org/10.1890/10-1510.1.

Barounis, N , Saul, G , and Lally, D (2013), Estimation of vertical subgrade reaction coefficient from cpt investigations: applications in christchurch. In *Proceedings 19th NZGS Geotechnical Symposium*.

Barounis, Nick , Orr, Trevor LL , McMahon, Paul H , and Barounis, Aristides (2009), Modulus of subgrade reaction for foundations on clay from unconfined compression tests. In *Proceedings of the 17th International Conference on Soil Mechanics and Geotechnical Engineering (Volumes 1, 2, 3 and 4)*, pages 249–252. IOS Press.

Baruah, B and Borah, S (2015), Effect of lime-mud on undrained shear strength of soil. In *Proceedings of the 5th Indian Young Geotechnical Engineers Conference (5IYGEC): Extended Abstracts. Shweta Publications*.

BioManCo (2019). Soil properties in demak - report of laboratory experiments.

Bischetti, G.B. , Chiaradia, E.A. , Simonato, T. , Speziali, B. , Vitali, B. , Vullo, P. , and Zocco, A. (2005). Root strength and root area ratio of forest species in lombardy (northern italy). 278:11–22. doi: 10.1007/s11104-005-0605-4.

Borsje, B.W. , van Wesenbeeck, B.K. , Dekker, F. , Paalvast, P. , Bouma, T.J. , van Katwijk, M.M. , and de Vries, M.B. (2010). How ecological engineering can serve in coastal protection. (37):113–122.

Bouma, AL (1993). Mechanica van constructies. *Delftse Uitgevers Maatschappij bv, Delft*.

Bouma, T.J. , van Belzen, J. , Balke, T. , Zhu, Z. , Airoldi, L. , Blight, A.J. , Davies, A.J. , Galvan, C. , Hawkins, S.J. , Hoggart, S.P.G. , Lara, J.L. , Losada, I.J. , Maza, M. , Ondiviela, B. , Skov, M.W. , Strai, E.M. , Thompson, R.C. , Yang, S. , Zanuttigh, B. , Zhang, L. , and Herman, P.M.J. (2014). Identifying knowledge gaps hampering application of intertidal habitats in coastal protection: Opportunities & steps to take. 87:147–157.

Breda, Angelo , Saco, Patricia M , Sandi, Steven G , Saintilan, Neil , Riccardi, Gerardo , and Rodríguez, José F (2021). Accretion, retreat and transgression of coastal wetlands experiencing sea-level rise. *Hydrology and Earth System Sciences*, 25(2):769–786.

Brodbeck, Beau and Rowe, William (2019). Verzadigde bodems en wind: een recept voor omvallende bomen. URL https://www.aces.edu/blog/topics/forestry/saturated-soils-and-wind-a-recipe-for-toppling-trees/.

Böhm, C. (2018). Morphological changes in the root-zones of dead mangrove trees (avicennia marina). a response to subsidence?

Canakci, Hanifi , Yavuz, H Erdem , Celik, Fatih , and Gullu, Hamza (2013), Interface friction between organic soil and construction materials. International Balkans Conference on Challenges of Civil Engineering.

Chave, Jérôme , Andalo, Christophe , Brown, Sandra , Cairns, Michael A , Chambers, Jeffrey Q , Eamus, Derek , Fölster, Horst , Fromard, François , Higuchi, Niro , Kira, Tatuo , et al. (2005). Tree allometry and improved estimation of carbon stocks and balance in tropical forests. *Oecologia*, 145 (1):87–99.

Clough, BF (1984). Growth and salt balance of the mangroves avicennia marina (forsk.) vierh. and rhizophora stylosa griff. in relation to salinity. *Functional Plant Biology*, 11(5):419–430.

Coder, K.D. (2014). Tree anchorage & root strength.

Comley, Bradley WT and McGuinness, Keith A (2005). Above-and below-ground biomass, and allometry, of four common northern australian mangroves. *Australian Journal of Botany*, 53(5):431–436.

Danjon, F. , Fourcaud, T. , and Bert, D. (2005). Root architecture and wind-firmness of mature pinus pinaster. 168(2):387–400. doi: 10.1111/j.1469-8137.2005.01497.x.

Day, J.W. , Psuty, N.P. , and Perez, B.C. (2008). Consequences of climate change on the ecogeomorphology of coastal wetlands. (31):477–491. doi: 10.1007/s12237-008-9047-6.

De Petris, Samuele , Sarvia, Filippo , and Borgogno-Mondino, Enrico (2020). Rpas-based photogrammetry to support tree stability assessment: Longing for precision arboriculture. *Urban Forestry & Urban Greening*, 55:126862.

Dharmawan, I Wayan Susi and Siregar, Chairil Anwar (2008). Karbon tanah dan pendugaan karbon tegakan avicennia marina (forsk.) vierh. di ciasem, purwakarta. *Jurnal Penelitian Hutan dan Konservasi Alam*, 5(4):317–328.

Di Iorio, Antonino , Lasserre, Bruno , Scippa, Gabriella S , and Chiatante, Donato (2005). Root system architecture of quercus pubescens trees growing on different sloping conditions. *Annals of Botany*, 95(2):351–361.

DM, NAVFAC 7.1 (1982). *Soil Mechanics, Design Manual*, 7.

Dupuy, L. , Stokes, A. , and Fourcaud, T. (2007). A numerical investigation into the influence of soil type and root architecture on tree anchorage. 278:119–134. doi: 10.1007/978-1-4020-5593-5_17.

Ervita, Komariah , Marfai, Muh Aris , et al. (2017). Shoreline change analysis in demak, indonesia. *Journal of Environmental Protection*, 8(08):940.

Ewel, Katherine , TWILLEY, ROBERT , and Ong, JIN (1998). Different kinds of mangrove forests provide different goods and services. *Global Ecology & Biogeography Letters*, 7(1):83–94.

Expertisenetwerk waterveiligheid (2017). Grondslagen voor hoogwaterbescherming. 2.

Fan, Chia-Cheng , Lu, Jin Zong , and Chen, Hsin Hung (2021a). The pullout resistance of plant roots in the field at different soil water conditions and root geometries. *Catena*, 207:105593.

Fan, Chia-Cheng , Lu, Jin Zong , and Chen, Hsin Hung (2021b). The pullout resistance of plant roots in the field at different soil water conditions and root geometries. *Catena*, 207:105593.

Florida Museum (2019). Species of florida's mangroves. URL https://www.floridamuseum.ufl.edu/southflorida/habitats/mangroves/species/.

Fonseca, M.S. and Cahalan, J.A. (1992). A preliminary evaluation of wave attenuation by four species of seagrass. 35:565–576. doi: 10.1016/S0272-7714(05)80039-3.

Fourcaud, T. , Ji, J. , Zhang, Z. , and Stokes, A. (2008). Understanding the impact of root morphology and overturning mechanisms: A modelling approach. 101:1267–1280. doi: 10.1093/aob/mcm245.

Gacia, E. and Duarte, C.M. (2001). Sediment retention by a mediterranean posidonia oceanica meadow: The balance between deposition and resuspension. 52:505–514. doi: 10.1006/ecss.2000.0753.

Gardenia BVAvicennia germinans (black mangrove). URL https://gardenia.net/plant/avicennia-germinans.

Gardiner, BA , Stacey, GR , Belcher, RE , and Wood, CJ (1997). Field and wind tunnel assessments of the implications of respacing and thinning for tree stability. *Forestry: An International Journal of Forest Research*, 70(3):233–252.

Gardiner, Barry , Berry, Peter , and Moulia, Bruno (2016). Wind impacts on plant growth, mechanics and damage. *Plant science*, 245:94–118.

Genet, M. , Stokes, A. , Saline, F. , Mickovski, S.B. , Fourcaud, T. , Dumail, J.F. , and van Beek, R. (2005). The influence of cellulose content on tensile strength in tree roots. 278:1–9. doi: 10.1007/s11104-005-8768-6.

Giadrossich, F , Schwarz, Massimiliano , Cohen, D , Cislaghi, A , Vergani, C , Hubble, T , Phillips, C , and Stokes, Alexia (2017). Methods to measure the mechanical behaviour of tree roots: a review. *Ecological engineering*, 109:256–271.

Gindl, Wolfgang , Teischinger, Alfred , Schwanninger, Manfred , and Hinterstoisser, Barbara (2001). The relationship between near infrared spectra of radial wood surfaces and wood mechanical properties. *Journal of Near Infrared Spectroscopy*, 9(4):255–261.

Guo, Ping , Xia, Zhenyao , Liu, Qi , Xiao, Hai , Gao, Feng , Zhang, Lun , Li, Mingyi , Yang, Yueshu , and Xu, Wennian (2020). The mechanism of the plant roots' soil-reinforcement based on generalized equivalent confining pressure. *PeerJ*, 8:e10064.

Halder, N.K. , Merchant, A. , Misbahuzzaman, K. , Wagner, S. , and Mukul, S.A. (2021). Why some trees are more vulnerable during catastrophic cyclone events in the sundarbans mangrove forest of bangladesh. 490. doi: https://doi.org/10.1016/j.foreco.2021.119117.

Hansen, Brinch et al. (1961). A general formula for bearing capacity. *Danish Geotechnical Institute, Bulletin*, 11:38–46.

Hansen, J Brinch (1970). A revised and extended formula for bearing capacity.

Hao, S. , Su, W. , and Li, Q.Q. (2021). Adaptive roots of mangrove avicennia marina: Structure and gene expressions analyses of pneumatophores. 757. doi: https://doi.org/10.1016/j.scitotenv.2020.143994.

Herrera Silveira, JA , Hernandez, CT , Fajardo, FS , Braun, R , Bowman, J , Geselbracht, L , Musgrove, M , Rogers, M , Schmidt, J , Robles Toral, PJ , Canul Cabrera, JA , and Guerra Cano, L (2022). Hurricane damages to mangrove forests and post-storm restoration techniques and costs. *The Nature Conservancy*.

Hilmi, Endang (2018). Mangrove landscaping using the modulus of elasticity and rupture properties to reduce coastal disaster risk. *Ocean & Coastal Management*, 165:71–79.

Huizinga, F. (2012). The economics of flood prevention, a dutch perspective. pages 1–27.

Ifuku, M. and Hayashi, H. (1998). Development of eelgrass (zostera marina) bed utilizing sand drift control mats. 40(3):223–239. doi: 10.1142/S0578563498000145.

Ikpotokin, Peace Modulus of subgrade reaction of soils. URL https://structville.com/2020/07/modulus-of-subgrade-reaction-of-soils.html.

Indrayani, Ervina , Kalor, John Dominggus , Warpur, Maklon , and Hamuna, Baigo (2021). Using allometric equations to estimate mangrove biomass and carbon stock in demta bay, papua province, indonesia. *Journal of Ecological Engineering*, 22(5).

IWA PublishingFlood control and disaster management.

Jacobsen, Anna L , Agenbag, Lize , Esler, Karen J , Pratt, R Brandon , Ewers, Frank W , and Davis, Stephen D (2007). Xylem density, biomechanics and anatomical traits correlate with water stress in 17 evergreen shrub species of the mediterranean-type climate region of south africa. *Journal of Ecology*, 95(1):171–183.

Jayabalan, Jagan , Roy, Sanjiban Sekhar , Samui, Pijush , and Kurup, Pradeep . Intelligent models applied to elastic modulus of jointed rock mass. In *Handbook of Research on Trends and Digital Advances in Engineering Geology*, pages 1–30. IGI Global (2018).

Jerez Nova, Kelvin (2022). Geometrical mangrove models: Quantifying frontal surface area distribution for avicennia marina vegetation: an important parameter for estimating wave attenuation.

John, DM and Lawson, GW (1990). A review of mangrove and coastal ecosystems in west africa and their possible relationships. *Estuarine, Coastal and Shelf Science*, 31(5):505–518.

Jommi, Cristina (2021). Aesm1700: Consolidation of soils lecture slides, Technical University of Delft.

Kaimal, Jagadish Chandran and Finnigan, John J (1994). *Atmospheric boundary layer flows: their structure and measurement*. Oxford university press.

Kalloe, Su (2022a). Close up roots big tree (wijk aan zee, suriname) [photograph].

Kalloe, Su (2022b). Close up of soil near a mangrove (wijk aan zee, suriname) [photograph].

Kalloe, Su (2022c). Erosion exposing root system of big mangrove tree (wijk aan zee, suriname) [photograph].

Kalloe, Su (2022d). Eriosion exposing root system of a medium size tree (wijk aan zee, suriname) [photograph].

Kalloe, Su (2022e). Visisble root system of big mangrove tree at wijk aan zee, suriname [photograph].

Kalloe, Su (2022f). Broken roots at the seaward side of the mangrove forest at wijk aan zee, suriname [photograph].

Kalloe, Su (2022g). Close up of the broken roots at the seaward side of the mangrove forest at wijk aan zee, suriname [photograph].

Kalloe, Su (2022h). Close up soil (wijk aan zee, suriname) [photograph].

Kalloe, Su (2022i). Digging up the soil at the seaward edge of the forest (wijk aan zee, suriname) [photograph].

Kalloe, Su (2022j). Fallen mangrove tree at wijk aan zee, suriname [photograph].

Kalloe, Su (2022k). Fallen small mangrove tree at wijk aan zee, suriname [photograph].

Kalloe, Su (2022l). Close up of surroundings of small mangrove tree at wijk aan zee, suriname [photograph].

Kalloe, Su (2022m). Close up of surroundings of second small mangrove tree at wijk aan zee, suriname [photograph].

Kalloe, Su (2022n). Close up of surroundings of third small mangrove tree at wijk aan zee, suriname [photograph].

Kalloe, Su (2022o). Old mangrove tree at wijk aan zee, suriname [photograph].

Kelty, K. , Tomiczek, T. , Cox, D.T. , Lomonaco, P. , and Mitchell, W. (2022). Prototype-scale physical model of wave attenuation through a mangrove forest of moderate cross-shore thickness: Lidar-based characterization and reynolds scaling for engineering with nature. 8. doi: 10.3389/fmars.2021.780946.

Kim, Yongmin , Rahardjo, Harianto , and Tsen-Tieng, Daryl Lee (2020). Stability analysis of laterally loaded trees based on tree-root-soil interaction. *Urban Forestry & Urban Greening*, 49:126639.

Knappett, Jonathan (2012). *Craig's soil mechanics*, volume 8. spon press London.

Kobashi, Daijiro and Mazda, Yoshihiro (2005). Tidal flow in riverine-type mangroves. *Wetlands Ecology and Management*, 13:615–619.

Komiyama, A. , Eong Ong, J. , and Poungparn, S. (2008). Allometry, biomass, and productivity of mangrove forests: A review. 89:128–137. doi: :10.1016/j.aquabot.2007.12.006.

Komiyama, Akira , Poungparn, Sasitorn , and Kato, Shogo (2005). Common allometric equations for estimating the tree weight of mangroves. *Journal of tropical ecology*, 21(4):471–477.

Koninklijke Burgers' ZooRode mangrove - rhizophora mangle. URL https://www.burgerszoo.nl/rode-mangrove.

Lancellotta, Renato (2008). *Geotechnical engineering*. CRC Press.

Li, Pengcheng , Xiao, Xuepei , Wu, Lizhou , Li, Xu , Zhang, Hong , and Zhou, Jianting (2022). Study on the shear strength of root-soil composite and root reinforcement mechanism. *Forests*, 13(6):898.

Lynch, James C , Meriwether, John R , McKee, Brent A , Vera-Herrera, Francisco , and Twilley, Robert R (1989). Recent accretion in mangrove ecosystems based on137cs and210pb. *Estuaries*, 12(4):284–299.

Madrid, Eric N , Armitage, Anna R , and López-Portillo, Jorge (2014). Avicennia germinans (black mangrove) vessel architecture is linked to chilling and salinity tolerance in the gulf of mexico. *Frontiers in Plant Science*, 5:503.

Maffra, Charles , Sousa, Rita , Sutili, Fabrício , and Pinheiro, Rinaldo (2019). The effect of roots on the shear strength of texturally distinct soils. *Floresta e Ambiente*, 26.

Manchenõ, A. Gijón (2022).

Manguriu, G , Oyawa, W , and Abuodha, S (2013). Physical and mechanical properties of mangrove from kilifi in kenya. *Global Engineers & Technologists Review*, 3(3):1–5.

Mase, Hajime and Kirby, James T (1992). Hybrid frequency-domain kdv equation for random wave transformation. *Coastal Engineering Proceedings*, (23).

Masi, Elena Benedetta , Tofani, Veronica , Rossi, Guglielmo , Cuomo, Sabatino , Wu, Wei , Salciarini, Diana , Caporali, Enrica , and Catani, Filippo (2023). Effects of roots cohesion on regional distributed slope stability modelling. *Catena*, 222:106853.

Maza, M. , Lara, J.L. , and Losada, I.J. (2019). Experimental analysis of wave attenuation and drag forces in a realistic fringe rhizophora mangrove forest. 131. doi: 10.1016/j.advwatres.2019.07.006.

Maza, M. , Lara, J.L. , and Losada, I.J. (2021). Predicting the evolution of coastal protection service with mangrove forest age. 168. doi: https://doi.org/10.1016/j.coastaleng.2021.103922.

Mazda, Y. , Magi, M. , Ikeda, Y. , Kurokawa, T. , and Asano, T. (2006). Wave reduction in a mangrove forest dominated by sonneratia sp. 14:365–378. doi: 10.1007/s11273-005-5388-0.

Mazda, Yoshihiro and Wolanski, Eric (2009). Hydrodynamics and modeling of water flow in mangrove areas. *Coastal wetlands: An integrated ecosystem approach*, 8:231–262.

Mazda, Yoshihiro , Wolanski, Eric , King, Brian , Sase, Akira , Ohtsuka, Daisuke , and Magi, Michimasa (1997). Drag force due to vegetation in mangrove swamps. *Mangroves and salt marshes*, 1(3):193–199.

Mazda, Yoshihiro , Kobashi, Daijiro , and Okada, Satoshi (2005). Tidal-scale hydrodynamics within mangrove swamps. *Wetlands Ecology and Management*, 13:647–655.

McIvor, AL , Möller, Iris , Spencer, Tom , and Spalding, Mark (2012). Reduction of wind and swell waves by mangroves. *Natural Coastal Protection Series: Report 1. Cambridge Coastal Research Unit Working Paper 40. ISSN 2050-7941.*

Mcleod, E. , Chmura, G.L. , Bouillon, S. , Salm, R. , Björk, M. , Duarte, C.M. , Lovelock, C.E. , Schlesinger, W.H. , and Silliman, B.R. (2011). A blueprint for blue carbon: toward an improved understanding of the role of vegetated coastal habitats in sequestering co_2. 9. doi: doi:10.1890/110004.

Mendez, F.J. and Losada, I.J. (2004). An empirical model to estimate the propagation of random breaking and nonbreaking waves over vegeation fields. (51):103–118.

Menendez, Pelayo , Losada, Inigo J , Beck, Michael W , Torres-Ortega, Saul , Espejo, Antonio , Narayan, Siddharth , Díaz-Simal, Pedro , and Lange, Glenn-Marie (2018). Valuing the protection services of mangroves at national scale: The philippines. *Ecosystem services*, 34:24–36.

Menéndez, Pelayo , Losada, Iñigo J , Torres-Ortega, Saul , Narayan, Siddharth , and Beck, Michael W (2020). The global flood protection benefits of mangroves. *Scientific reports*, 10(1):1–11.

Menéndez, P , Losada, I.J. , S.Torres-Ortega, Narayan, S. , and Beck, M.W. (2020). The global floor protection benefits of mangroves. doi: https://doi.org/10.1038/s41598-020-61136-6.

Meyerhof, GG (1951). The ultimate bearing capacity of foudations. *Geotechnique*, 2(4):301–332.

Meyerhof, G.G. (1953). The bearing capacity of foundations under eccentric and inclined loads. *Proc. 3rd ICSMFE*, 1:440 – 445.

Montgomery, John . *Attenuation of tides and storm surges in coastal mangroves*. PhD thesis, The University of Waikato (2021).

Morison, JR , Johnson, JW , and Schaaf, SA (1950). The force exerted by surface waves on piles. *Journal of Petroleum Technology*, 2(05):149–154.

Muhammad-Nor, Siti Mariam , Huxham, Mark , Salmon, Yann , Duddy, Symone Jade , Mazars-Simon, Alban , Mencuccini, Maurizio , Meir, Patrick , and Jackson, Gail (2019). Exceptionally high mangrove root production rates in the kelantan delta, malaysia; an experimental and comparative study. *Forest Ecology and Management*, 444:214–224.

NAVFAC, Design Manual (1986). 7.02, foundations & earth structures. *Department of the Navy, Naval Facilities Engineering Command, Alexandra, VA*.

Nicoll, Bruce C and Ray, Duncan (1996). Adaptive growth of tree root systems in response to wind action and site conditions. *Tree physiology*, 16(11-12):891–898.

Nicoll, Bruce C , Gardiner, Barry A , Rayner, Bill , and Peace, Andrew J (2006). Anchorage of coniferous trees in relation to species, soil type, and rooting depth. *Canadian Journal of Forest Research*, 36 (7):1871–1883.

Niklas, Karl J and Spatz, Hanns-Christof (2010). Worldwide correlations of mechanical properties and green wood density. *American Journal of Botany*, 97(10):1587–1594.

Njana, Marco Andrew , Eid, Tron , Zahabu, Eliakimu , and Malimbwi, Rogers (2015). Procedures for quantification of belowground biomass of three mangrove tree species. *Wetlands Ecology and Management*, 23(4):749–764.

Obasi, NL and Anyaegbunam, AJ (2005). Correlation of the undrained shear strength. *Nigerian Journal of Technology*, 24(2):1–11.

Ong, J.E. , Gong, W.K. , and Wong, C.H. (2004). Allometry and partitioning of the mangrove, rhizophora apiculata. 188:395–408. doi: :10.1016/j.foreco.2003.08.002.

Parkinson, Randall W , DeLaune, Ron D , and White, John R (1994). Holocene sea-level rise and the fate of mangrove forests within the wider caribbean region. *Journal of Coastal Research*, pages 1077–1086.

Preston, Katherine A , Cornwell, William K , and DeNoyer, Jeanne L (2006). Wood density and vessel traits as distinct correlates of ecological strategy in 51 california coast range angiosperms. *New Phytologist*, 170(4):807–818.

Purnobasuki, H. and Suzuki, M. (2005). Aerenchyma tissue development and gas-pathway structure in root of avicennia marina (forsk.) vierh. 118:285–294. doi: 10.1007/s10265-005-0221-7.

Quartel, S. , Kroon, A. , Augustinus, P.G.E.F. , van Santen, P. , and Tri, N.H. (2007). Wave attenuation in coastal mangroves in the red river delta, vietnam. 29:576–584. doi: 10.1016/j.jseaes.2006.05.008.

Raven, Olivier , van Bijsterveldt, Celine , and van Hespen, Rosanna (2020). Mangrove stability; the effect of different sediment compositions, root complexities and erosion on the stability of mangrove mimics.

Rodtassana, Chadtip , Poungparn, Sasitorn , et al. (2012). Quantitative analysis of the root system of avicennia alba based on the pipe model theory. *Sci. Asia*, 38:414–418.

Roszyk, Edward , Moliński, Waldemar , and Fabisiak, Ewa (2013). Radial variation of mechanical properties of pine wood (pinus sylvestris l.) determined upon tensile stress. *Wood Res*, 58(3):329–342.

Roth, L.C. (1992). Hurricanes and mangrove regeneration: Effects of hurricane joan, october 1988, on the vegetation of isla del venado, bluefields, nicaragua. 24(3):375–384.

Rudnicki, Mark , Mitchell, Stephen J , and Novak, Michael D (2004). Wind tunnel measurements of crown streamlining and drag relationships for three conifer species. *Canadian Journal of Forest Research*, 34(3):666–676.

Saintilan, Neil , Khan, NS , Ashe, E , Kelleway, JJ , Rogers, Kerrylee , Woodroffe, Colin D , and Horton, BP (2020). Thresholds of mangrove survival under rapid sea level rise. *Science*, 368(6495):1118–1121.

Santini, Nadia S , Schmitz, Nele , and Lovelock, Catherine E (2012). Variation in wood density and anatomy in a widespread mangrove species. *Trees*, 26(5):1555–1563.

Schlue, Benjamin Friedrich , Mörz, Tobias , and Kreiter, Stefan (2011). Undrained shear strength properties of organic harbor mud at low consolidation stress levels. *Canadian Geotechnical Journal*, 48(3):388–398.

Schwarz, M , Cohen, D , and Or, Dani (2011). Pullout tests of root analogs and natural root bundles in soil: Experiments and modeling. *Journal of Geophysical Research: Earth Surface*, 116(F2).

Shahriar, Minhaz M , Wang, Jay X , Alam, Shaurav , and Patterson, William B (2016). Soil-binding ability of vegetation roots in enhancing erosion resistance of a shallow slope. *International Journal of Geotechnical Engineering*, 10(4):409–417.

Shan, Yuqi , Liu, Chao , and Nepf, Heidi (2019). Comparison of drag and velocity in model mangrove forests with random and in-line tree distributions. *Journal of Hydrology*, 568:735–746.

Sharma, Binu and Bora, Padma K (2003). Plastic limit, liquid limit and undrained shear strength of soil-reappraisal. *Journal of Geotechnical and Geoenvironmental engineering*, 129(8):774–777.

Skempton, AW (1951). The bearing capacity of clays. *Selected papers on soil mechanics*, pages 50–59.

Smith, Edward H (2013). *Mechanical engineer's reference book*. Butterworth-Heinemann.

Smith III, T.J. (1994). Mangroves, hurricanes, and lightning strikes: Assessment of hurricane andrew suggests an interaction across two differing scales of disturbance. 44(4):256–262. doi: 10.2307/1312230.

Spalding, M.D. and Leal, M. (2021). The state of the world's mangroves.

Spetea, Cornelia . Role of chloroplast thylakoid lumen in photosynthetic regulation and plant cell signaling. In *Progress in Botany 73*, pages 207–230. Springer (2012).

Srikanth, S. , Chen, Z. , and Lum, S. (2015). Mangrove root: adaptations and ecological importance. 30(3):451–465. doi: 10.1007/s00468-015-1233-0.

Stokes, A. (1999). Strain distribution during anchorage failure of pinus pinaster ait. at different ages and tree growth response to wind-induced root movement. 217:17–27. doi: 10.1023/A:1004613126353.

Stokes, A. , Dorren, L. , Salin, F. , and Ghani, M.A. (2005). Mechanical resistance of different tree species to rockfall in the french alps. 278:107–117. doi: 10.1007/s11104-005-3899-3.

Su, S.H. , Guan, B.T. , Chang-Yang, C. , Sun, I. , Wang, H. , and Hsieh, C. (2020). Multi-stemming and size enhance survival of dominant tree species in a frequently typhoon-disturbed forest. 31:419–439. doi: 10.1111/jvs.12858.

Sugianto, Denny N , Zainuri, Muhammad , Darari, Alfin , Suripin, S Darsono , and Yuwono, N (2017). Wave height forecasting using measurement wind speed distribution equation in java sea, indonesia. *International Journal of Civil Engineering and Technology*, 8(5):604–619.

Temmerman, S. , Meire, P. , Bouma, T.J. , Herman, P.M.J. , Ysebaert, T. , and de Vriend, H.J. (2013). Ecosystem-based coastal defence in the face of global change. (504):79–83.

Terzaghi, K (1943). Theoretical soil mechanics john wiley and sons inc. *New York*, 314.

Thornton, Edward B and Guza, RT (1983). Transformation of wave height distribution. *Journal of Geophysical Research: Oceans*, 88(C10):5925–5938.

Tjosvold, Steven (2017). How-to caring for plant roots: What you need to know. *Fine Gardening*, 174.

Tomlinson, P.B. (2016). *The Botany of Mangroves*. Cambridge University Press. ISBN 9781107080676.

Tosi, M. (2007). Root tensile strength relationships and their slope stability implications of three shrub species in the northern apennines (italy). 87(4):268–283. doi: 10.1016/j.geomorph.2006.09.019.

Ubani, OU , Nwaiwu, CMO , Obiora, JI , and Mezie, EO (2020). Effect of soil compressibility on the structural response of box culverts using finite element approach. *Nigerian journal of technology*, 39 (1):42–51.

University of FloridaLaguncularia racemosa, white mangrove. URL https://edis.ifas.ufl.edu/publication/FR325.

van Domburg, Tim (2018). Identifying windows of opportunity for mangrove establishment on a mud coast: A case study for the biomanco project in demak, indonesia.

van Hespen, R. , Hu, Z. , Peng, Y. , Borsje, B.W. , Kleinhans, M. , Ysebaert, T. , and Bouma, T.J. (2021). Analysis of coastal storm damage resistance in successional mangrove species. 66:3221–3236. doi: 10.1002/lno.11875.

van Wesenbeeck, B.K. , Wolters, G. , Antolínez, J.A.A. , Kalloe, S.A. , Hofland, B. , de Boer, W.P. , Cete, C. , and Bouma, T.J. (2022). Wave attenuation through forests under extreme conditions. 12 (1884). doi: 10.1038/s41598-022-05753-3.

van Zelst, Vincent , Dijkstra, Jasper T , van Wesenbeeck, Bregje K , Eilander, Dirk , Morris, Edward P , Winsemius, Hessel C , Ward, Philip J , and de Vries, Mindert B (2021). Cutting the costs of coastal protection by integrating vegetation in flood defences. *Nature communications*, 12(1):1–11.

Vardanega, PJ and Haigh, Stuart K (2014). The undrained strength–liquidity index relationship. *Canadian Geotechnical Journal*, 51(9):1073–1086.

Venugopal, Vengatesan , Varyani, KS , and Westlake, PC (2009). Drag and inertia coefficients for horizontally submerged rectangular cylinders in waves and currents. *Proceedings of the Institution of Mechanical Engineers, Part M: Journal of Engineering for the Maritime Environment*, 223(1):121–136.

Vesić, Aleksandar Sedmak (1973). Analysis of ultimate loads of shallow foundations. *Journal of the Soil Mechanics and Foundations Division*, 99(1):45–73.

Vesic, AS (1975). Bearing capacity of shallow foundations, foundation engineering handbook, ed. winterkorn, fs and fand, hy, Van Nostrand Reinhold, New York.

Vovides, Alejandra G Behind the mangroves' roots of cooperation. URL https://ecoevocommunity.nature.com/posts/behind-the-mangrove-s-roots-of-cooperation#:~:text=And%20yet%2C%20mangrove%20trees%2C%20growing,in%20fact%20protect%20each%20other.

Vuik, V. (2019). Building safety with nature. doi: 10.4233/uuid:9339474c-3c48-437f-8aa5-4b908368c17e.

Vuik, Vincent , Jonkman, Sebastiaan N , Borsje, Bas W , and Suzuki, Tomohiro (2016). Nature-based flood protection: The efficiency of vegetated foreshores for reducing wave loads on coastal dikes. *Coastal engineering*, 116:42–56.

W. Wen, F.F. Li et al , Y.R. Li (2016). Experimental study on reinforcement effect of herbaceous roots on soil under different confining pressures. *Mech. Q.*, 37(1):124 – 130. doi: 10.15959/j.cnki.0254-0053.2016.01.014.

Webb, E.L. , van der Bult, M. , Fa'aumu, S. , Webb, R.C. , Tualaulelei, A. , and Carrasco, L.R. (2014). Factors affecting tropical tree damage and survival after catastrophic wind disturbance. 46(1):32–41. doi: 10.1111/btp.12067.

Wu, Tien H , McKinnell III, William P , and Swanston, Douglas N (1979). Strength of tree roots and landslides on prince of wales island, alaska. *Canadian Geotechnical Journal*, 16(1):19–33.

Yamase, Keitaro , Todo, Chikage , Torii, Nobuyuki , Tanikawa, Toko , Yamamoto, Tomonori , Ikeno, Hidetoshi , Ohashi, Mizue , Dannoura, Masako , and Hirano, Yasuhiro (2021). Dynamics of soil reinforcement by roots in a regenerating coppice stand of quercus serrata and effects on slope stability. *Ecological Engineering*, 162:106169.

Zainorabidin, Adnan and Agustina, Dian Hastari (2018), Effect of moisture content of cohesive subgrade soil. In *MATEC Web of Conferences*, volume 195, page 03010. EDP Sciences.

Zolkhiflee, Nurhafiza , Yahya, Khairun , and Shuib, Shuhaida (2021). Intertidal zone preferences of fiddler crabs in tropical mangroves reflect species specific selection across multiple spatial and temporal scales. *Regional Studies in Marine Science*, 48:101994.

Zuidhoff, F. and Dijkstra, J. (2011). De oudste dijk van zeeland? vondst van een dijkje en terp uit de romeinse tijd op walcheren. 20(2):53–61.

A

Extra theoretical background

A.1. Rootsystem

The stability of the mangrove trees is determined by the roots. Those roots grow differently for different species. The different roots developed because of the enduring of different conditions, such as lack of oxygen or persistent wind forces. Therefore, all roots have different functions (Tomlinson, 2016). Importance factors for resistance to tree anchorage failure are root system structural characteristics, like the root diameter, the root number, root density per soil volume and the cross-sectional area (Coder, 2014). Due to the responsive character of roots, the roots are asymmetric around the trunk, but are different between the leeward and windward site, increasing their stability. Those characteristics and growth incentives of the roots are influenced by the soil properties (Fourcaud et al., 2008; Dupuy et al., 2007).

A.2. Mangrove growth

Mangroves are the only woody halophyten who live in the inter-tidal zone of tropical areas (Alongi, 2002). Limiting growth factor defining their habitat is the seawater temperature. Some mangrove forests are also find in the subtropical regions due to warmer oceanic currents. An important characteristic of mangroves is their high salinity tolerance of up to 2.5 times the concentration of sea water. Furthermore, mangroves have several types of aerial roots (Tomlinson, 2016). The roots of mangrove aren't only essential for their stability, but also provide a crucial habitat for the terrestrial and marine biota, for example as nursery grounds and breeding sites for fish, shell-fish, birds and many more (Alongi, 2002).

Around the world, roughly 70 different species of mangroves can be found, all slightly different. As mangroves are located in the intertidal zone, the roots must be able to handle short periods of anoxia, as the growth of a plant is dependent on the ability to maintain oxygen levels in the roots. Mangroves have adapted to these circumstances with special features, like pneumatophores, knee roots, silt roots or plank roots (Srikanth et al., 2015). These adaptation of mangrove species have resulted in many specialized roots, like buttress roots, flying buttresses, surface roots, prop roots, spreading roots, cable roots with pneumatophores and cone roots. Adaptations of mangrove roots include a higher proportion of gas space and the capability of salt exclusion, or the tolerance to high tissue salt concentration and the excrete excess salt from leaves and many more. (Srikanth et al., 2015)
Some mangrove species have developed above-ground root systems. Soil compaction, competition for assimilates, water logging, wind force, direction of wave or storm surges can all affect the stability of the mangroves. In those situation, creating above-ground root systems can increase the physical stability of mangrove trees compared to the below-ground tap root system. The above-ground root system, like buttress roots or stilt roots/prop roots, enables the mangroves to withstand currents and storms along shorelines in unstable mud and soft sediments (Srikanth et al., 2015).
As mentioned, a lot of mangrove species exists, all slightly different. The three main species are the black, red and white mangroves. The white mangrove is located at higher land compared to the red

and black mangrove (University of Florida). If this tree is subjected to oxygen-deficient conditions, the tree could develop peg roots. The red mangrove (Rhizophora), shown in figure A.1a, lives along the edge of the shoreline and is characterised by the red aerial roots. Those roots supply oxygen to the underground roots and increase the stability of the tree (Florida Museum, 2019). The black mangrove (Avicennia), shown in figure A.1b, is also characterised by aerial roots, but different roots from the red mangrove. The black mangrove has pneumatophores which arise from long horizontal cable roots (Florida Museum, 2019).



(a) Red mangrove - Rhizophora (Koninklijke Burgers' Zoo)



(b) Black mangrove - Avicennia (Gardenia BV)

Figure A.1: Difference in aerial roots of black and red mangroves

When the mangrove forest is exposed to sea level rise and also the sediment budget is large enough, the root map will submerge. As a response, the tree grows a new root mat. The tree grows a new root map above the old submerged root map, the effect on tree stability of the submerged root map stays unknown. Although as shown in the research of Böhm (2018), the submerged root map does not disappear.

Pneumatophores arise from the cable roots till above the water level and cause the mangrove to breath. If the sea level is rising to fast and the sediment supply can't keep up, the waterdepth becomes larger. As a consequence, the pneumatophores will grow larger, but can loose their stability and tumble down. That being the case, the mangrove dies due to not being able to breath.

A.3. Species: *Avicennia marina*

The *Avicennia marina* is a Avicennia species which is often called the gray mangrove or a white mangrove (Baishya et al., 2020). The Avicennia species belong to the Acanthaceae family (Baishya et al., 2020; Almahasheer et al., 2016). *Avicennia marina* are often between the 10-14 meters (Baishya et al., 2020). The adaptive behaviour of the tree causes the ability to grow in a wide range of latitude as longitude (Almahasheer et al., 2016; Baishya et al., 2020).

The roots of the Avicennia species are characterised by a root mat which consists of cable roots, anchor roots, feeding roots and pneumatophores (Böhm, 2018; Baishya et al., 2020; Hao et al., 2021; Purnobasuki and Suzuki, 2005). Figure A.2 and A.3 show the roots of the *Avicennia marina*.

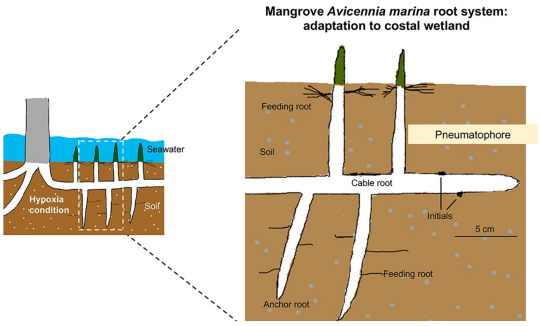


Figure A.2: schematization of the *Avicennia marina* roots (Hao et al., 2021)

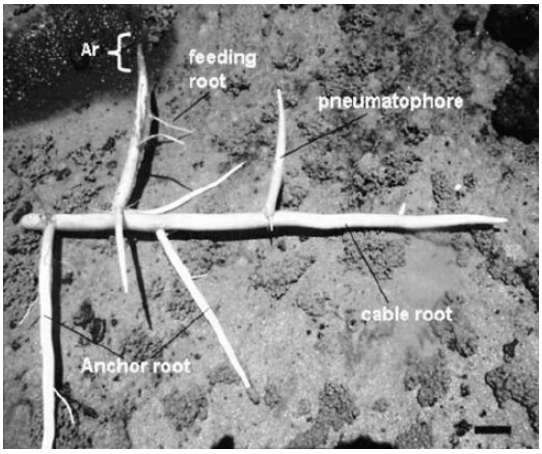


Figure A.3: Picture of the *Avicennia marina* roots (Purnobasuki and Suzuki, 2005)

A.4. Waves and water levels through a mangrove forest

A.4.1. Waves

Bao (2011) shows that the bandwidth of the mangrove forest is very important for the amount of wave attenuation by the forest. The complex network of trunks, branches, and above-ground roots of mangrove trees, which increases bed roughness, causes more friction, and dissipates more wave energy, can explain the exponential fall in wave height in mangroves (Quartel et al., 2007). The exponential equation A.1 can be used to model the effect of mangrove forest band width on wave height:

$$W_h = a * e^{b*B_w} \tag{A.1}$$

The relation between the intercept coefficient a and the initial wave height (i.e. at the edge of the mangrove forest, distance=0), can be described using a linear equation. Where coefficient a is directly proportional to the initial wave height. The slope coefficient b is associated with tree height, tree density and canopy closure. The exponential coefficient in equation A.1 is inversely proportional to those three independent variables. Those three variables account for 71% of the total variations in coefficient b.

$$a = 0.9899 * I_{wh} + 0.3526 \tag{A.2}$$

$$b = 0.048 - 0.0016 * H_{avg_{tree}} - 0.00178 * \ln(N) - 0.0077 * \ln(CC) \tag{A.3}$$

With I_{wh} being the initial sea wave height [cm], H the average tree height [m], N the tree density [tree/ha] and CC the canopy closure [%] (Bao, 2011). The equations for a and b show the importance of the bandwidth and the density of the forest. The influence of the bandwidth and the density of the forest is underlined by (Maza et al., 2021; Kelty et al., 2022). Kelty et al. (2022); McIvor et al. (2012) showed that on average, the wave decay coefficent could be multiplied by a factor 2.0 for the random wave conditions and by 2.2 for regular wave conditions, by doubling the density of the mangrove forest.
Another influence is the age of the mangrove forest (Maza et al., 2021). This arises from the assumption that the age of the tree is largely responsible for the size of the tree. Indicating the size of the tree differs with age. Suggesting the amount of submerged tree differs. The highest amount of submerged tree, indicates the largest wave attenuation. Resulting in the fact that after a certain age, the wave attenuation decreases, due to the fact the canopy will start to rise above water. During the research of Maza et al. (2021), the trees were fully submerged till an age of 5, which can be seen in figure A.4. After the age of 5, a smaller amount of tree was submerged, causing less attenuation. After the point, the canopy isn't submerged anymore, the wave attenuation increases again. This increase is caused by the again increasing amount of submerged volume, as the volume of roots and trunk increase.

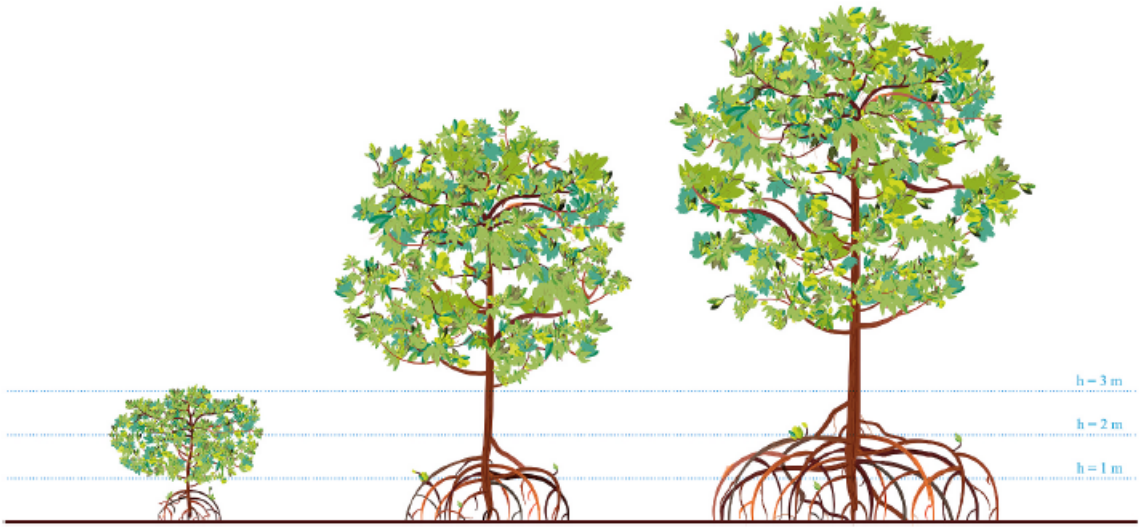


Figure A.4: Three Rhizophora mangroves at different ages: 5, 15, and 30 years. h = 1, 2, and 3 m are represented by horizontal dotted blue lines (Maza et al., 2021)

Multiple research show larger waves are attenuated more effectively than smaller waves (Maza et al., 2021, 2019; Mazda et al., 2006). Wave periods that are shorter are attenuated more than those that are longer, but the differences in attenuation rates are fewer than those reported for different wave heights. The attenuation rates found for varied mangrove forest ages differ by less than the attenuation rates for variable wave height.

Looking at the total forest, the highest rate of wave height attenuation per unit distance can be found near the mangrove seaward edge (McIvor et al., 2012). This is caused by the fact the waves begin their passage through the forest at this point. Another important observation is the fact that the density of a forest often decreases when the forest matures. The trees grow taller and need more space, which decreases the density.

Summary effect on total mangrove forest

An important factor of how the total forest reacts to cyclones and high forces is the tree itself. But looking at the total forest, some other factors are of high influence. The total wave attenuation of the forest is also dependent on the initial conditions of the waves/forces, the bandwidth of the forest, the density of the forest and the submerged volume, suggesting age, of the forest.

A.4.2. Water level

Mangrove forest characteristics, like the width and the vegetation density, and flood characteristics, like the inundation duration and amplitude, are responsible for the attenuation rate, so the water exchange and storage (Montgomery, 2021; Mazda et al., 2005). Peak water levels degrade more quickly in broader forests than in narrower forests, owing to increased water storage within the wider forest and corresponding water flux through the vegetation. Montgomery (2021) looked at overall water level reduction in mangrove forests and found that when the degradation length scale and forest width are almost equal, total attenuation of water level increases most rapidly (with additional forest width). Mangroves successfully attenuate water levels by limiting fluid exchange across the forest when the forest width is significant in relation to the decay length of the surge event (Montgomery, 2021).

Less flood dissipation is generated by steeper bottom slopes due to having less water storage. Which means less water flows through the vegetation, reducing the flow limiting impact of the vegetation. A mangrove forest's ability to reduce peak flood levels is likely a compromise between higher hydraulic efficiency due to larger water depths and the ability to control the increased flow due to more landward fluid storage. Stop-banking behind the forest will reduce the amount of storage available. The greater the depth of water in the forest, the less flow resistance the vegetation provides, and hence the less flood protection. With higher bottom slope, the peak water level reduction was reduced (Montgomery,

2021).

Montgomery (2021) showed the difference between forest which are channelized and forests which are unchannelized. Channelization is important for the water conveyance on flood reduction. The canals create an effective flow path and prevent vegetation from restricting water exchange through the forest, resulting in no flood attenuation. If the daily flow of tides maintains channel networks, an unusually high flood event is necessary for water to penetrate places without a channel network. This unchannelized network is needed for vegetation to restrict water conveyance and lower peak water levels. As a result, forests may only serve to reduce the landward flow of water when the channel network is insufficient to transport it, and hence provide flood protection only during extreme events. Therefore, channels reduce flood protection provided by mangroves (Montgomery, 2021).

Summary of waterlevel through forest
The water level through the mangrove forest is highly complex due to the factors it is dependent upon. The most important factors are the bottom slope, the width of the forest and the geometry (like channels and density). The forest serves as water storage, restriction landward flow, and reduces hydraulic conductivity. All influencing the water depth through the forest.

A.5. Additional eco-services of aquatic vegetation

Besides the ability to reduce hydrodynamic energy, the aquatic vegetation is able to operate as food and shelter for many organisms and to control biogeochemical cycles in the coastal zone (Ifuku and Hayashi, 1998; Gacia and Duarte, 2001; Fonseca and Cahalan, 1992). For example, marshes and mangroves contribute to climate change mitigation as they are important sinks for atmospheric CO_2 (Mcleod et al., 2011). Also, the water quality of estuaries can be improved by tidal wetlands (Temmerman et al., 2013). Tidal wetlands deliver scarce nutrients such as silica and act as a sink for abundant nutrients such as nitrogen and contaminants such as heavy metals. Due to the improved water quality, the growth of toxic algae is suppressed and phytoplankton growth is stimulated (Temmerman et al., 2013). Due to this additional functions, coastal ecosystems are more and more considered as an alternative or addition to the grey traditional coastal safety structures. (Temmerman et al., 2013).

B

Short recall of useful concepts of soil mechanics

In this section important soil mechanics will be explained. This will make clear why some properties are important and which properties influence for example the shear strength.

B.1. Atterberg Limits:

The Atterberg limits are a basic measure of the critical water contents of soil.
Consistency is the resistance of soil against deformation and rupture. The physical properties of soil are influenced by the amount of water which is present. The consistency of soil changes with the amount of water. Depending on the water content, the soil can be in the following states (Lancellotta, 2008; Knappett, 2012):

1. Liquid state: soil has no shear strength and has no resistance to flow (flows like a liquid))
2. Plastic state: soil has shear strength, water content has decreased. Soil can be moulded into different shapes without rupturing because of plasticity
3. Semi-solid state: If you try to mould the soil it ruptures. The soil loses its plasticity and becomes brittle
4. Solid state: no volume change with water content reduction

Till the semi-solid state the soil remains fully saturated. Therefore when the water content decreases, the soil weight and volume decrease. The point where further reduction in water content does not change the volume, is the point where the semi-solid state changes to the solid state. For every state, the consistency is different and so are the engineering properties. The water content at which the soil changes from state is known as the consistency limits (Lancellotta, 2008; Knappett, 2012).

1. Liquid limit → the limit at which the soil doesn't flow like liquid anymore (from liquid state to plastic state)
2. Plastic limit → from plastic state to semi-solid state
3. Shrinkage limit → lowest water content at which the soil is fully saturated.

These limits are consistency parameters and have a relation with undrained shear strength of the soil. The relation of the Atterberg limits and the undrained shear strength is often described in literature (Sharma and Bora, 2003; Obasi and Anyaegbunam, 2005). By knowing the liquidity index of a soil, see equation B.1, the undrained shear strength of a soil can be approximated (Vardanega and Haigh, 2014; Lancellotta, 2008).

$$I_L = \frac{w - w_p}{w_l - w_p} \tag{B.1}$$

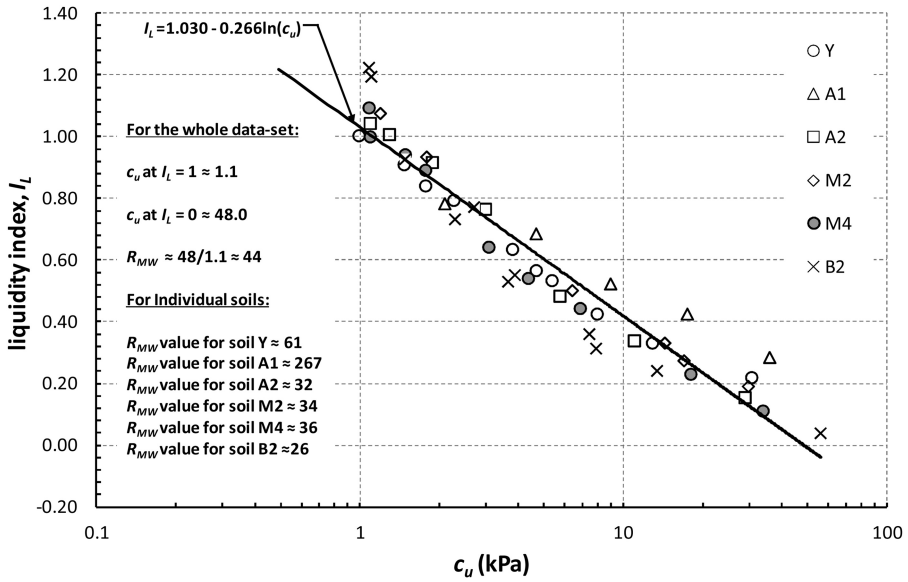
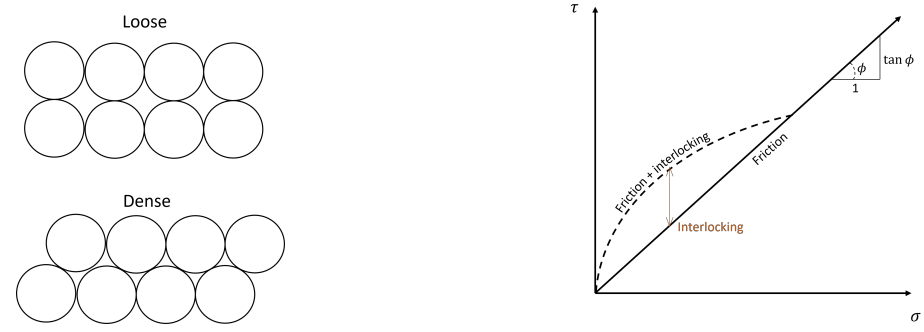


Figure B.1: Relation liquidity index and undrained shear strength (Vardanega and Haigh, 2014)

B.2. Shear stress and normal stress

As shown in Equation B.2 the shear stress τ can be described in terms of the normal effective stress σ and coefficient of friction, $\tan\phi$. The coefficient of friction, being an intrinsic material property, is connected to the shear plane roughness (i.e. the size, shape and angularity of the soil particles) (Knappett, 2012). Instead of total stress, the shear strength of a soil at a given position on a specific plane is typically stated as a function of effective normal stress, acccording to the theory that only the skeleton of solid particles and not pore water can sustain shear stress in a soil. This theory is based on the assumption of a non-compressible fluid, while the skeleton is compressible.
Densely packed soil can have a higher frictional resistance τ_f than the predicted one considering only friction as shown in Equation B.2 (Knappett, 2012). However, the normal stress can become high enough to initiate particle breakage, reducing the degree of interlocking and causing purely frictional material behaviour.

$$\tau_f = (\tan\phi)\sigma' \tag{B.2}$$



(a) Densely and loosely packed soil

(b) Friction strength

Figure B.2: Shear stress determination in a soil element

B.3. The Mohr-Coulomb model

The normal and shear stresses that are applied to the boundaries of a soil element are used to characterize the state of stress in a soil element. A plot of shear stress (τ_f) against effective normal stress (σ') can be used to show states of stress in two dimensions, as well as a Mohr circle defined by the effective principal stresses σ_1' and σ_3'. The stress conditions on a plane at an angle of θ to the minor principal effective stress are represented by the stress points at either end of a diameter via a Mohr circle at an angle of 2θ to the horizontal. As a result, the circle reflects all conceivable stress levels on all planes within the soil element. Because it reduces the number of stress variables from three (σ_x', σ_z', τ_{zx}) to two (σ_1', σ_3'), the major stress components are frequently employed to characterize the stress state (Knappett, 2012). Figures B.3 and B.4 show the relation between the different stresses. The angle θ is a theoretical angle between the plane of failure and minor principal plane.

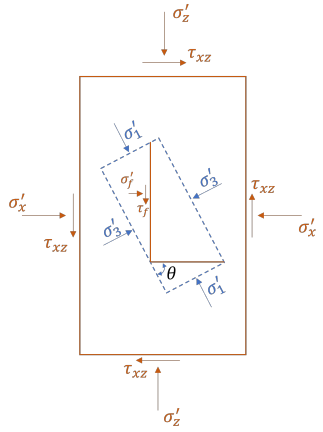


Figure B.3: Stresses on a soil element, after Knappett (2012)

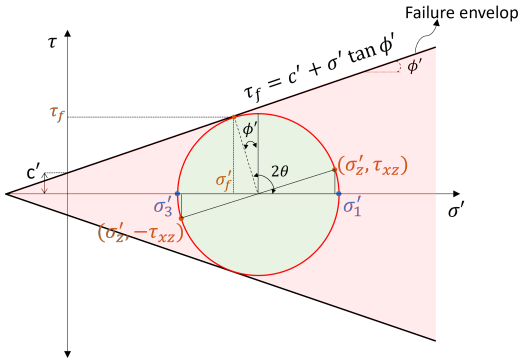


Figure B.4: Mohr-Coulomb failure criterion after Knappett (2012)

When the circle touches the failure envelop, the soil element reaches failure. In common practise, the failure envelope is approximated by a straigth line due to difficulties with the non-linearly caused by interlocking as shown in Figure B.2b (Knappett, 2012). The failure envelope is described by Equation B.3. It should be noticed that the determination of the shear stress is in term of effective stress. If the Mohr circles will be drawn for the total stresses, the circles have the same diameter but the difference between their centres is equal to the pore water pressure. So, all effective and total stress points are separated by the value of the pore water pressure.

$$\tau_f = c' + \sigma' \tan\phi' \tag{B.3}$$

In this equation c' is equal to the cohesion intercept and ϕ' to the angle of shearing resistance. Failure can happen anywhere in the soil where a crucial interaction between effective normal stress and shear stress arises.
Using Figure B.4, the value of τ_f and σ_f' can be determined. Those values are given in Equation B.4 and B.5 respectively. In the figure, it can also be seen that $2\theta = 90° + \phi'$. Using the relationship between those angles, the Mohr-Coulomb failure criterion, for given material properties c' and ϕ', can be determined, as shown in Equation B.6. The Mohr-Coulomb failure criterion defines the correlation between the principal stresses (Knappett, 2012).

$$\tau_f = \frac{1}{2}(\sigma_f' - \sigma_3')\sin 2\theta \tag{B.4}$$

$$\sigma_f' = \frac{1}{2}(\sigma_1' + \sigma_3') + \frac{1}{2}(\sigma_1' - \sigma_3')\cos 2\theta \tag{B.5}$$

$$\sigma_1' = \sigma_3' \tan^2\left(45° + \frac{\phi'}{2}\right) + 2c' \tan\left(45° + \frac{\phi'}{2}\right) \tag{B.6}$$

B.4. Effect of drainage conditions on shear strength

The failure envelope is defined in terms of effective stress. The difference between drained and undrained conditions is that in undrained loading, the effective stresses within the soil will change due to generated excess pore pressures. In drained conditions, no excess pore pressures will be generated, as the water is able to flow out of the pores. According to the Mohr-Coulomb criterion, if a soil sample is subjected to the same change in total stress under drained and undrained drainage conditions, the strength of the samples will be different.
In reality, distinguishing between perfectly drained (i.e. no excess of pore pressure) and undrained (i.e. no dissipation of excess pore pressure) conditions is not always straightforward. In general the soil response is ruled by the rate of pore pressure dissipation given by the coefficient of consolidation and by the loading rate applied to the soil element in each specific engineering problem.

B.5. Stress paths of saturated fine-grained soils

Due to the low permeability of most fine-grained soils, often, consolidated undrained (CU) triaxial tests are used to determine the shear strength of a soil. In contrast to the drained test, in the undrained tests, the soil samples will experience high excess pore pressures, which will cause the total stress path (TSP) and effective stress path (ESP) to differ. So it is necessary to measure the specimen's pore water pressure in order to calculate the ESP under undrained conditions using the sample's known TSP. Undrained tests can be used to determine drained properties as the ultimate state will always occur when the ESP reaches the critical state line (Knappett, 2012).
The test results for normally consolidated (NC) and overconsolidated (OC) clays are different, due to the different development of pore water pressures. In Figure B.5 and B.6, the pore water pressures (u_e) and deviatoric stress (q) are plotted against axial strain (ε_a). For NC clays the deviatoric stress, as well as the pore water pressure, reaches a maximum at relatively large strain. For OC clays, the deviatoric stress and pore pressures increase till a peak value, after they decrease while the strain increases (Knappett, 2012), shown by the dotted line in Figure B.6. However, because of severe specimen deformation, it is typically impossible to reach the ultimate stress. Pore water pressure initially rises and subsequently falls; the larger the decline, the higher the overconsolidation ratio. The dotted line illustrates how strongly overconsolidated clays can cause pore water pressure to become negative.

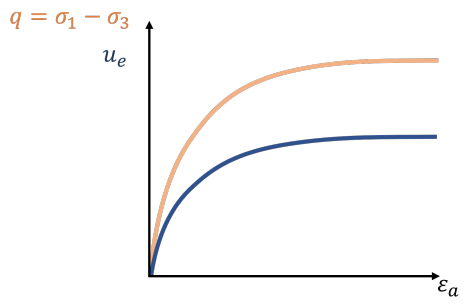


Figure B.5: CU test on normally consolidated clay, after Knappett (2012)

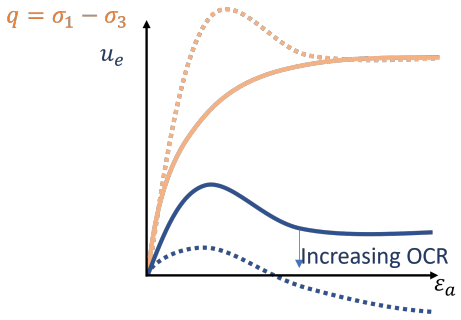


Figure B.6: CU test on normally overconsolidated clay, after Knappett (2012)

It should be noted that the CU test should run at a slow enough rate to equalize the pore pressures through the soil element. This equalization is a function of the hydraulic conductivity of the soil (Knappett, 2012).

Figure B.7 and B.8 show the failure envelops of normally and overconsolidated clays. The critical state line (CSL) is the ratio between deviatoric stress q and mean effective stress p'. The deviatoric stress invariant is function of the principal stresses, causing only shear strain within an element of soil (Knappett, 2012). The mean stress invariant, also, is a function of the principal stresses, causing only volumetric strain within an element of soil (Knappett, 2012). The definition of the stress invariants are reported in Equation B.7 and B.8 where σ_1' and σ_3' are the major and minor principal effective stress respectively.

$$q = \sigma_1' - \sigma_3' \tag{B.7}$$

$$p' = \frac{\sigma_1' + \sigma_2' + \sigma_3'}{3}; \qquad \text{if: } \sigma_2' = \sigma_3' \quad \Rightarrow \quad p' = \frac{\sigma_1' + 2\sigma_3'}{3} \tag{B.8}$$

For NC clays, the value critical state line (CSL) goes through the origin, as $c' \approx 0$. While heavily overconsolidated clays show some curvature over the stress range, due to interlocking as shown in B.2b (Knappett, 2012).

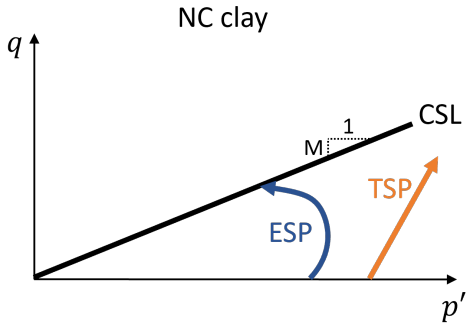


Figure B.7: Effective and total stress path of normal consolidated clay, after Knappett (2012)

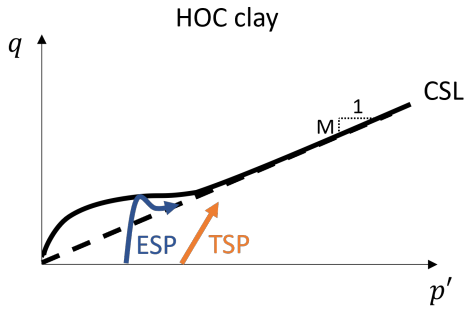


Figure B.8: Effective and total stress path of heavely overconsolidated clay, after Knappett (2012)

B.6. Undrained strength

The undrained strength of fine-grained soils can be determined using unconsolidated-undrained (UU) tests. To determine the in-situ undrained strength, the void ratio of the soil element at the start of the test should be equal to the in-situ value at the sampling depth (Knappett, 2012). In reality, the void ratio is slightly increased by the sampling and preparation due to swelling as a result of the removed in-situ stresses.

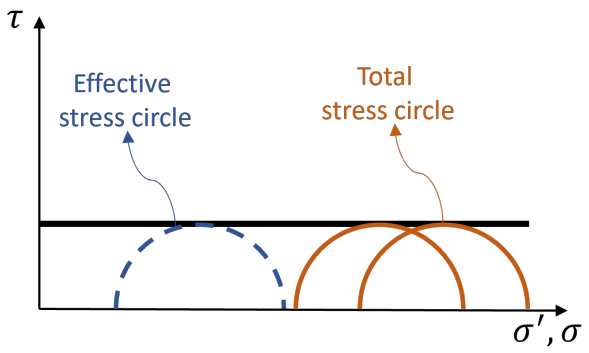


Figure B.9: Result of UU triaxial test for saturated clay

The saturated fine-grained soil sample has an initial negative pore water pressure due to capillary tension, positive effective stresses and the total stresses equal to zero (Knappett, 2012). In fully saturated undrained conditions, the increase in confining pressure is taken by the pore water and therefore the effective stresses remain unchanged from the start of the test (Knappett, 2012). If the test is done multiple times, assuming equal composition and void ratio, at different confining pressures, the principal stress difference at failure remains equal. This equal principal stress difference at failure results in a horizontal failure envelope, e.g. $\phi_u = 0$. The shear strength is given by $\tau_f = c_u$, with c_u being the undrained shear strength (Knappett, 2012). The principal stress difference at failure (q_f) is equal to the diameter of the Mohr circle, $\frac{\sigma_1' - \sigma_3'}{2}$, and τ_f is equal to the radius. Using these properties, the undrained strength is equal to $c_u = q_f/2$ (Knappett, 2012).

If the tangent of the Mohr circles is not horizontal, a reduction of void ratio has taken place, which means that the soil element was not fully saturated, which could be due to multiple reasons like entrapped air or drying of soil prior to testing.

Unconsolidated-undrained test findings are often displayed as a c_u plot against the equivalent depth where the soil element was taken. The undrained strength for NC fine-grained soils will typically grow linearly with increasing effective vertical stress σ_v', in other words with depth when the water table is at

the surface. The undrained strength between the surface and the water table, caused by drying, will be much higher than that directly below the water table if the water table is below the surface of the clay (Knappett, 2012).

B.7. Coefficient of Consolidation

In reality the soil behaviour in field application is neither perfectly undrained nor perfectly drained. The response of the soil is ruled by the rate of loading (depends of the problem) and the rate of excess pore pressure dissipation. The latter is given by the coefficient of consolidation, C_v. The time needed for the consolidation process also depends on the maximal drainage path (Jommi, 2021). The consolidation coefficient is a function of the hydraulic conductivity and the stiffness of the soil, as stated in Equation B.9. As the hydraulic conductivity among soil can very largely, the coefficient of consolidation has a larger dependence on the hydraulic conductivity (Jommi, 2021).

$$c_v = \frac{k_v}{m_v \gamma_w} \tag{B.9}$$

In Equation B.9, γ_w is the unit weigth of water, k_v the hydraulic conductivity and m_v the compressibility of the soil skeleton.

C

schematization Appendix

C.1. Failure mechanisms which are excluded from the research

Breakage of leaves and branches

The leaves and branches cannot be considered a stiff cylinder pillar, due to their bending character. The bending decreases the area subjected to the wave or wind action, decreasing the acting force due to drag (Rudnicki et al., 2004).

The breakage of the leaves and branches reduces the area subjected to wind and wave forces. When this area decreases, the total drag and drag coefficient decreases (Rudnicki et al., 2004). This lead to a decreased force on the tree. When breakage happens under wave forces, less dissipation of waves will occur due to the decreasing density of vegetation and vegetation area. When breakage happens under wind forces, the decreased area will again decrease the total force on the tree. The decreasing vegetation density will decrease the gust factor, again decreasing the force.

This failure mechanism causes less severe consequences compared with tree death, due to the fact that the stem can still dissipate waves and the tree will stay alive. Therefore, this failure mechanism will not be analysed in this research.

Erosion of sediment causing instability

Confining Pressure is defined as the stress or pressure forced on a layer of soil or rock by the heaviness of the overlying substance (Jayabalan et al., 2018). So, erosion decreases the confining pressure of the soil. The confining pressure influences the maximum pull-out force of roots and the soil shear strength (Fan et al., 2021a; W. Wen, 2016; Guo et al., 2020). Also, the moments created by the wave and wind forces increases due to erosion, because the arm of the forces increases. Furthermore, the layer of soil above the roots determines the resisting moment against soil uplift. Those effects combined can create instability, which causes the tree to tumble over. The pneumatophores can also get unstable due to erosion, causing breaking or tumbling over. Without the pneumatophores the mangroves can not exchange their gasses, which can cause the death of mangroves.

While the failure mechanism erosion results in instability of the tree, it will not be the cause of failure of the tree. In case of erosion, the cause of failure will always be another failure mechanism that is reinforced by erosion, as erosion decreases the resistance of other failure mechanisms that occur. Therefore erosion will not be analysed individually in this research.

Sea level rise

Failure due to sea level rise is governed by the fact that the roots may stop emerging and become permanently submerged, preventing the tree from changing its gasses, causing the death of the tree. Since the death of the tree is not related to instability of the tree itself and will not be analysed in this research.



(a) Healthy mangrove tree



(b) Failure mechanism: Breakage of leaves and branches



(c) Failure mechanism: Dying of trees as the sea level is rising too fast for the mangroves to compensate this



(d) Failure mechanism: Erosion of sediment occurring toppling over

Figure C.1: Failure mechanisms of the mangrove trees which will not be analysed

C.2. Bearing capacity

The bearing capacity of a shallow foundation refers to the maximum value of the load applied, for which no point of the subsoil reaches the failure point.
By assuming that soil would generally fail under the influence of an ultimate load per unit area (q_u), as illustrated in figure C.2, Terzaghi's bearing capacity equation was created. Three zones of plastic equilibrium are created in the soil below the footing as a result of the action of this load, forming failure surfaces. There are three zones (Terzaghi, 1943):

- Zone I: Elastic Equilibrium
- Zone II: Radial Shear
- Zone III: Rankine Passive State

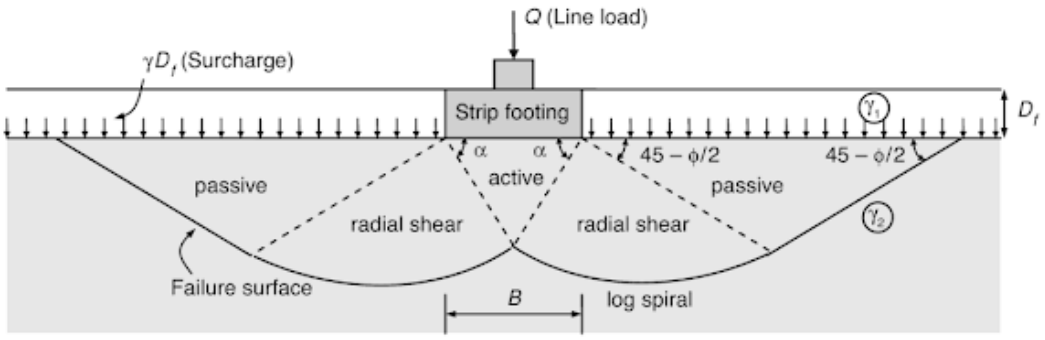


Figure C.2: Terzaghi's bearing Capacity Equation - Failure mode (Terzaghi, 1943)

The zone of influence of a shallow foundation is important when the soil properties are not homogeneous. The zone of influence is important for the failure surface. If the failure surface is located at another location due to a different size of the shallow foundation and the shear undrained shear strength differs over depth, the bearing capacity will differ.

C.2.1. Undrained conditions

The bearing capacity of a shallow foundation during undrained loading can be determined using equation C.1 (Lancellotta, 2008).

$$q_{lim} = s_u N_c s_c^0 d_c^0 i_c^0 b_c^0 g_c^0 + q \tag{C.1}$$

The shape coefficient, is based on model tests, and different for every shape. For a rectangular shape equation C.2 can be used (Lancellotta, 2008). For a circular shape s_c^0 is equal to 1.3 (Terzaghi, 1943).

$$s_c^0 = 1 + 0.2\frac{B}{L} \tag{C.2}$$

The depth coefficient d_c^0 is determined by (Meyerhof, 1951; Skempton, 1951; Hansen et al., 1961).

$$\begin{aligned} d_c^0 &= 1 + 0.4\frac{D}{B} \qquad (if: D \leq B) \\ d_c^0 &= 1 + 0.4tan^{-1}\frac{D}{B} \qquad (if: D > B) \end{aligned} \tag{C.3}$$

The presence horizontal load component is integrated in the formula by including the coefficient i_c^0 (Vesic, 1975):

$$i_c^0 = 1 - \frac{mH_h}{BLs_u N_c} \quad ; \quad m = \frac{2 + \frac{B}{L}}{1 + \frac{B}{L}} \tag{C.4}$$

The coefficient N_c can be found in table C.1.

φ'[°]	0	22	24	26	28	30	32	34	36	38	40	42
N_c	5.14	16.88	19.32	22.25	25.80	30.14	35.49	42.16	50.59	61.35	75.31	93.71
N_q	1.00	7.82	9.60	11.85	14.72	18.40	23.18	29.44	37.75	48.93	64.20	85.38
N_γ	0.00	7.13	9.44	12.54	16.72	22.40	30.22	41.06	56.31	78.03	109.4	155.6

Table C.1: Coefficients of bearing capacity (Lancellotta, 2008)

The following coefficient evaluates the inclination of the founding base (Hansen, 1970):

$$b_c^0 = 1 - \frac{2\alpha}{1+\pi} \tag{C.5}$$

Lastly, a sloping ground surface also introduces a coefficient (Vesic, 1975):

$$g_c^0 = 1 - \frac{2\omega}{1+\pi} \tag{C.6}$$

If a sloping ground surface is present, the following term should be added to equation C.1:

$$\frac{1}{2}\gamma B\left(1 - 0.4\frac{B}{L}\right)(-2\omega) \tag{C.7}$$

C.2.2. Drained conditions

The drained bearing capacity can be estimated with the extended formula suggested by (Hansen, 1970):

$$q_{lim} = \frac{1}{2}\gamma B N_\gamma s_\gamma i_\gamma b_\gamma g_\gamma + c' N_c s_c d_c i_c b_c g_c + q' N_q s_q d_q i_q b_q g_q \tag{C.8}$$

The bearing capacity coefficients can be determined by using a unique relation with the angle of shear resistance in table C.1.

The three-dimensional geometry footings, like square or circular, need a shape factor. The shape coefficient can be determined using (Meyerhof, 1951):

$$s_q = s_y = 1 + 0.1\frac{1+sin(\varphi')}{1-sin(\varphi')}\frac{B}{L}; \qquad s_c = 1 + 0.2\frac{1+sin(\varphi')}{1-sin(\varphi')}\frac{B}{L} \tag{C.9}$$

The depth coefficient is important for the greater depths, due to the shear strength of the overlying soil contributing to the bearing capacity (Hansen, 1970; Vesić, 1973). For the more shallow depths, the assumption of considering the soil above the founding level as a surcharge without strength is reasonable. Since cracks and weathering exist to relatively shallow depths (i.e. up to 2 meter) (Lancellotta, 2008):

$$\begin{aligned} d_q &= 1 + 2tan(\varphi')(1-sin(\varphi'))^2\frac{D}{B} \quad (D \le B) \\ d_q &= 1 + 2tan(\varphi')(1-sin(\varphi'))^2 tan^{-1}\frac{D}{B} \quad (D > B) \\ d_c &= d_q - \frac{1-d_q}{N_c tan\varphi'} \end{aligned} \tag{C.10}$$

The horizontal load H can produce failure by sliding, if this is not the case, a coefficient should be taken into account (Vesić, 1973):

$$
\begin{aligned}
i_y &= \left(1 - \frac{H}{N + BLc'cot\varphi'}\right)^{m+1} \\
i_q &= \left(1 - \frac{H}{N + BLc'cot\varphi'}\right)^{m} \\
i_c &= i_q - \frac{1 - i_q}{N_c tan\varphi'} \\
m &= \frac{2 + \frac{B}{L}}{1 + \frac{B}{L}}
\end{aligned}
\tag{C.11}
$$

For a inclined founding base the following coefficient should be taken into account:

$$
\begin{aligned}
b_q = b_\gamma &= 1 - \alpha tan\varphi')^2 \\
b_c &= b_q - \frac{1 - b_q}{N_c tan\varphi'}
\end{aligned}
\tag{C.12}
$$

For a sloping ground surface, Hansen (1970) suggested the following coefficient:

$$g_q = (1 - tan\omega)^2 \tag{C.13}$$

And if the resultant has an eccentricity e, for a rectangular footing, the value of B is different (Meyerhof, 1953) :

$$B = B_R - 2e \tag{C.14}$$

For a circular problem the following steps should be taken (Meyerhof, 1953):

$$
\begin{aligned}
e &= \frac{M}{n} \\
B &= B_R - 2e \\
\frac{B}{L} &= \frac{DC}{AB} \\
Area(BL) &= 2 * \left[R^2 * cos^{-1}\left(\frac{R - h}{R}\right) - (R - h)(2Rh - h^2)^{0.5}\right] \\
h &= R - e
\end{aligned}
\tag{C.15}
$$

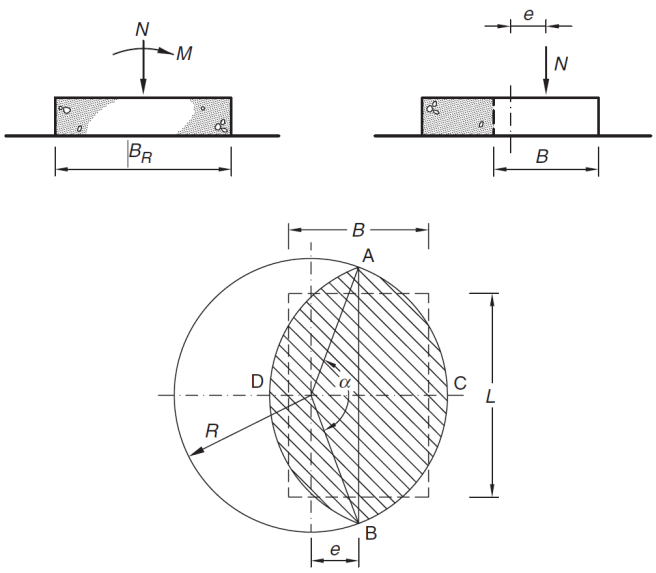


Figure C.3: Eccentricity by a circular footing (Lancellotta, 2008)

C.3. Methods to determine the bonding strength

C.3.1. Interface shear strength

The shear strength at the interface between soil and another medium can be computed by Equation C.16. As shown in Equation C.16 the shear strength is proportional to the effective stress acting at the interface and the friction coefficient which depends on the material type.

$$\tau = k * \sigma_v' * \tan\delta \tag{C.16}$$

With k being the neutral groundpressure factor, σ_v' the effective vertical stress and δ the friction angle. The determination of the pull out force can be done by integrating the interface shear strength over the area, as shown in Equation C.17.

$$Re = \pi * D * L_k * k * \sigma_v' * \tan\delta \tag{C.17}$$

With D being the diameter of the root and L_K the length of the root.
The application of Equation C.16 requires the knowledge of the pore water pressure at any time and depth. In addition the interface properties in terms of friction angle must also be known. While this approach is commonly used in geotechnical applications such as piles foundations, its application on soil-roots problems is more difficult.

From the one side the frictional properties at the interface between soil and roots are not known. Some indication can be used from NAVFAC (1986) and Canakci et al. (2013), shown in section C.3.1. In addition, for this the problem considered in this thesis, the magnitude of the pore water pressure during the storm event is not know. This hinders the possibility to estimate effective stress in the soil.

Determination the friction angle between soil and wood

The bonding strength between a material and soil is dependent on the material and the soil type. According to NAVFAC (1986), the friction angle between a timber pile and granular soil is equal to $\frac{3}{4}\phi$. If the friction angle is assumed a certain value, ϕ is equal to $\delta * 4/3$. DM gives correlations between strength characteristics for granular soils. Combining this with the information of the friction angle between mansory and wood, equal to 26 degrees, could give a first assumption of ϕ. As the soil in the test case is very different from granular soil, this method will not be a good assumption for the case in this research.

Canakci et al. (2013) researched the interface friction angle between organic soil and different materials under different moisture contents. The interface friction angle of dry wood and organic soil is equal to 45 degrees. The organic soil exists for 50-70% from organic content and has a water keeping capacity of 85-95%. The wood used was sound pine. The interface friction angle for 75% water content is equal to 38 degrees. The friction angle between an organic soil and material is dependent on the surface roughness and the moisture content. A higher moisture content decreases the interface friction angle (Canakci et al., 2013). Again, the soil is different from the soil in the test case. As stated above, the bonding strength and friction angle between a material and soil is dependent on the material and the soil.

C.4. Primary schematizations Uplift

C.4.1. Short roots - situation 1

The first situation describes the situation with short roots. If the roots are short, the end of the roots will also move or rotate slightly. This can be schematised with a rolled support at the end of the roots, shown in Figure C.4. The schematization on the leeward and windward sides are equal. As there is no difference in support on both side, the distribution of the moment over all the roots is dependent on the length, diameter and number of roots.

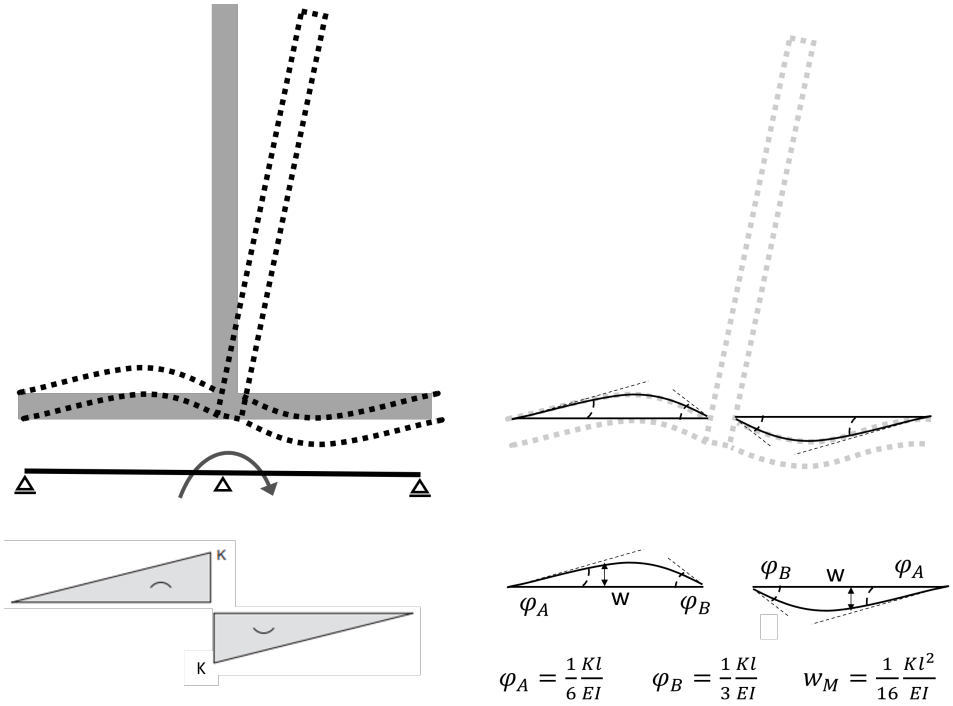


Figure C.4: schematization of the short roots - situation 1

C.4.2. No movement at the end of the leeward root - situation 2

In this situation, no movement is present at the end of the leeward root comparable with a longer root. On the windward side, the moment becomes zero at the end of the root, but there will still be a slight rotation, comparable to a rolled support. The schematization at the leeward and windward sides are different, as shown in Figure C.5. Due to this difference, the moment distribution over the roots is dependent on the length, diameter, number of roots and location of the roots. With the location of the root, the leeward or windward side is meant.

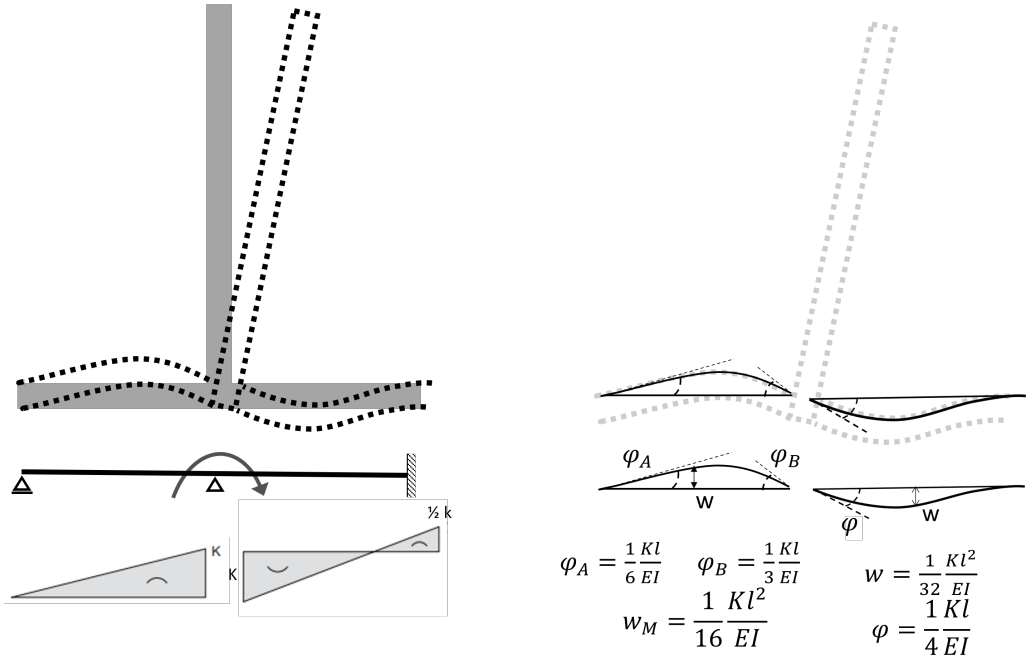


Figure C.5: schematization with a fixed support on the leeward side and a rolled support on the windward side - situation 2

C.4.3. No movement at the end of both roots - situation 3

In the third situation, the movement of the end of both roots is equal to zero, which could happen when the roots are very long and no movement is visible at the end of the root. The effect of the forces is now negligible small. This can be schematised with a fixed support. For both sides, the roots are assumed to be long enough to create this situation; therefore, both leeward and windward ends have a fixed support. It should be noted that the rotation at a hinged and rolled support, and on the other side a fixed support, can be assumed equal when the horizontal displacement remains small. The assumption is made that the horizontal displacements below the trunk are very small, which gives the maximum values for the rotation and indentation, for the situation with a fixed support on the end, as shown in Figure C.6.

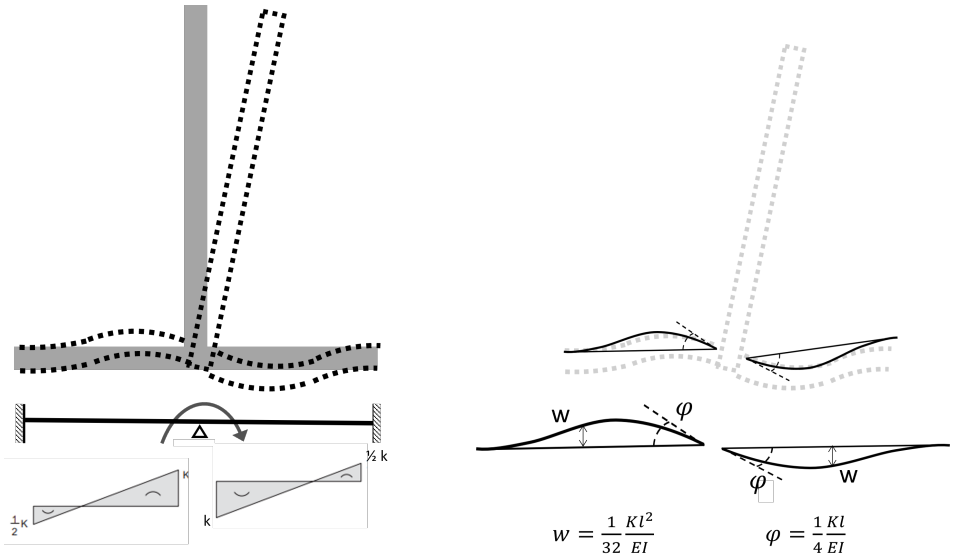


Figure C.6: schematization of no movement at the end of both roots - situation 3

Determination uplift

The determination of uplift is the same as explained in Chapter 3, only for situation 3 a different formula

for φ is used. The angle created by the moment is equal in situations 1, 2, 4 and 5, caused by the fact that the windward side is modelled with a rolled support in all situations. The moment inside the roots will be different, but the angle created by an equal moment does not differ and is equal to φ in Equation C.18. Situation 3 has a fixed support on the windward side, therefore the maximal angle caused by the moment due to wind and wave forces is different, see Equation C.19 and Figure C.6.

$$\varphi_{1245} = \frac{\frac{1}{3} * M * L}{E * I} \tag{C.18}$$

$$\varphi_{3} = \frac{\frac{1}{4} * M * L}{E * I} \tag{C.19}$$

With *M* being the maximum moment inside the root, *L* being the length of the root, *E* being the elasticity of the root and *I* being the quadratic area moment of the root.
The values for φ can be used to determine the uplift as described in Chapter 3

D

Modelling wave and wind forces

[-]

D.1. Calculation wave forces through the forest

To determine the differences in wave forces at the edge of the forest and at the interior, a model described by Mendez and Losada (2004) is used. The formulation of Mendez and Losada (2004) includes wave breaking and wave damping over vegetation fields at different depths. The approach of Mendez and Losada (2004) is concentrated on flexible vertical cylinder-like plants. The wave damping and wave breaking across vegetation fields at various depths are included. Using this formulation, it is possible to simulate either the transformation of monochromatic waves or random waves using a non-linear formulation of the drag force while taking into account the geometric and physical properties of the vegetation field.
The waves create orbital velocities, which cause horizontal motion. This horizontal motion is different in deep, intermediate and shallow water, as shown in Figure D.1. The mangrove forest is in shallow waters, which causes the horizontal motion to be equal over the water depth, as shown in Figure D.2. This horizontal velocity is needed for to determine the dragforce.

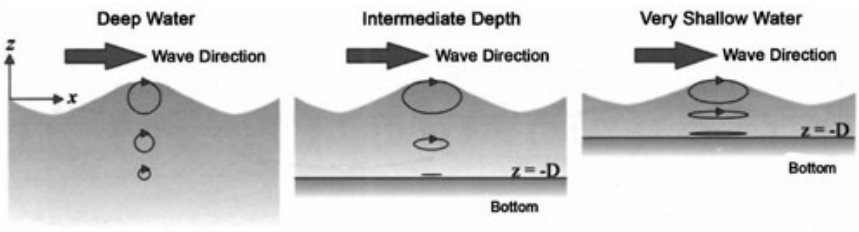


Figure D.1: Orbital velocities at deep, intermediate and shallow water depth

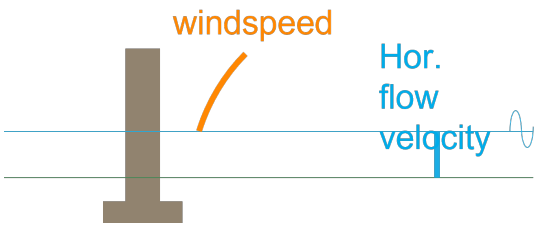


Figure D.2: Wind and flow velocity over a tree profile

D.1.1. Formulas

Formula D.1 describes the conservation of energy, using linear wave theory and considering regular waves which normally incident on a straight coastline with parallel contours.

$$\frac{\delta E c_g}{\delta x} = -\epsilon_v \tag{D.1}$$

with:

$$E = \frac{1}{8}\rho_w g H^2 \tag{D.2}$$

$$c = \frac{\omega}{k} \tag{D.3}$$

$$n = \frac{1}{2} * \left(1 + \frac{(2kh)}{sinh(2kh)}\right) \tag{D.4}$$

$$c_g = c * n \tag{D.5}$$

Symbol	Parameter	Unit
E	Energy density	$[N/m]$
H	Wave height	[m]
g	acceleration of gravity	$[m/s^2]$
ρ_w	water density	$[kg/m^3]$
c	individual celerity	[m/s]
c_g	group celerity	[m/s]
ω	wave angular frequency	[rad/s]
n		[-]
k	wave number	[1/m]
x	onshore coordinate	[m]
ϵ_v	time-averaged rate of energy dissipation induced by vegetation	[N/m/s]

By calculating the horizontal force F_x acting on the vegetation per unit volume, the relative motion between the fluid and the plant should be taken into account. Also the inertial and drag forces should be taking into account. The approach of Mendez and Losada (2004) neglects the plant motion. Neglecting swaying motion and inertial force results in a Morison-type equation, like D.6. If the relative velocity u_r between plant and fluid is used instead of u, the non-linear force F_x also valid for non-rigid plants. Due to the ignorance of the plant motion, a different value of the bulk drag coefficient C_D should be considered, to obtain a valid definition for F_x for flexible plants.

$$F_x = \frac{1}{2}\rho C_D b_v N_v u|u| \tag{D.6}$$

with:

u	horizontal velocity	[m/s]
u_r	relative horizontal velocity	[m/s]
b_v	the plant area per unit height of each vegetation stand normal to u	[m]
N_v	number of vegetation stands per unit horizontal area	$[1/m^2]$
C_D	depth-averaged drag coefficient	[-]

The total force acting on trees per unit area is dependent on a drag term and a inertia term. The drag term, as described by D.6, is dependent on the flow velocity squared. The inertia term is dependent on the flow acceleration. Adding both terms gives the total force acting on the trees per unit area, as given in equation D.7.

$$F_w = \frac{1}{2}_{D,w} A N_v u^2 +_M V N_v \frac{du}{dt} \tag{D.7}$$

An important assumption in this research is that u within the vegetation area can, just like for the water region, be calculated using the linear wave theory for waves propagating over an impermeable bottom.

Mendez and Losada (2004) describes the energy conservation equation for normally incident waves, for straight and parallel contours as given in equation D.8. The linear summation of the dissipation due to vegetation and due to wave breaking is an assumption, caused by the difficulty of the identification of the contribution of each term when a wave is breaking along a vegetation field. This assumption is valid when the drag coefficient $\tilde{C}_D$ in equation D.11 is calibrated (Mendez and Losada, 2004).

$$\frac{\delta E c_g}{\delta x} = -\langle \epsilon_b \rangle - \langle \epsilon_v \rangle \tag{D.8}$$

D.1.2. Wave breaking

The breaking of the waves is indicated by $\langle \epsilon_b \rangle$, while the dissipation caused by the vegetation is indicated by $\langle \epsilon_v \rangle$.
Equation D.9 uses a periodic bore to illustrate how energy dissipates in breaking waves. The equation describes the rate of energy dissipation per unit area for each bore. The energy dissipation is largely attributed to the transformation of turbulent kinetic energy from potential wave energy, which is ultimately lost to heat during wave breaking, and secondly to bottom frictional losses (Thornton and Guza, 1983).

$$\epsilon_b = \frac{\bar{f}}{4} \rho g \frac{(BH)^3}{h} \tag{D.9}$$

The dissipation for a single breaking wave of height H is multiplied by the probability of wave breaking at each height to end up with the average rate of energy dissipation. This average rate of energy dissipation per unit area is given by equation D.10 (Thornton and Guza, 1983).

$$\langle \epsilon_b \rangle = \frac{3\sqrt{\pi}}{16} \rho g \frac{B_b^3 f_p}{\gamma_b^4 h^5} H_{rms}^7 \tag{D.10}$$

with:

B_b	adjusting parameter = 1 (Mase and Kirby, 1992)
γ_b	adjusting parameter = 0.6 (Mase and Kirby, 1992)
f_b	average frequency corresponding to T_p
T_p	peak period

D.1.3. Breaking due to vegetation

By assuming a invariant Rayleigh distribution, the dissipation of waves due to the present vegetation can be determined, as described in equation D.11.

$$\langle \epsilon_v \rangle = \frac{1}{2\sqrt{\pi}} \rho \tilde{C}_D b_v N \left(\frac{kg}{2\sigma} \right)^3 * \frac{sinh^3(k\alpha h_v) + 3sinh(k\alpha h_v)}{3kcosh^3(kh)} H_{rms}^3 \tag{D.11}$$

D.2. Calculating wind forces through the forest

To be able to indicate at which location in the forest the wind forces as highest, the formulas of (Gardiner et al., 2016; Kaimal and Finnigan, 1994; Gardiner et al., 1997). The wind loads can be schematized using a quadratic drag law, as shown in formula D.12.

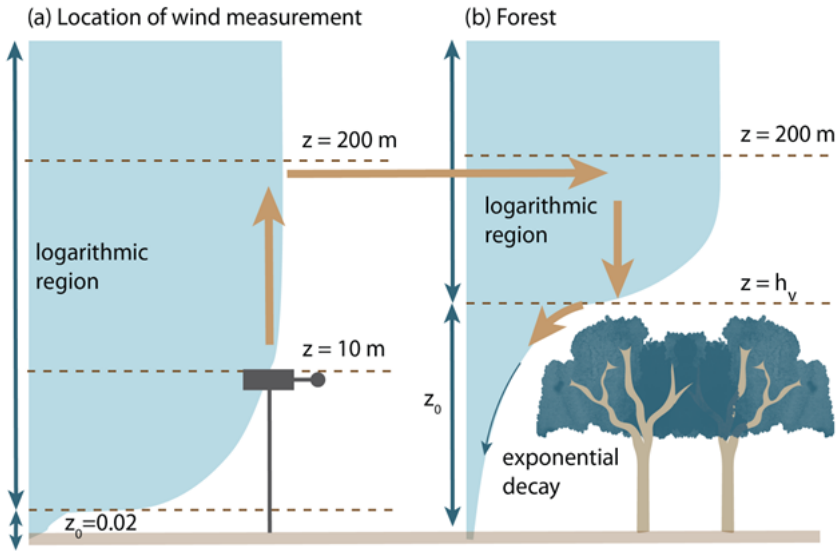


Figure D.3: Assumptions for wind velocity profile (Manchenõ, 2022)

$$F_a = \frac{1}{2}\rho_a c_{D,c} A G u_a^2 \tag{D.12}$$

with:

ρ_a	air density
$c_{D,c}$	drag coefficient for wind currents
A	frontal tree area
G	schematiz
u_a	wind speed relative to tree motion

$$u_a(z) = \frac{u*_a}{k} ln\left(\frac{z}{z_0}\right) \tag{D.13}$$

$$u_a(z) = e^{-v_e(1-z/h_v)} \tag{D.14}$$

Equation D.13 (Gardiner et al., 2016) and D.14 (Kaimal and Finnigan, 1994)are used to determine the determine the wind velocity profile. D.13 is used to determine the velocity above the vegetation, which follows a logarithmic profile over the vertical coordinate z. Equation D.14 is used for the velocity between the trees, which follows a exponential decay towards the ground.

$$G = \frac{\left(2.7193\left(\frac{D}{h_v}\right) - 0.061\right) + \left(-1.273\left(\frac{D}{h_v}\right) + 0.9701\right)\left(1.1127\left(\frac{D}{h_v}\right) + 0.0311\right)^{x/h_v}}{\left(0.68\left(\frac{D}{h_v}\right) - 0.0385\right) + \left(-0.68\left(\frac{D}{h_v}\right) + 0.4785\right)\left(1.7239\left(\frac{D}{h_v}\right) + 0.0316\right)^{x/h_v}} \tag{D.15}$$

The gust factor, G, which is shown in equation D.15, this factor shows the change in velocity profile in the x-direction of the forest (Gardiner et al., 1997).

In this analyses, the input windspeed is measured at a location without vegetation 10 m above the ground. The velocity profiles of sites with or without vegetation differ, which causes the 10 meter above ground windspeed not very useful. Therefore, the 200 meter above ground windspeed is calculated. It is assumed that 200 meter above ground, the windspeed is equal for site with or without vegetation.

E

Detailed explanation determination parameter case study Demak

E.1. Input parameters

E.2. Wave height, wave period and waterlevel

As described in chapter 2, every mangrove forest is different. Therefore, the input variables like the water depth, wave height and wave periods differ per location. Those input variables partly determine the forces on the trees. The mangrove forest located at Demak, Indonesia is used as test case.

E.2.1. Offshore wave height and wave period

During the thesis of Alferink (2022), the hydrodynamics of the mangrove forest of Demak was analysed. The results of the significant wave height and peak wave period for different return periods are indicated in table E.1.

The offshore wave data used by Alferink (2022) were obtained from two main data sources:

- Predictions by the WaveWatch III model by NOAA over the period of 2007-2019
- Measurements of Van Bijsterveldt and Bouma (2021). These measurements were done over periods between November and December in 2017 and 2018 during the NW monsoon with a wave buoy. This buoy, the WaveDroid, was located 5.5 km offshore around a depth of 12 meters.

The data from WaveWatch III is was interpolated by Alferink (2022) at the location of the WaveDroid.

R	H_{m0}	St. dev.	Lower bound.	Upper bound	T_p	Lower bound.	Upper bound.
[years]	[m]	[-]	[m]	[m]	[s]	[s]	[s]
1	2.08	0.0483	2.00	2.16	6.9	6.6	7.4
5	2.39	0.0671	2.28	2.50	7.5	7.0	7.9
10	2.47	0.0724	2.35	2.59	7.7	7.3	8.0
15	2.51	0.0749	2.39	2.63	7.7	7.3	8.1
20	2.53	0.0765	2.41	2.66	7.7	7.3	8.1
50	2.59	0.0805	2.46	2.73	7.8	7.4	8.2

Table E.1: H_{m0} and T_p with their 90% confidence interval for a storm of 48 hours and a wave threshold of 1.3m for site in Demak, Indonesia (Alferink, 2022)

E.2.2. Surge at 5.5 km offshore

Alferink (2022) also analysed the surge for different return periods. Comparing these return periods with the high water of 2009, indicated that this high water would have a higher return period than 20 years.

Return period [years]	1	5	10	15	20
Offshore waves [H_{m0}]	2.08	2.39	2.47	2.51	2.53
Surge [m]	0.63	0.68	0.72	0.74	0.76

Table E.2: Wave heights and surge levels for different return periods (Alferink, 2022)

Daily design conditions
The daily design conditions found by (Alferink, 2022) are:

- H_{m0} = 0.25 m
- T_p = 3 sec

The upper data can be used to analyse different situation and analyse which input variables are most important. The different wave periods, wave heights and water levels for each return period can be used to determine the forces in different situations.

E.2.3. Waterlevel at different location in the forest

Another important factor is the water level in at the edge of the forest. The surge due to a storm is strongly correlated with the wave height due to the fact they are often created by the same cause, a storm. Böhm (2018) measured the water level at different locations in the Demak forest. The five measurement locations, as indicated in E.3, all have a different distance from the edge of the forest. The distance from the edge of the forest is indicated in table E.4 below. As stated in the report of Böhm (2018), the data is collected over a time period of seven months, in which one storm was indicated. Although during the measurements, some loggers felt dry, the mean gives a good approximation for the average water level at near the edge of the mangrove forest.

Water level [cm]	Semarang	Bedono	Kanal	Surodadi	Tambakbulasan
Minimum	100.4	100.4	100.3	100.2	100.2
Maximum	109.8	111.9	106.8	109.9	106.5
Mean	101.4	102.9	101.1	101.9	101.0
Water level 15m offshore	77	74			

Table E.3: Range of initial water level in Demak, Indonesia between 01 Aug 2017 - 01 March 2018

Table E.4 shows the coordinates of the data collection point of the research of Böhm (2018). At these coordinates, the water depths are measured, which can be used as a reference for the initial values of the water depth

Name study site (acronym)	Coordinates (WSG84)		Approximately distance
	Latitude	Longitude	from forest edge [m]
Tambakbulasan (T)	$06°50'11.70"S$	$110°31'22.822''E$	40
Surodadi (Su)	$06°51'39.47"S$	$110°30'56.04"E$	5
Kanal (K)	$06°53'09.22''S$	$110°30'23.88"E$	25
Bedono (B)	$06°54'51.29''S$	$110°29'10.25''^{E}$	88
Semarang (S)	$06°56'01.25''S$	$110°27'51.83''^{E}$	19

Table E.4: Coordinates of datapoint-locations

The data from Böhm (2018) can be used to validate the model and the water depth at certain locations from the forest edge.

Another research on the Demak coast was done by Ervita et al. (2017). Ervita et al. (2017) analysed the difference in shoreline in Demak from 2002 till 2012. The highest high water was 238.6 cm occurring in 2009, while the lowest water happened in 2002 with a height of 3.6 cm. The mean sea level (MSL) in the period 2002-2012 was equal to 59 cm while the mean high water level (MHWL) and mean low water level (MLWL) were, respectively, equal to 99 cm and 31 cm.

E.3. Canopy width - vegeation with

	Open tree			Dense tree	
Tree height section [m]	1. 5 years old	2. 5 years old	Tree height section [m]	1. 5 years old	2. 5 years old
2.4 - 2.8	0.001	0.001	1.8 - 2.1	0.002	0.001
2.0 - 2.4	0.017	0.018	1.5 - 1.8	0.014	0.013
1.6 - 2.0	0.041	0.048	1.2 - 1.5	0.089	0.088
1.2 - 1.6	0.180	0.133	0.9 - 1.2	0.098	0.098
0.8 - 1.2	0.140	0.129	0.6 - 0.9	0.074	0.071
0.4 - 0.8	0.034	0.033	0.3 - 0.6	0.042	0.042
0.0 - 0.4	0.022	0.021	0.0 - 0.3	0.029	0.029
Total area [m^2]:	0.435	0.383		0.348	0.342

Table E.5: Frontal area of a 5 years old tree per section of height (Jerez Nova, 2022)

E.3.1. Average DHB in Demak

Appendix **??** gives the coordinates of the different areas investigated in the research of Böhm (2018).

Parameter	Location		
	Semarang	Bedono	Wedung
Depth in m (15m offshore)	0.77	0.74	0.7
Forest age in years (Google earth)	3	13	3
Mean DHB in cm (indication forest age)	6.9	11.5	7.7

Table E.6: DHB, waterdepth and age of tree test location in Demak (Böhm, 2018)

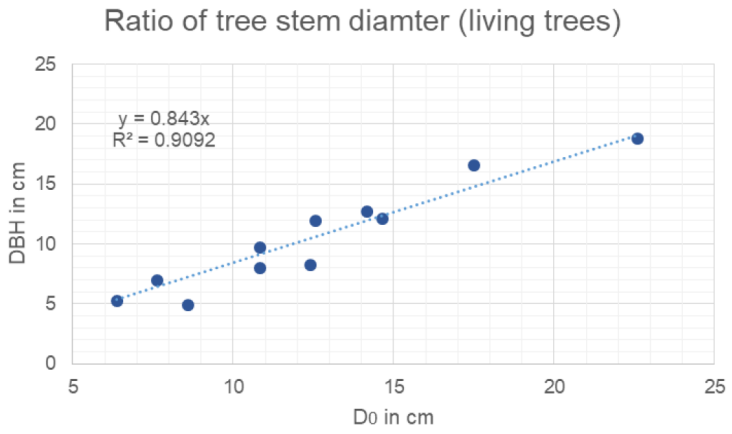


Figure E.1: Ratio between the DBH and D_0 for all living trees (Böhm, 2018)

Figure E.1 presents the different DHB's measured at Demak. These DHB's can be used to determine the above and underground biomass.

E.4. Soil properties

E.5. D_{50}

Böhm (2018) indicated the D_{50} for the three locations of Semarang, Bedono and Wedung. In the area of living trees, the D_{50} is respectively 201.68, 71.42 and 220.82 μm. While the D_{50} in the area of dead trees are respectively, 19.81, 6.26 and 7.79 μm.

Another research investigation the soil properties is done by BioManCo (2019), the most important results are shown below.



Figure E.2: Location of the sediment samples, which were collected in August 2017

E.5.1. Particle size distribution

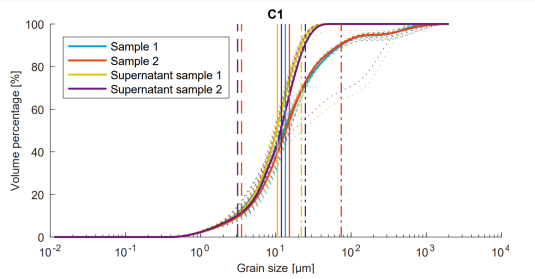


Figure E.3: Particle size distribution sample C1

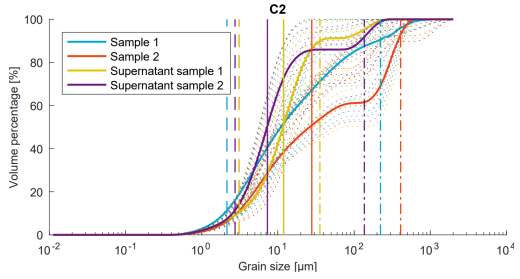


Figure E.4: Particle size distribution sample C2

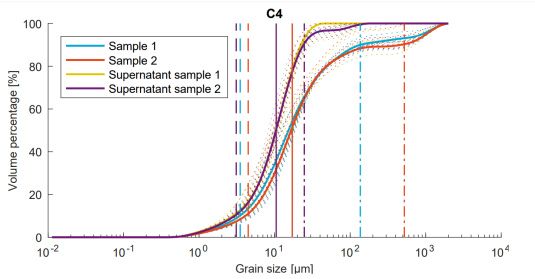


Figure E.5: Particle size distribution sample C4

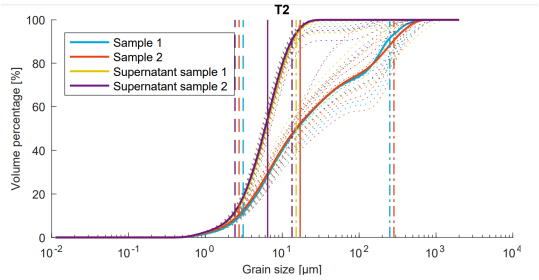


Figure E.6: Particle size distribution sample T2

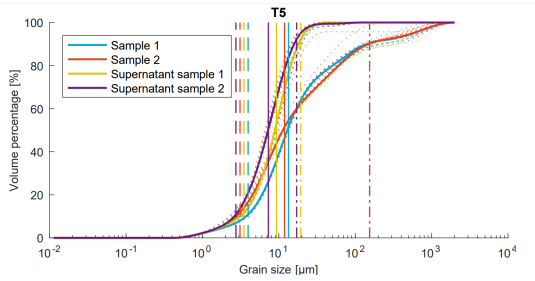


Figure E.7: Particle size distribution sample T5

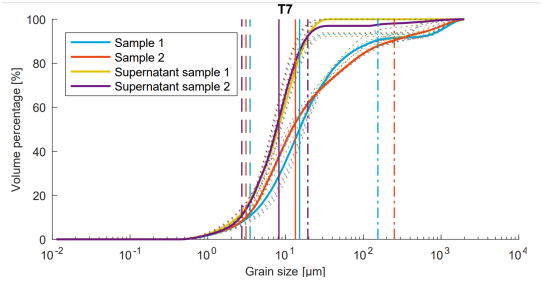


Figure E.8: Particle size distribution T7

E.5.2. Bulk density

Property	value	unit
Bulk density project area	1391.3	kg/m^3
Dry density project area	585.0	kg/m^3
Water content project area	57.94	%
Bulk density chenier	1584.1	kg/m^3
Dry density chenier	1079.44	kg/m^3
Water content chenier	31.2	%

Table E.7: Caption

The mud samples in the project area are characterised by a bulk density of 1390 kg/m3 and a dry density of 585 kg/m3. The samples collected at the chenier have a higher sand content and are characterised by a bulk density of 1580 kg/m3 and a dry density of 1080 kg/m3. The salt content of the samples turned out to be an important factor in determining the sediment concentration. Therefore, the concentrations used in this research have been corrected for salt. Shear vane measurements were conducted on mud samples, submerging the intermediate-sized vane just below the surface. Measured peak strength values varied between 58.9 and 78.6 Pa.

E.5.3. Consolidation tests

Column	K_k	n_f	k (bulk permeability)
C2.1	1.54E-12	2.6304	8.82E-04
C2.2	1.62E-13	2.6909	1.09E-01
C2.3	5.98E-13	2.6457	1.21E-02
C2.4	2.39E-12	2.6172	6.10E-02
C2.5	2.14E-12	2.6139	5.10E-02

Table E.8: Obtained values from the consolidation tests in the first time series (BioManCo, 2019)

Column	K_p [Pa] with 0% sand	K_p [Pa] with 20% sand
C2.1	3.82E+05	8.11E+05
C2.2	5.41E+08	1.63E+09
C2.3	8.00E+06	1.96E+07
C2.4	1.82E+06	4.11E+06
C2.5	2.13E+06	4.79E+06

Table E.9: Obtained values from the consolidation tests in the second time series (BioManCo, 2019)

To determine the permeability of the soil, two time series were conducted. The first time series represents the consolidation during the settling phase and during the first phase of consolidation. The second time series represents the tests using the Merkelbach and Kranenburg procedures. This test is used to determine the effective stress parameter K_p that governs Consolidation Phase II.

E.5.4. Vane shear tests

During Van shear tests, the peak strength τ_p is measured by BioManCo (2019). Below, the results of the vane shear test on multiple samples are shown. On the vertical axis of these graphs, the percentage of stress over 98.31 kPa is pictured.
The vane shear test also give the undrained shear strength, c_u. Both the mean and standard deviation of τ_p and c_u are shown in table E.10.
E.10 shows the mean and standard deviation of all the samples. The values of sample T5 and T7 is significantly higher than the rest. This can be caused by the available sediment being less, which causes the vane to be very close to touching the bottom of the breaker. Therefore, T5 and T7 were not used in further calculations. As the undrained shear strength determined in the lab is likely to be different in the field, some vane shear test are conducted in the field. The results of these tests can be found in chapter 5.2

Sample	mean τ_p [Pa]	deviation τ_p [%]	mean c_u [Pa]	deviation c_u [%]	available weight [g]
C1	72.07	3.5	50.07	4.0	581.80
C2	61.56	4.9	49.78	1.6	603.43
C4	71.53	3.0	54.40	5.8	469.19
T2	55.78	4.5	42.42	5.2	772.58
T5	217.99	6.4	154.34	9.3	318.86
T7	142.81	7.6	111.68	6.2	320.13

Table E.10: Mean and standard deviation of the undrained shear strength and peak strength of six samples (BioManCo, 2019)

Using the mass concentration, c, or dry density and the specific density, which was assumed 2650 g/l, the solid fraction, ϕ_p can be calculated:

$$\phi_p = c/\rho_s \tag{E.1}$$

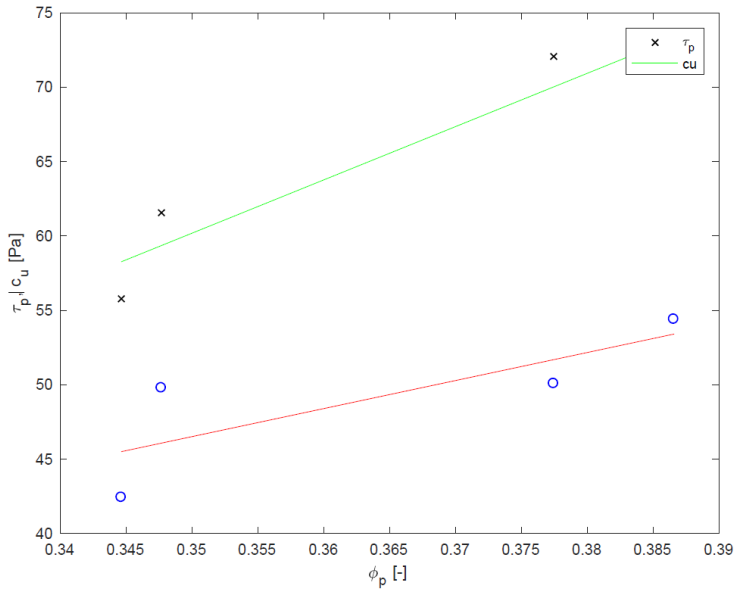
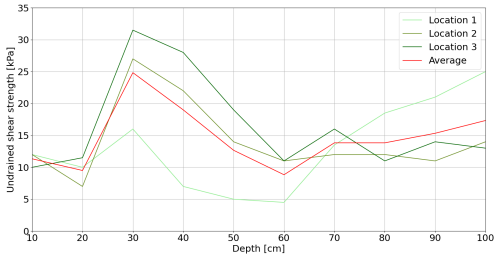


Figure E.9: Peak strength and undrained shear strength as a function of the solid fraction (BioManCo, 2019)

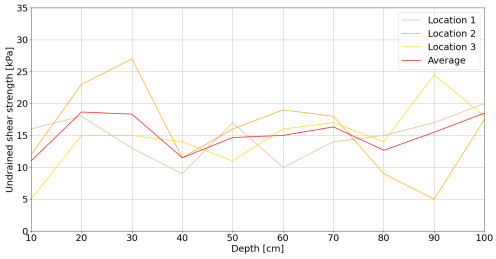
The determination of the solid fraction while working in salt water can be found in appendix E in section E.5.5

E.5.5. Salt factor determination

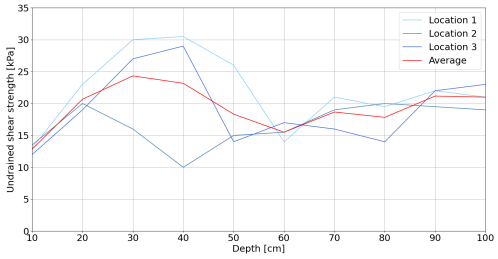
During the research of (BioManCo, 2019), the salt factor was plotted as a function of conductivity using a second order polynomial trend line. The equation of relative salt weight [per gram water] as a function



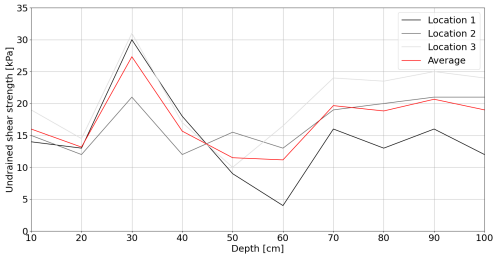
(a) Landward side - away from the trees



(b) Interior side - away from the trees



(c) Seaward side - away from the trees



(d) Interior side - nearby roots

Figure E.10: Results of the vane shear test conducted in Weg naar Zee, Paramaribo, Suriname

of the conductivity is given by this trend line. Knowing the weight of water in a sample, the weight of salt of any sample can be determine using this equation.
The conductivity of water is important in salt water. The conductivity can be measured and used to correct for the weight of salt in the sample.

E.6. Result vane shear test in Suriname

The laboratory results of the undrained shear strength seemed extremely low. Furthermore, the samples were conducted on the upper part of the soil, while the roots are located deeper into the soil. Therefore, multiple vane shear test were conducted in the Suriname. The goal was to determine whether the undrained shear strength increased over depth, and whether differences between the landward and seaward side were visible. As literature states (Maffra et al., 2019), the drained shear strength increases when roots are present. The third goal was check whether a significant increase in undrained shear strength was visible near the roots.

At the landward, interior and seaward side, three tests each were conducted away from the trees. Those tests represent the undrained shear strength without distortion of the roots. At the interior side, also three tests were conducted with distortion of the roots. The results can be found in figure E.10a, E.10b, E.10c and E.10d. The width of the forest was approximately 50 meters. Table E.11 shows the the detailed information for every test.

Location	Latitute	Longitude	Altitude	Date	Time
Landward	N 5◦553'44.53110"	W 55◦12'45.59500"	1 m a.s.l	08/09/2022	15.59
Interior - no roots	N5◦53'44.71420"	W 55◦12'45.37810"	1 m a.s.l	08/09/2022	15:22
Seaward	N 5◦53'45.74210"	W 55◦12'45.88810"	0 m a.s.l	08/09/2022	14:20
Interior - near roots	N 5◦53'44.80010"	W 55◦12'45.60080"	1 m a.s.l	08/09/2022	15.41

Table E.11: Location and time data for every test

All the graphs show an increase in the undrained shear strength around 30 cm. After digging the soil, it showed that some old fibre roots were present. Noticeable is, that also the tests away from the roots also show an increase in undrained shear strength at 30 centimeter. This could indicate that the roots

are old, and arise from dead old plants. As shown in figure E.11, the roots present are very small and fibre.



(a) Depth at which the sample is taken (Kalloe, 2022i)



(b) Picture of the soil samples, which show the fibre roots (Kalloe, 2022h)

Figure E.11: Pictures of the soil at 30 centimeter depth in Suriname

Between the three locations, no significant differences in undrained shear strength are visible. Due to the small distance between the three locations, this seems logical. As no indication is present that the undrained shear strength changes of the x-coordinate, an equal value for every x-coordinate is taken.

F

Validation of modelling

F.1. Validation Vuijk

To validate the wave transformation model, the measurements were collected at a salt marsh fringe by Vuik et al. (2016). The wave propagation through the salt marshes is modelled using the following parameters:

- H_{m0} = 0.6 m, therefore, /sqrt(2)
- T_p = 3.5 s
- Bathymetry varying between 2 and 0.5 meters
- Length of the saltmarsh equals 55 meters
- $c_{D,w}$ = 0.4
- Varying vegetation properties equal to table F.1

Section	$h_{v,mean}$ [m]	N_v [plants/m^2]	b_v [m]
S1 - S2	0.2	944	0.0030
S2 - S3	0.29	1136	0.0034
S3 - S4	0.27	1520	0.0037

Table F.1: Salt marsh properties used for the validation according to (Vuik et al., 2016)

In Figure F.1 shows that the model predictions for the situation with and without vegetation are in good agreement with the field measurements from Vuik et al. (2016). Therefore, it can be concluded that the vegetation and wave breaking module are both well implemented.

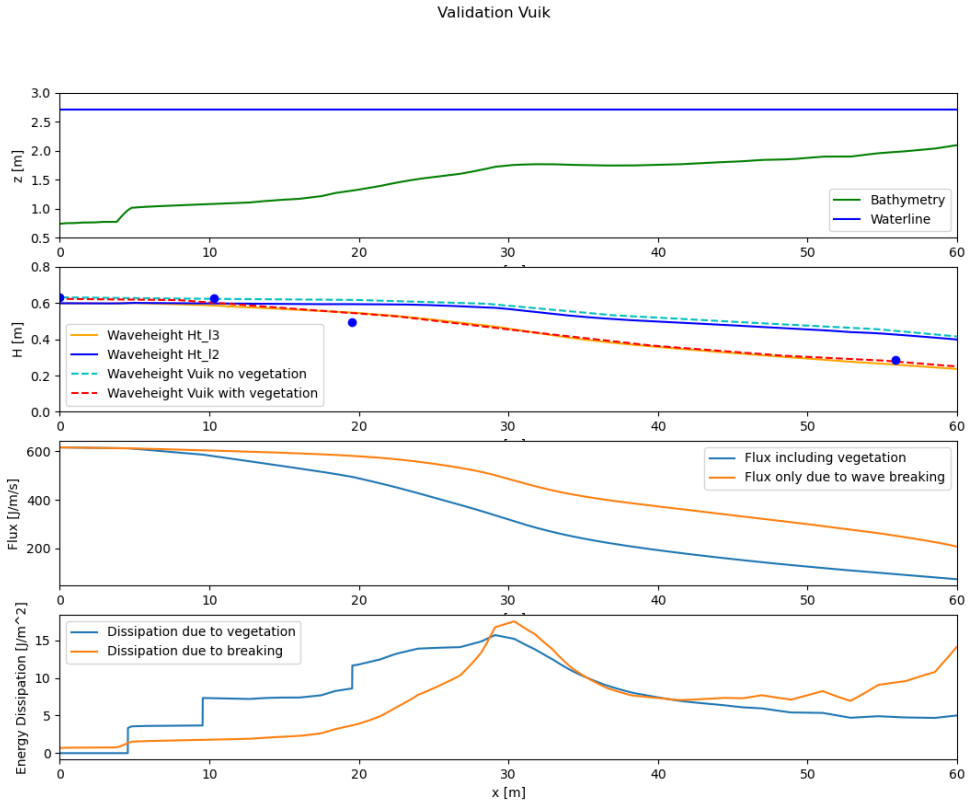


Figure F.1: Caption

F.2. Validation drag and inertia force

The part of the model which calculates the force of one wave on a certain tree is validated using a simple case with the parameters listed below. This wave condition is chosen as it is a long wave which can be easily double check by hand. As it is a very long wave, the total force will be almost equal to the drag force. So the inertia force can be neglected, caused by the fact the acceleration and thus the inertia component is small for long waves. The long wave also implies shallow water conditions, and therefore the assumption that the velocity is uniform over the vertical is valid. Which gives $u = \omega * a\ (k * d)$.
As in the above situation, the sine signal is analysed, it is assumed that $sin(\omega * t - k * x) = 1$ in formula F.1. Formula F.1 is the equation for the vertical velocity in shallow water conditions.

$$u = \frac{\omega a}{kd} \sin(\alpha x - kx) \tag{F.1}$$

- H = 0.2 m, therefore wave amplitude = 0.1 m
- T = 20 s
- waterdepth = 5 m
- vegetation width = 0.1 m
- vegetation height = 5 m
- $C_d = 1$
- $rho_w = 1000$

For the calculation the vegetation properties are assumed to be constant over the vertical. The calculations by hand would therefore give:

- Wave number is equal to 0.045
- Horizontal particle velocity is equal to 0.139 m/s
- F_{drag} = $\frac{1}{2} * \rho * 0.1 * 5 * (0.139^2)$ = 4.830 N

Figure F.2 shows max value of the drag force is equal to approximately 4.9 N. For the comparison, the maximum value of the drag force should be analysed as the assumption of $sin(\omega * t - k * x) = 1$ has been made. In the figure, it can be seen that for this point, indeed the inertia force is equal to zero. The difference with the hand calculation can be explained by the rounding of values. Therefore, the calculation is well implemented in the model.

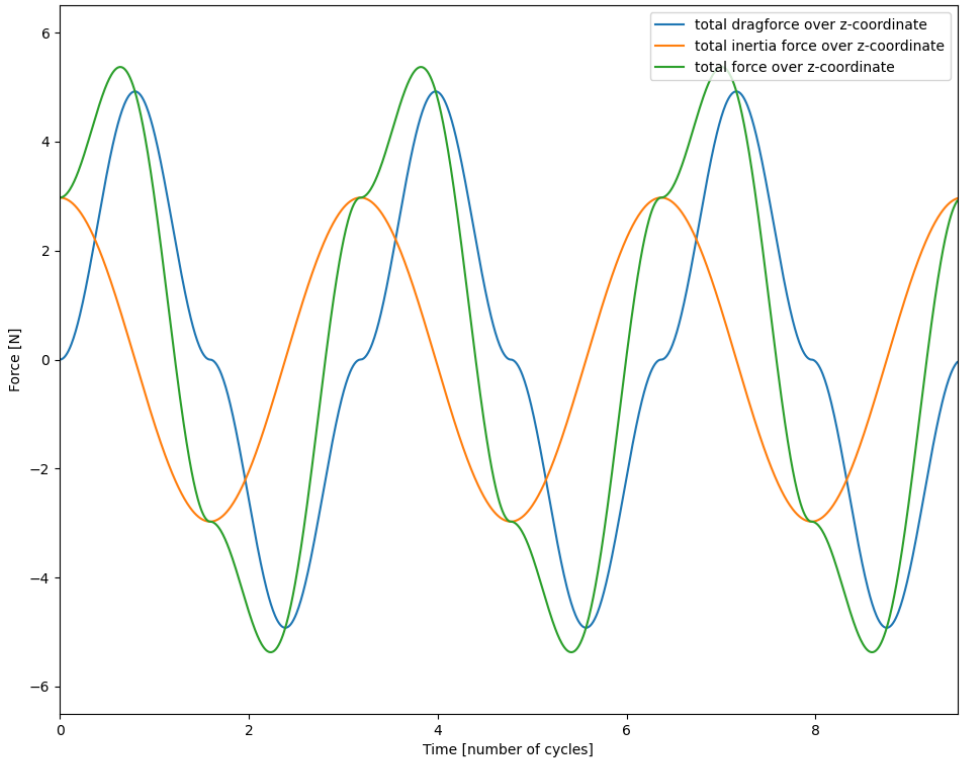


Figure F.2: Caption

F.3. Wind Validation

To validate the wind calculation, the paper of Rudnicki et al. (2004) is used. As the tests in this paper were conducted in a wind tunnel on a single row of tree, no exponential decay between the vegetation can be validated. Therefore, only the first row of the forest in the created model is compared to the results of Rudnicki et al. (2004).
In the paper multiple species are tested, for the validation, the data of the unproned pine species with a height of 1.9 meter is used. The roughness height was set equal to the height of the wind tunnel, so 2.44 meters, as in the model a exponential decay is assumed over this roughness height.

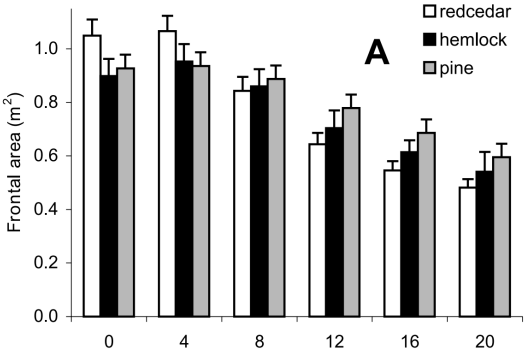


Figure F.3: Frontal area used in Rudnicki et al. (2004)

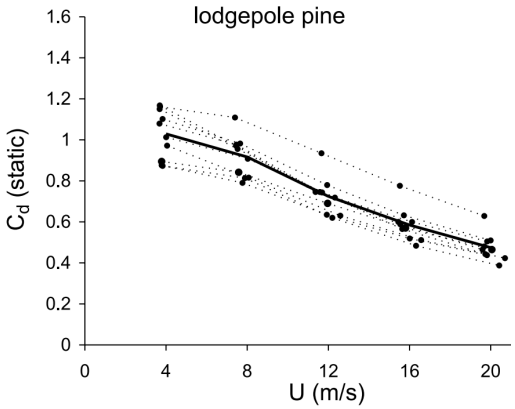


Figure F.4: Drag coefficient used in Rudnicki et al. (2004)

Wind velocity [m/s]	Frontal area [m^2]	C_d [-]
0	0.9	-
4	0.91	1.02
8	0.86	0.92
12	0.78	0.74
16	0.69	0.60
20	0.6	0.48

Table F.2: Frontal area use from Figure F.3

Using the values listed in Table F.2, the tree height and roughness height, the total force per unit area was measured. The results are shown in Figure F.5. Although some differences are displayed, the results are close enough to conclude the wind module is well implemented. Mainly, as the difference can also be explained by small mistakes by reading the input values from the graphs of the paper.

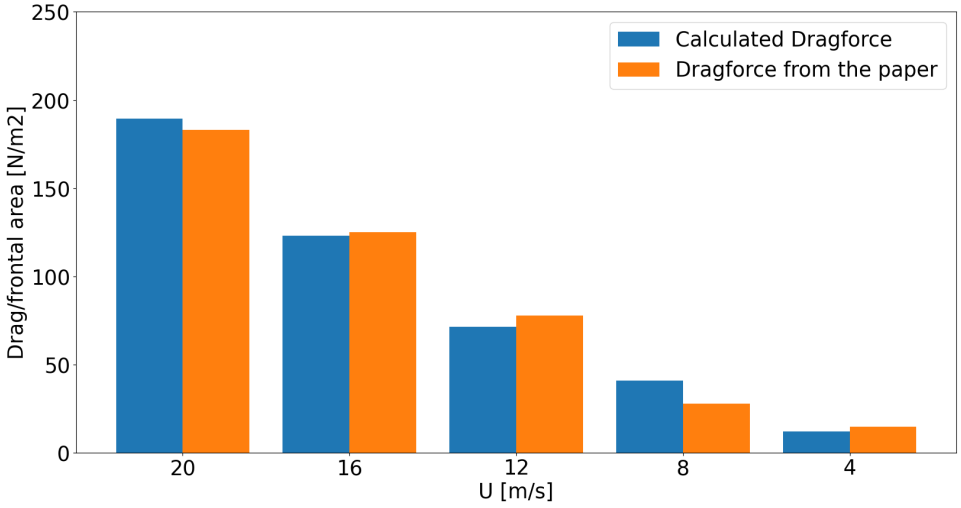


Figure F.5: Comparision between model results and the results of Rudnicki et al. (2004)

G

Extra graphs of loads

G.1. Wave forces

The following plot shows the dissipation of wave energy through the forest to the shoreline, where a waterdepth of 0.01m is reached at x = 6000m. The plot shows, from left to right, the daily conditions, return period of 1, 5, 10, 15, 20 years.

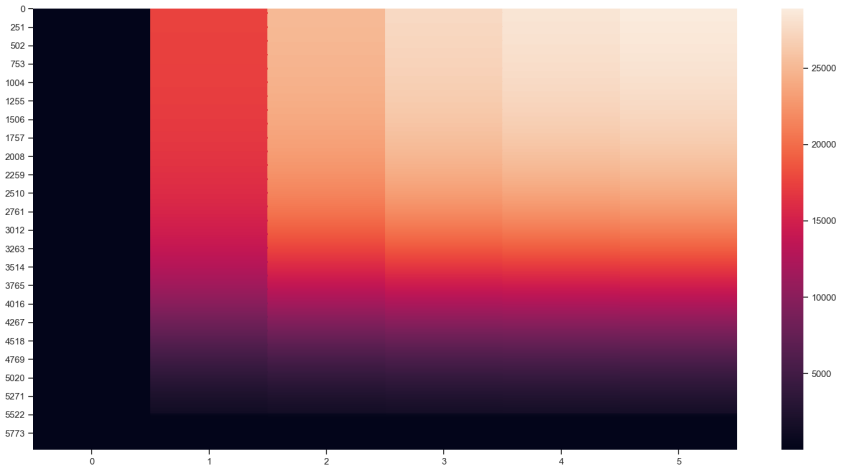


Figure G.1: Dissipation of wave energy through the forest

G.1.1. Results for daily conditions

For every return period the following graphs could be made. In this section the results of the daily conditions are shown. Figure G.2 shows the change in wave height and dissipation during daily condition. This graph also indicates the differences between the dissipation due to wave breaking and due to the interaction with vegetation. For the three locations in the foreset, as indicated in Section 5.1, the inertia, drag and total force over time are determined. Those graphs can be found in figure G.4, G.5 and G.6.

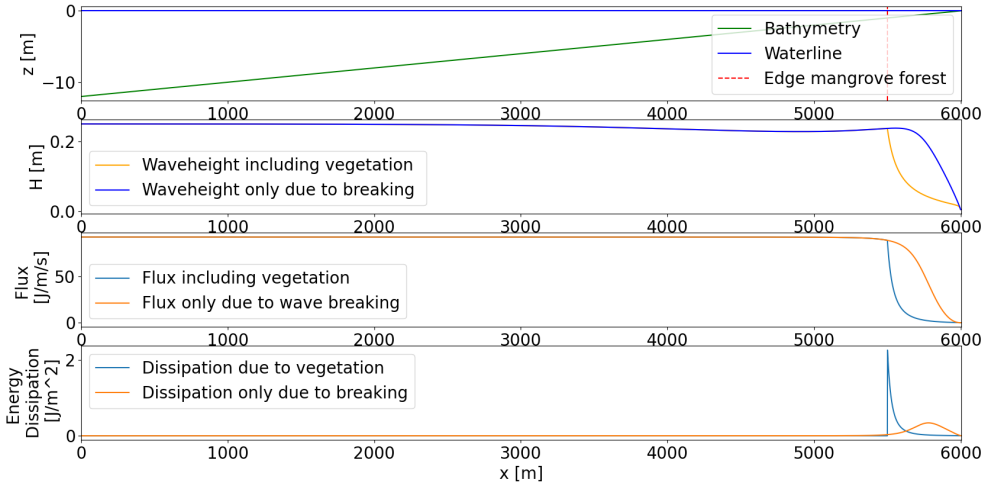


Figure G.2: The change in wave height and dissipation of wave energy through the forest for daily conditions

In figure G.3, a more detailed graph of the dissipation through the forest is shown. It can be seen that the dissipation at the edge of the forest is the largest, at the first interaction with the trees.

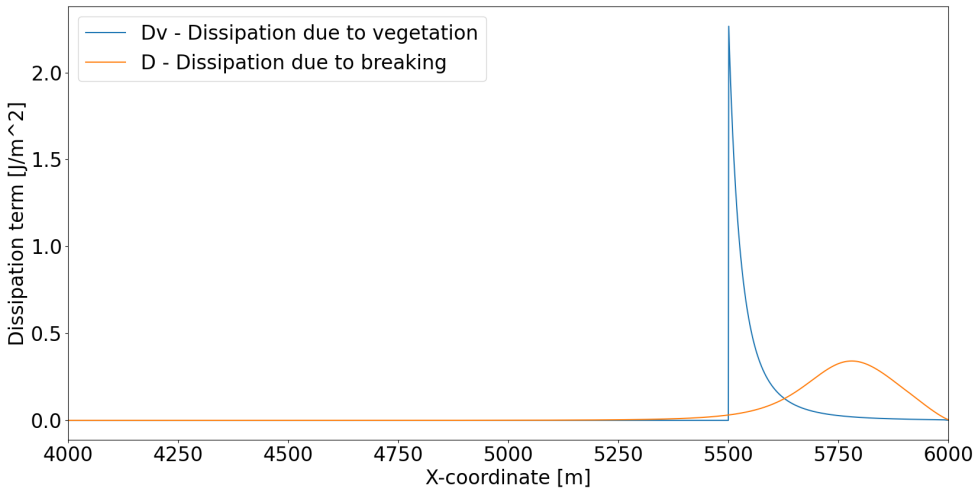


Figure G.3: Detailed representation of the dissipation of wave energy in daily conditions for daily conditions

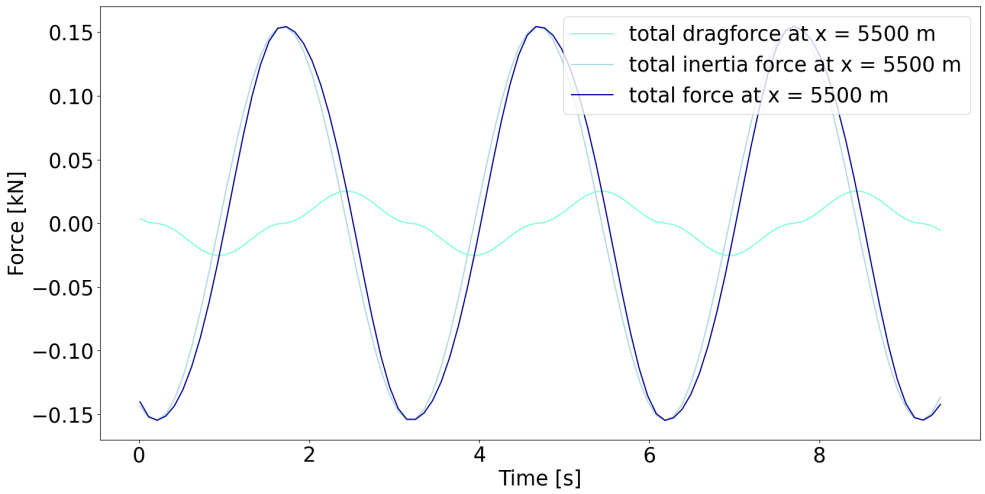


Figure G.4: Different wave force components over time at location X = 5500m, the seaward edge of the forest for daily conditions

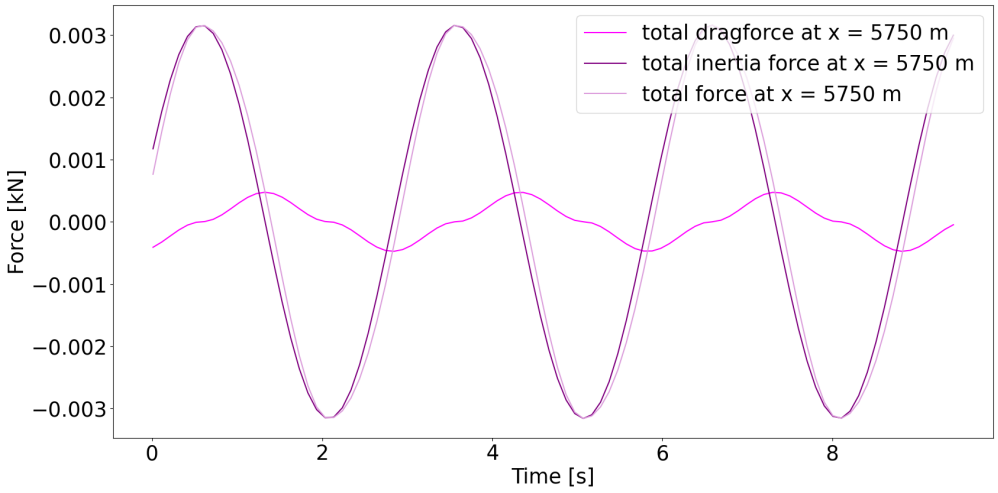


Figure G.5: Different wave force components over time at location X = 5750m, the seaward edge of the forest for daily conditions

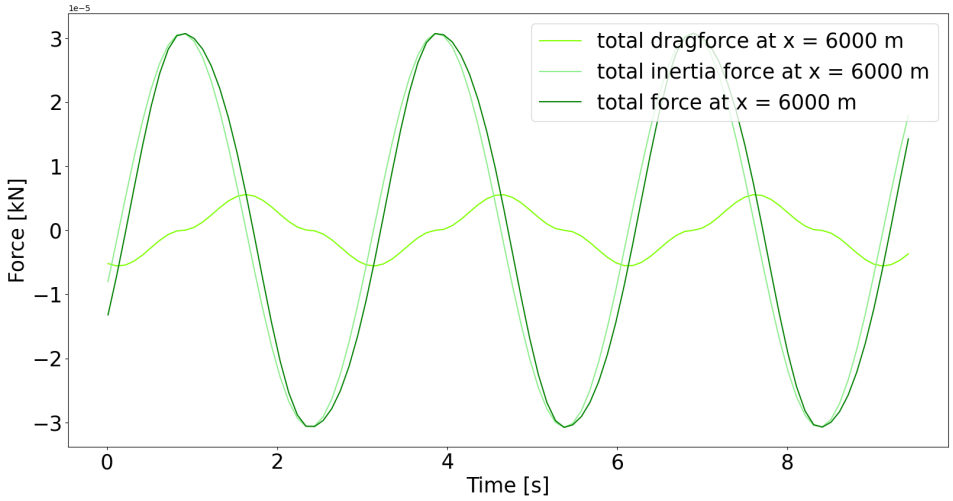


Figure G.6: Different wave force components over time at location X = 6000m, the seaward edge of the forest for daily conditions

From this graphs it can be seen that the total force decreases and the inertia components highly dominates the total wave force. Figure G.7 shows figure G.4, G.5 and G.6 combined, which nicely shows the decreasing wave force towards the landward site of the forest.

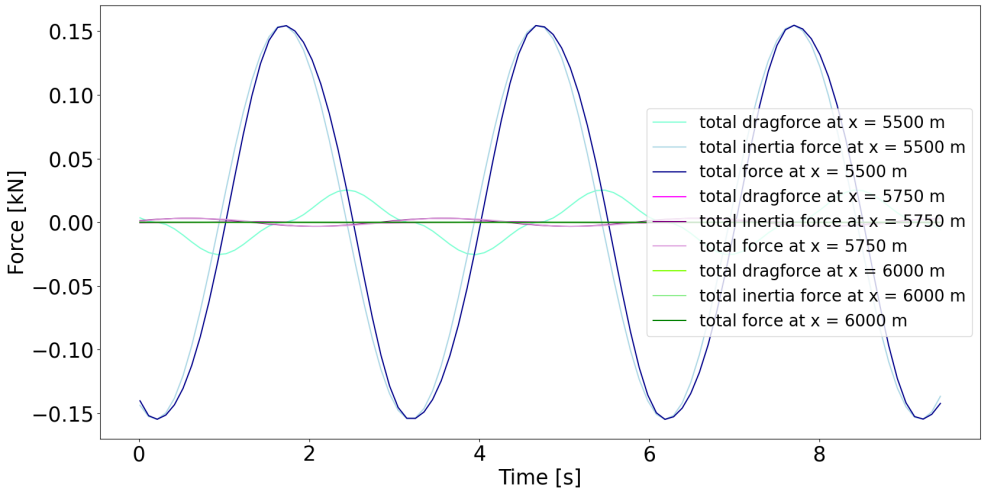


Figure G.7: Different drag and inertia components of the wave force throughout the forest during daily conditions

When the waves are in intermediate wave conditions the velocity differs over the water depth. For shallow wave conditions the velocity stays equal over the vertical. Combined with the fact that the width of the vegetation differs over the vertical, the wave force differs over the vertical. This is shown in figure G.8. The graph shows at x-coordinate indicated what will be the force per meter over the vertical. The force indicated in the graph is the total force on the area (width of vegetation times dz) divided by the Δz.

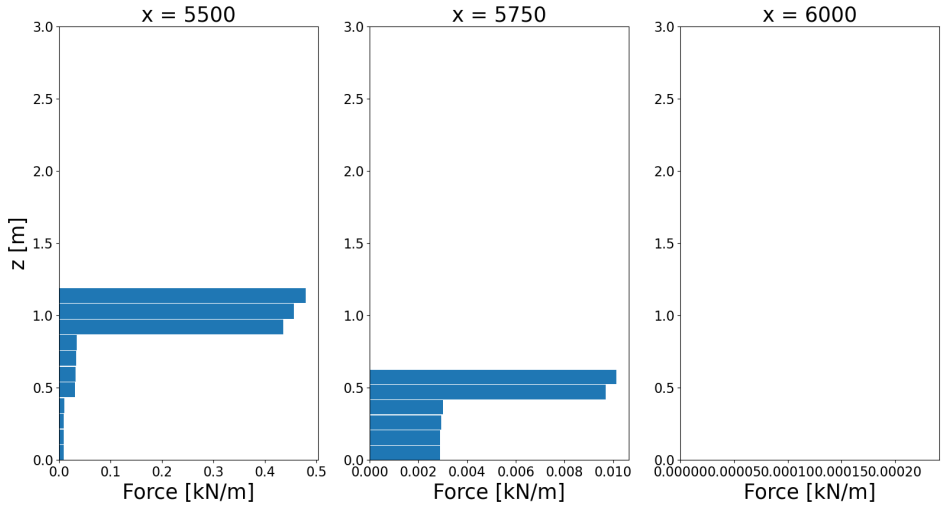


Figure G.8: Wave forces over the z-axis at different locations in the forest for daily conditions

G.1.2. Extra results for a return period of 20 years

This section will show some detailed graphs for a return period of 20 years. First, the decrease in wave height and dissipation due to the wave breaking and interaction with vegetation is shown in figure G.9 and G.10. Secondly, Figure G.11, G.12 and G.13, are a detailed representation of the total force at different locations of the forest, while figure G.14 shows the three locations all together. From these graphs it can be seen that for a larger waterdepth the drag component of the total force becomes more important.

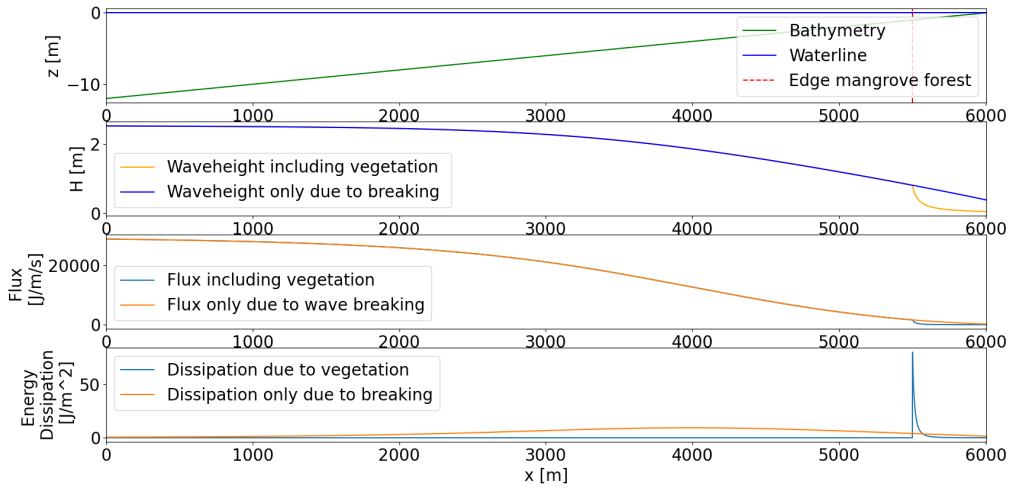


Figure G.9: The change in wave height and dissipation of wave energy through the forest for a return period of 20 years

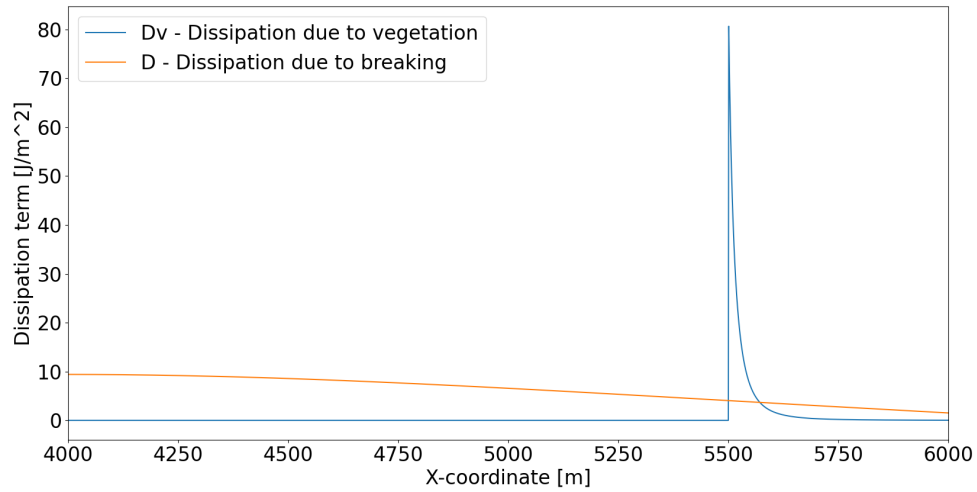


Figure G.10: Detailed representation of the dissipation of wave energy in daily conditions for a return period of 20 years

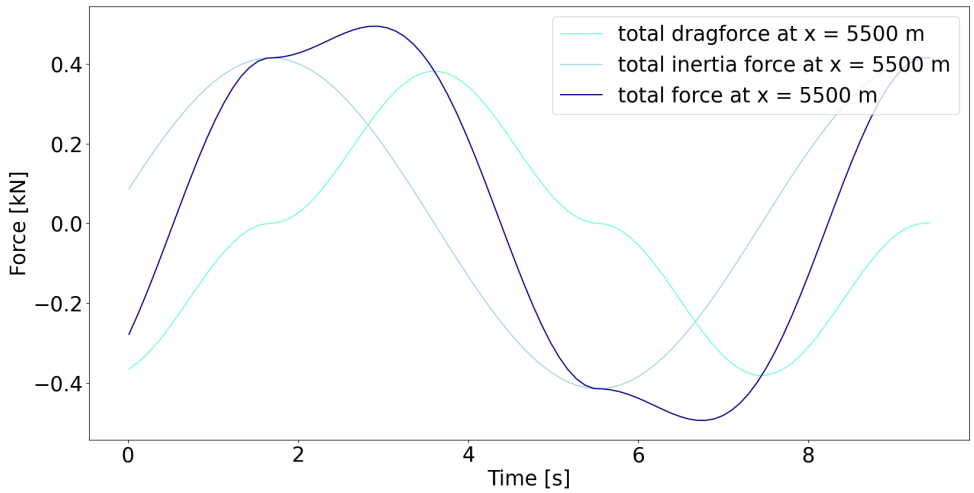


Figure G.11: Different wave force components over time at location X = 5500m, the seaward edge of the forestfor a return period of 20 years

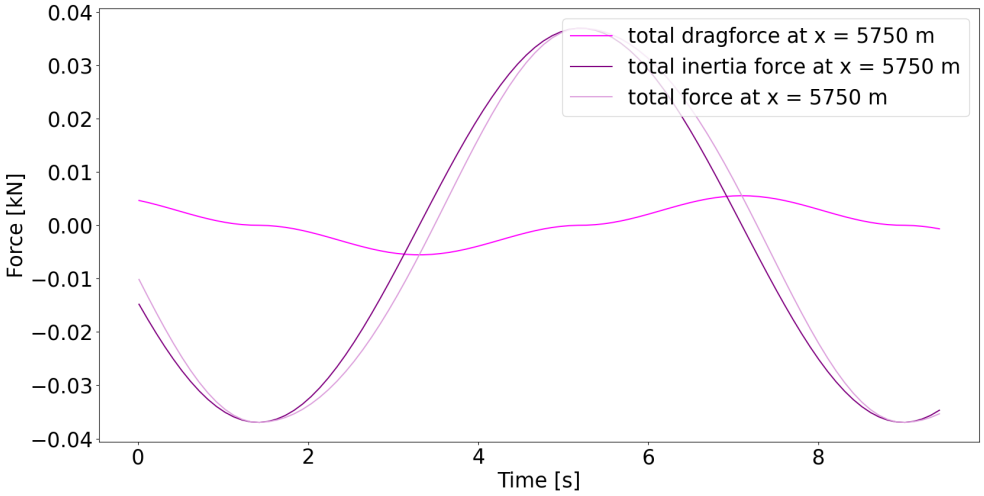


Figure G.12: Different wave force components over time at location X = 5750m, the seaward edge of the forest for a return period of 20 years

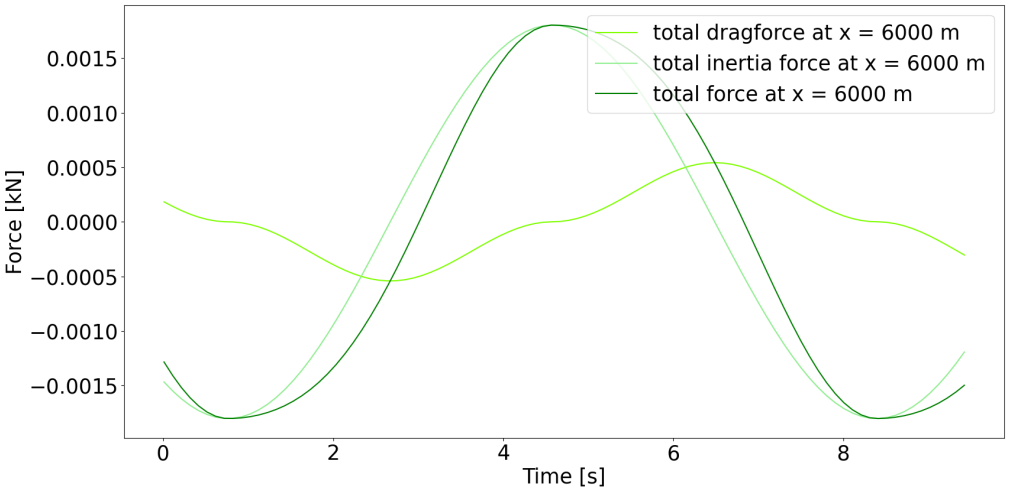


Figure G.13: Different wave force components over time at location X = 6000m, the seaward edge of the forest for a return period of 20 years

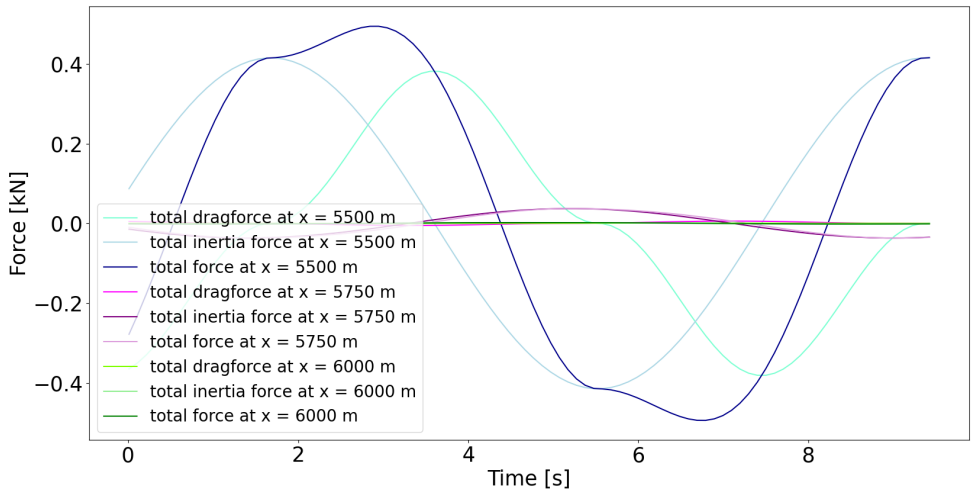


Figure G.14: Different drag and inertia components of the wave force throughout the forest for a return period of 20 years

Figure G.15 shows the wave forces over the vertical for three different location of the forest. At the seaward edge of the forest, x=5500, the waves are still in intermediate conditions, which can be seen from the decrease in force while the vegetation width stays equal. At the intermediate and landward location, the waves are in shallow conditions, shown by the constant force when the vegetation width stays equal.

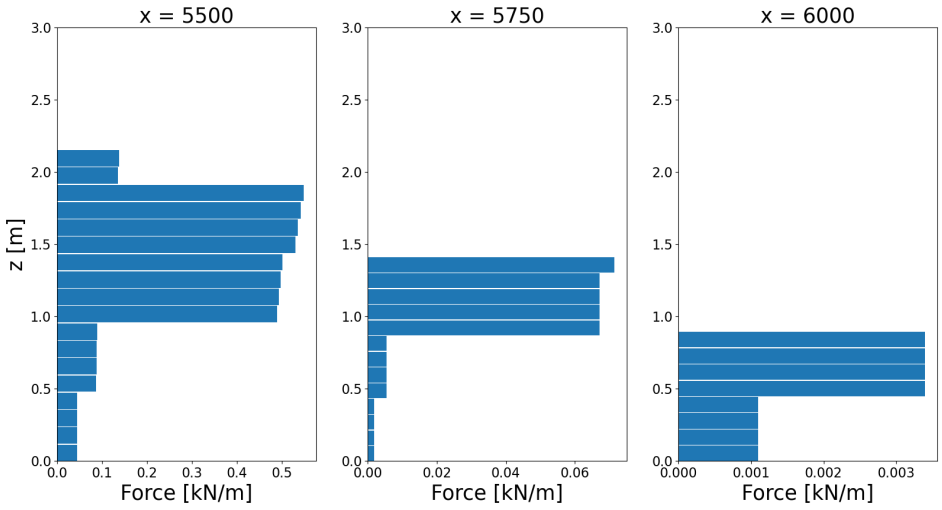


Figure G.15: Wave force at tree different locations during conditions with a return period of 20 years

G.1.3. Total wave force for different return periods

Figure G.16, G.17 and G.18 show the total wave force for different return periods. From this graph it can be seen that for every return period, the contribution of the drag- and inertia force is different in the total force. It should also be noted that the difference in total force between the conditions for a return period of 10, 15 and 20 years is relatively small.

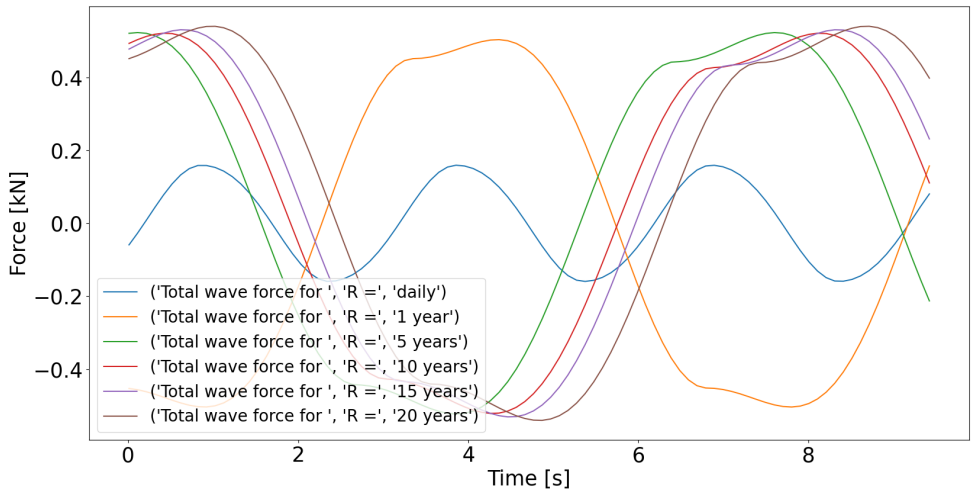


Figure G.16: Total wave force for different return periods at the seaward edge of the forest

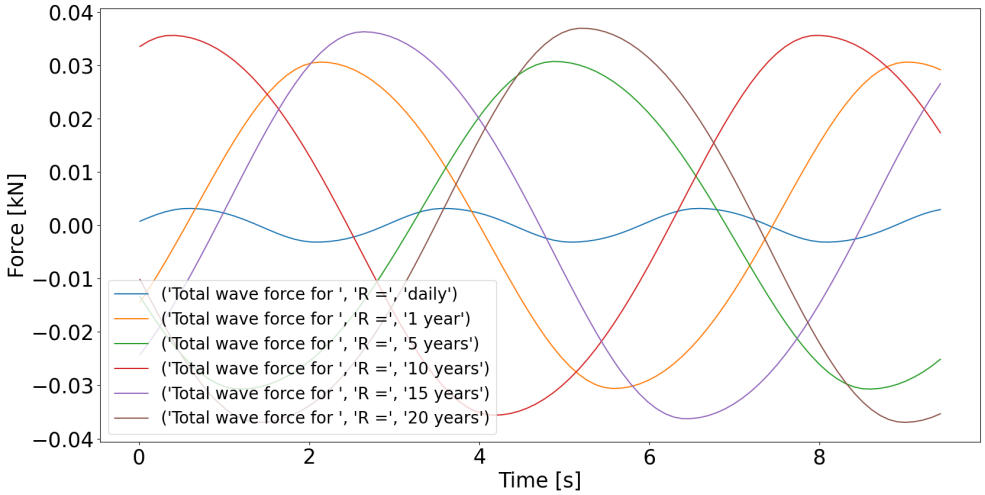


Figure G.17: Total wave force for different return periods at the interior of the forest at X=5750

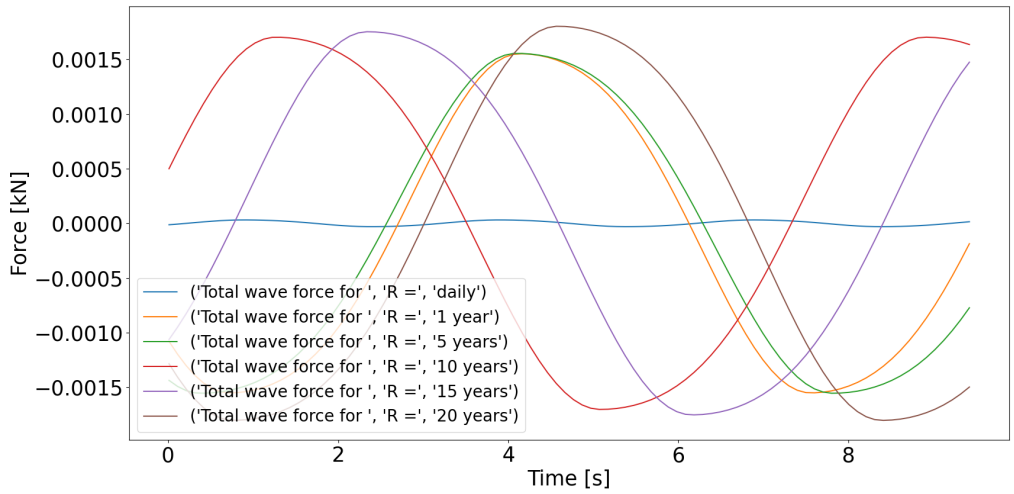


Figure G.18: Total wave force for different return periods at the landward edge of the forest

G.2. Wind forces

Table G.1 shows the calculated wind velocities at different locations and for different return periods.

Return period	Daily conditions	1 year	5 years	10 years	15 years	20 years
measured velocity [m/s]	3.73	18.23	19.97	20.40	20.61	20.71
velocity: z = 200m [m/s]	5.52	27.02	29.59	30.23	30.54	30.70
velocity: z = h_v [m/s]; x = 5500	2.31	10.73	11.71	11.92	12.01	12.05
velocity: z = h_v [m/s]; x = 5750	2.38	11.22	12.24	12.47	12.58	12.62
velocity: z = h_v [m/s]; x = 6000	2.44	11.59	12.65	12.90	13.02	13.07

Table G.1: Wind velocities of different return periods

G.2.1. Wind force over the vertical for daily conditions and a return period of 20 years

Figure G.19 and G.20 show the wind force over the vertical of a tree at four different locations. The first row of trees on the seaward side of the forest are subjected by a wind velocity with an logaritmic decay, while the trees below experience a exponential decay. This causes the difference between the force at x = 5500 and x = 5502. Figure G.21 shows the velocity profile of the conditions with a return period of 20 years. In this figure, the difference in wind velocity between x = 5500 and x = 5502 is clearly visible. Also, it can be noted that the increase in wind velocity is small. This is caused by the gust factor only increasing slightly after x = 5550 meter, shown in Figure G.25.
Secondly, for daily conditions a larger part of the tree is exposed to the wind at the seaward edge of the forest, due to the surge created by the storm conditions with a return period of 20 years.

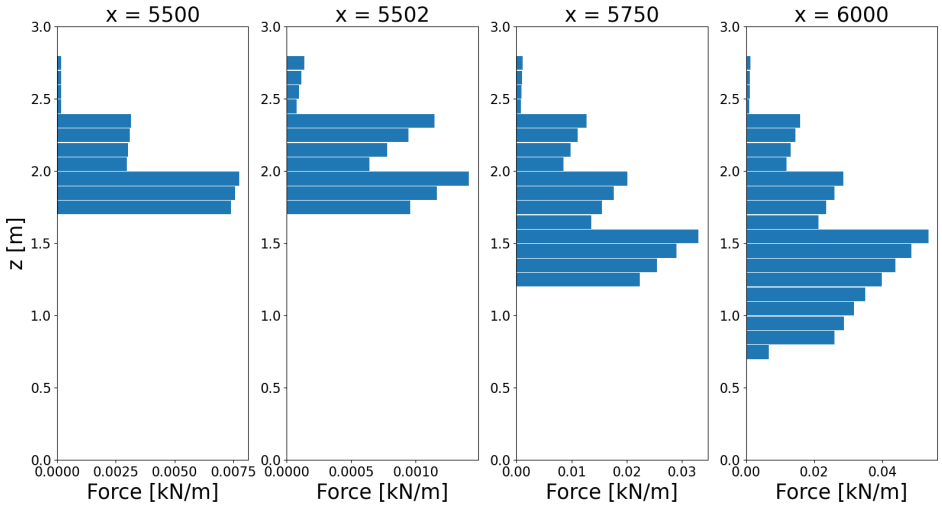


Figure G.20: Boxplot of the wind force for different location in the forest for conditions with a return period of 20 years

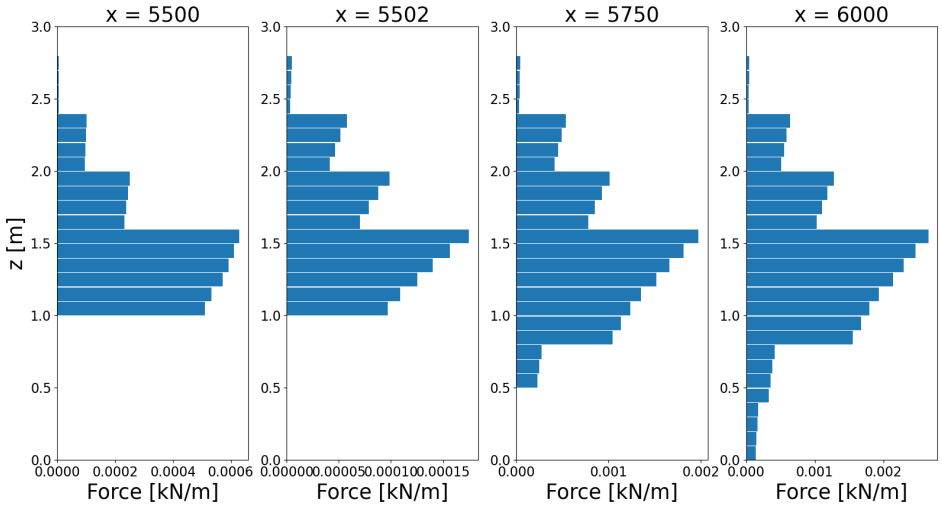


Figure G.19: Boxplot of the wind force for different location in the forest for daily conditions

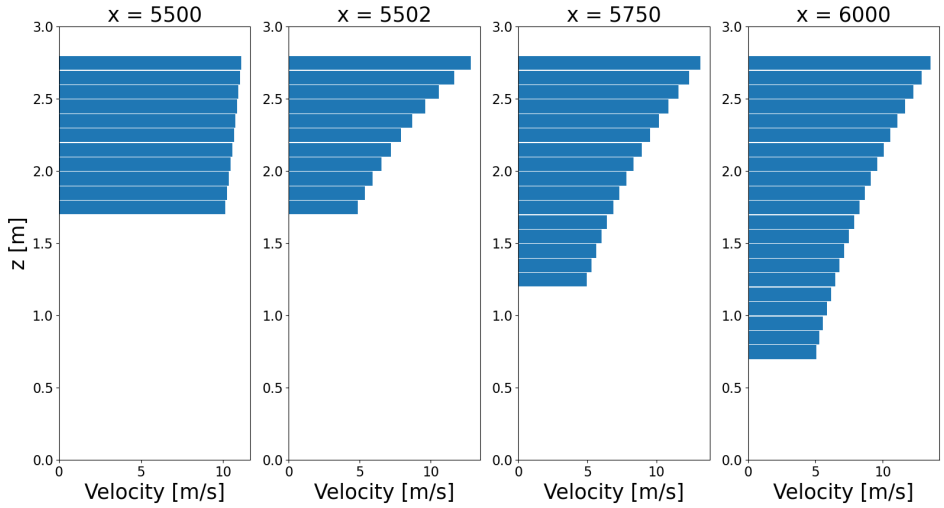


Figure G.21: Wind velocity profile of different locations of the forest for conditions with a return period of 20 years

Figure G.22 shows the total wind force through the forest for different return periods. Again, it can be observed that the differences in larger return periods are small.

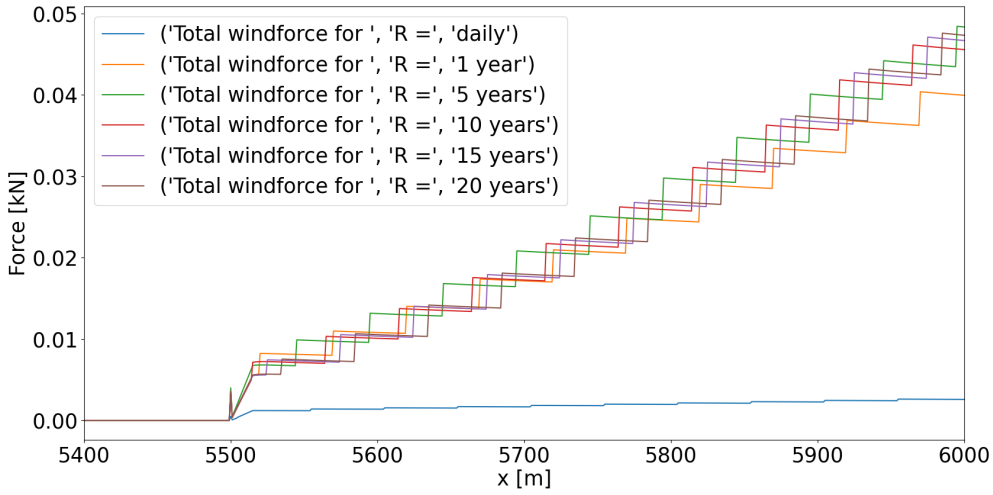


Figure G.22: The wind force through the forest for different return periods

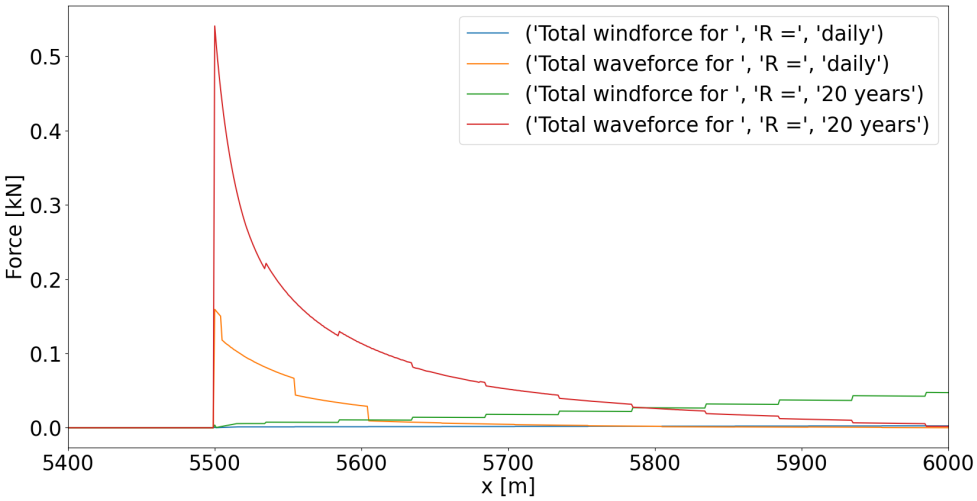


Figure G.23: Wind and wave force for a return period of 20 years and daily conditions

G.3. Gust factor

The gust factor influences the increase in wind force through the forest. As the DBH through the forest stays relatively constant, no changes in tree height are added to the model. Therefore, the gust factor with constant tree height is used in this thesis. Without using a transition zone, the forces between the first row of trees and the second row of trees is large, with is quite unrealistic. The different length of transitionzones can be seen in Figure G.25, for this thesis a length of 15 meters has been chosen.

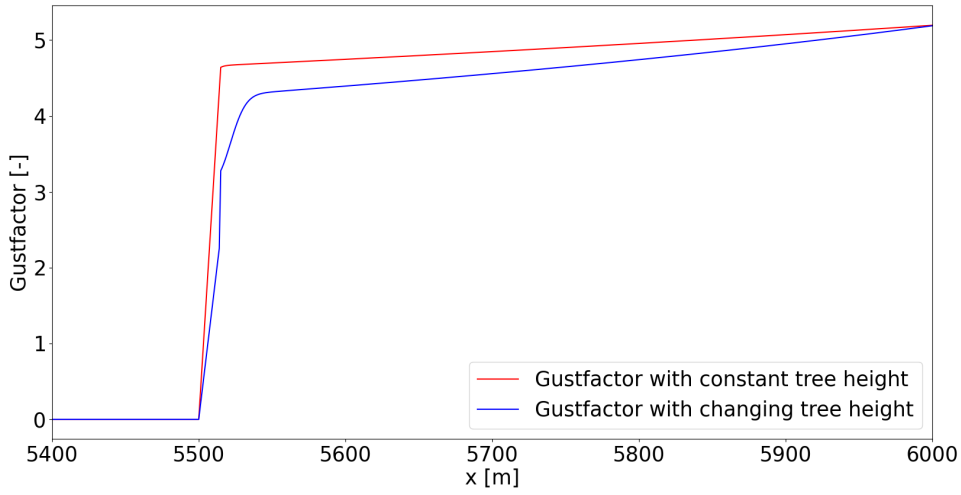


Figure G.24: Differencee in gust factor by using a constant or changing tree height through the forest

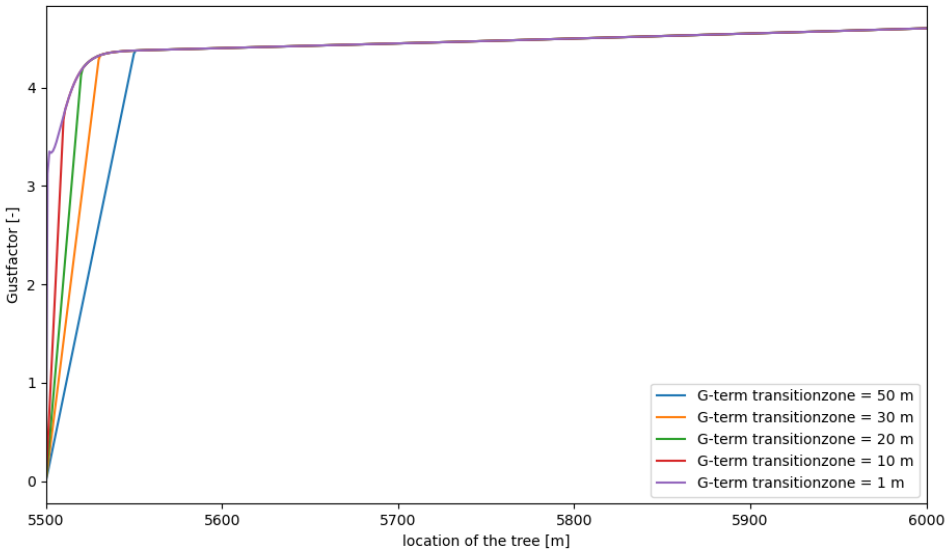


Figure G.25: Different transitionzones for the gust factor

G.3.1. Total force

Figure G.26 shows the total force due to wind and waves for the different return periods. Again, showing the small difference between the larger return periods.

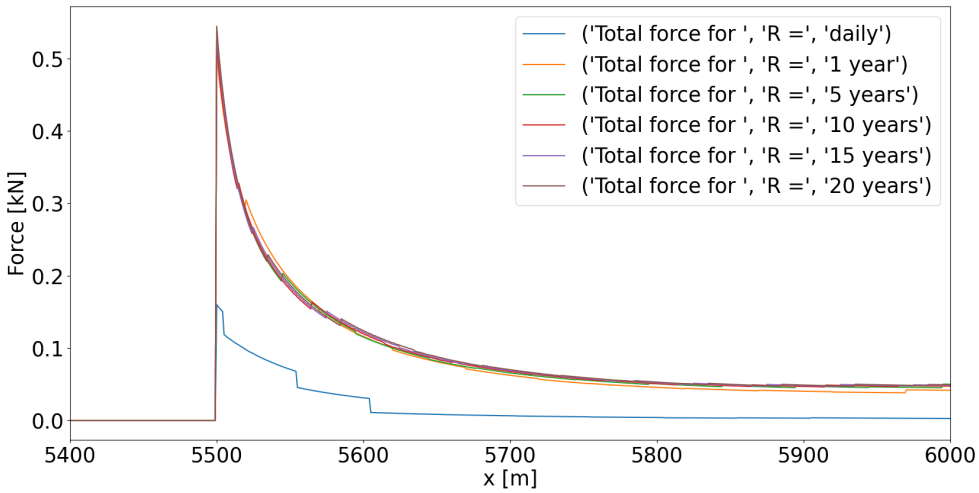


Figure G.26: Total force for different return periods

Figure G.27 shows the contribution of the wind and wave force in the total force for a return period of 20 years. At the seaward edge the wave force dominates the total force, while at the landward edge the wind force controls the total force. Comparing Figure G.27 with Figure G.28, it can be noticed that the point were the moment caused by the wind governs the total moment lies more seaward compared to the force.

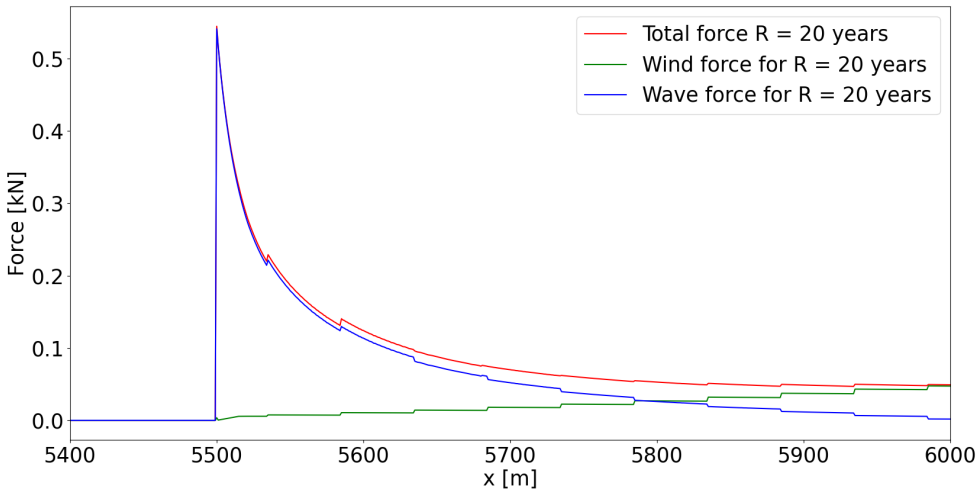


Figure G.27: Total force cause by the wind and de waves for a return period of 20 years

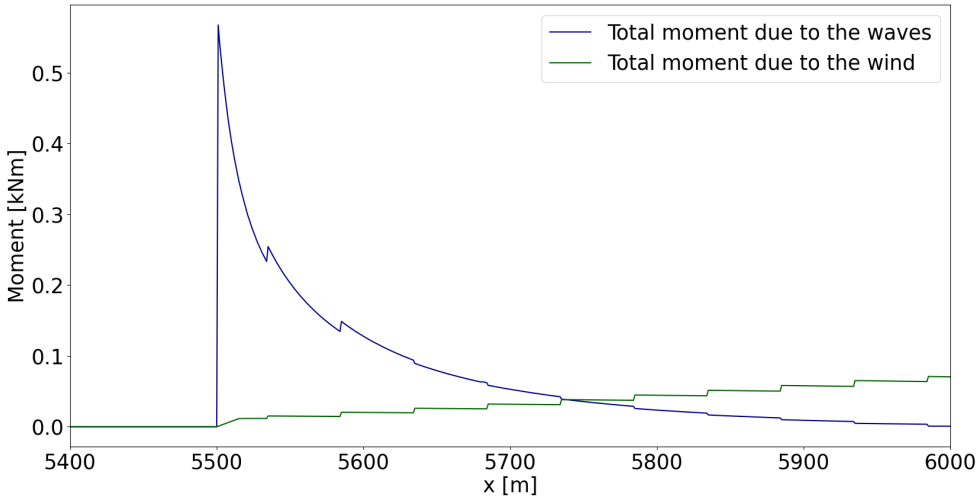


Figure G.28: Total moment cause by the wind and de waves for a return period of 20 years

G.3.2. Extra results for the increase of tree height

As explained in section 5.1.2, when the tree height increase the wind force increases. Figure G.29 shows the increasing wind force for a return period of 20 years for different tree heigths. Figure G.30 the same values, only for three tree heights.

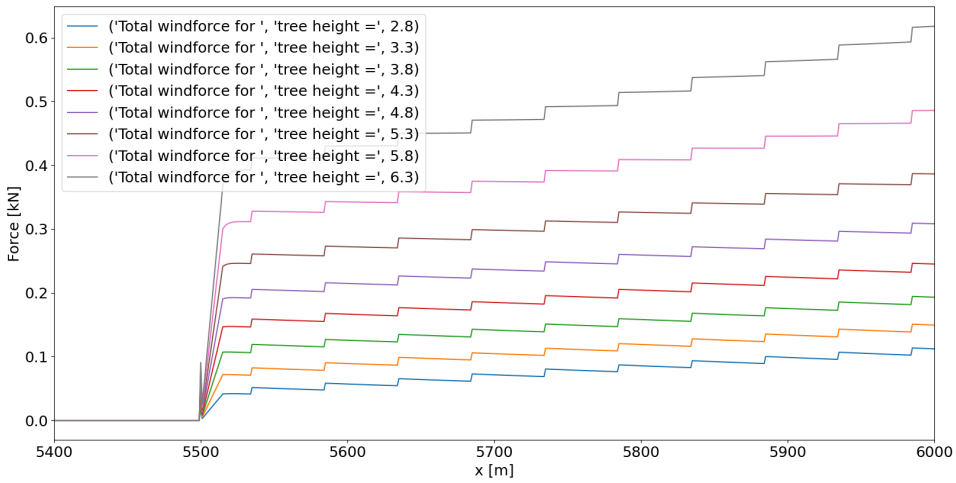


Figure G.29: Wind force during conditions with a return period of 20 years for different tree heights

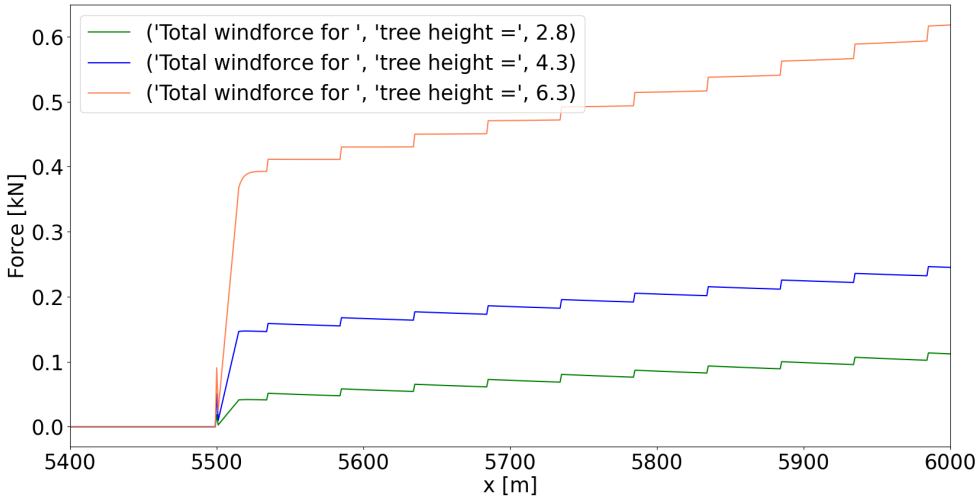


Figure G.30: The wind force for 2.8, 4.3 and 6.3 meter trees during the conditions with a return period of 20 years

The total force and total moment, as well as the wind and wave contribution is given in Figure G.31 and G.32, respectively. In both graphs, the maximal value occurs at the landward edge of the forest.

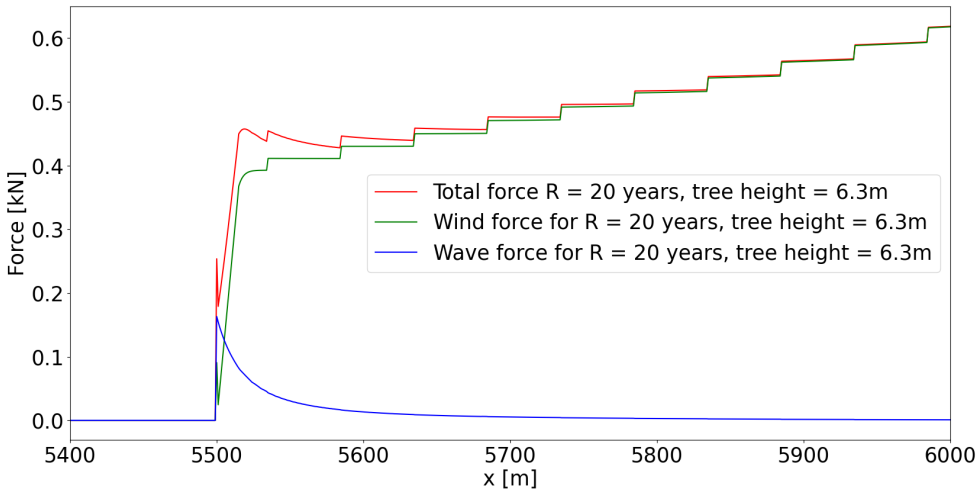


Figure G.31: Contribution of wind and wave force in total force for a return period of 20 years with a tree height of 6.3m

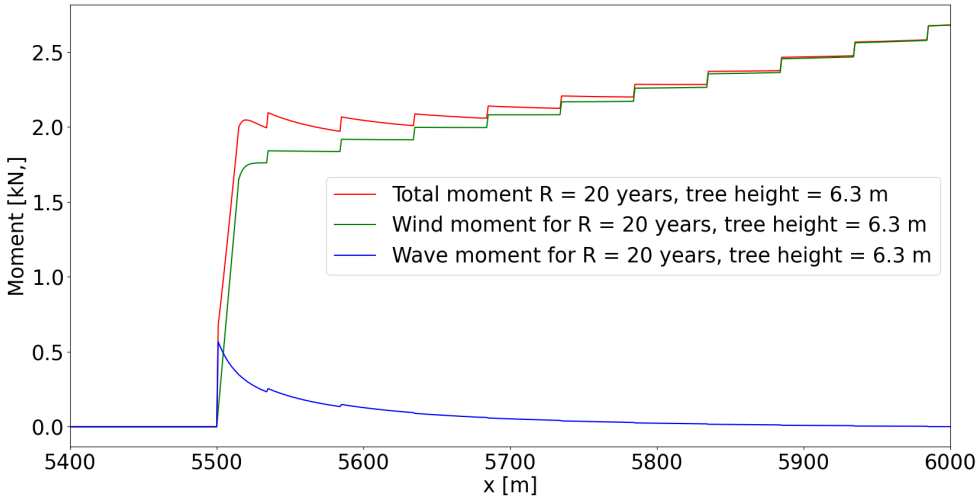


Figure G.32: Contribution of wind and wave force in the total moment for a return period of 20 years with a tree height of 6.3m

Figure G.33 shows the wind and wave moment of different tree heights. The figure clearly shows the large increase in the moment caused by the wind, which is significantly larger than the decrease in the moment origining from the wave force.

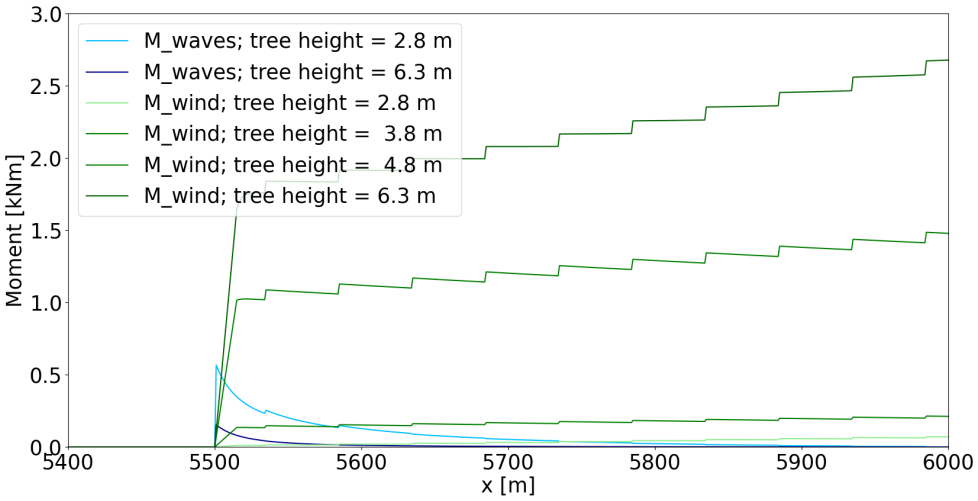


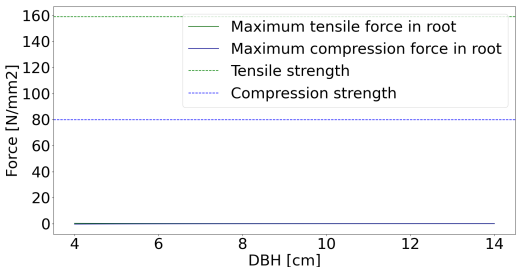
Figure G.33: Wind and wave moment for different tree heights

H

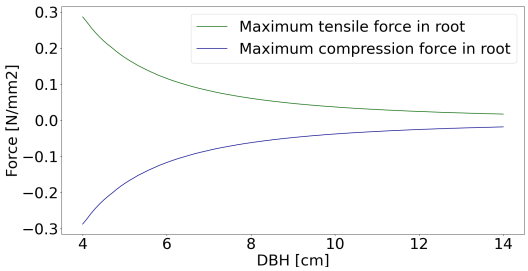
Detailed results resistance modelling

H.1. Breakage

The three graphs below show that the DBH, the root length and the external force do influence the resistance against breakage. Only, figure H.1a, H.2a and H.3a shows that compared with the compression and tension strength, this influence is negligible.

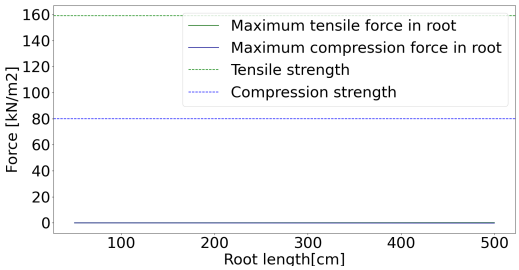


(a) Relationship with the tension and compression strength indicated

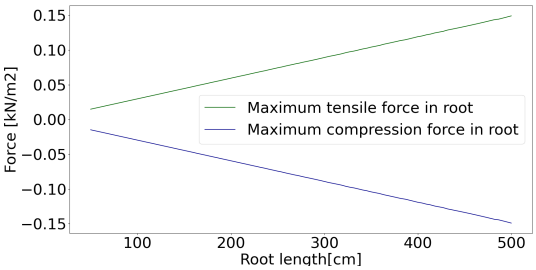


(b) Relationship without the tension and compression strength indicated

Figure H.1: Relationship between the resistance against root breakage and the DBH

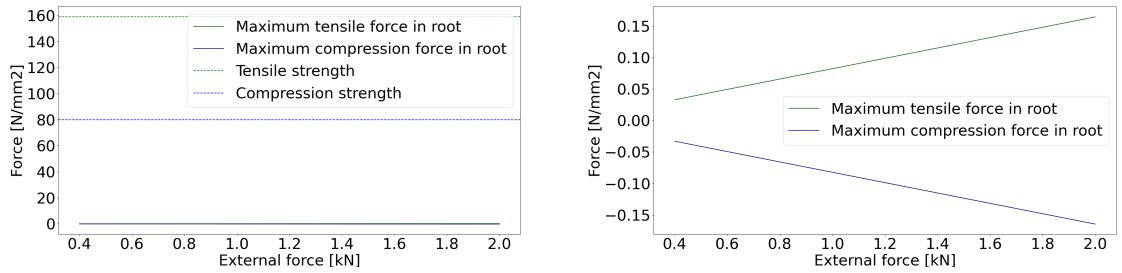


(a) Relationship with the tension and compression strength indicated



(b) Relationship without the tension and compression strength indicated

Figure H.2: Relationship between the resistance against root breakage and the root length



(a) Relationship with the tension and compression strength indicated (b) Relationship without the tension and compression strength indicated

Figure H.3: Relationship between the resistance against root breakage and the external force

H.2. Slippage

In figure H.4 and H.5 the relationship between the resistance against slippage and, respectively, the bonding strength and the diameter is shown. From both it can be concluded that they do influence the resistance against slippage, but in both situation the roots will not go into failure. Only if the value of the soil-bonding strength becomes below $0.001kPa$ the resistance becomes less than the force, which is unrealistic. For the diameter, the system only goes to failure when no roots are present due to the large diameter. This is caused by the fact the model determines the number of roots by the total rootsystem volume and the volume of a single root. When the volume of a single root becomes significantly higher than the belowground volume dependent on the DBH, the model gives zero roots, causing the system to go to failure. So this failure is caused by model limitations.

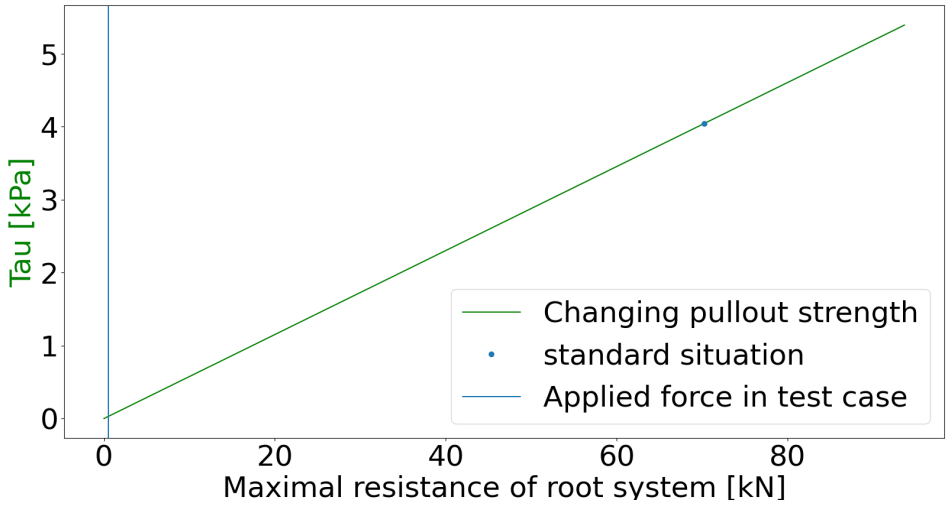


Figure H.4: Relationship between τ and the maximum resistance against slippage

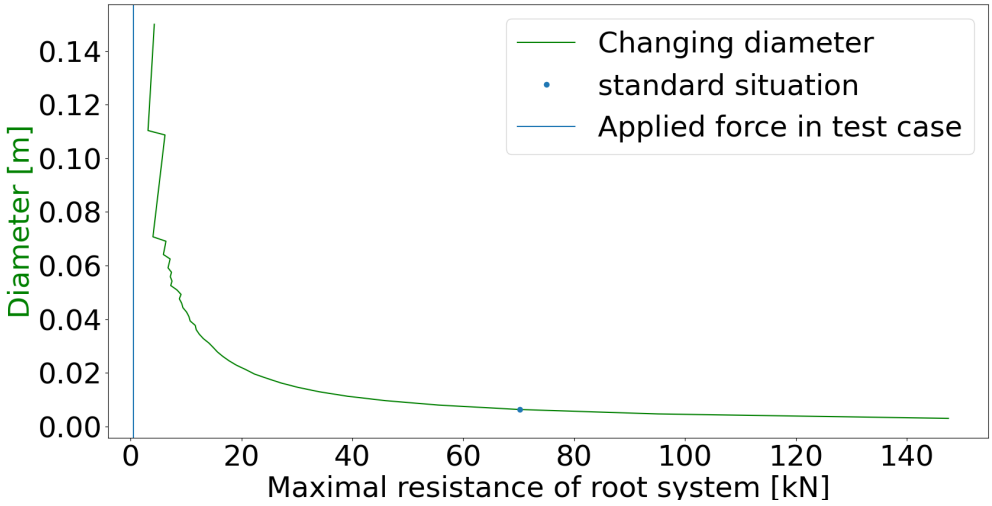
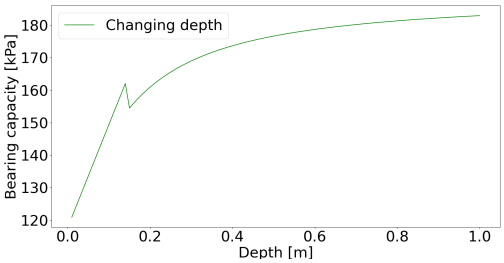


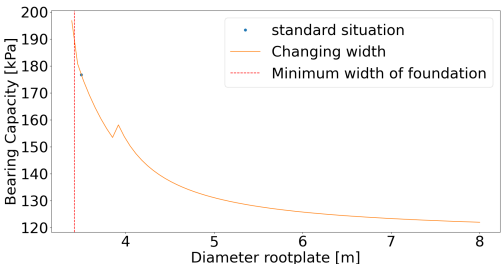
Figure H.5: Relationship between the root diameter and the maximum resistance against slippage

H.3. Shallow foundation

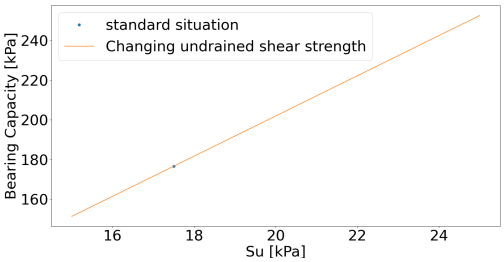
In Figure H.6, the relationship between different influence factors and the bearing capacity of the shallow foundation is given. Although, those factors do influence the bearing capacity, the bearing capacity stays way larger than the needed bearing capacity.



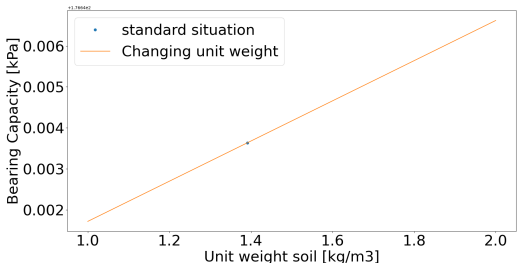
(a) Relationship between the depth of the shallow foundation and bearing capacity



(b) Relationship between the rootplate diameter of the shallow foundation and bearing capacity



(c) Relationship between the undrained shear strength and bearing capacity of the shallow foundation



(d) Relationship between the unit weight of the soil and bearing capacity of the shallow foundation

Figure H.6: Relationships between the bearing capacity of the shallow foundation and different influence factors

H.4. Uplift

H.4.1. Equal root length and diameter

The length does influence the stress inside the root and whether the root uplifts or not. In Figure H.7, this relationship is shown. The root inside Figure H.7 has a diameter of 6.3 mm, and does not uplift or

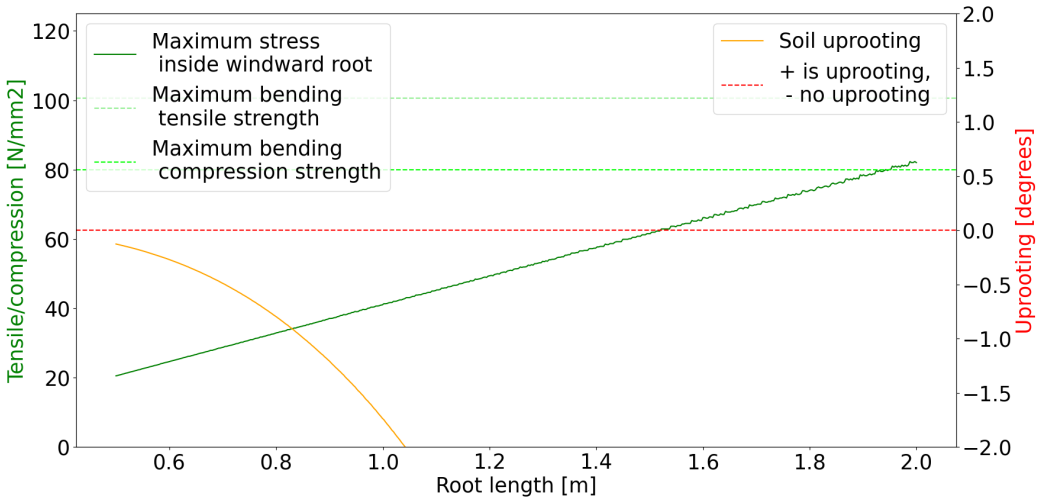


Figure H.7: Relationship between the root length and the stress inside a root and uplift of the root for situation 3

exceeds the strengths. The length of the root mainly influences the number of roots, as the number of roots is based on the belowground biomass and belowground volume. If the length of a root increases the volume of one root increases and therefore the number of roots decreases. As the moment stays the same, the moment taken by each root increases, which increases the stresses inside a root. This also influences the uplift. Figure H.7 shows this relationship for situation 3. The relationships for the other situations will have different number, but the linear or non-linear increase will be equal.

H.4.2. Multiple root lengths and diameters

Graphs for situation 1, 2 and 3

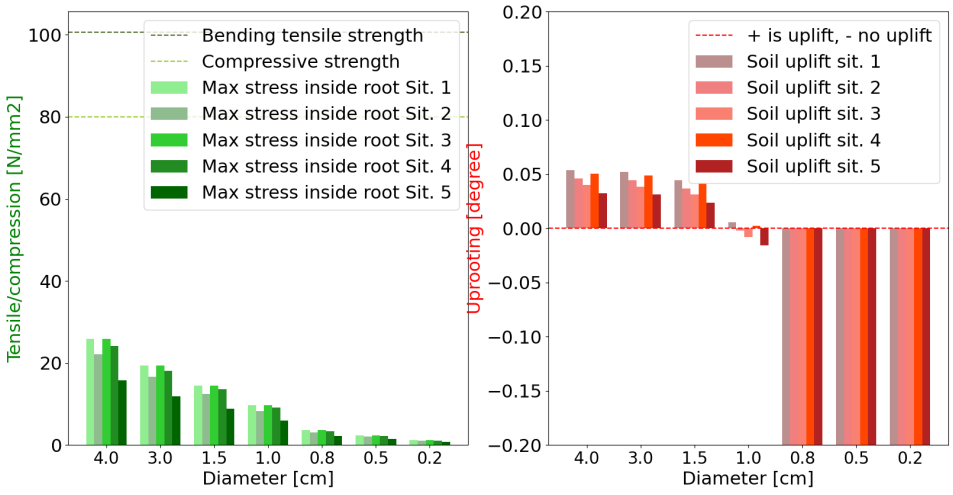


Figure H.8: The stress inside the roots and uplift of the windward roots for all five situations

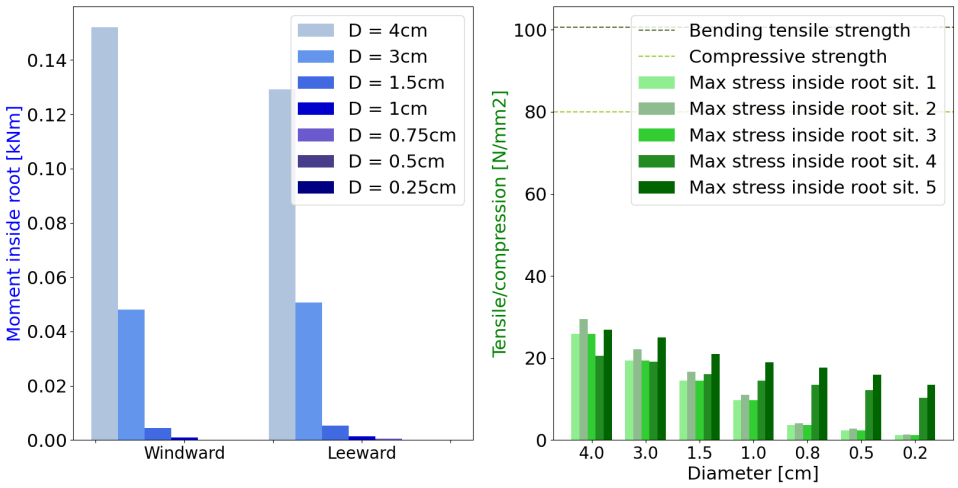


Figure H.9: Moments inside the roots for situation 4 and the stresses inside the leeward roots for all five situations

Influential factors all five situations

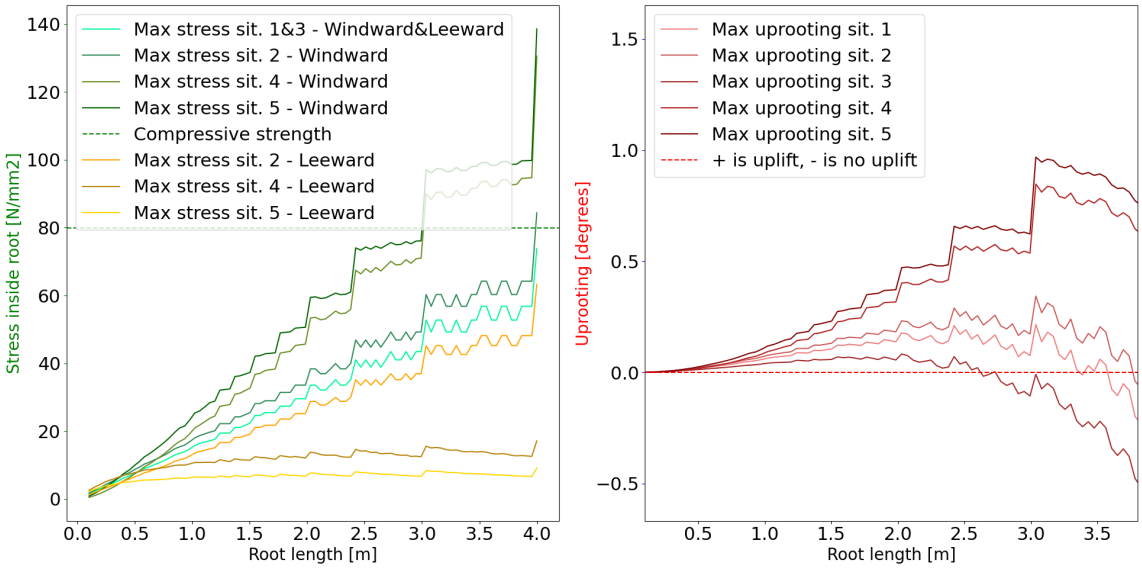


Figure H.10: Relationship between the length of a root and uprooting and stress inside the root for all five situations

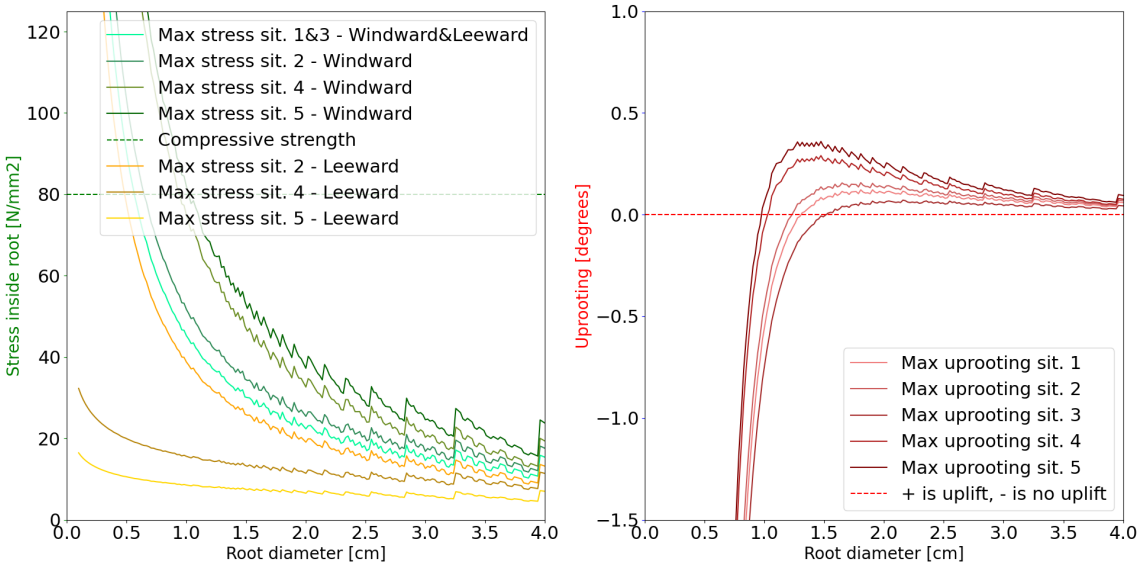


Figure H.11: Relationship between the diameter of a root and uprooting and stress inside the root for all five situations

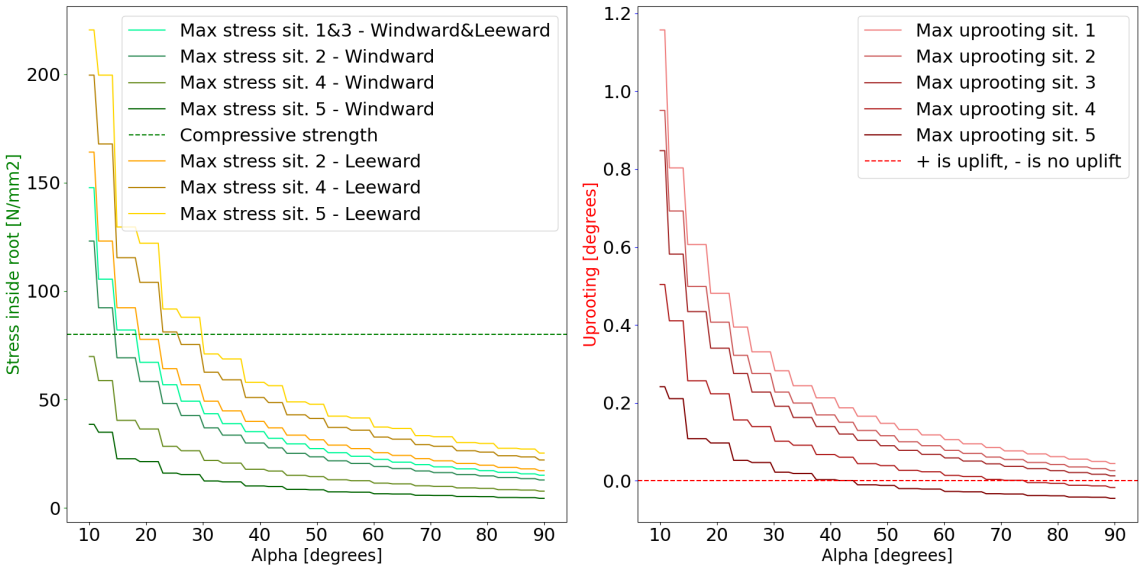


Figure H.12: Relationship between the contributing angle α and the stress inside a root and uprooting of a root for all five situations

Moment distribution between the leeward and windward side

Figure H.13 and H.14 show the moment distribution between the leeward and windward side for all five situations. In situation 1 and 3 the moment inside the roots on the leeward and windward side are equal, due to the fact the schematization on both sides is equal.

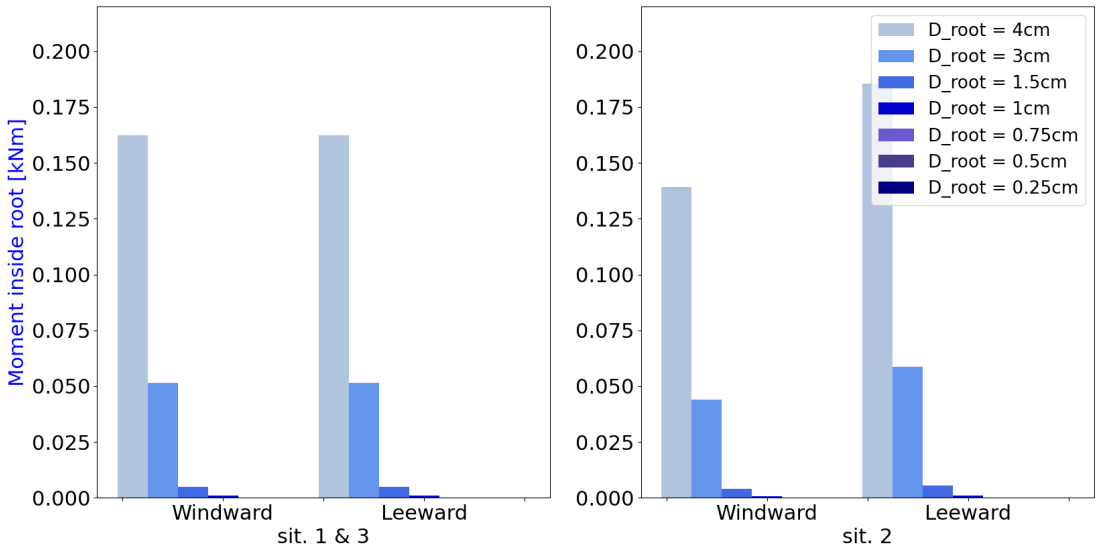


Figure H.13: The distribution of the moment over the leeward and windward roots for situation 1, 2 and 3

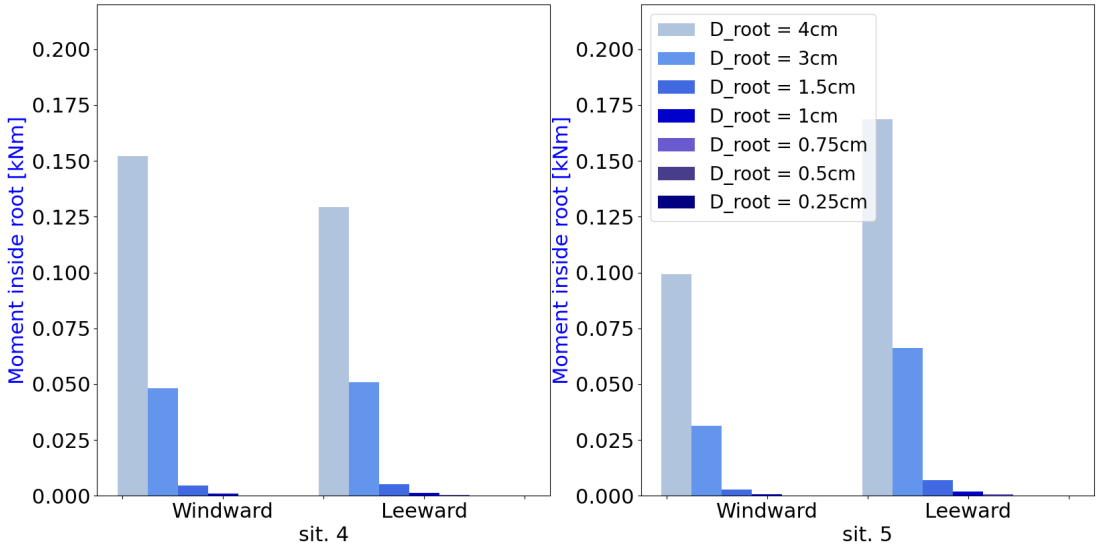


Figure H.14: The distribution of the moment over the leeward and windward roots for situation 4 and 5

Pictures mangrove trees and other species

I.1. Pictures of the mangrove forest in Wijk aan Zee, Paramaribo, Suriname



Figure I.1: Old mangrove tree with a large root system in Wijk aan Zee, Paramaribo, Suriname (Kalloe, 2022a)



Figure I.2: Close up of soil near mangrove tree (Kalloe, 2022b)



Figure I.3: Erosion exposing root system of large tree (Kalloe, 2022c)



Figure I.4: Root system of medium size tree exposed due to erosion (Kalloe, 2022d)



Figure I.5: Failed small mangrove tree with visible root system (Kalloe, 2022k)



Figure I.6: Failed mangrove tree (Kalloe, 2022j)



Figure I.7: Visible root system of an old big mangrove tree (Kalloe, 2022e)



Figure I.8: Close up of surrounding of small mangrove tree (Kalloe, 2022l)



Figure I.9: Close up of surrounding of second small mangrove tree (Kalloe, 2022m)



Figure I.10: Close up of surrounding of third small mangrove tree (Kalloe, 2022n)



Figure I.11: Broken roots at the seaward side (Kalloe, 2022f)



Figure I.12: Close up of the broken roots at the seaward side (Kalloe, 2022g)



Figure I.13: Broken roots at the seaward side (Kalloe, 2022f)



Figure I.14: Close up of the broken roots at the seaward side (Kalloe, 2022g)

I.2. Fallen trees of other species





Figure I.16: Fallen tree showing the root mat (Brodbeck and Rowe, 2019)

J

Python code

J.1. Wind and wave modelling

```
import numpy as np
import pandas as pd
import matplotlib.pyplot as plt
from operator import truediv
import seaborn as sns
import cmath
import math
import time
from numpy import ndarray
from Ftot_waves63 import Ftot_wave_per_x as Ftot_wave_per_x_63
from Ftot_waves63 import x as x_waves_tree
from Ftot_waves48 import Ftot_wave_per_x as Ftot_wave_per_x_48
from Ftot_waves38 import Ftot_wave_per_x as Ftot_wave_per_x_38
from Ftot_waves28 import Ftot_wave_per_x as Ftot_wave_per_x_28

start = time.time()

def wavenumber(T_formula, h_formula):
    eps = 1 * (10 ** (-5))
    omega_formula = 2 * np.pi / T_formula
    k0_formula = (omega_formula ** 2) / 9.81
    x_formula = k0_formula * h_formula
    diff_f = 1
    if x_formula > 2 * np.pi:
        k_formula = k0_formula
    else:
        while diff_f > eps:
            f_formula = k0_formula * h_formula - x_formula * np.tanh(x_formula)
            df_formula = np.tanh(x_formula) + x_formula *
                                        np.cosh(x_formula) / np.cosh(x_formula)
            dx_formula = f_formula / df_formula
            xc_formula = x_formula + dx_formula
            diff_f = abs(xc_formula - x_formula)
            x_formula = xc_formula
        k_formula = x_formula / h_formula
    return k_formula
```

```
def calc_parabol_equation(x1, y1, x2, y2, x3, y3):
    denom = (x1 - x2) * (x1 - x3) * (x2 - x3)
    A_par = (x3 * (y2 - y1) + x2 * (y1 - y3) + x1 * (y3 - y2)) / denom
    B_par = (x3 * x3 * (y1 - y2) + x2 * x2 * (y3 - y1) + x1 * x1 *
                                                    (y2 - y3)) / denom
    C_par = (x2 * x3 * (x2 - x3) * y1 + x3 * x1 * (x3 - x1) *
                                y2 + x1 * x2 * (x1 - x2) * y3) / denom
    return A_par, B_par, C_par


def sumcolumn(matrix):
    return np.sum(matrix, axis=0)


# # Defining bathymetry
##### Demak
T = np.array([3, 6.9, 7.5, 7.7, 7.7, 7.7])  # wave period
surge = np.array([0, 0.63, 0.68, 0.72, 0.74, 0.76, 0])  # initial water depth
H_s = np.array([0.25, 2.08, 2.39, 2.47, 2.51, 2.53, 1.4142*np.sqrt(2)])
                                                        # initial wave height
H = H_s/np.sqrt(2)  # the formulas need the root mean square
                    # wave height, while the significant wave height is given.
a = 1/H  # amplitude of a wave
R = np.array(['daily', '1 year', '5 years', '10 years',
                                '15 years', '20 years', 'Testcase'])
int_z = 0.4


######## Standard situation
x0 = float(0)
x_end = float(6000)
x_int = float(1)
x_steps = int(x_end/x_int+1)  # dus elke 10 centimeter een gridpoint
x = np.linspace(x0, x_end, x_steps)  # x is the offshore coordinate
# (therefore x0 gives
# the offshore, while x_end is the onshore) For the calculation of the
#dissipation of energy
# the equation x[i] > x_veg is given. Therefore, the x0 is the offshore,
#while the x_end is the onshore
# this could be turned around
x_veg = float(5500)
z_interval = 0.4
z_interval_waves = 0.1
z_interval_wind = 0.1

deepwaterdepth = 12

depth0 = float(0.01)  # [m] #depth at the landside
depth_h0 = np.linspace(deepwaterdepth + surge[0], depth0 + surge[0], x_steps)
depth_h01 = np.linspace(deepwaterdepth + surge[1], depth0 + surge[1], x_steps)
depth_h02 = np.linspace(deepwaterdepth + surge[2], depth0 + surge[2], x_steps)
depth_h03 = np.linspace(deepwaterdepth + surge[3], depth0 + surge[3], x_steps)
depth_h04 = np.linspace(deepwaterdepth + surge[4], depth0 + surge[4], x_steps)
depth_h05 = np.linspace(deepwaterdepth + surge[5], depth0 + surge[5], x_steps)
depth_h06 = np.linspace(5, 5, x_steps)
h0 = ([depth_h0[0], depth_h01[0], depth_h02[0], depth_h03[0], depth_h04[0],
```

```
                                                depth_h05[0], depth_h06[0]])
x_steps = int(len(x))

total_depth = np.stack((depth_h0, depth_h01, depth_h02, depth_h03, depth_h04,
                                                depth_h05, depth_h06), axis=-1)

dx = x[2] - x[1]
nd: float = (x[1] - x[-1]) / (len(x) - 1)

g = float(9.81)
rho = float(1025)  # density sea water [kg/m3]
# rho = 1000
f = 1/T  # wave frequency

# Calculate offshore wave parameters
omega0 = []
k0 = []
n0 = []
c0 = []
cg0 = []
E0 = []
Flux0 = []
FluxN0 = []
lambda_wave = []
u0 = []
acc0 = []
# F0 = []

z = 0  # is this correct?
for i in range(len(T)):
    omega0.append(2 * np.pi / T[i])
    k0.append(wavenumber(T[i], h0[i]))  # wavenumber
    lambda_wave.append(2 * np.pi / k0[i])  # wavelength from equation k = 2pi/lambda
    if h0[i]/lambda_wave[i] < 1/20:
        u0.append(omega0[i] * a[i] / (k0[i] * h0[i]) * 1)
        acc0.append((omega0[i]**2 * a[i]) / (k0[i] * h0[i]) * 1)

    elif h0[i] / lambda_wave[i] > 1/2:
        u0.append(omega0[i] * a[i] * np.e**(k0[i]*z) * 1)
        acc0.append(((omega0[i]**2) * a[i]) * np.e**(k0[i] * z) * 1)
    else:
        u0.append(
            omega0[i] * a[i] * np.cosh(k0[i] * (z + h0[i])) /
                                                    np.sinh(k0[i] * h0[i]) * 1)
        acc0.append(((omega0[i]**2) * a[i]) * np.cosh(k0[i] * (z + h0[i])) /
                                                    np.sinh(k0[i] * h0[i]) * 1)

    n0.append(0.5 * (1 + (2 * k0[i] * h0[i]) / np.sinh(2 * k0[i] * h0[i])))
    c0.append(omega0[i] / k0[i])  # individual celerity
    cg0.append(c0[i] * n0[i])  # group celerity
    E0.append(1/8*rho*g*(H[i]**2))  # initial energy, formula 1 from the paper,
    # energy density assuming linear wave theory with regular waves normally incident
    # on acoastline with straight and parallel contours
    Flux0.append(E0[i] * cg0[i])  # initial energy flux
    FluxN0.append(E0[i] * cg0[i] / omega0[i])  # initial energy flux
```

```
# First values (giving variables their value at the sea side of the domain)
cg_l = np.array(pd.Series(cg0))
u = np.array(pd.Series(u0))
acc = np.array(pd.Series(acc0))


Ht_l2 = np.zeros((x_steps, len(H)))
Ht_l2[0, :] = pd.Series(H).values

Ht_l3 = np.zeros((x_steps, len(H)))
Ht_l3[0, :] = pd.Series(H).values

Et_l = np.zeros((x_steps, len(E0)))
Et_l[0, :] = pd.Series(E0).values

Et_l2 = np.zeros((x_steps, len(E0)))
Et_l2[0, :] = pd.Series(E0).values

Et_l3 = np.zeros((x_steps, len(E0)))
Et_l3[0, :] = pd.Series(E0).values

Flux = np.zeros((x_steps, len(Flux0)))
Flux[0, :] = pd.Series(Flux0).values

Fluxb = np.zeros((x_steps, len(Flux0)))
Fluxb[0, :] = pd.Series(Flux0).values

FluxN = np.zeros((x_steps, len(Flux0)))
FluxN_divider = list(map(truediv, Flux0, omega0))
FluxN[0, :] = pd.Series(FluxN_divider).values

FluxNb = np.zeros((x_steps, len(Flux0)))
FluxNb_divider = list(map(truediv, Flux0, omega0))
FluxNb[0, :] = pd.Series(FluxNb_divider).values

# Calculating the wave energy flux per grid point
Cd = float(1.0)  # drag coefficient #chosen as random value here
Cm = float(2.0)  # inertia coefficient
B = float(1)  # Adjusting parameter --> formula 34 of paper -->
              # part 3.2 proposed values Mase and Kirby (1993)
gamma_b = float(0.6)  # Adjusting parameter --> formula 34 of paper
              # --> part 3.2 proposed values Mase and Kirby (1993)

E = np.empty((0, len(f)), int)
E_mv = np.empty((0, len(f)), int)
N = np.empty((0, len(f)), int)
N_mv = np.empty((0, len(f)), int)
k = np.empty((0, len(f)), int)
k = np.vstack((k, k0))
n = np.empty((0, len(f)), int)
c = np.empty((0, len(f)), int)
omega = np.empty((0, len(f)), int)
omega = np.vstack((omega, omega0))

cg = np.empty((0, len(f)), int)
```

```
D = np.empty((0, len(f)), int)
Dv_test = np.empty((0, len(f)), int)
D_mv = np.empty((0, len(f)), int)
Dv = np.empty((0, len(f)), int)


tree_height = np.ones(x_steps)*2.8
hv_waterdepth = np.empty((0, len(f)), int)
for i in range(x_steps):
    hv1 = []
    for j in range(len(f)):
        if tree_height[i] >= total_depth[i, j]:
            hv1.append(total_depth[i, j])
        else:
            hv1.append(tree_height[i])
    hv_waterdepth = np.vstack((hv_waterdepth, hv1))


bv_z_values = np.array([0.0525, 0.0925, 0.3225, 0.3325, 0.1200, 0.0450, 0.0025])
bv_z_values_test = np.array([0.002252, 0.002252, 0.002252, 0.002252,
                                                    0.002252, 0.002252, 0.002252])
bv_z = np.transpose(np.vstack((bv_z_values, bv_z_values, bv_z_values,
            bv_z_values, bv_z_values, bv_z_values, bv_z_values_test)))
bv_formula1 = np.ones(x_steps) * (0.4*0.0525+0.4*0.0925+0.2*0.3225)/1.0
bv_formula1_test = np.ones(x_steps) * 0.002252
bv_formula = np.transpose(np.vstack((bv_formula1, bv_formula1, bv_formula1,
                        bv_formula1, bv_formula1, bv_formula1, bv_formula1_test)))

Nv2 = np.ones(x_steps)*4.4
Nv3 = np.ones(x_steps)*1
Nv = np.transpose(np.vstack((Nv2, Nv2, Nv2, Nv2, Nv2, Nv2, Nv3)))

# energy dissipation through the forest
for i in range(1, len(total_depth)):
    E1 = []
    E_mv1 = []
    N1 = []
    N_mv1 = []
    # k1 = np.zeros(len(f))
    k1 = []
    n1 = []
    c1 = []
    cg1 = []
    cg_l1 = []
    D1 = []
    D_mv1 = []
    Dv1 = []
    Dv1_test = []
    u1 = []
    acc1 = []
    omega1 = []
    for j in range(len(f)):  # loop for every frequency
        k1.append(wavenumber(T[j], total_depth[i, j]))
        k1_a = np.array(k1)
        if total_depth[i, j] / (2 * np.pi / k1_a[j]) < 1 / 20:
            omega1.append(np.sqrt(g*(k1_a[j]**2)*total_depth[i, j]))
```

```
elif total_depth[i, j] / (2 * np.pi / k1_a[j]) > 1 / 2:
    omega1.append(np.sqrt(g*k1_a[j]))
else:
    omega1.append(np.sqrt(g*k1_a[j]*np.tanh(k1_a[j]*total_depth[i, j])))
omega1_a = np.array(omega1)
E1.append(1/8 * rho * g * (Ht_l2[i-1, j]**2))
E1_a = np.array(E1)
E_mv1.append((1 / 8) * rho * g * (Ht_l3[i-1, j] ** 2))
N1.append(E1[j]/omega1_a[j])
N_mv1.append(E1[j] / omega1_a[j])
n1.append(0.5 * (1 + (2.0 * k1_a[j] * total_depth[i, j]) / np.sinh(2.0 *
                                                    k1_a[j] * total_depth[i, j])))
n1_a = np.array(n1)
# factor to change individual celerity into group celerity
c1.append(omega1_a[j] / k1_a[j])   # individual celerity
                                                    #(phase speed of a wave)
cg1.append(c1[j] * n1_a[j])  # group celerity
cg_l1.append(cg1[j])
cg_l1_a = np.array(cg_l1)  #

D1.append((3 * np.sqrt(np.pi) / 16) * (rho * g * f[j] * (B ** 3)) /
                          ((gamma_b ** 4) * (total_depth[i, j] ** 5))
          * (Ht_l2[i - 1, j] ** 7))
# # dissipation by breaking formula 34 in paper
D1_a = np.array(D1)

D_mv1.append((3 * np.sqrt(np.pi) / 16) * (rho * g * f[j] * B ** 3) /
                               ((gamma_b ** 4) * total_depth[i, j] ** 5)
             * (Ht_l3[i - 1, j] ** 7))
# # dissipation by breaking formula 34 in paper
D_mv1_a = np.array(D_mv1)

# distribution of plants per area [#/m2] in the depth (less roots in lower
# part/what is the distribution of stem

if x[i] > x_veg:
    Dv1.append((1 / (2 * np.sqrt(np.pi))) * rho * bv_formula[i, j] *
                                       Nv[i, j] * Cd * ((k1[j] * g /
                    (2 * omega1_a[j])) ** 3) * ((np.sinh(k1[j] *
                    hv_waterdepth[i, j]) ** 3 + 3 * np.sinh(k1[j] *
                            hv_waterdepth[i, j])) / (3 * k1[j] *
                            (np.cosh(k1[j] * total_depth[i, j])) ** 3)) *
                                (Ht_l3[i - 1, j]) ** 3)

else:
    Dv1.append(0)  # (% if there is no vegetation,
                    # the dissipation by vegetation is set to zero)

Fluxb[i, j] = Fluxb[i - 1, j] - D1[j] * dx  # (% Fluxb is the flux
    #if I neglect the effect of the vegetation, so there is only breaking)
Flux[i, j] = Flux[i - 1, j] - D_mv1[j] * dx - Dv1[j] * dx
FluxNb[i, j] = FluxNb[i - 1, j] - D1[j] * dx / omega1_a[j]  #
        # ( Fluxnb also includes dissipation by breaking))
FluxN[i, j] = FluxN[i - 1, j] - D_mv1[j] * dx / omega1_a[j] - Dv1[j] *
                                                        dx / omega1_a[j]
```

```
        if Flux[i, j] < 0:
            Flux[i, j] = 0

        if Fluxb[i, j] < 0:
            Fluxb[i, j] = 0

        Et_l3[i, j] = omega1_a[j] * FluxN[i, j] / cg1[j]  # transmitted energy
        Ht_l3[i, j] = np.sqrt(Et_l3[i, j] / ((1 / 8) * rho * g))  # transmitted
        Et_l2[i, j] = omega1_a[j] * FluxNb[i, j] / cg1[j]  # transmitted energy
        Ht_l2[i, j] = np.sqrt(Et_l2[i, j] / ((1 / 8) * rho * g))  # transmitted

k = np.vstack((k, k1_a))
omega = np.vstack((omega, omega1_a))
E = np.vstack((E, E1_a))
E_mv = np.vstack((E_mv, E_mv1))
D = np.vstack((D, D1_a))
cg_l = np.vstack((cg_l, cg_l1_a))
D_mv = np.vstack((D_mv, D_mv1_a))
Dv = np.vstack((Dv, Dv1))

def calculation_force_wave(frequency, location_x, time0, time_end,
                                        timesteps, interval, z_interval):
a_1wave = Ht_l3[location_x, frequency]/2
k_1wave = k[location_x, frequency]
total_depth_onewave = total_depth[location_x, frequency]
Nv_1wave = Nv[location_x, frequency]

bv_z_waves = np.concatenate([np.ones(int(z_interval / interval))*
                        bv_z[0, frequency], np.ones(int(z_interval /
                            interval))*bv_z[1, frequency],
                            np.ones(int(z_interval / interval))
                                                *bv_z[2, frequency],
                             np.ones(int(z_interval / interval))
                                                *bv_z[3, frequency],
                             np.ones(int(z_interval / interval))
                                                * bv_z[4, frequency],
                             np.ones(int(z_interval / interval))
                                                *bv_z[5, frequency],
                             np.ones(int(z_interval / interval))
                                                *bv_z[6, frequency]])

if total_depth_onewave >= tree_height[location_x]:
    z = np.linspace(-total_depth_onewave, -(total_depth_onewave -
    tree_height[location_x]), int(tree_height[location_x] / interval + 1))
else:
    z = np.linspace(-total_depth_onewave, +1 / 2 * Ht_l3[location_x, frequency],
                    int(total_depth[location_x, frequency] / interval + 1))

if len(z) == 1:
    dz = z[0]
else:
    dz = z[1] - z[0]

Locatie_x = x[location_x]  # locatie offshore
time = np.linspace(time0, time_end, timesteps)
```

```
watercondition = np.empty((0, len(time)), int)
u_onewave = np.empty((0, len(time)), int)
acc_onewave = np.empty((0, len(time)), int)
Fd = np.empty((0, len(time)), int)
Fi = np.empty((0, len(time)), int)
Ftot = np.empty((0, len(time)), int)

for i in range(len(z)):
    watercondition1 = []
    u_onewave1 = []
    acc_onewave1 = []
    Fd1 = []
    Fi1 = []
    Ftot1 = []
    for j in range(len(time)):
        if total_depth_onewave / (2 * np.pi / k_1wave) < 1 / 20:
            watercondition1.append('Shallow')
            omega_1wave = np.sqrt(g * k_1wave**2 * total_depth_onewave)
            u_onewave1.append(omega_1wave * a_1wave / (
                    k_1wave * total_depth_onewave) * np.sin(omega_1wave *
                                                time[j] - k_1wave * Locatie_x))
            # horizontal orbital flow velocity
            acc_onewave1.append((omega_1wave ** 2 * a_1wave) / (
                    k_1wave * total_depth_onewave) * np.cos(omega_1wave *
                                                time[j] - k_1wave * Locatie_x))
            # horizontal orbital acceleration
            G = 2 * k_1wave * total_depth_onewave / np.sinh(2 * k_1wave *
                                                        total_depth_onewave)
        elif total_depth_onewave / (2 * np.pi / k_1wave) > 1 / 2:
            omega_1wave = np.sqrt(g*k_1wave)
            watercondition1.append('Deep')
            u_onewave1.append(omega_1wave * a_1wave * np.e **
                                                        (k_1wave * z[i]) *
                              np.sin(omega_1wave * time[j] - k_1wave
                                                        * Locatie_x))
            acc_onewave1.append(((omega_1wave ** 2) * a_1wave) *
                                                    np.e ** (k_1wave * z[i])
                                * np.cos(omega_1wave * time[j]
                                                    - k_1wave * Locatie_x))
            G = 2 * k_1wave * total_depth_onewave /
                                np.sinh(2 * k_1wave * total_depth_onewave)
        else:
            omega_1wave = np.sqrt(g * k_1wave *
                                  np.tanh(k_1wave * total_depth_onewave))
            watercondition1.append('Interm.')
            u_onewave1.append(
                omega_1wave * a_1wave *
                np.cosh(k_1wave * (z[i] + total_depth_onewave)) / np.sinh(
                    k_1wave * total_depth_onewave) *
                        np.sin(omega_1wave * time[j] - k_1wave * Locatie_x))
            acc_onewave1.append(((omega_1wave ** 2)
                * a_1wave) * np.cosh(k_1wave * (z[i] + total_depth_onewave)) /
                                np.sinh(k_1wave * total_depth_onewave)
                        * np.cos(omega_1wave * time[j] - k_1wave * Locatie_x))
            # G = 2*k_1wave*total_depth_onewave/
                                    np.sinh(2*k_1wave*total_depth_onewave)
```

```
            Fd1.append(0.5 * rho * Cd * dz * bv_z_waves[i] *
                                Nv_1wave * u_onewave1[j] * abs(u_onewave1[j]))
            Fi1.append(0.25 * rho * Cm * dz * np.pi *
                                (bv_z_waves[i]**2) * Nv_1wave * acc_onewave1[j])
            Ftot1.append(Fd1[j] + Fi1[j])
        watercondition = np.vstack((watercondition, watercondition1))
        u_onewave = np.vstack((u_onewave, u_onewave1))
        acc_onewave = np.vstack((acc_onewave, acc_onewave1))
        Fd = np.vstack((Fd, Fd1))
        Fi = np.vstack((Fi, Fi1))
        Ftot = np.vstack((Ftot, Ftot1))

    Fdtotal = []
    Fitotal = []
    Ftotal = []
    for i in range(len(time)):
        Fdtotal.append(sum(Fd[:, i]))
        Fitotal.append(sum(Fi[:, i]))
        Ftotal.append(Fdtotal[i] + Fitotal[i])
    return np.array(Fdtotal)/1000,
        np.array(Fitotal)/1000, np.array(Ftotal)/1000, time,
        u_onewave, acc_onewave, watercondition, z, np.array(Fd)/1000,
        np.array(Fi)/1000, np.array(Ftot)/1000, bv_z_waves,
        omega_1wave, k_1wave, Ht_l3[location_x, frequency],
                    total_depth_onewave  # result is in kN


    def windforce_paper(H_wave_to_wind):
    a_ww = 0.00162
    b_ww = 0.0275
    c_ww = -0.707 * H_wave_to_wind  # change to root mean
            square wave height (paper is Hs (significant wave height))

    # calculate the discriminant
    d_ww = (b_ww**2) - (4*a_ww*c_ww)

    # find two solutions
    sol1 = (-b_ww-cmath.sqrt(d_ww))/(2*a_ww)
    sol2 = (-b_ww+cmath.sqrt(d_ww))/(2*a_ww)

    # return sol1.real, sol2
    if sol1.real < 0:
        return sol2.real
    else:
        return sol1.real, sol2.real


u_wind = np.ones(len(f))
for i in range(len(f)):
    u_wind[i] = windforce_paper(H[i])

z0_smooth = 0.02  # (Gardiner et al, 2016 --> given value)
Karman_constant = 0.4  # (given value)
v_e = 1
xtree = x  # distance from the edge of the forest
rho_air = 1.2041  # [kg/m3] at 20 degrees celcius
```

```
c_Dc = 1.0  # NOT TRUE ; drag coefficient for wind currents

z_10 = 10
z_200 = 200
G = np.zeros(len(x))
term1 = np.zeros(len(x))
term2 = np.zeros(len(x))


# ####function instead of for loop:
def function_wind_forcing(frequency, len_x, dx, interval, z_interval,
                                                    tree_height, x_transition):
    Ft_wavesair_edge = []
    u_z_edge = []
    tree_height_wind = []
    G_edge = 1.0

    z_exp_wind = np.linspace(interval, tree_height[0], int(tree_height[0] /
                                                              interval + 1))

    bv_z_wind = np.concatenate([np.ones(int(round(z_interval / interval, 0))) *
                                                        bv_z[0, frequency],
                                np.ones(int(round(z_interval / interval, 0))) *
                                                        bv_z[1, frequency],
                                np.ones(int(round(z_interval / interval, 0))) *
                                                        bv_z[2, frequency],
                                np.ones(int(round(z_interval / interval, 0))) *
                                                        bv_z[3, frequency],
                                np.ones(int(round(z_interval / interval, 0))) *
                                                        bv_z[4, frequency],
                                np.ones(int(round(z_interval / interval, 0))) *
                                                        bv_z[5, frequency],
                                np.ones(int(round(z_interval / interval, 0))) *
                                                        bv_z[6, frequency]])

    u_wind_f = u_wind[frequency]
    ustar = u_wind_f * Karman_constant / np.log(z_10 / z0_smooth)
    u200 = ustar / Karman_constant * np.log(z_200 / z0_smooth)

    tree_height_edge = tree_height[int(x_veg/dx)] -
                                            total_depth[int(x_veg/dx), frequency]
    tree_height_wind.append(tree_height_edge)
    z0_rough = ([tree_height_edge/30])
    ustar2 = ([u200 * Karman_constant / np.log(z_200 / z0_rough[0])])
    utop = ([ustar2[0] / Karman_constant * np.log(tree_height_edge / z0_rough[0])])
    term1_1 = ([0])
    term2_1 = ([0])
    G1 = ([0])
    D_wind = ([np.sqrt(1 / Nv[0, frequency])])

    for j in range(len(z_exp_wind)):  # Determination of the wind at the first row
        ustar_a_edge = u_wind[frequency] * Karman_constant /
                    np.log(z_200 / z0_smooth)  # check which value needs to be u_wind
        u_z_edge.append(ustar_a_edge / Karman_constant *
                                            np.log(z_exp_wind[j] / z0_smooth))
        Ft_wavesair_edge.append(0.5 * rho_air * bv_z_wind[j] * interval
```

```
                                                * c_Dc * G_edge * u_z_edge[j] ** 2)
Ft_wavesair_test = np.zeros(len(z_exp_wind))
u_air_test = np.zeros(len(z_exp_wind))
Moment_wind = np.zeros(len(z_exp_wind))

term1_x_veg = (
        (2.7193 * ((np.sqrt(1 / Nv[int((x_veg+x_transition)/dx), frequency]))
                / tree_height_edge) - 0.061) + (-1.273 * ((np.sqrt(1 /
                Nv[int((x_veg+x_transition)/dx), frequency])) /
                tree_height_edge) + 0.9701) * (1.1127 * ((np.sqrt(1 /
                Nv[int((x_veg+x_transition)/dx), frequency])) /
                (tree_height_edge)) + 0.0311) ** ((x[int((x_veg+
                    x_transition)/dx)]-x_veg) / tree_height_edge))
term2_x_veg = ((0.68 * ((np.sqrt(1 / Nv[int((x_veg+x_transition)/dx),
                frequency])) / tree_height_edge) - 0.0385) + (-0.68 *
                ((np.sqrt(1 / Nv[int((x_veg+x_transition)/dx),
                frequency])) / tree_height_edge) + 0.4785) * (
                1.7239 * ((np.sqrt(1 / Nv[int((x_veg+x_transition)/dx),
                frequency])) / tree_height_edge) + 0.0316) ** ((
                x[int((x_veg+x_transition)/dx)]-x_veg)/ tree_height_edge))
G_x_veg_transition = term1_x_veg / term2_x_veg

for i in range(1, len_x):
    D_wind.append(np.nan_to_num(np.sqrt(1 / Nv[i, frequency]), neginf=0,
                                                               posinf=0))
    tree_height_wind.append(tree_height[i] - total_depth[i,frequency])
    Ft_wavesair1 = []
    u_air1 = []
    Moment_wind1 = []
    z0_rough.append(tree_height_wind[i]/30)
    ustar2.append(u200 * Karman_constant / np.log(z_200 / z0_rough[i]))
    utop.append(ustar2[i] / Karman_constant * np.log(tree_height_wind[i] /
                        z0_rough[i]))  # (velocity on top of the vegetation)

    term1_1.append(
        (2.7193 * (D_wind[i] / tree_height_wind[i]) - 0.061) + (-1.273 *
                            (D_wind[i] / tree_height_wind[i]) + 0.9701) * (
                1.1127 * (D_wind[i] / tree_height_wind[i]) + 0.0311) **
                                        ((x[i]-x_veg) / tree_height_wind[i]))
    term2_1.append((0.68 * (D_wind[i] / tree_height_wind[i]) - 0.0385) +
                    (-0.68 * (D_wind[i] / tree_height_wind[i]) + 0.4785) * (
                    1.7239 * (D_wind[i] / tree_height_wind[i]) + 0.0316) **
                                        ((x[i]-x_veg)/ tree_height_wind[i]))
    if x[i] < x_veg:
        G1.append(0)
    elif (x[i]-x_veg) < x_transition:
        f_G = 1/x_transition*(x[i]-x_veg)*G_x_veg_transition
        G1.append(f_G)
    else:
        G1.append(term1_1[i] / term2_1[i])

    count = 0
    for N in range(len(z_exp_wind)):
        if z_exp_wind[N] >= total_depth[i, frequency]:
            u_air1.append(utop[i] * np.exp(-v_e * (1 -
                        (z_exp_wind[N]-interval*count) / tree_height_wind[i])))
```

```
                Ft_wavesair1.append(0.5 * rho_air * bv_z_wind[N] * interval
                                                * c_Dc * G1[i] * u_air1[N] ** 2)
                Moment_wind1.append(Ft_wavesair1[N]*(z_exp_wind[N] - 0.5 * interval))
            else:
                count += 1
                u_air1.append(0)
                Ft_wavesair1.append(0)
                Moment_wind1.append(0)

        Ft_wavesair_test = np.vstack((Ft_wavesair_test, Ft_wavesair1))
        u_air_test = np.vstack((u_air_test, u_air1))
        Moment_wind = np.vstack((Moment_wind, Moment_wind1))

        if i == int(x_veg/dx):
            Ft_wavesair_test[i] = np.nan_to_num(Ft_wavesair_edge, neginf=0,
                                                                    posinf=0)
            u_air_test[i] = pd.Series(u_z_edge).values
            for N in range(len(z_exp_wind)):
                if z_exp_wind[N] <= total_depth[i, frequency]:
                    Ft_wavesair_test[i, N] = 0
                    u_air_test[i, N] = 0

    total_wind_force = sumcolumn(np.transpose(np.array(Ft_wavesair_test)/1000))

    Mtot_wind = sumcolumn(np.transpose(np.array(Moment_wind)/1000))

    return np.transpose(np.array(Ft_wavesair_test))/1000, np.array(G1),
        np.transpose(u_air_test), np.array(D_wind), np.array(tree_height_wind),
        np.array(z0_rough), np.array(ustar2), np.array(utop), total_wind_force,
        u200, G_x_veg_transition, term1_x_veg, term2_x_veg, tree_height_edge,
        z_exp_wind, bv_z_wind, Moment_wind, Mtot_wind,
                                        np.transpose(np.array(Moment_wind)/1000)

    def changing_treeheight(frequency, x_end, x_veg, start_tree_height):
    tree_height_changing2 = []
    for i in range(int(x_veg/dx)):
        tree_height_changing2.append(0)
    tree_height_changing1 = np.ones(int((x_end - x_veg)/dx+1)) * start_tree_height
    for i in range(len(tree_height_changing1)):
        tree_height_changing2.append((tree_height_changing1[i]-
        total_depth[int(x_veg/dx+1), frequency])+(1/(int((x_end-x_veg)/dx))*
                                    (total_depth[int(x_veg/dx+1), frequency]-
                                total_depth[int((x_end/dx)), frequency]))*i)
    return np.array(tree_height_changing2)

    def moments(frequency, location_x, tree_height, time0, time_end, timesteps,
    interval, z_interval):

    dragforce = calculation_force_wave(frequency, location_x, time0, time_end,
                                            timesteps, interval, z_interval)[8]
    inertiaforce = calculation_force_wave(frequency, location_x, time0, time_end,
                                            timesteps, interval, z_interval)[9]
    M_waves = []
    max_value = np.argmax(calculation_force_wave(frequency, location_x, time0,
                                    time_end, timesteps, interval, z_interval)[2])
    total_depth_onewave = total_depth[location_x, frequency]
```

```
    if total_depth_onewave >= tree_height[location_x]:
        z_waves = np.linspace(0, tree_height[location_x],
                                        int(tree_height[location_x] / interval + 1))
    else:
        z_waves = np.linspace(0, total_depth[location_x, frequency],
                              int(total_depth[location_x, frequency] / interval + 1))
    if len(z_waves) == 1:
        z_interval_waves = z_waves[0]
    else:
        z_interval_waves = z_waves[1] - z_waves[0]

    for i in range(len(z_waves)):
        M_waves.append(dragforce[i, max_value] * (z_waves[i] - 0.5 *
                                z_interval_waves) + inertiaforce[i, max_value] * (
                                                z_waves[i] - 0.5 * z_interval_waves))

    Mtot_waves = sumcolumn(M_waves)

    return M_waves, Mtot_waves  # kNm

    Ftot_wave_per_x = np.empty((0, len(x)), int)
Ftot_ww_force_tree = np.empty((0, len(x)), int)
Ftot_wind_per_x = np.empty((0, len(x)), int)
for j in range(len(f)):
    Ftot_wind_per_x1 = []
    Ftot_wind_per_x1 = sumcolumn(function_wind_forcing(j, len(x), dx,
                                z_interval_wind, z_interval, tree_height, 15)[0])
    Ftot_wave_per_x1 = []
    Ftot_ww_force_tree1 = []
    for i in range(len(x)):
        if x[i] < x_veg:
            Ftot_wave_per_x1.append(0)
        else:
            Ftot_wave_per_x1.append(np.max(calculation_force_wave(j, i, 0.01,
                                    5*np.pi, 50, z_interval_waves, z_interval)[2]))
        Ftot_ww_force_tree1.append(Ftot_wave_per_x1[i] + Ftot_wind_per_x1[i])

    Ftot_wind_per_x = np.vstack((Ftot_wind_per_x, Ftot_wind_per_x1))
    Ftot_wave_per_x = np.vstack((Ftot_wave_per_x, Ftot_wave_per_x1))
    Ftot_ww_force_tree = np.vstack((Ftot_ww_force_tree, Ftot_ww_force_tree1))
```

J.2. Failure mechanisms

J.2.1. Root breakage

```
import numpy as np
import pandas as pd
import matplotlib.pyplot as plt
from operator import truediv
import seaborn as sns
import math

from Resistance_forces_anchoring2 import formula_pulloutforce_adhesion
from Resistance_forces_anchoring2 import formula_pulloutforce_data
```

```
from Resistance_forces_anchoring2 import belowground_structure
from Resistance_forces_anchoring2 import max_resistance_forcing
from Resistance_forces_anchoring2 import force_in_roots
from Resistance_forces_anchoring2 import sum_moment_hor_vert



def force_to_tensile_strength(DBH, L, D, F, direction_force,
            direction_first_root, max_tensile_strength, max_compressive_strength):
    diameter_root = D
    force = force_in_roots(DBH, L, D, F, direction_force, direction_first_root)[4]
    number_roots = int(belowground_structure(DBH, L, D)[2])

    tensile_compression_in_root = []
    SF_tensile = []
    max_force_in_root = []
    for i in range(number_roots):
        area = np.pi * (0.5 * diameter_root)**2
        tensile_compression_in_root.append(force[i] / area)
        # SF_tensile.append(max_tensile_strength / tensile_compression_in_root[i])

        if force[i] < 0:
            SF_tensile.append(max_tensile_strength /
                                        abs(tensile_compression_in_root[i]))
            max_force_in_root.append(max_tensile_strength * area)
            # if abs(max_tensile_strength) > abs(tensile_compression_in_root[i]):
            #     print('No failure for root', i)
            # else:
            #     print('Failure for root', i)
        if force[i] > 0:
            SF_tensile.append(max_compressive_strength /
                                        abs(tensile_compression_in_root[i]))
            max_force_in_root.append(max_compressive_strength*area)
            # if abs(max_tensile_strength) > abs(tensile_compression_in_root[i]):
            #     print('No failure for root', i)
            # else:
            #     print('Failure for root', i)
        if force[i] == 0:
            SF_tensile.append('Bending')
            max_force_in_root.append('Bending')
            # if abs(max_tensile_strength) > abs(tensile_compression_in_root[i]):
            #     print('No failure for root', i)
            # else:
            #     print('Failure for root', i)

    return tensile_compression_in_root, SF_tensile, np.array(max_force_in_root),
                                                                    force, area
```

J.2.2. Root slippage

```
    import numpy as np
import pandas as pd
import matplotlib.pyplot as plt
from operator import truediv
import seaborn as sns
import math
```

```
def formula_pulloutforce_adhesion(D, L, bulk_density, z, phi, k):
    sigma_v = g * bulk_density * z / 1000  # [kN/m3]
    tau_r = k*np.tan(phi)*sigma_v  # [kN/m2 - kPa]
    Ra = np.pi*D*L*tau_r  # [kN]
    return np.tan(phi)*k, sigma_v, tau_r, Ra


def formula_pulloutforce_data(Ra, L, D):
    tau_r = Ra/(np.pi * D * L)
    return tau_r #  kN/m2 alles invullen in kN en m


def belowground_structure(DBH, length_root, diameter_root):
                                    # DBH in cm, diameter/length in m
    p = 0.732
    BGB = 0.199 * p**0.899 * (DBH)**2.22
    # BGV = BGB * 1000 / 0.455 * 1 * 10 ** (-6)
    BGV = BGB * 1000 / 0.732 * 1 * 10 ** (-6)
    # 0.455 g/cm3 = 455 kg/m3 of 1 cm3 = 1*10^-6 m3
    area = np.pi * (diameter_root / 2) ** 2
    number_of_roots = BGV / (length_root * area)
    return BGB, BGV, number_of_roots

def max_resistance_forcing(DBH, L, D, tau_r, direction_first_root):
    number_roots = int(belowground_structure(DBH, L, D)[2])
    angle_with_first_root = np.ones(int(number_roots))
    F_x_component = np.ones(int(number_roots))
    F_z_component = np.ones(int(number_roots))
    for i in range(number_roots):
        #  angle_with_vertical[i] = 90+360/float(number_roots)*i
        angle_with_first_root[i] = direction_first_root + 360 /
                                            float(number_roots) * i
        F_x_component[i] = abs(np.cos(angle_with_first_root[i] *
                                            #  tau_r is in kN/m2
                                  np.pi / 180)) * tau_r * D * np.pi * L
                                    # *np.pi/180 degrees instead of radian
        F_z_component[i] = abs(np.sin(angle_with_first_root[i] * np.pi / 180)) \
                           * tau_r * D * np.pi * L
                           # *np.pi/180 degrees instead of radian

    Ra = np.pi*L*D*tau_r # kN
    # angle_between_roots = 360 / float(number_roots)

    tot_x = sum(F_x_component) # kN
    tot_z = sum(F_z_component) # kN
    return tot_x, tot_z, F_x_component, F_z_component, Ra

def force_in_roots(DBH, L, D, F, direction_force, direction_first_root):
    # direction_force = 90 if along the coast, 0 if horizontal
                                  to towards the coast x = direction to land,
    # z = along the coast
    number_roots = int(belowground_structure(DBH, L, D)[2])
    x_coord_rootsystem = np.ones(int(number_roots))
    z_coord_rootsystem = np.ones(int(number_roots))
```

```
    angle_with_force = np.ones(int(number_roots))
    z_factor_of_tot_slippage = np.ones(int(number_roots))
    x_factor_of_tot_slippage = np.ones(int(number_roots))
    z_force_in_root = np.ones(int(number_roots))
    x_force_in_root = np.ones(int(number_roots))
    for i in range(number_roots):
        angle_with_force[i] = float(direction_first_root)-
                float(direction_force) + 360 / float(number_roots) * i
        if abs(angle_with_force[i]) == 90:
            z_factor_of_tot_slippage[i] = 0
            x_factor_of_tot_slippage[i] = 0
        elif abs(angle_with_force[i]) == 270:
            z_factor_of_tot_slippage[i] = 0
            x_factor_of_tot_slippage[i] = 0
        else:
            z_factor_of_tot_slippage[i] = math.sin(angle_with_force[i] *
                                math.pi / 180)    # degrees instead of radian
            x_factor_of_tot_slippage[i] = abs(
                                math.cos(angle_with_force[i] * math.pi/180))
            if np.allclose(0, z_factor_of_tot_slippage[i],
                                                    rtol=1e-05, atol=1e-08):
                z_factor_of_tot_slippage[i] = 0
            if np.allclose(0, x_factor_of_tot_slippage[i],
                                                    rtol=1e-05, atol=1e-08):
                x_factor_of_tot_slippage[i] = 0

    tot_contribution_z = sum(abs(z_factor_of_tot_slippage))
    tot_contribution_x = sum(abs(x_factor_of_tot_slippage))

    # F_x = np.cos(direction_force)*F
    # F_z = np.sin(direction_force)*F
    for i in range(number_roots):
        x_force_in_root[i] = x_factor_of_tot_slippage[i] /
                                                        tot_contribution_x * F
        # z_force_in_root[i] = z_factor_of_tot_slippage[i] /
                                                        tot_contribution_z * F
        z_force_in_root[i] = math.tan(angle_with_force[i] *
                                        math.pi / 180) * x_force_in_root[i]
        # if abs(angle_with_force) ==0:
        #     z_coord_rootsystem[i] = np.sin(angle_with_force[i])
        #     x_coord_rootsystem
        # else:
        # x_coord_rootsystem[i] = np.cos(angle_with_force[i]
                                                        * np.pi / 180) * L
        # z_coord_rootsystem[i] = np.sin(angle_with_force[i]
                                                        * np.pi / 180) * L
        # plt.plot([0, x_coord_rootsystem[i]], [0,
                            z_coord_rootsystem[i]], label=('number root =', i))
        # # plt.plot([0, x_coord_rootsystem[i]],
                                        [0, z_coord_rootsystem[i]], color='black')
        # plt.legend()


    # tau_r = formula_pulloutforce_data(Ra, L, D)
    angle_between_roots = 360 / float(number_roots)
```

```
    tot_z_force_in_roots = round(sum(z_force_in_root), 4)
    tot_x_force_in_roots = round(sum(x_force_in_root), 4)

    F_inside_root_with_z = []
    F_inside_root_with_x = []
    for i in range(number_roots):
        F_inside_root_with_z.append(z_force_in_root[i] /
                            math.sin(angle_with_force[i] * math.pi / 180))
        F_inside_root_with_x.append(x_force_in_root[i] /
                            math.cos(angle_with_force[i] * math.pi / 180))
    return tot_x_force_in_roots, tot_z_force_in_roots, x_force_in_root,
    z_force_in_root, np.array(F_inside_root_with_x), np.array(F_inside_root_with_z),
    tot_contribution_x, tot_contribution_z, angle_with_force, x_factor_of_tot_slippage

    # return 'with the direction of the force being', direction_force, \
    #        'degrees with the parallel of the coast the forces in the roots ' \
    #                                              'in parallel to the beach are', \
    #        tot_z_force_slippage, 'while the forces towards the beach are',
    #                                                    tot_x_force_slippage


def sum_moment_hor_vert(DBH, L, D, F, direction_force,
                                                    direction_first_root, tau_r):
    number_roots = int(belowground_structure(DBH, L, D)[2])
    forces_in_roots = force_in_roots(number_roots, L, F,
                                            direction_force, direction_first_root)
    resistance = max_resistance_forcing(number_roots, L, D,
                                                    tau_r, direction_first_root)

    # sum_moment =
    sum_x = resistance[0] - forces_in_roots[0]
    sum_z = resistance[1] - forces_in_roots[1]

    return sum_x, sum_z
```

J.2.3. Soil movement - shallow foundation

```
    def bearing_capacity(shape, DBH, M, s_u, Br, L, D, N_c, H, unit_weight,
                            omega, alpha, gamma): #horizontal load in kN/m
    g = 9.81  # m/s^2
    weight = (0.1848 * (DBH) ** 2.3524)
    ### weight of the roots + weight of the soil
    N = weight * g / 1000  # allometric formula gives kg --> * g /
                # 1000 --> / by width to get kN/m --> niet delen door Br
                # wnat je wilt geen kN/m
    # wanneer je e berekent moet je op m uitkomen,
            # of the wel je N moet gelijk zijn aan kN
    e = M / N
    B = Br - 2 * e
    # B_e / L_e = DC / AB
    R = 0.5 * L  # R is the straal -->
                L is the input from the circle or B --> those are equal
    h = R - e
    areaBL = 2 * (R ** 2 * np.arccos((R - h) / R) - (R - h) *
                                                    (2 * R * h - h ** 2) ** 0.5)
    if shape == 'Circle':
```

```
        s_c = 1.3  # terzaghi
    # if q_weight == 'zero':
    #     q = 0
    # if q_weight == 'self-weight':
    #     ### weight of the roots + weight of the soil
        q = g * weight / areaBL / 1000 + unit_weight * g / 1000 *
            D  # kPa (kg naar N = *9.81 --> kN = 9.81/1000 ==> kN/m2 = kPa)
    if shape == 'Rectangular':
        s_c = 1 + 0.2*Br/L
        area = Br*L
        # if q_weight == 'zero':
        #     q = 0
        # if q_weight == 'self-weight':
        q = g*weight/area/1000 + unit_weight*g/1000*D # kPa
    if D <= B:
        d_c = 1 + 0.4*D/B
    else:
        d_c = 1 + 0.4*np.arctan(D/B)
    m = (2 + B/L)/(1 + B/L)
    i_c = 1 - (m*H)/(B*L*s_u*N_c)
    if alpha != 0:
        b_c = 1 - (2*alpha)/(1 + np.pi)
    else:
        b_c = 1
    if omega != 0:
        g_c = 1-2*omega/(2+np.pi)
        q_lim = s_u * N_c * s_c * d_c * i_c * b_c * g_c + q +
                                        1/2*gamma*B*(1-0.4*B/L)*(-2*omega)
    else:
        g_c = 1
        q_lim = s_u*N_c*s_c*d_c*i_c*b_c*g_c+q
    return q_lim, weight, N, e, B, areaBL, 1/2*Br*N  #kPa
    # return q_lim, weight, 1, 1, B, 1, 1/2*Br *1  #kPa

def beam_calculation(shape, L, B, M): #alles in meters en kNm invullen

    if shape == 'Circle':
        I = 1/4 * np.pi * (1/2*L*1000)**4
    if shape == 'Rectangular':
        I = 1/12 * B*1000 * (L*1000)**3
    if shape == 'Triangular':
        I = 1/3 * B*1000 * (L*1000)**3
    if shape == 'Halfcircle':
        I = 1/8 * np.pi * (1/2*L*1000)**4
    sigma = M * 1000000  * (1/2 * L*1000) / (I)
    return sigma, I
```

J.2.4. Soil movement - Uplift

```
    import numpy as np
import pandas as pd
import matplotlib.pyplot as plt
from operator import truediv
import seaborn as sns
import math
import array
```

```
from Resistance_forces_soilrupture_shallowfoundation import bearing_capacity
from Resistance_forces_soilrupture_shallowfoundation import beam_calculation
from Resistance_forces_anchoring2 import belowground_structure

from Resistance_forces_anchoring2 import formula_pulloutforce_adhesion
from Resistance_forces_anchoring2 import formula_pulloutforce_data
from Resistance_forces_anchoring2 import max_resistance_forcing
from Resistance_forces_anchoring2 import force_in_roots
from Resistance_forces_anchoring2 import sum_moment_hor_vert
from root_breakage import force_to_tensile_strength

### 1 N/mm2 equals 1000 kN/m2
max_compressive_strength = 79.96
max_M = 0.58  # kNm
max_F = 0.5413  # kN
unit_weight_gl = 1391.3  # kg/l
unit_weight = unit_weight_gl / 1000 # kg/m3
g = 9.81

BGV_925 = belowground_structure(9.25, 3, 1)[1] # diameter doesn't matter,
                                                    is not used in volume
diameter_combination = np.array([0.05, 0.025, 0.01, 0.005])

L = 3 # length root [m]
volume005 = 2 * L * np.pi * (diameter_combination[0]/2)**2
volume0025 = 2 * L * np.pi * (diameter_combination[1]/2)**2
volume001 = 70 * L * np.pi * (diameter_combination[2]/2)**2
rest_volume = BGV_925 - volume0025 - volume005 - volume001

area001 = np.pi * (diameter_combination[2] / 2) ** 2
area0005 = np.pi * (diameter_combination[3] / 2) ** 2
number_of_roots001 = rest_volume / (L * area001)

number_roots_changing = np.array([2, 2, 70, rest_volume / (L * area0005)])
int_number_roots = np.array([2, 2, 70, 253])

I_combination = []
contribution_moment1 = []
for i in range(len(diameter_combination)):
    I_combination.append(beam_calculation('Circle', diameter_combination[i],
                                          diameter_combination[i], max_M)[1])
    contribution_moment1.append(number_roots_changing[i] * I_combination[i]/L)

total_contribution_moment = sum(contribution_moment1)
contribution_moment = []
moment_root = []
for i in range(len(diameter_combination)):
    contribution_moment.append(contribution_moment1[i] /
                    (total_contribution_moment * number_roots_changing[i]))
    moment_root.append(max_M * contribution_moment[i])

max_bending_root = []
for i in range(len(diameter_combination)):
    max_bending_root.append(moment_root[i]*1000000 *
                        (1/2*diameter_combination[i]*1000 / I_combination[i]))
```

```
def moment_soil_weight(unit_weight, depth, diameter):
    radius = 1/2 * diameter
    area = np.pi * (radius)**2
    tot_weight_moment = unit_weight * depth * area
    force_weight = g / 1000 * tot_weight_moment
    moment_weight = force_weight * 1/2 * radius
    return moment_weight #kNm

test_moment_weight = moment_soil_weight(unit_weight, 0.8, 3)
print(test_moment_weight)

def moments_in_roots(DBH, L, D, direction_first_root, direction_force,
                                                            moment_forcing):
    # direction_force = 90 if along the coast, 0 if horizontal to
    #                                 towards the coast x = direction to land,
    # z = along the coast
    number_roots = int(belowground_structure(DBH, L, D)[2])
    angle_with_force = np.ones(int(number_roots))
    count_up = 0
    count_down = 0
    count_rest = 0
    for i in range(number_roots):
        angle_with_force[i] = float(direction_first_root)-float(direction_force)
                                                    + 360 / float(number_roots) * i
        if angle_with_force[i] < float(30) or angle_with_force[i] > float(330):
            count_down += 1
        elif angle_with_force[i] > float(150) and angle_with_force[i] < float(210):
            count_up += 1
        # moment_contribution_changing_values =+ 1 * I / L
        # elif angle_with_force[i] < (45) and angle_with_force[i] > (270+45):
        #     count_down[N] += 1
        else:
            count_rest += 1

    moment_contribution = count_down * 4 + count_up * 3
    Mtot_roots_windward = moment_forcing * (count_up * 3) / moment_contribution
    Mtot_roots_leeward = moment_forcing * (count_down * 4) / moment_contribution
    Msingle_root_windward = Mtot_roots_windward / count_up
    Msingle_root_leeward = Mtot_roots_leeward / count_down

    return Mtot_roots_windward, Mtot_roots_leeward, Msingle_root_windward,
    Msingle_root_leeward, number_roots, count_up, count_down, len(angle_with_force)

test = moments_in_roots(9.25, 3, 0.0063, 0, 0, max_M)

def belowground_structure(DBH, length_root, diameter_root):
        # DBH in cm, diameter/length in m
    p = 0.732
    BGB = 0.199 * p**0.899 * (DBH)**2.22
    BGV = BGB * 1000 / 0.455 * 1 * 10 ** (-6)
    # 0.455 g/cm3 = 455 kg/m3 of 1 cm3 = 1*10^-6 m3
    area = np.pi * (diameter_root / 2) ** 2
    number_of_roots = BGV / (length_root * area)
```

```
    return BGB, BGV, number_of_roots


def moments_in_roots_changing_diff2(situation, DBH, Length_roots, D, ratio,
        E, c, direction_first_root, direction_force, moment_forcing, alpha):
    # I is in mm4 naar m4 geeft * 10**-12
    # daardoor moet E in kPa dit is gelijk aan 1 kN/m2 = 1 kPa
    # direction_force = 90 if along the coast, 0 if horizontal to
    #                         towards the coast x = direction to land,
    # z = along the coast
    volume_roots = belowground_structure(DBH, Length_roots[0], D[0])[1] # m3
    number_roots_CH = []
    for i in range(len(Length_roots)):
        partial_volume = ratio[i] * volume_roots
        number_roots_CH.append(int(partial_volume / (Length_roots[i]*np.pi *
                                                     (D[i]/2)**2)))

    I_mm4 = []
    moment_contribution_CH = []
    moment_contr_windward_CH = []
    moment_contr_leeward_CH =[]
    count_up = np.zeros(len(Length_roots))
    count_down = np.zeros(len(Length_roots))
    count_rest = np.zeros(len(Length_roots))
    for i in range(len(Length_roots)):
        I_mm4.append(beam_calculation('Circle', D[i], D[i], max_M)[1]*10**(-12))
                                                     #eenheid is mm4

    for N in range(len(Length_roots)):
        k = c * D[N]
        angle_with_force = np.zeros(number_roots_CH[N])
        for i in range(number_roots_CH[N]):
            angle_with_force[i] = float(direction_first_root+ N*5 )-
                    float(direction_force) + 360 / float(number_roots_CH[N]) * i
            # if angle_with_force[i] < 270 and angle_with_force[i] > 90:
            if angle_with_force[i] < float(0+1/2*alpha) or
                                angle_with_force[i] > float(360 - 1/2*alpha):
                count_down[N] += 1
            elif angle_with_force[i] > float(180 - 1/2*alpha) and
                                 angle_with_force[i] < float(180+1/2*alpha):
                count_up[N] += 1
            else:
                count_rest[N] += 1
        if situation == '1':
            moment_contr_windward_CH.append(count_up[N] * 3 * I_mm4[N] /
                                                    Length_roots[N] * E)
            moment_contr_leeward_CH.append(count_down[N] * 3 * I_mm4[N] /
                                                     Length_roots[N]* E)
            moment_contribution_CH.append(count_down[N] * 3 * I_mm4[N] /
            Length_roots[N] * E + count_up[N] * 3 * I_mm4[N] / Length_roots[N] * E)
        if situation == '2':
            moment_contr_windward_CH.append(count_up[N] * 3 * I_mm4[N] /
                                                     Length_roots[N] * E)
            moment_contr_leeward_CH.append(count_down[N] * 4 * I_mm4[N] /
                                                     Length_roots[N] * E)
            moment_contribution_CH.append(count_down[N] * 4 * I_mm4[N] /
```

```
                                Length_roots[N] * E + count_up[N] * 3 * I_mm4[N] /
                                                                    Length_roots[N] * E)
        if situation == '3':
            moment_contr_windward_CH.append(count_up[N] * 4 * I_mm4[N] /
                                                                    Length_roots[N] * E)
            moment_contr_leeward_CH.append(count_down[N] * 4 * I_mm4[N] /
                                                                    Length_roots[N] * E)
            moment_contribution_CH.append(count_down[N] * 4 * I_mm4[N] /
            Length_roots[N]  * E + count_up[N] * 4 * I_mm4[N] / Length_roots[N] * E)
        if situation == '4':
            moment_contr_windward_CH.append(count_up[N] * 3 * (E * I_mm4[N]) /
                                                                    Length_roots[N])
            moment_contr_leeward_CH.append(count_down[N] * (k / 4) * 1 /
                                                ((k / (4*E*I_mm4[N]))**(3/4)))
            moment_contribution_CH.append(count_up[N] * 3 * (E * I_mm4[N]) /
                                Length_roots[N] + count_down[N] * (k / 4) * 1 /
                                                ((k / (4*E*I_mm4[N]))**(3/4)))
        if situation == '5':
            moment_contr_windward_CH.append(count_up[N] * 3 * (E * I_mm4[N]) /
                                                                    Length_roots[N])
            moment_contr_leeward_CH.append(count_down[N] * (k / 2) * 1 /
                                            ((k / (4 * E * I_mm4[N])) ** (3 / 4)))
            moment_contribution_CH.append(count_up[N] * 3 * (E * I_mm4[N]) /
                                Length_roots[N] + count_down[N] * (k / 2) * 1 /
                                                ((k / (4*E*I_mm4[N]))**(3/4)))

tot_moment_contribution_CH = sum(moment_contribution_CH)

Mtot_roots_windward = sum(moment_contr_windward_CH)
Mtot_roots_leeward = sum(moment_contr_leeward_CH)

Mtot2_root_windward = np.zeros(len(Length_roots))
Mtot2_root_leeward = np.zeros(len(Length_roots))
Msingle_root_windward = np.zeros(len(Length_roots))
Msingle_root_leeward = np.zeros(len(Length_roots))
test = []

for J in range(len(Length_roots)):
    if situation == '1':
        test.append('Situation1')
        # Mtot2_root_windward[J] = moment_forcing / tot_moment_contribution_CH
                                * (count_up[J] * 1 * I_mm4[J] * Length_roots[J])
        # Mtot2_root_leeward[J] = moment_forcing / tot_moment_contribution_CH
                            * (count_down[J] * 4 * I_mm4[J] * Length_roots[J])

        Mtot2_root_windward[J] = moment_forcing / tot_moment_contribution_CH * (
                    count_up[J] * 3 * I_mm4[J] / Length_roots[J] * E)
        Mtot2_root_leeward[J] = moment_forcing / tot_moment_contribution_CH * (
                    count_down[J] * 3 * I_mm4[J] / Length_roots[J] * E)
    if situation == '2':
        test.append('Situation2')
        Mtot2_root_windward[J] = moment_forcing / tot_moment_contribution_CH * (
                    count_up[J] * 3 * I_mm4[J] / Length_roots[J] * E)
        Mtot2_root_leeward[J] = moment_forcing / tot_moment_contribution_CH * (
                    count_down[J] * 4 * I_mm4[J] / Length_roots[J] * E)
    if situation == '3':
```

```
            test.append('Situation3')
            Mtot2_root_windward[J] = moment_forcing / tot_moment_contribution_CH * (
                        count_up[J] * 4 * I_mm4[J] / Length_roots[J] * E)
            Mtot2_root_leeward[J] = moment_forcing / tot_moment_contribution_CH * (
                        count_down[J] * 4 * I_mm4[J] / Length_roots[J] * E)
        if situation == '4':
            test.append('Situation4')
            Mtot2_root_windward[J] = moment_forcing / tot_moment_contribution_CH *
                                                      moment_contr_windward_CH[J]
            Mtot2_root_leeward[J] = moment_forcing / tot_moment_contribution_CH *
                                                      moment_contr_leeward_CH[J]
        if situation == '5':
            test.append('Situation5')
            Mtot2_root_windward[J] = moment_forcing / tot_moment_contribution_CH *
                                                      moment_contr_windward_CH[J]
            Mtot2_root_leeward[J] = moment_forcing / tot_moment_contribution_CH *
                                                      moment_contr_leeward_CH[J]
        Msingle_root_windward[J] = Mtot2_root_windward[J] / count_up[J]
        Msingle_root_leeward[J] = Mtot2_root_leeward[J] / count_down[J]

    # moment_contribution = count_down * 4 + count_up * 1
    # Mtot_roots_windward = moment_forcing * (count_up * 1) / moment_contribution
    # Mtot_roots_leeward = moment_forcing * (count_down * 4) / moment_contribution
    # Msingle_root_windward = Mtot_roots_windward / count_up
    # Msingle_root_leeward = Mtot_roots_leeward / count_down

    total_moment_leeward = sum(Mtot2_root_leeward)
    total_moment_windward = sum(Mtot2_root_windward)

    return tot_moment_contribution_CH, Mtot2_root_windward, Mtot2_root_leeward,
    Msingle_root_windward, Msingle_root_leeward, I_mm4, number_roots_CH,
    volume_roots, total_moment_windward, total_moment_leeward, count_up,
    count_down, count_rest, angle_with_force, moment_contr_windward_CH,
    moment_contr_leeward_CH


### comparison Mroot and Msoil:
# if angle_rotation is positive, the soil is coming up

def force_rotation_single_root(situation, E, length_root, diameter_root,
                                        moment, max_M, unit_weight, depth):
    I_m4 = beam_calculation('Circle', diameter_root, diameter_root, max_M)[1] *
                                                                  10 ** (-12)
    q = unit_weight * g / 1000 * depth
    if situation == '1245':
        force_angle = 1/3 * moment * length_root / (E*I_m4)
        resistance_angle = 1 / 6 * q * length_root ** 3 / (E * I_m4)
        pos_neg_rot = force_angle - resistance_angle
    elif situation == '3':
        force_angle = 1/4 * moment * length_root / (E * I_m4)
        resistance_angle = 1/6 * q * length_root**3 / (E * I_m4)
        pos_neg_rot = force_angle - resistance_angle
    return force_angle - resistance_angle, force_angle, resistance_angle
```

```
def uprooting_changing_parameter_single(depth, unit_weight, length_root, E,
                                                    diameter_root, max_M):
    q = unit_weight * g / 1000 * depth
    I_m4 = beam_calculation('Circle', diameter_root, diameter_root, max_M)[1] *
                                                                    10 ** (-12)
    angle_resistance = 1/6 * q * length_root**2 / (E * I_m4)
    return angle_resistance


#total resistance
def resistance_one_root(unit_weight, depth, length_root):
    q = unit_weight * g / 1000 * depth
    M = 1/2 * q * length_root**2
    return M

def total_resistance_rootmat(straal, depth, unit_weight, alpha):
    area = (alpha/360) * np.pi * straal**2
    M = unit_weight * g / 1000 * area * depth * 4 * straal / ( 3* np.pi)
    return M
```